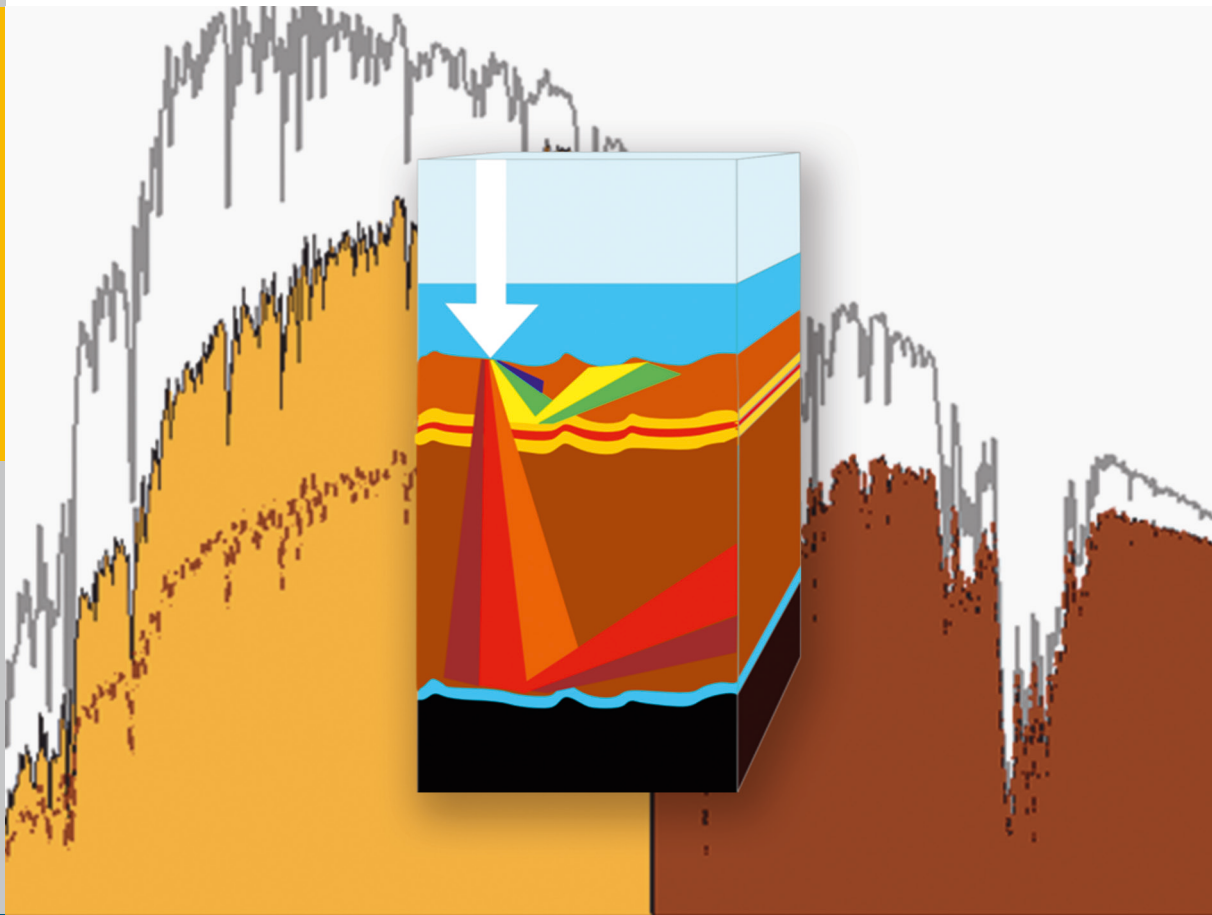


Light Management by Intermediate Reflectors in Silicon-based Tandem Solar Cells

André Hoffmann



Energie & Umwelt /
Energy & Environment
Band/ Volume 345
ISBN 978-3-95806-186-6

Forschungszentrum Jülich GmbH
Institute of Energy and Climate Research
IEK-5 Photovoltaics

Light Management by Intermediate Reflectors in Silicon-based Tandem Solar Cells

André Hoffmann

Schriften des Forschungszentrums Jülich
Reihe Energie & Umwelt / Energy & Environment

Band / Volume 345

ISSN 1866-1793

ISBN 978-3-95806-186-6

Bibliographic information published by the Deutsche Nationalbibliothek.
The Deutsche Nationalbibliothek lists this publication in the Deutsche
Nationalbibliografie; detailed bibliographic data are available in the
Internet at <http://dnb.d-nb.de>.

Publisher and
Distributor: Forschungszentrum Jülich GmbH
Zentralbibliothek
52425 Jülich
Tel: +49 2461 61-5368
Fax: +49 2461 61-6103
Email: zb-publikation@fz-juelich.de
www.fz-juelich.de/zb

Cover Design: Grafische Medien, Forschungszentrum Jülich GmbH

Printer: Grafische Medien, Forschungszentrum Jülich GmbH

Copyright: Forschungszentrum Jülich 2016

Schriften des Forschungszentrums Jülich
Reihe Energie & Umwelt / Energy & Environment, Band / Volume 345

D 82 (Diss. RWTH Aachen University, 2016)

ISSN 1866-1793
ISBN 978-3-95806-186-6

The complete volume is freely available on the Internet on the Jülicher Open Access Server (JuSER)
at www.fz-juelich.de/zb/openaccess.



This is an Open Access publication distributed under the terms of the [Creative Commons Attribution License 4.0](https://creativecommons.org/licenses/by/4.0/),
which permits unrestricted use, distribution, and reproduction in any medium, provided the original work is properly cited.

I say it is impossible that so sensible a people, under such circumstances, should have lived so long by the smoky, unwholesome, and enormously expensive light of candles, if they had really known that they might have had as much pure light of the sun for nothing.

Benjamin Franklin

1. Abstract

Multijunction solar cells provide a route to further increase the efficiency of solar cells. By stacking different band-gap materials, thermalization losses can be decreased. Maximizing the efficiency of series-connected multijunction solar cells gets complex as a variety of different layers is involved. The application of nano-scale textures which scatter and diffract the light in order to increase the light path and absorption. An advanced light management combining light trapping and spectral distribution is necessary to gain maximal output. In this work, light management in silicon-based multijunction solar cells by intermediate reflectors (IR) is studied. As soon as the thickness of absorber layers in multijunction devices is physically limited, IRs increase the light path in the sub cells and contribute to the matching of currents and power of the sub cells in series-connected multijunction solar cells. As each element added to a working device increases its complexity, the understanding of their interplay and underlying loss mechanisms is crucial to obtain an improvement of the device. Thin-film silicon tandem solar cells made of hydrogenated amorphous and microcrystalline silicon (also called 'micromorph') are chosen as model system for the analysis of the optics in silicon-based multijunction solar cells, as they are a well established industrially up-scalable technology and exhibit the important characteristics of other multijunction cell material systems: Thin-film layers, nano-structured surfaces, as well as physical limitations of thicknesses and a broad utilization of the solar spectrum. The combination of thin-film layer stack and nano-structured surfaces demands for a treatment of the solar cell as a nano-optical device. Motivated by the results of experimental studies, tandem solar cells are modeled by thin-film optics and rigorous optical simulations. An agreement between simulation to experimental results allows for an investigation and optimization of these devices.

First, the optical losses induced by intermediate reflectors in tandem solar cells were studied. Therefore, tandem solar cells without and with micro-crystalline silicon oxide intermediate reflectors were fabricated on different aluminum -doped

zinc oxide front contacts which had partially been treated to decrease absorption within the zinc oxide. Increased cell reflectance and parasitic absorption due to the IR were observed. The comparison to tandem solar cells on non-treated front contacts showed that in spite of the increased reflectance, parasitic absorption in the front contacts due to the IR is negligible. The results are supported by optical simulations of tandem solar cells with intermediate reflector which, additionally, allowed to quantify parasitic losses. Furthermore, it is shown that the decrease of the refractive index of the silicon oxide intermediate reflector results in a decrease of parasitic absorption and an increase of total tandem cell current if layer thicknesses are adapted. In this case, parasitic reflection of light by the IR out of the solar cell is determined to be the dominating optical loss mechanism.

Second, the reflection losses were assigned to the low spectral selectivity of reflection of single layer IRs. Basing on this, a 1D photonic crystal produced of conductive and low absorptive thin-film materials which are available in-situ in thin-film silicon solar cell production is designed for a flat layer stack. The influence of surface texture on the effectiveness of the multilayer IR is studied and it is shown that the IR functionality remains for a textured solar cell. A multilayer IR consisting of aluminum-doped zinc oxide (ZnO:Al) and microcrystalline silicon oxide ($\mu\text{c-SiO}_x\text{:H}$) layers was successfully integrated into a nano-textured thin-film silicon solar cell and decreases the bottom cell losses in comparison to other IRs while still increasing the top cell current density by $\Delta J_{\text{sc,top}} = 1.2 \text{ mA/cm}^2$. A further optimization of material choice and layer quantity shows that the potential of further increasing top cell enhancement and spectral selectivity by increasing the number of layers exists but that possible gains are low.

Third, the top cell current increase was investigated in detail. Therefore, a new method to extract the angular distribution of light within a thin amorphous silicon film from rigorous optical simulations was developed and applied to a-Si:H cells on both, periodic gratings and randomly textured front structures. For photonic structures, absorption in the silicon film is assigned to the coupling of incident light to leaky waveguide modes by the grating. It is shown that in case of silicon films on randomly textured surfaces, these waveguide modes are present as well but broadened due to the superposition of a variety of distinct periods and heights. As a quantity for light trapping in thin films, the integrated scattering intensity *ISI* could be established which describes the coupling to waveguide modes and correlates well to the absorption enhancement in a-Si:H film with different reflec-

tors.

Fourth, absorption and transmission enhancements are investigated on a variety of periodic and randomly textured substrates. In a broad experimental and simulation study, tandem solar cells on various substrates have been deposited and reproduced by rigorous optical simulations. An artificial modification of the substrate texture, revealed the front texture scattering distribution and the surface angles at the IR to be the decisive surface parameters to determine the effectiveness of the IR. A large dependence of the functionality of the IR on the angular intensity distribution in the top cell is observed. In particular, two different reflection modes of the IR are observed: In reflection mode (A) below the critical angle of total internal reflection, light propagates into the IR and the reflectance was dependent on interference of the incident light and light reflected at the back IR interface. The effectiveness of the IR on surface textures comprising low surface angles and low parallel wave vector transfer as APCVD $\text{SnO}_2\text{:F}$ or sputter-etched ZnO:Al textures can be well reproduced by a thin-film model applying the angular scattering distribution at the front side. If the critical angle is surpassed, light was totally internally reflected and tunnels through the IR as an evanescent wave. This reflection mode (B) results in large absorption enhancements for thick intermediate layers but is always connected to reflection losses. A spectral reflectance parameter *SRP* was introduced. It was used as a tool to analyze the influence of IR refractive index and thickness on the absorption enhancement and bottom cell transmission losses. The theory was successfully applied to understand the interplay of front side texture and IR reflectance on the relevant randomly textured surfaces. The study of the IR effectiveness on photonic structures emphasized the importance to examine the waveguide modes, which do not just increase top cell enhancement, but further induce parasitic reflection losses in the NIR range which are disadvantageous to the current of further bottom cells. The analysis reveals that these losses can be decreased by broadening the resonances as it is the case in randomly textured solar cells. Simulations on tandem solar cells on LPCVD ZnO:B reproduce the results of previous experimental studies.

Contents

1 Abstract	3
2 Zusammenfassung	9
3 Introduction	13
4 Fundamentals	19
4.1 Electrodynamics and Optics	19
4.1.1 Classical Electrodynamics	19
4.1.2 Absorption in Semiconducting Materials	22
4.1.3 Nano-Optics and Photonics	23
4.1.4 Computational Electrodynamics	27
4.1.5 Fourier Analysis	31
4.2 Thin-film Silicon Tandem Solar Cells	34
4.2.1 Photovoltaic devices	34
4.2.2 Solar Spectrum	35
4.2.3 Device Structure of Thin-Film Silicon Solar Cells	35
4.2.4 Light Trapping in Solar Cells	37
4.2.5 Multi-junction Solar Cells	41
4.3 Experimental Methods	46
4.3.1 Solar Cell Fabrication	46
4.3.2 Device Characterization	49
5 Intermediate Reflectors in Tandem Solar Cells - Identification of Loss Mechanisms	53
5.1 Motivation	53
5.2 Parasitic Losses in Tandem Solar Cells	54
5.3 Annealing Experiment	55
5.4 Rigorous Optical Simulation	58
5.4.1 Influence of Refractive Index	60
6 Spectrally Selective Intermediate Reflectors	63

6.1	Design Criteria	63
6.2	Design of Multilayer Filters	65
6.3	Experimental Realization	70
6.3.1	Integration into flat solar cells	71
6.4	Influence of the Roughness on Multilayer Intermediate Reflector . .	73
6.5	Fabrication of Thin-Film Silicon Prototype on Textured Substrates	74
6.6	Additional Improvements	77
6.6.1	Variation of the Materials	77
6.6.2	Influence of the Quantity of Layers	78
6.7	Comparison to Other Spectrally Selective Intermediate Reflectors .	79
6.7.1	3D Photonic Crystal IR	79
6.7.2	Plasmonic IR	81
6.7.3	Discussion	83
6.8	Summary	84
7	Investigation of Light Trapping by Coupling into Guided Modes in the a-Si:H Top Cell	85
7.1	Waveguide Modes in Thin-Films on 2D Grating Structures	85
7.1.1	Evaluation of different grating geometries	86
7.1.2	Variation of the back/ intermediate reflector	87
7.2	Waveguide Modes in Randomly Textured a-Si:H Films	91
7.3	Local Effects of Surface Features in a-Si:H Films	94
8	Interplay of Intermediate Reflector and Surface Texture	99
8.1	Multilayer IR on Various Substrates	99
8.2	Substrate Variation	101
8.2.1	From Experiment to Simulation	101
8.2.2	Variation of Surface Parameters	104
8.2.3	Conclusion	107
8.3	Angular Reflection Modes	109
8.3.1	Reflection of Thin Layers	109
8.3.2	Summary	113
8.4	Theory applied to Randomly Textured Tandem Solar Cells	113
8.4.1	Spatial Dependence	113
8.4.2	Intermediate Reflector Thickness Dependence	118
8.5	Theory applied to Tandem Solar Cells on Periodic Grating Textures	122

8.5.1	Influence of the Grating Height on IR Reflectance	124
8.5.2	Influence of the IR Texture and Geometry on Absorption . .	127
8.5.3	Influence of the Grating Height on Absorption	132
8.5.4	Role of Leaky Waveguide Modes in a-Si:H Top Cell	138
8.5.5	Influence of the Refractive Index of the IR on Absorption Enhancement	143
8.5.6	Figure of Merit for Spectral Selectivity	150
8.6	From Periodic to Random Textures	156
8.7	Summary and Discussion	159
8.7.1	Design Workflow For IR Optimization for Multijunction So- lar Cells	161
9	Summary and Outlook	163
A	Appendix	167
A.1	Optical Data	167
A.2	FDTD simulations	167
B	Publications	191
B.1	Journal publications related to this work	191
B.2	Further contributions to journal publications	192
C	Danksagung	193
D	Curriculum Vitae	197

2. Zusammenfassung

Stapelsolarzellen stellen eine vielversprechende Methode dar, die Effizienz von Solarzellen weiter zu steigern. Durch das Aufeinanderstapeln von Materialien unterschiedlicher Bandlücken können Thermalisierungsverluste erheblich verringert werden. Da eine Vielzahl unterschiedlicher Schichten involviert sind, ist die Maximierung des Wirkungsgrades serienverschalteter Stapelsolarzellen äußerst komplex. Eine weitere Herausforderung stellt die Anwendung nanoskopischer Texturen dar, die das Licht streuen und beugen; und so den Lichtweg innerhalb des Absorbers und folglich die Absorption erhöhen. Ein ausgeklügeltes Management des Lichtes, welches sowohl das Einfangen des Lichtes, als auch seine spektrale Verteilung beinhaltet, ist notwendig, um den bestmöglichen Ertrag zu erzielen. In der vorliegenden Arbeit wird Lichtmanagement in Silizium-basierten Stapelsolarzellen durch Zwischenreflektoren untersucht. Zwischenreflektoren ermöglichen durch partielle Rückreflexion eine Erhöhung des Lichtwegs im Absorber und folglich auch der Absorption in der vorgeschalteten Topzelle mit höherer Bandlücke. Im Fall physikalisch limitierter Schichtdicken ermöglicht ein Zwischenreflektor außerdem eine Strom-Anpassung zwischen Top- und Bottomzelle in serienverschalteten Stapelsolarzellen. Da durch jedes optische Element die Komplexität des Gesamtsystems erhöht wird, ist ein Verständnis des Zusammenspiels der unterschiedlichen optischen Komponenten, sowie der einzelnen Verlustmechanismen entscheidend für das Design eines verbesserten Bauteils. Als Modellsystem werden in dieser Arbeit Dünnschichtsilizium-Solarzellen aus amorphem und mikroristallinem Silizium verwendet. Diese stellen sowohl ein weitverbreitetes, industriell hochskalierbares System dar; vereinen aber auch die Charakteristika anderer Stapelsolarzellen: Dünne Schichten, nano-strukturierte Oberflächen sowie eine physikalische Limitierung der Dicken und eine breite Ausnutzung des Sonnenspektrums. Die Kombination von komplexen Dünnschichtstapeln und nano-strukturierten Oberflächen bedarf einer nano-optischen Betrachtung der Solarzelle. Motiviert durch die Ergebnisse experimenteller Studien, wurden Solarzellen durch Dünnschichtoptik und rigorose optische Simulationen auf

Hochleistungsrechnern modelliert. Eine gute Übereinstimmung zwischen Simulation und Experiment ermöglicht hierbei die Untersuchung und Optimierung solcher Solarzellen. Der Ergebnisteil dieser Arbeit ist in vier Teile unterteilt:

Zuerst werden optische Verluste durch Zwischenreflektoren in Tandemsolarzellen untersucht. Dazu wurden Tandemsolarzellen ohne und mit mikrokristallinen Siliziumoxid Zwischenreflektoren auf unterschiedliche Vorderseitenkontakte aufgebracht, die für eine Verringerung der parasitären Absorption im Vorderseitenkontakt behandelt wurden. Erhöhte Zellreflexion und parasitäre Absorption durch den Zwischenreflektor konnten so festgestellt werden. Beim Vergleich von Tandemsolarzellen auf nicht behandelten und behandelten Substraten zeigte sich, dass trotz erhöhter Reflexion parasitäre Absorption in den Frontkontakten keine wesentliche Rolle spielt. Die Ergebnisse konnten durch optische Simulationen der Stapelsolarzellen bestätigt und quantifiziert werden. Außerdem konnte gezeigt werden, dass sich eine Verringerung des Brechungsindex des Zwischenreflektors in einer Verringerung der parasitären Absorption und einer Erhöhung der Gesamtstromdichte auswirkt. In diesem Fall ist der dominierende Verlustmechanismus die unvollständige Absorption.

In einem zweiten Teil wird eine Strategie gegen die hohe parasitäre Absorption durch spektrale Selektivität entwickelt. Eindimensionale photonische Kristalle aus leitfähigen und transparenten Materialien, die in-situ bei der Deposition von Dünnschichtsolarzellen abgeschieden werden können, werden für eine flache, nicht-texturierte Zellkonfiguration designt. Ein Mehrlagenzwischenreflektor aus Aluminiumdotiertem Zinkoxid und mikrokristallinem Siliziumoxid wurde numerisch optimiert und in nanotexturierte Tandem-Dünnschichtsolarzellen integriert. Der Mehrlagenzwischenreflektor verringert die Verluste in der Bottomzelle im Vergleich zu herkömmlichen Zwischenreflektoren erheblich. Die Kurzschlussstromdichte in der Topzelle konnte um $\Delta J_{sc,top} = 1.2 \text{ mA/cm}^2$ erhöht werden. Eine weitere Optimierung der Materialwahl und Schichtzahl zeigt, dass die experimentell umgesetzte Konfiguration nahezu die maximale Verbesserung für reale Materialien darstellt und auch unter höherem Aufwand nur sehr geringe Verbesserungen erzielt werden.

Im dritten Teil wird die Verlängerung des Lichtwegs in der Topzelle detailliert untersucht. Dazu wurde eine Methode entwickelt, aus rigorosen optischen Simulationen die Verteilung von Wellenvektoren in dünnen Absorberschichten zu bestimmen und darüber die Absorption in der Schicht zu extrahieren. Die Auswertung wurde

für eine Serie von optischen Simulation von amorphen Siliziumschichten sowohl auf periodischen Gittern, als auch auf ungeordneten, stochastischen Strukturen angewendet. Für optische Gitter kann die Absorption in der Siliziumschicht auf das Ankoppeln des einfallenden Sonnenlichtes in 'leaky' [engl. undichte] Wellenleitermoden durch Interaktion mit dem Gitter zurückgeführt werden. Es wird gezeigt, dass im Fall von Siliziumschichten auf ungeordneten, stochastischen Strukturen, diese Wellenleitermoden auch vorhanden sind und das Licht an sie koppeln kann. Die Resonanzen werden allerdings durch die Überlagerung unterschiedlicher Raumfrequenzen und Höhen stark verbreitert. Die Kopplung an Wellenleitermoden wird quantitativ durch die Größe der integrierten Streuintensität *ISI* beschrieben. Diese Größe korreliert zu den tatsächlich in Experimenten gemessene Erhöhung der Absorption in Topzellen aus amorphem Silizium bei unterschiedlichen Zwischen- und Rückreflektoren und liefert so eine gute Erklärung des Verhaltens von

Der vierte Teil widmet sich der Untersuchung der Absorptionserhöhung in Top- und Bottomzelle für eine Vielzahl verschiedener periodischer und ungeordneter, stochastischer Oberflächentexturen. In einer breit-angelegten experimentellen und Simulationsstudie, wurden Tandemsolarzellen auf verschiedenen Substraten deponiert und durch rigorose optische Simulationen reproduziert. Eine künstliche Modifikation der Oberflächentextur zeigt, dass die Streuwinkelverteilung an der Frontseitentextur, sowie die Oberflächenwinkel am Zwischenreflektor die entscheidenden Parameter zur Bestimmung der Effektivität eines Zwischenreflektors sind. Eine starke Abhängigkeit der Funktionsweise des Zwischenreflektors von der internen Winkelverteilung in Topzelle wurde beobachtet. Es lassen sich zwei Reflexionsmodi unterscheiden: Im Reflexionsmodus A (unterhalb des kritischen Winkels der Totalreflexion) propagiert das Licht in den Zwischenreflektor und die Reflexion wird durch Interferenz ein und auslaufender Welle bestimmt. Die Wirkungsweise des Zwischenreflektors auf Oberflächentexturen, die niedrige Oberflächenwinkel und kleine Wellenvektorüberträge aufweisen kann durch dieses Modell sehr gut durch ein flaches Dünnschichtmodell reproduziert werden. Wird der kritische Winkel der Totalreflexion überschritten, so wird das Licht totalreflektiert und kann als evaneszente Welle den Zwischenreflektor durchtunneln. Dieser Reflexionsmodus B führt zu höheren Absorptionsverstärkungen in der oberen Zelle, ist allerdings immer mit optischen Verlusten verknüpft. Ein spektraler Reflexionsparameter *SRP* wurde eingeführt und verwendet, um den Einfluss des Brechungsindex und der Schichtdicke des Zwischenreflektors auf die Absorptionserhöhung in Top-

und Bottomzelle zu charakterisieren. Das Model wurde erfolgreich angewendet um das Zusammenspiel von Vorderseitentexturen und Reflektivität des Zwischenreflektors auf üblichen Oberflächentexturen zu verstehen. Die Untersuchung der Effektivität des Zwischenreflektors auf Gitter-Strukturen unterstreicht die Wichtigkeit einer genauen Betrachtung der Wellenleitermoden, die nicht nur eine Erhöhung der Absorption in der Topzelle herbeiführen, sondern auch parasitäre Verluste im Nahinfrarot auslösen, welche sich negativ auf die Gesamt-Kurzschlussstromdichte auswirken. Die Analyse zeigt, dass diese Verluste erheblich vermindert werden können, wenn die scharfen Wellenleiterresonanzen verbreitert werden und die Ordnung der Gitterstrukturen gebrochen wird. Simulationen von Tandemsolarzellen auf LPCVD-hergestelltem Bor-dotiertem Zinkoxid bestätigen die Trends experimenteller Studien aus der Literatur.

3. Introduction

Photovoltaic energy conversion provides a direct way of converting available sun irradiance into electric current. To compete with conventional electricity generation processes which predominantly base on the combustion of fossile fuels, the main aim is the reduction of costs per produced electrical power [1, 2]. Since the first solar cell has been developed in the 1960s [3], materials, devices and systems have been highly optimized [4]. The combination of large scientific progress and a political framework for the emerging solar industry has set the path to a dramatic cost reduction in the last decades. Solar module prices have come down to a price of 0.60 EUR/W_p in Germany by November 2014 [5]. The global electricity production by PV reached 139 GW in 2012 and will rise up to 320 - 430 GW in 2018 [6, 7]. Although various thin-film technologies such as chalcopyride- and kesterite-based, cadmium telluride, and thin-film silicon have entered the market and reached laboratory efficiencies of 21.7% [8], the largest share is still hold by crystalline silicon (c-Si) solar cells [5]. Price reduction and efficiency of thin-film technologies have not yet been high enough to outperform the industrially advanced c-Si technology. Yet, other significant improvements in material quality and optical concepts of the device have led to conversion efficiencies of up to 25.6% [9] approaching the thermodynamic Shockley-Queisser limit [10].

Since PV device efficiencies have not yet reached a saturation and further cost reduction is necessary, state-of-the-art research aims for an increase of the open-circuit voltage V_{oc} by reduction of entropic losses [11, 12] and an increase of current generation while reducing material usage at the same time. By diffraction and scattering, light can be deflected into large angles, such that it is totally internally reflected at the interfaces between the absorber and the contact layers and, thus, trapped therein. The term **light trapping** has been established for the discipline optimizing the optical performance of the solar cell and de-coupling optical from physical thickness [4].

Light trapping can be achieved by patterning the solar cell's interfaces by di-

electric or plasmonic periodic gratings [13–20], randomly distributed stochastic (predominantly as-grown or by wet-chemical etching) textures [21–23] or patterning the contacts and absorbers as photonic crystals [24–29]. Due to its simplicity, random textures have been established as the standard for both, high efficiency c-Si solar cells, as well as thin-film silicon solar cells. Although a variety of investigations about randomly textured and periodic light trapping concepts have been conducted, the question if periodic or disordered surfaces exhibit the superior effect on absorption, is not yet answered [30–34].

Multijunction solar cells provide the possibility to decrease thermalization losses [35] and increase the energy yield of the incident solar radiation [36,37]. Multijunctions can be arranged either horizontally demanding for advanced optical elements for spectral splitting or grown on top of each other, monolithically contacted and connected in series [38]. III-V semiconductor-based multijunction solar cells have been fabricated with up to four junctions for space and ultra-high efficiency concentrated PV applications [39,40]. High costs and low material abundance make them not yet feasible for large-scale market. Due to their band gaps, hydrogenated amorphous silicon (a-Si:H) and the mixed-phase material $\mu\text{c-Si:H}$ are feasible tandem partners in a multijunction thin-film solar cell [41]. Their abundance and non-toxicity qualify them for large production. Such tandem or ‘micromorph’ solar cells combine the abundance and low cost with the reduction of thermalization losses. As the sub cells in a monolithically connected multijunction cell are series-connected, the output current of the tandem cell is limited by the sub cell with lowest short-circuit current density. To minimize current losses, an advanced light management is necessary. The device architecture is tailored such that photons is trapped and absorbed in the particular sub cell. The simplest way of current-matching is adjusting the layer thicknesses of the sub cells. However, light induced degradation of a-Si:H known as Staebler-Wronsky effect [42], leads to a drop of fill factor and conversion efficiency depending and increases with the a-Si:H layer thickness. To maximize V_{oc} and long-term stability, the top cell thickness needs to be reduced.

A prolongation of the light path in the a-Si:H top cell can be facilitated by an intermediate reflector (IR) between top and bottom cell. This is usually done by inserting a single layer of low refractive index material which possesses sufficient conductivity and low absorptance between top and bottom cell. Investigated materials are aluminum-doped zinc oxide (ZnO:Al) [43–46] and the mixed-phase

material hydrogenated microcrystalline silicon oxide $\mu\text{c-SiO}_x\text{:H}$ hydrogenated microcrystalline silicon oxid [47–49]. p - or n -doped $\mu\text{c-SiO}_x\text{:H}$ can substitute doped p and n -layers a-Si:H and $\mu\text{c-Si:H}$ layers at the tunnel recombination junction and is deposited in-situ in the same deposition chamber. However, even state-of-the-art IRs cause optical losses. These losses occur by parasitic absorption in the front contact, in the doped silicon layers, within the IR or by reflection out of the solar cell stack. To further increase the conversion efficiency of multijunction solar cells, decreasing optical losses plays a decisive role. Therefore, the losses have to be localized and the dominating loss mechanisms should be determined and quantified. Reflection losses are due to imperfect absorption of back reflected light in the top cell. These are caused by a lack of spectral selectivity of common IRs in state-of-the-art tandem solar cells. Tailoring the spectral selectivity of the IR is essential to minimize the reflection losses caused by IRs. Photonic crystals exhibit a photonic band gap [50] and provide excellent spectral selective reflectance. In comparison to 2D and 3D photonic crystals [51–53], 1D photonic crystals provide high reflectance and can be easily implemented into thin-film silicon solar cells as a stack of different semiconducting layers within the thin-film production process chain. The combination of flat 1D photonic crystals and surface textures for light trapping, however, has to be carefully investigated in order to prove its feasibility as IR in tandem solar cells.

While simple reflection at the IR may induce a prolongation of the optical path length by a factor of two, in combination with surface textures much longer optical paths can be achieved [53, 54]. As the layer thickness of the top cell is smaller than the wavelength of the light, it can no longer be described by rays. Rather, the top cell absorber is described as a waveguide [55]. Incident light can couple into waveguide modes enabling much higher absorption enhancement. The interplay between scattering and diffraction at different textured interfaces in the tandem cell with partial reflection and diffraction at the IR has already been studied for individual geometries (different textures, materials, refractive indices, photonic structures) [54, 56–58]. However, state-of-the-art thin-film tandem solar cells suffer from parasitic losses due to the IR [44, 45, 49, 59, 60]. To surpass the thermodynamic limit of conventional single junction c-Si solar cells, multijunction solar cells on c-Si are a possible opportunity [61, 62]. In this case, a thin top cell absorber is put on state-of-the-art high efficiency c-Si cells reducing thermalization losses. High efficiency organic or halide-perovskite absorbers could be possible can-

didates [63]. A spectrally selective and highly transmissive top cell and IR layer stack is essential for such solar cell systems.

A profound understanding of the optical behavior and limitations of light management in silicon-based multijunction solar cells is fundamental to further increase the efficiency. a-Si:H/ μ c-Si:H tandem solar cells were chosen as model system, because they are a well established industrially up-scalable technology. Furthermore, they exhibit the important characteristics of other multijunction cell material systems. They combine thin-film layers, nano-structured surfaces, as well as, physical limitations of thicknesses and a broad utilization of the solar spectrum. The combination of thin-film layer stack and nano-structured surfaces demands for a treatment of the solar cell as a nano-optical device. Motivated by the results of experimental studies, tandem solar cells are modeled by thin-film optics and computationally extensive rigorous optical simulations. An agreement between simulation to experimental results allows for an investigation and optimization of these devices.

Basing on the addressed questions, this thesis is organized as follows:

Chapter 4 presents the theoretical background of the work. In Section 4.1, the electrodynamic theory of the interaction of light and semiconducting material is introduced and the applied simulation methods are derived. Section 4.2, focusses on the optoelectronic properties of thin-film silicon solar cells with a focus on light trapping and light management. In Section 4.3, fabrication and characterization methods are reviewed.

In **Chapter 5**, optical losses in tandem solar cells with intermediate reflector are systematically studied. Tandem solar cells are deposited on annealed front contacts with decreased parasitic absorption and compared to solar cells without these contacts. With both front contacts, cells with and without IR were deposited. Additional rigorous optical simulations enable to localize the optical losses within the tandem cell. Depending on the refractive index of the IR, parasitic absorption within the IR and parasitic reflection due to the IR are identified as the major source of optical losses.

Chapter 6 focuses on the parasitic reflection losses. The spectrally selective reflectance is carefully studied. To improve the spectral selectivity of the IR, in Section 6.2, multilayer IRs from available thin-film materials ZnO:Al and μ c-SiO_x:H are designed and optimized. In Section 6.3, they are fabricated and integrated into

flat tandem solar cells. The influence of texture on the layer stack is investigated by rigorous optical simulations in Section 6.4. Section 6.5 shows the implementation of the IR, into a prototype tandem solar cell on state-of-the-art texture. Top cell quantum efficiency and short-circuit current are increased compared to the tandem solar cell without IR, while, at the same time, the bottom cell quantum efficiency is increased compared to tandem cells with $\mu\text{c-SiO}_x\text{:H}$ and ZnO:Al reference IRs processed in parallel. Subsequent, a further improvement of multilayer IRs by varying IR multilayer materials, as well as layer quantity is numerically studied in Section 6.6 and comparison to different spectrally selective filters in Section 6.7.

Chapter 7 focuses on the effect of various intermediate reflectors on light trapping in the top cell. The effect of guided modes on absorption enhancement is identified. A Fourier-based method is developed to describe and quantify the coupling to guided modes for a periodical grating texture. It is shown that the same method can be applied to analyze light trapping in the top cell of randomly textured tandem solar cells. A quantity integrated scattering intensity is derived and correlated to the absorption enhancement by coupling to guided modes in the a-Si:H absorber layer.

The interplay of different interface texture and the intermediate reflector is investigated in **Chapter 8**. A special emphasis of this Chapter is to obtain a universal description of the interplay of IRs with versatile front textures which is able to explain the variety of experimental data and simulation studies in literature and cover both, randomly textured and periodic light trapping concepts. Section 8.2 is dedicated to elaborate which are the surface parameters of randomly textured solar cells that determine the effectiveness of the IR in tandem solar cells. Surface angles are shown to be the decisive factor. As a consequence, the angular reflection characteristic of thin-film IR layers is investigated in Section 8.3. The derived theory is applied to common randomly textured substrates in Section 8.4. To understand the effectiveness of the IR for tandem cells on surfaces comprising large angles and photonic structures with large diffraction angles remain, Section 8.5 presents a series of studies which decouple the interplay of front textures and reflectors. The results are generalized to randomly textured surfaces in Section 8.6. A final discussion in Section 8.7 summarizes the results of this chapter and puts them into connection to the diversified literature. The thesis is summarized in Chapter 9 and prospects on future investigations are given.

4. Fundamentals

This chapter introduces the theoretical background and experimental basis of this work. Fundamental equations for the description of light-matter interaction are deduced starting from fundamental equations. The applied methods of computational electrodynamics are reviewed. A solar cell is introduced as an opto-electronic device and its device physics is summarized. In particular, the device structure of the used thin-film silicon solar cells and the applied experimental methods of device characterization are shown.

4.1. Electrodynamics and Optics

4.1.1. Classical Electrodynamics

The theory of electrodynamics mathematically describes the electric and magnetic field \mathbf{E} and \mathbf{H} and their generation and conversion. The fundamental basis is given by Maxwell's equations. They were introduced by the Scottish physicist James Clerk Maxwell in his publication 'A Dynamical Theory of the Electromagnetic Field' from 1864 [64]. Maxwell's equations describe the temporal and spatial evolution of electromagnetic fields. The following four equations represent the macroscopic description of Maxwell's equations:

$$\nabla \mathbf{D}(\mathbf{x}, t) = \rho_{\text{ext}}(\mathbf{x}, t) , \text{ (Gauss' law)} \quad (4.1)$$

$$\nabla \mathbf{B}(\mathbf{x}, t) = 0 , \text{ (Gauss' law for magnetism)} \quad (4.2)$$

$$\nabla \times \mathbf{E}(\mathbf{x}, t) = -\frac{\partial \mathbf{B}(\mathbf{x}, t)}{\partial t} , \text{ (Faraday's law of induction)} \quad (4.3)$$

$$\nabla \times \mathbf{H}(\mathbf{x}, t) = \mathbf{J}_{\text{ext}}(\mathbf{x}, t) + \frac{\partial \mathbf{D}(\mathbf{x}, t)}{\partial t} , \text{ (Ampere's law)} \quad (4.4)$$

In this formulation, the microscopic interactions between charged particles and the electromagnetic fields are averaged resulting in a macroscopic response. The physical quantities are the electric field $\mathbf{E} = \langle \mathbf{E} \rangle (\mathbf{x}, t)$ and the magnetic field $\mathbf{H} = \langle \mathbf{H} \rangle (\mathbf{x}, t)$. The scalar free charge density $\rho_{\text{ext}}(\mathbf{x}, t)$ and the external electric current density $\mathbf{J}_{\text{ext}}(\mathbf{x}, t)$ are the sources of electromagnetic fields. Furthermore, the dielectric displacement $\mathbf{D}(\mathbf{x}, t)$ and the magnetic induction $\mathbf{B}(\mathbf{x}, t)$ are introduced as macroscopic quantities which are related to the fundamental fields by:

$$\mathbf{D} = \epsilon_0 \epsilon \mathbf{E} = \epsilon_0 \mathbf{E} + \mathbf{P}, \quad (4.5)$$

$$\mathbf{B} = \mu_0 \mu \mathbf{H} = \mu_0 (\mathbf{H} + \mathbf{M}), \quad (4.6)$$

introducing the electric polarization \mathbf{P} and the magnetization \mathbf{M} . The vacuum permittivity ϵ_0 and vacuum permeability μ_0 are universal constants which are linked to the speed of light c by

$$c = \frac{1}{\sqrt{\epsilon_0 \mu_0}}. \quad (4.7)$$

The dielectric function $\epsilon(\mathbf{x}, \omega)$ and the permeability $\mu(\mathbf{x}, \omega)$ describe the optical, magnetic and electric properties of the material. They can be deduced from the solid state theory of the certain material [65] or determined experimentally by ellipsometry [66] or RT -measurements (Section 4.3.2). Combining the vector equations Eq. 4.3 and Eq. 4.4 and inserting Eq. 4.5 and Eq. 4.6 results in the inhomogeneous wave equations:

$$\nabla \times \nabla \times \mathbf{E} = -\frac{1}{c^2} \frac{\partial^2 \mathbf{E}}{\partial t^2} - \mu_0 \frac{\partial}{\partial t} \left(\mathbf{j} + \frac{\partial \mathbf{P}}{\partial t} + \nabla \times \mathbf{M} \right), \quad (4.8)$$

$$\nabla \times \nabla \times \mathbf{H} = -\frac{1}{c^2} \frac{\partial^2 \mathbf{H}}{\partial t^2} + \nabla \times \mathbf{J}_{\text{ext}} + \mu_0 \frac{\partial \mathbf{M}}{\partial t} + \nabla \times \frac{\partial \mathbf{M}}{\partial t}. \quad (4.9)$$

In absence of charges and currents ($\rho_{\text{ext}} = 0$, $\mathbf{J}_{\text{ext}} = 0$), the inhomogeneous terms vanish and Eq. 4.8 and Eq. 4.9 turn into homogeneous partial equations. One time harmonic solution is a superposition of plain electromagnetic waves with a variety of angular frequencies ω :

$$\mathbf{E}(\mathbf{x}, t) = \mathbf{E}_0 \cdot e^{i(\mathbf{k} \cdot \mathbf{x} - \omega t)} \text{ and } \mathbf{B}(\mathbf{x}, t) = \mathbf{B}_0 \cdot e^{i(\mathbf{k} \cdot \mathbf{x} - \omega t)} \quad (4.10)$$

The wave vector \mathbf{k} directs in propagation direction of the electromagnetic wave and its absolute value $|\mathbf{k}| = \frac{\omega |\tilde{n}|}{c}$ contains the propagation speed in the certain material. The complex refractive index for non-magnetic materials

$$\tilde{n}(\omega) = n(\omega) + i\kappa(\omega) = \sqrt{\epsilon(\omega)}; \quad (4.11)$$

is related to the dielectric function $\epsilon(\omega)$. n and κ denote the real and imaginary part of the refractive index \tilde{n} . The real ϵ_r and imaginary part ϵ_i of the dielectric function can be deduced as:

$$\epsilon_r(\omega) = n^2(\omega) - \kappa^2(\omega) \quad (4.12)$$

$$\epsilon_i(\omega) = 2n(\omega)\kappa(\omega) \quad (4.13)$$

They are inter-dependent and coupled by the Kramer-Kronig-relation [65].

Interface Optics

Geometric optics or ray optics, describes light propagation in terms of 'rays'. A light ray is a line or curve that is perpendicular to the light's wave fronts (wave vector). It follows Fermat's principle, which states that the path taken between two points by a ray of light is the path that can be traversed in the least time. Ray optics allows to deduce the fundamental laws of reflection and refraction geometrically. At the interface between two different materials, electric and magnetic fields and their derivations are continuous. The refraction of light at the interface between two media of the refractive indices n_1 and n_2 with an incidence angle θ_1 and a refracted angle in the second medium (θ_2), Snell's law of refraction is given by [65]:

$$n_1 \cdot \sin(\theta_1) = n_2 \cdot \sin(\theta_2). \quad (4.14)$$

However, the ray optics approximation does not include phase information and optical frequency and diffraction, as well as, interference. For layer sizes and thicknesses $tn \gg \lambda$ like in crystalline silicon wafer solar cells with texture sizes $> 10 \mu\text{m}$ and layer thicknesses $> 100 \mu\text{m}$ [4, 67], this is a valuable approximation. At an interface between two optical materials, continuity of optical fields is required. From these conditions, Fresnel's equations can be deduced [65]. For normal incidence, the reflection coefficients $r_{s,p}$ and transmission coefficients $t_{s,p}$ are determined by the ratio of reflected/ transmitted and incident electric field for s and p-polarized light:

$$r_s = r_p = \frac{|E_{\text{refl}}|}{|E_{\text{in}}|} = \frac{\tilde{n}_1 - \tilde{n}_2}{\tilde{n}_1 + \tilde{n}_2} \quad (4.15)$$

$$t_s = t_p = \frac{|E_{\text{trans}}|}{|E_{\text{in}}|} = \frac{2 \cdot \tilde{n}_1}{\tilde{n}_1 + \tilde{n}_2} \quad (4.16)$$

The transmittance T and reflectance R are determined from the reflection and transmission coefficients r and t :

$$R_i = r_i \cdot \bar{r}_i, \quad (4.17)$$

$$T_i = \left| \frac{n_2 \cos \theta_2}{n_1 \cos \theta_1} \right| t_i \cdot \bar{t}_i. \quad (4.18)$$

This formulation is just valid for one interface. In the presence of more interfaces, interference plays a decisive role and optical phase has to be included. The common approach to recursively couple certain interfaces is the transfer matrix method described in Section 4.1.4.

4.1.2. Absorption in Semiconducting Materials

The attenuation of the intensity of the electric field by transit through an absorbing substance as a function of the wavelength, absorption coefficient α and thickness is described by Lambert-Beer's law [68]:

$$I = |\mathbf{E}|^2 = |\mathbf{E}|_0^2 \cdot e^{-\alpha(\omega)x}. \quad (4.19)$$

The absorption coefficient $\alpha(\omega)$ is linked to the extinction coefficient $\kappa(\omega)$ by:

$$\alpha(\omega) = \frac{4\pi\kappa(\omega)}{\lambda}. \quad (4.20)$$

Poynting Theorem

To describe the energy balance in electrodynamics, the vectorial quantity called 'Poynting vector' is introduced:

$$\mathbf{S}(\mathbf{r}, \omega) = \mathbf{E}(\mathbf{r}, \omega) \times \mathbf{H}(\mathbf{r}, \omega) \quad (4.21)$$

The Poynting vector describes the energy flow and is directed in propagation of the electromagnetic field. Using the Poynting vector, the time-averaged energy balance equation for the electromagnetic fields reads as follows: The rate of energy transfer (per unit volume) from a region of space equals the rate of work done on a charge distribution plus the energy flux leaving that region:

$$\frac{\partial}{\partial t} \frac{1}{2} (\mathbf{E}(\mathbf{r}, \omega) \cdot \mathbf{D}(\mathbf{r}, \omega) + \mathbf{B}(\mathbf{r}, \omega) \cdot \mathbf{H}(\mathbf{r}, \omega)) = \nabla \cdot \mathbf{S}(\mathbf{r}, \omega) + \mathbf{J} \cdot \mathbf{E}(\mathbf{r}, \omega). \quad (4.22)$$

In absence of currents and magnetic materials Eq. 4.22 is simplified to

$$\nabla \mathbf{S}(\mathbf{r}, \omega) = -\frac{1}{2} \omega \epsilon_0 \epsilon_i \mathbf{E}(\mathbf{r}, \omega) \mathbf{E}^*(\mathbf{r}, \omega). \quad (4.23)$$

$\mathbf{E}^*(\mathbf{r}, \omega)$ is the complex-conjugated local electric field. As a consequence, a non-vanishing imaginary part of the dielectric function results in a reduction of energy flow by absorption. The 'Poynting Theorem' can be used to calculate absorptance within certain layers from the electric fields.

4.1.3. Nano-Optics and Photonics

Evanescent waves

If an electromagnetic wave from an optically dense medium reaches the interface to an optically thinner medium ($n_1 > n_2$), Eq. 4.14 results in a particular critical angle θ_{TIR} which corresponds to a refraction into an angle of 90° , parallel to the interface [65]:

$$\theta_{\text{TIR}} = \arcsin\left(\frac{n_2}{n_1}\right). \quad (4.24)$$

The z -component of the wave vector of the transmitted electromagnetic wave in the medium n_2

$$k_{2,z} = k_2 \sqrt{1 - \left(\frac{n_2}{n_1}\right)^2 \arcsin^2(\theta_1)}, \quad (4.25)$$

gets imaginary if $\theta_1 > \theta_{\text{TIR}}$. The electromagnetic wave that does not propagate into the material but exponentially decays, is called evanescent wave and its electric field is described by [69]:

$$E_2 = \begin{pmatrix} -iE_1^p t_p(\theta_1) \sqrt{\left(\frac{n_1}{n_2}\right)^2 \sin^2 \theta_1 - 1} \\ E_1^s t_p(\theta_1) \\ E_1^p t_p(\theta_1) \frac{n_1}{n_2} \sin \theta_1 \end{pmatrix} \cdot e^{i \sin \theta_1 k_1 x} \cdot e^{-\gamma z}. \quad (4.26)$$

The decay constant γ is defined as:

$$\gamma(\theta_1, n_1, n_2, \lambda) = k_2 \sqrt{\left(\frac{n_1}{n_2}\right)^2 \sin^2 \theta_1 - 1}. \quad (4.27)$$

The index t_p and t_s indicate the Fresnel coefficients for transmission of p- and s-polarized light, respectively (Chapter 4.1.1) and E^p and E^s the absolute value

of the electric field of p- and s-polarized light, respectively. In case of an infinite thickness of the low index film, the evanescent field intensity decays to zero and all the light is totally internally reflected resulting in $R = 1$. In the presence of a second interface to a material $n_3 > n_2$, k_z may get real again (Eq. 4.25) allowing for a propagation of the electromagnetic wave in the medium. This process is analogous to the tunneling of a quantum mechanical wave function through a finite potential barrier and is, therefore, also described as **photon tunneling**. In this case, the Poynting vector does not vanish and energy is transmitted into the medium n_3 . As a result, the reflectance of this optical system is decreased from 1. The effect is also commonly known as **frustrated total internal reflection**, **attenuated total internal reflection** or **evanescent wave coupling**.

Planar Waveguides

The effect of total internal reflection is used in optical waveguides. Electromagnetic waves are guided within a dielectric material by total internal reflection at the adjacent materials which are either highly reflective or inhibit a refractive index lower than the waveguide material. Common applications are glass fibers [70] used e.g. for telecommunication. The effect is the same in a slab of dielectric material. In such a system, certain angles exist for which the phase ϕ_r of twice reflected wave and the incident wave are equal. The constructive and destructive interference of these waves result in a periodic electric field pattern. The following resonance condition can be deduced:

$$\frac{2\pi}{\lambda} \cdot n \cdot \cos \theta + \pi = 2\pi m, \text{ with } m = 0, 1, 2, 3, \dots, \quad (4.28)$$

with the incidence angle θ and the phase ϕ_r . These modes are confined in the waveguide. Figure 4.1 shows a dispersion plot where the photon energy E_{ph} is shown in dependence of the parallel wave vector $k_{||}$. Dotted diagonal lines indicate the escape cone for ZnO:Al ($n = 2$) and a-Si:H ($n = 4$). Full black curves show the waveguide modes of the order $m^* = 1, 2, 3, 4$ for a 330 nm thick a-Si:H film between two perfect reflectors $E_{ph} = \frac{h \cdot c}{n} \cdot \sqrt{k_{||}^2 + \left(\frac{m^* \cdot \pi}{t}\right)^2}$ [71]. Dashed vertical line indicate the transfer of parallel wave vector $k_{||,gr}$ induced by a grating of the period $p = 400$ nm. Red circles indicate intersections between the grating momentum $k_{||,gr}$ and the waveguide modes of the a-Si:H film.

To couple ambient electromagnetic waves into the waveguide, a parallel momentum $k_{||}$ has to be transferred to the photon. This can be done by the diffraction or

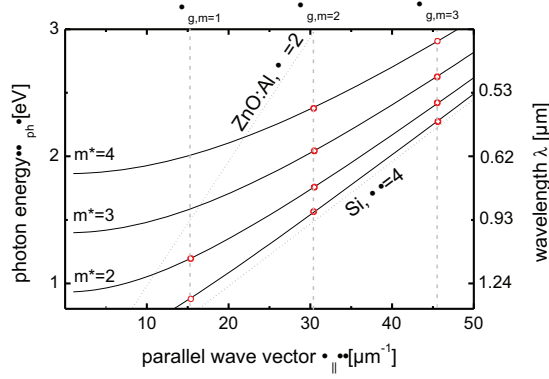


Figure 4.1.: Dispersion relation of photon energy E_{ph} over the parallel wave vector k_{\parallel} . Dotted diagonal lines indicate the escape cone for ZnO:Al ($n = 2$) and a-Si:H ($n = 4$). Full black curves show the waveguide modes of the order $m^* = 1, 2, 3, 4$. Dashed vertical line indicate the transfer of parallel wave vector k_{\parallel} induced by a grating of the period $p = 400$ nm.

scattering process. By the transfer of parallel momentum, incident light can couple into the waveguide and, following reciprocity, waveguide modes can couple to the ambient (also known as **leaking**). These modes are called **leaky waveguide modes**.

Diffraction Gratings

A diffraction grating is an optical component with a periodic surface structure diffracting light into different directions. Diffraction is a direct consequence of Huygen's principle of elementary waves [72]. The directions of these beams depend on the period of the grating p and the wavelength of the light:

$$m \cdot \lambda = p \cdot \sin(\theta_n), \quad (4.29)$$

where m is the diffraction order $m = (0, 1, 2, 3, \dots)$. The zeroth grating order is the specular light, which is transmitted in 0° without transfer of parallel momentum.

Photonic Crystals

Analogous to electrical crystals where the free electron gas is affected by a periodic ion lattice, a photonic crystal (PhC) is a periodical optical nanostructure. The

English physicist Lord Rayleigh showed in 1887 that for certain layer thicknesses t and refractive indices n , dielectric multilayer stack transmission vanishes at certain incidence angles due to destructive interference [73]. As Fig. 4.3(a) shows, this multilayer stack follows the condition

$$\frac{\lambda_0}{4n} = m \cdot t. \quad (4.30)$$

This 1D photonic crystal is also called Bragg stack and shows an optical band gap centered at λ_0 . Like in electronics, propagation for photons which inhibit an energy within the band gap is prohibited. Such multilayer thin-film coatings are known as **dielectric mirrors** or **interference narrow-band filters** and used as optical components [74]. Starting with the prediction of this omnidirectional photonic band gap by E. Yablonovitch [75] and S. John [76] in 1987, the field of photonic crystals has attracted large attention and large efforts have been done to produce such structures either 2D like in [77] (Fig. 4.2(a)) or 3D like the inverted opal structure in [78] (Fig. 4.2(b)). The 3D inverted opal structure was theoretically calculated in [79]. An excellent overview of the theory and application of PhC, is found in [50].

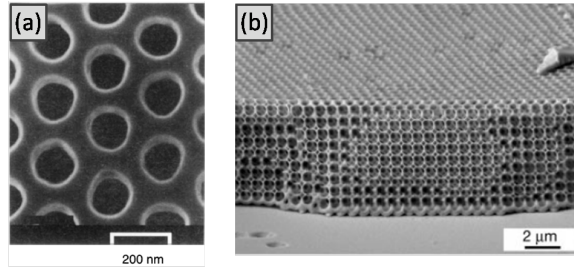


Figure 4.2.: Scanning electron microscopy (SEM) images of a 2D photonic crystal (a) [77] and 3D photonic crystal (b) [78] taken from literature .

Figure 4.3 shows the photonic band structure in the optical dispersion $\omega(k)$ for a 1D photonic crystal (PhC) or Bragg stack (a) and a 3D PhC (b) calculated by a plane wave approximation method [80]. The shown 3D PhC is an inverted opal structure produced by periodic self-assembly of diluted nano spheres from Fig. 4.2(b). The photonic band gap in the 1D stack is just in one symmetry direction. In contrast, the 3D PhC structure exhibits an omnidirectional band gap if the refractive index contrast $\frac{n_1}{n_2}$ is large enough [50]. Due to their potential to

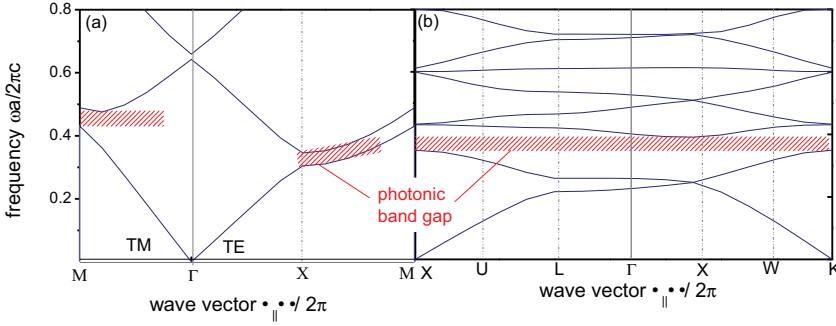


Figure 4.3.: Calculated photonic band structure in the optical dispersion $\omega(k)$ for a 1D photonic crystal (PhC) or Bragg stack (a) and a 3D PhC (b). The shown 3D photonic crystal is an inverted opal structure produced by periodic self-assembly of diluted SiO_2 nanospheres in a silicon matrix.

guide, reflect and diffract the light, photonic crystals are now used in PhC glass fibers [81,82], lasers, light emitting diodes and solar cells [26,27,53,83].

4.1.4. Computational Electrodynamics

The fast advances in supercomputing have made it possible to perform simulations of various photonic elements. Computational demand increases with the complexity of the studied system. Flat layer stacks can be easily computed by transfer matrix models, while more complex geometries and, in particular, randomly textured structures require larger computational domain and have to be simulated rigorously. Approximate methods like scalar scattering theory help to understand the physical processes and enable parameter sweeps.

Transfer Matrix Method (TMM)

For the calculation of optical properties of stacked media on flat substrate, the Fresnel equations (Section 4.1.1) at each interface have to be prevailed. Reflection and transmission coefficients r_{ij} , t_{ij} at each interface are summed up in matrices which can be multiplied to couple several interfaces. A schematic drawing of a calculated cell stack and the quantities r_{ij} , t_{ij} is shown in Fig. 4.4.

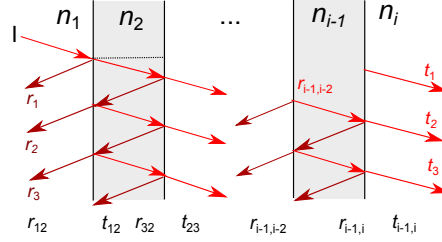


Figure 4.4.: *Configuration of interfaces in TMM method.*

For this work, two versatile coherent transfer-matrix algorithm implementations in Python and C++ [84], [85] were used to calculate reflectance and transmittance of the flat layer stacks. Matrix calculations are computationally fast and allow for optimization. In case of this work, the TMM algorithm was coupled to a genetic algorithm for layer thickness optimization [86, 87]. The genetic algorithm was implemented in C++. It allows to vary starting values, number of the population and mutation rate.

Finite-Difference Time Domain Method (FDTD)

Optical simulations of devices with textured surfaces are much more complex as a statistical, sufficiently large area has to be chosen and Maxwell's equations have to be solved rigorously [56, 88–92]. For the rigorous optical simulations of such three-dimensional systems, various commercial and free solvers are available basing on finite elements method (FEM) [93–95], rigorously-coupled wave analysis (RCWA) or Fourier-Modal method (FMM) [96–98], finite integration technique (FIT) [99] and finite-difference time-domain method (FDTD) [100–102]. The good scaling of parallelization of the FDTD methods makes it a suitable method for the rigorous simulation of large randomly textured domains. Within this work, simulations were done by FDTD method using a in-house developed interface [103] to the open-source software package Meep [100]. In 3D, Maxwell's equations have six electromagnetic field components: E_x , E_y , E_z and H_x , H_y and H_z . Maxwell's equations split into two independent sets of equations composed of three vector quantities which can be each solved in the x - y plane only. These are termed the TE (transverse electric), and TM (transverse magnetic) equations. Both sets of equations can be solved with the following components for a z being the propaga-

tion direction: TE: E_x, E_y, H_z

TM: H_x, H_y and E_z .

For example, in the TM case, Maxwell's equations reduce to:

$$\frac{\partial D_z}{\partial t} = \frac{\partial H_y}{\partial x} - \frac{\partial H_x}{\partial y} \quad (4.31)$$

$$D_z(\omega) = \epsilon_0 \epsilon_r(\omega) E_z(\omega) \quad (4.32)$$

$$\frac{\partial H_x}{\partial t} = -\frac{1}{\mu_0} \frac{\partial E_z}{\partial y} \quad (4.33)$$

$$\frac{\partial H_y}{\partial t} = -\frac{1}{\mu_0} \frac{\partial E_z}{\partial x} \quad (4.34)$$

The FDTD method solves these equations on a discrete spatial and temporal grid substituting the differentials in Eq. 4.31-4.34 by differences. Each field component is solved at a slightly different location within the grid cell (Yee cell), as shown in Fig. 4.5. By default, data collected from the FDTD solver is automatically interpolated to the origin of each grid point [104].

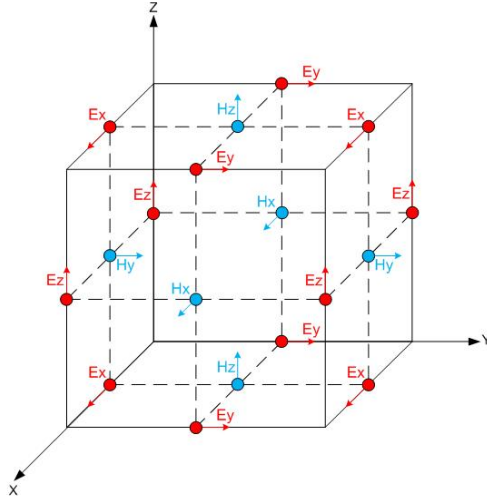


Figure 4.5.: 3D Yee grid (i,j,k) for the discretization of the computational domain. Electric fields (E_x, E_y, E_z) are indicated by red and magnetic fields (H_x, H_y, H_z) by blue arrows. Illustration taken from [105].

Scalar Scattering Theory

Rigorous optical simulations facilitate an accurate description of a photonic system. However, computational effort is still high, especially for complex geometry like randomly textured substrates which require large simulation domains. To calculate generation profiles for electric simulations, as well as for optimization of surface textures, scalar scattering theory provides a powerful tool but is, however, restricted to certain limitations. Commercially-available device simulators like ASA imply empirical correction functions which are not physically driven [106–108]. In the last years, a new scalar model has been developed on the basis of Fast Fourier Transform (FFT) [109–112]. Surface morphologies measured by atomic force microscopy (AFM) are used to extract the collected optical phase difference $\Delta\phi$ induced within the transition zone between z_{\max} and z_{\min} (Fig. 4.6) from one optical material ($n = n_1$) to another ($n = n_2$):

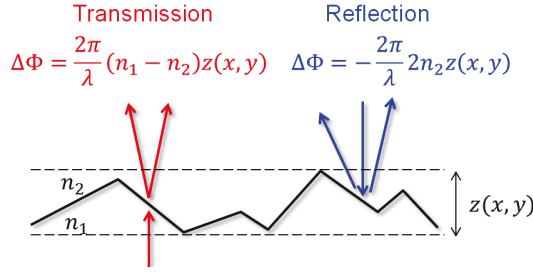


Figure 4.6.: Schematic sketch of the collection of optical phase ϕ within the transition zone of an interface between z_{\min} and z_{\max} .

$$\Delta\phi = \frac{2\pi}{\lambda}(z_{\max} - z_{\min})n_2 + \frac{2\pi}{\lambda}z(x,y)(n_1 - n_2), \quad (4.35)$$

The radiance L is the radiant power per unit solid angle per projected unit area and describes the scattered light intensity.

$$L(k_x, k_y) = \frac{\lambda^2}{A_S} |F(U_0(x, y))|^2, \quad (4.36)$$

including the scattering surface A_S and the Fourier transform F of the pupil function $U_0(x, y)$:

$$U_0(x, y) = \frac{1}{(1 + \epsilon)^2} \cdot e^{i\Delta\phi} \quad (4.37)$$

ϵ is the ratio of the diameter of the incident wave front to the observation distance. From L , spectral quantities like the haze or angular intensity distribution (AID) can be deduced. The $AID(\theta)$ is calculated as:

$$AID(\theta) = L(k_x, l_y) \cdot \frac{2\pi n_2}{\lambda} \cos(\theta). \quad (4.38)$$

The model has been extended to reflection [113], compared to measurements [111,112], [114] rigorous FDTD simulations for each random [92] [115] and periodic grating surface textures [116].

4.1.5. Fourier Analysis

The distribution of the complex electric fields obtained from rigorous optical simulations contains information about propagating light modes inside the absorber layer as well as near-field modes. All those modes can be discriminated by fast Fourier transform (FFT) [109,117]. To extract the information, a plane of the complex electric field distribution is chosen. This distribution can be either a plane extracted out of rigorous optical simulations (Section 4.1.4) or calculated from a surface topography using the phase model (Section 4.1.4). The real part of the electric field in x -direction is plotted in Fig. 4.7(a). It shows a periodic pattern determined by the waveguide modes within the film. The FFT of this 2D output plane provides the amplitude and phase of each mode as a function of the periodicity of the electric field. The real part of the FFT is presented in Fig. 4.7(b).

It is visible that the grating diffracts into discrete orders which are visible in the FFT. In order to evaluate the amount of light modes with large wave vectors, i.e. large propagation angles, the FFT result is spherically integrated around the center point. The center point corresponds specular light with $k_{\parallel} = 0$. The dotted circle shows the condition $k_{\parallel} = |k| = \frac{2\pi n_{\text{am}}}{\lambda}$ which is equivalent to the escape cone to the ambient (n_{am}). All light modes with $k_{\parallel} > \frac{2\pi n_{\text{air}}}{\lambda}$ are not able to propagate in air. In this range, leaky waveguide modes are present. The incident light can couple to these modes by scattering at the textured interfaces. An angular intensity distribution AID or scattering intensity SI can be calculated by integrating the intensity in the FFT within thin circular rings of thickness dr . With $k_{\parallel} = \frac{2\pi n_{\text{Si}}}{\lambda} \cdot \sin \theta_{\text{sca}}$, the periodicity p of the field pattern can be transferred into a scattering

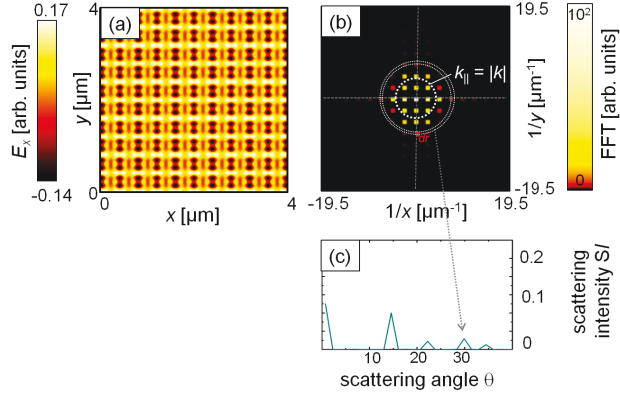


Figure 4.7.: (a) Real part of the E_z component in a plane within the a-Si:H top cell of a tandem solar cell on periodic grating. (b) The FFT of the complex electric field. The dotted circle depicts the limit of propagating light $k_{\parallel} = |k|$. (c) Scattering intensity SI over the scattering angle.

angle θ_{sca} by:

$$\theta_{\text{sca}} = \arcsin\left(\frac{\lambda}{2 \cdot n \cdot p}\right). \quad (4.39)$$

The geometry of the process is illustrated in Fig. 4.8. The scattering angle θ_{sca} is the angle between the incident wave front and scattered wave front. The wavefront pattern in an evaluation plane (dotted line) is characterized by a periodicity p . The SI for Fig. 4.7(a) is presented in (c).

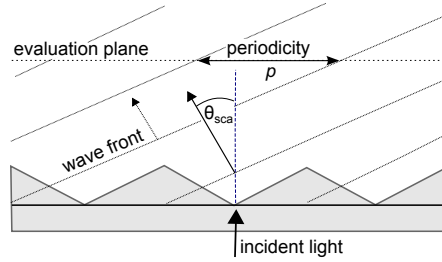


Figure 4.8.: Scheme of scattering at a textured interface. The incident wave front is scattered/diffracted at the surface features. The scattered wave fronts are depicted as full lines. The scattering angle θ_{sca} is the angle between the incident wave front and scattered wave front. The wavefront pattern in an evaluation plane (dotted line) is characterized by a periodicity p which is linked to the scattering angle by Eq. 4.39.

4.2. Thin-film Silicon Tandem Solar Cells

A solar cell is an optoelectronic device with the ability to convert broad-band light in the visible range into electrical energy. This section introduces the working principle of a general solar with focus on thin-film silicon solar cells.

4.2.1. Photovoltaic devices

Basis of energy conversion in solar cells is the photovoltaic effect. It bases on the photoelectric effect, described by Albert Einstein in 1905 [118]. The absorption of a photon with the sufficient energy $h\omega$ by an atom in a crystal leads to the excitation of the electron which is localized in the valence band into the conduction band of the semiconductor. This is the process of the generation of an electron-hole pair. In inorganic semiconductors, this leads to an increase of concentration of quasi-free charge carriers while in more complex systems like organic semiconductors or quantum well structures, electron-hole pairs stay bound in so-called excitonic states. To avoid recombination of the generated electron-hole pairs, selective contacts provide a transport of the electrons and holes to the circuit. Doping of the semiconductor to a p-doped (acceptor) and n-doped (donator) region builds up an electric field which ensures the transport of charge carriers to the contacts. The separation of charge carriers generates a voltage in the device, whereas the photo current J_{ph} is determined by the number of electrons and holes extracted at the contacts. A schematic band diagram of a typical p-i-n solar cell is shown in Fig. 4.9.

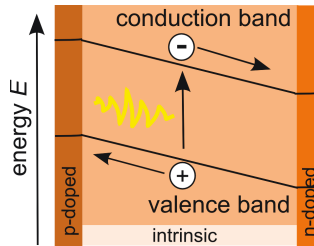


Figure 4.9.: Band diagram of a thin film p-i-n solar cell with valence and conduction band.

4.2.2. Solar Spectrum

The solar cell is illuminated by light from an external source which is, under normal conditions the sun. The incident power of sunlight at standard conditions are shown in Fig. 4.10 in space (AM0, yellow curve) and with an angle of incidence of 48° to the surface normal which corresponds to mid-latitude regions including the major PV markets US, Germany, China, Japan (AM1.5, orange curve) [119, 120]. The AM1.5 spectrum includes losses by light paths through the atmosphere including the absorption bands of atmospheric molecules like O_2 , H_2O etc.

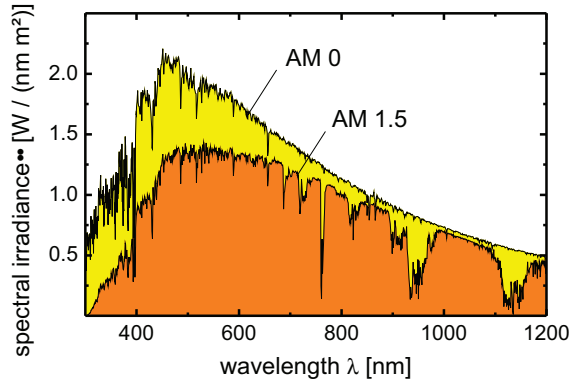


Figure 4.10.: Incident spectral irradiance in free space (AM0, yellow) and on Earth with an inclination angle of 48° (AM1.5, orange).

4.2.3. Device Structure of Thin-Film Silicon Solar Cells

To choose a suiting material for a solar cell, (i) band gap and (ii) absorption coefficient of the material are of decisive importance. Due to thermodynamic calculations of Shockley and Queisser [10], the conversion efficiency of sunlight shows to maxima reaching 34% for a band gap energy of $E_{\text{gap}} = 1.1 \text{ eV}$ and $E_{\text{gap}} = 1.34 \text{ eV}$. The dominating material for solar energy conversion is **crystalline silicon** (c-Si). It has been the dominant material in microelectronics, is well understood [121], and its band gap of $E_{\text{gap}} = 1.1 \text{ eV}$ is very suitable to absorb a large share of sunlight. As c-Si is an indirect semiconductor [121], absorption length is long for low energies (Fig. 4.11) and a large layer thickness of several

μm is necessary to absorb the full spectrum. The application of scattering and diffracting textures can further enhance the effective thickness of the absorber layer. Together with the optimization of material purity and, thus, charge carrier lifetime and mobility, surface passivation and doping [4] have lead to a record conversion efficiency for the passivated-emitter, rear-locally diffused (PERL) solar cells 24.6% [122, 123] and 25.6% in case of an a-Si:H passivated silicon heterojunction solar cells [9].

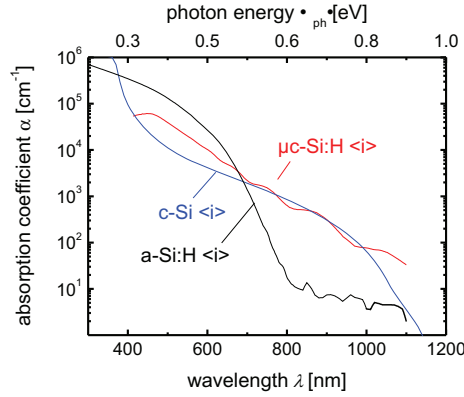


Figure 4.11.: Absorption lengths for silicon based intrinsic (*i*) materials crystalline silicon (*c-Si*) (taken from [124]), hydrogenated amorphous silicon (*a-Si:H*) and the mixed-phase material microcrystalline silicon ($\mu\text{c-Si:H}$).

A variety of materials has been proposed including high-quality semiconductors like GaAs [40], chalcogenides/ kersterides [125], dyes [126], organic semiconductors [127] and perovskites [128]. Stability, material availability and toxicity of the involved materials, disqualify them to meet a PV demand on the terawatt scale within some decades. Drawbacks of *c-Si* are mainly the necessary layer thicknesses and the resulting demand of silicon, as well as the energy consumption during the fabrication process. A possibility are thin-film silicon solar cells. The thin-film materials hydrogenated amorphous silicon (*a-Si:H*) and hydrogenated microcrystalline silicon ($\mu\text{c-Si:H}$) are used within this work. In a thin-film silicon solar cell configuration, the intrinsic *a-Si:H* / $\mu\text{c-Si:H}$ absorber layer is situated between thin *p*- and *n*-doped layers forming a *p-i-n*-diode. The electric field generated by the doped layers leads to a separation of charge carriers and directs them to the

contacts.

4.2.4. Light Trapping in Solar Cells

In the Shockley Queisser limit, it is assumed that all incident photons with ($E_{\text{ph}} > E_{\text{gap}}$) contribute to charge carrier generation and the charge carriers can be losslessly extracted from the solar cell. The external quantum efficiency as the ratio of extracted charge carrier divided by incoming photon is $EQE = 1$ in this case. This is achieved if the absorption coefficient α (Eq. (4.20)) is large enough like in III-V semiconductors, perovskites or organic absorbers and, consequently, all photons can be absorbed within one path through the material. In the case of indirect semiconductors like silicon which exhibit lower absorption coefficients close to the band gap, complete absorption can be ensured by increasing the absorber layer thickness and, thus, the optical path of the light. Classical crystalline silicon solar cells are several hundred micrometers thick and, thus, absorb a similar amount of light reaching high absorptance over a large spectral range. High efficiencies of up to 25.6% [9] and really high absorptance have been gained with thick c-Si wafer solar cells. To reach even higher efficiencies, the open-circuit voltage V_{oc} is the limiting factor. If the light is not absorbed within a diffusion length of the junction, the charge carriers are lost due to recombination. Furthermore, a thinner solar cell which retains the absorption of the thicker device may have a higher voltage. From the thermodynamic point of view, these processes create entropy which decreases the difference from the actual band gap to the open-circuit voltage [12]. One way of decreasing cell thickness is to increase the light path in the solar cell. This is facilitated by increasing the angle of light. Larger angles lead to an increasing light path and a larger amount of light which is totally internally reflected (Section 4.1.3). This approach is called light trapping and is facilitated by scattering or diffraction at the front or back side of the solar cell. An optimum solar cell structure will typically have light trapping in which the effective optical path length (\tilde{l}) is several times the actual device thickness.

Lambertian Light Trapping

Scattering denotes the process of redirecting any kind of radiation due to localized non-uniformities in the medium. In optics, this can be, for example, dielectric or metal particles or textured surfaces. A schematic sketch of light trapping in a

thin semiconductor film is shown in Fig. 4.12. An incident ray is scattered at the textured front interface and the back reflector in a variety of directions. The redirection is described by a scattering angle θ . If additionally a back mirror is applied, the light path in the absorber material with thickness t is $\tilde{l} = \frac{2t}{\cos \theta}$. To deduce a limit of absorptance in a high refractive index medium, I regard the absorber material as a black body emitting a photon flux $\Phi_{\text{bb}}^{\text{E}}$. In case of Lambertian light trapping, an isotropic distribution of scattering angles is assumed. That means that the radiance is redirected uniformly in all directions.

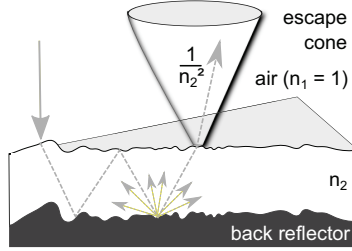


Figure 4.12.: Schematic sketch of light trapping in a thin semiconductor film.

In this system, the flux through an angular area $\frac{d\Phi}{dA_{\Omega}}$ is constant. The radiance L within the volume V of the layer is described as

$$L = \frac{d\Phi_V}{dV} = \alpha \Phi_{\text{bb}}^{\text{E}} \int_0^{2\pi} d\phi \int_0^{\pi} \sin(\theta) d\theta = 4\pi\alpha \Phi_{\text{bb}}^{\text{E}}. \quad (4.40)$$

As light escaping the solar cell must be below the critical angle of total internal reflection θ_{TIR} an additional factor

$$T = \int_0^{\theta_{\text{TIR}}} 2 \cos(\theta) \sin(\theta) d\theta = \sin^2(\theta_{\text{TIR}}) = \frac{1}{n^2} \quad (4.41)$$

is obtained. It resembles the reduction of the photon flux outside in comparison to within the solar cell. The emitted flux from the surface of the layer into the air free space is:

$$\frac{d\Phi_s}{dA_s} = \frac{1}{n^2} A \Phi_{\text{bb}}^{\text{E}} \int_0^{2\pi} d\phi \int_0^{\frac{\pi}{2}} \cos(\theta) \sin(\theta) d\theta = \frac{1}{n^2} A \pi \Phi_{\text{bb}}^{\text{E}}. \quad (4.42)$$

Combining Eq. 4.40 and Eq. 4.42, results in:

$$\int_0^t d\Phi_V dx = 4\pi n^2 \alpha t \Phi_{bb}^E = t\Phi_S = \frac{1}{n^2} A\pi\Phi_{bb}^E. \quad (4.43)$$

This results in the maximum absorptance:

$$A(\lambda)_{\max} = 4n^2 t \alpha(\lambda), \text{ (Yablonovitch limit [129])}. \quad (4.44)$$

The maximum path enhancement in a weakly absorbing medium amounts:

$$\tilde{l}_{\max} = 4n^2 t. \quad (4.45)$$

Further, the presented limit just applies for the case of vanishing absorption which is not the case for a large range of the spectrum ($\lambda < 900 \text{ nm}$) where a significant part of the light is absorbed in the first passages through the absorbing layer. A modification of Tiedje includes free carrier absorption as well by splitting the absorption coefficient α into a step function of high absorptance (α_1) and low absorptance (α_2):

$$A(\lambda)_{2,\max} = \frac{\alpha_2(\lambda)}{\alpha_1(E) + \alpha_2(E) + \frac{1}{4n^2 t}}, \text{ (Tiedje limit [130])}. \quad (4.46)$$

The influence of the Lambertian light trapping on the absorbed power determined by Eq. 4.44 and Eq. 4.46 in a $\mu\text{c-Si:H}$ solar cell are presented in Fig. 4.13. A big potential for light trapping for wavelength $\lambda > 750 \text{ nm}$ can be identified.

These approaches neglect any parasitic absorption, e.g. by the contact and doped layers. A limiting absorptance taking these losses into account can be found in Deckman et al. [131]. Light trapping by randomly textured surfaces is facilitated by a variety of different structures [132] including randomly textured as-grown substrates (Section) and photonic or periodic textures [13, 15, 16, 18, 133].

Coherent Theory of Leaky-Waveguide Coupling

The assumptions from [129] are not generally valid for thin-film silicon solar cells. For layer thicknesses in the order of the wavelength of incident light, geometrical optics cannot be applied as already discussed in Chapter 4.1.1. In particular, coherent properties of the light as diffraction and waveguide modes are not considered are not considered (Chapter 4.1.3). The work of Yu et al. [55, 134] proposed

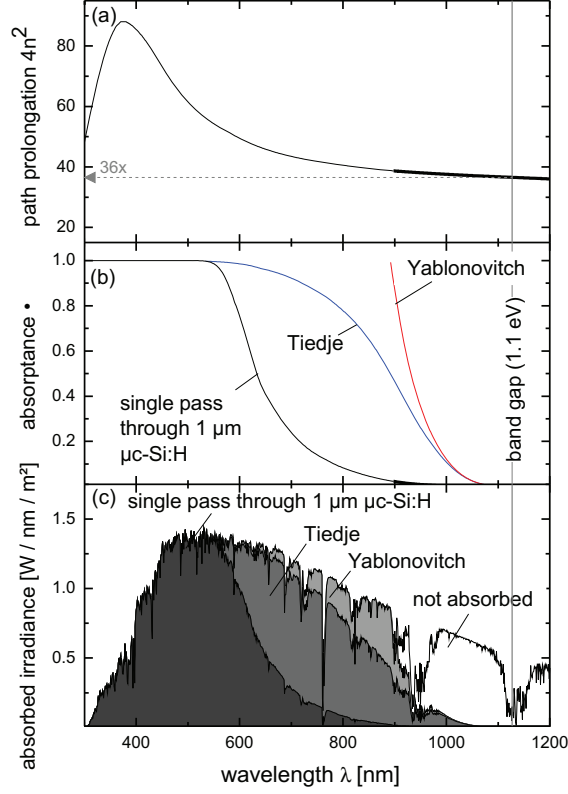


Figure 4.13.: (a) $4n^2$ for $\mu\text{c-Si:H}$. (b) Absorptance A in a $1\text{ }\mu\text{m}$ thick $\mu\text{c-Si:H}$ layer. (c) Absorbed irradiance I for a $1\text{ }\mu\text{m}$ thick $\mu\text{c-Si:H}$ solar cell.

a model which determines the maximum absorption of a solar cell as a thin-film system with coherent light basing on rigorous coupled mode theory. Lattice constants L close to the wavelength can result in absorption enhancements F which can highly surpass the $4n^2$ -limit. Figure 4.14 shows the example of a cubic lattice (k -space representation in (a)). In (b) the absorption enhancement is plotted over the ratio $\frac{L}{\lambda}$ reaching $F = 4\pi n^2$ at $L = \lambda$ (cubic case).

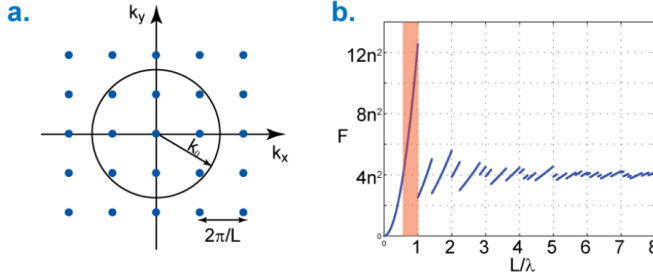


Figure 4.14.: (a) Channels in 2D k -space for a grating with cubic lattice periodicity. The lattice constant is L . (b) Upper limit of absorption enhancement for gratings with cubic lattice. The image is taken from [55].

4.2.5. Multi-junction Solar Cells

Two major effects limit the efficiency of single-junction solar cells: Photons with an energy below the band gap of the absorbing material cannot be absorbed as the sufficient energy for charge carrier generation is not provided. For the band gap of a c-Si solar cell, the light portion of the sunlight which is not available for solar energy conversion amounts 34%. Photons with a higher energy are absorbed in the semiconductor. However, the existence of just one fixed band gap leads to a loss of the additional energy a photon holds $\Delta E = \hbar\omega - E_g$. This energy leads to a further lattice excitation which is relaxed by phonons and is, thus, called **thermalization**. For c-Si solar cells, thermalization losses make out 57% of the incident light. These losses can be minimized by combining single junction solar cells of different band gap materials. [36, 37] showed that thermodynamically the possible conversion efficiency increases with the number of junctions. A hypothetical n-junction is able to vanish thermalization losses and reach the thermodynamic maximum conversion efficiency of 86%. This system is unrealistic, but world record conversion efficiencies have been reached with four junctions of III-V semiconductors reaching now 44.7% [40].

Basing on silicon technologies, a variety of different combinations for a dual-junction solar cell, also called tandem solar cells, are possible. Thermodynamic calculations by [36, 37] show that basing on c-Si or $\mu\text{c-Si:H}$, the perfect band gap for the partner solar cell would be $E_{\text{gap}} = 1.8\text{ eV}$ (see Fig 4.15(a)). Consequently, a tandem of a-Si:H as top cell and $\mu\text{c-Si:H}$ as bottom cell has proven to be a good

combination [41].

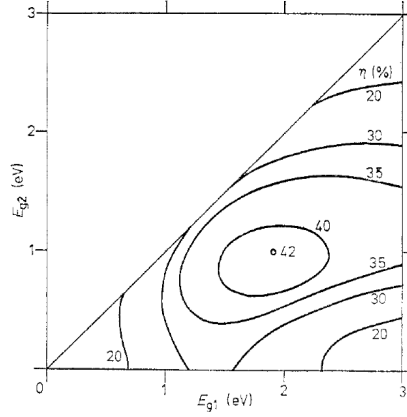


Figure 4.15.: Conversion efficiency for a tandem solar cell depending on the band gaps of top and bottom solar cell taken from [36].

Light Management in Tandem Solar Cells

Tandem and spectral-splitting configurations are of increasing importance and are also discussed for silicon technologies to go beyond the limiting efficiency of 27% [4, 35]. Therefore, it is necessary to determine an adequate partner for crystalline silicon which exhibits an appropriate band gap, low parasitic sub-band gap absorption and delivers sufficiently high short-circuit current density J_{sc} . An important question assesses the interconnection of the sub cells. Series connection requires a current matching of the sub cells to prevent a current loss due to the limiting sub cell. Achieving this with a high-band gap material is difficult as the maximum achievable short-circuit current is limited by this band gap. To avoid the current matching problem, four terminal devices have been proposed [135], where top and bottom cell are individually connected. An increasing number of junctions with certain doped contact layers increases the parasitic absorption in the device. Spectral-splitting solar cells place solar cells for different spectral ranges aside and apply optical elements like spectrally selective filters and mirrors and lenses or holographs to assign this certain spectral range of light to the associated solar cell [136–138]. This is, in particular, interesting for concentrating PV where the

space won by concentrating the light can be used for a horizontal adjustment of the particular solar cells. [139] gives an overview over activities in this sector. However, concentrating PV systems require complex tracking systems and lenses and base on non abundant III-V semiconducting materials. For chemically deposited and solution-processed solar cells, stacking of different absorbers with so-called tunnel recombination junctions is the straight-forward and dominant concept of producing multijunction solar cells. The overall design of these tandem devices is restricted by the requirement of current-matching at the maximum power point of both sub cells [140]. The matching requirement is usually achieved by adjusting the thickness of the a-Si:H top cell and $\mu\text{c-Si:H}$ bottom cell. An equivalent circuit is shown in Fig. 4.16(a) including non-radiative recombination represented by dark current densities J_0 , the photo current density J_{ph} and shunt and series resistances R_{sh} , R_{s} of the top and bottom cell.

The characteristic curve of a solar cell is its current-voltage JV -curve, which is depicted for top (orange), bottom (brown) and series-connected tandem solar cell (black) in Fig. 4.16(b). The current density J is observed depending on the voltage V . At short-circuit condition ($V = 0$), the short-circuit current density J_{sc} is generated. The voltage in case of $J = 0$ is called open circuit voltage V_{oc} . The point of maximal output power of the solar cell $P_{\text{MPP}} = J \cdot V$ is called maximum power point MPP . The conversion efficiency η is defined as

$$\eta = \frac{P_{\text{MPP}}}{P_{\text{in}}} = FF \cdot V_{\text{oc}} \cdot J_{\text{sc}}, \quad (4.47)$$

including the incident power P_{in} and the fill factor $FF = \frac{J_{\text{MPP}} \cdot V_{\text{MPP}}}{J_{\text{sc}} \cdot V_{\text{oc}}}$. The external quantum efficiency EQE of a tandem solar cell is shown in Fig. 4.16(c). It forms the ratio between incident power and the power absorbed in the solar cell. In case of perfect carrier collection, it is equivalent with the overall absorption within the absorber material. J_{sc} is obtained by integrating the $EQE(\lambda)$ weighted by the incident irradiance $\phi(\lambda)$

$$J_{\text{sc}} = e \int_0^{\infty} EQE(\lambda) \phi(\lambda) d\lambda. \quad (4.48)$$

However, the power-matching condition is also affected by the imperfect carrier collection, as well as, degradation mechanisms which are both inherent to the material [42, 141]. Physical constraints can be low diffusion lengths like in case of

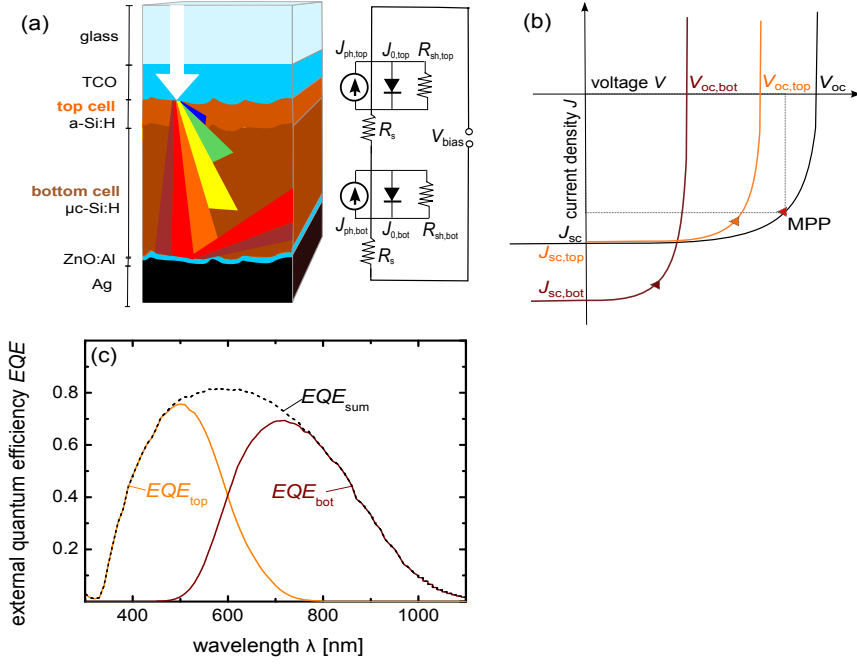


Figure 4.16.: (a) Sketch of a series-connected tandem solar cell and equivalent circuit. (b) JV -curves of top and bottom cell including short-circuit current density J_{sc} , open circuit voltage V_{oc} , as well as, the maximum power point MPP (indicated by triangle) for top cell (orange), bottom cell (brown) and series-connected tandem device (black). (c) External quantum efficiency (EQE) of top, bottom and sum of tandem solar cell.

organic semiconductors, a reduced open-circuit voltage V_{oc} , due to bulk recombination losses as well as light-induced degradation. Light-induced degradation in a-Si:H is known for decades and was reported 1962 by Staebler and Wronski [42]. A similar process is observed for organic absorber materials which exhibit a disordered structure as well [142]. Therefore, a central task for advanced optical concepts in tandem thin-film silicon solar cells is the minimization of the physical thickness and a maximization of the optical light path in the a-Si:H top cell. This is why, an intermediate reflector (IR) is employed between the a-Si:H top cell and the μc -Si:H bottom cell to reflect non-absorbed photons back to the top cell and,

thereby, increase the optical path and absorptance in the top cell [44]. Commonly, thin layers (30 – 150 nm) of transparent and conductive materials with a refractive index n lower than that of a-Si:H are used as IRs [44, 47, 49, 143]. The preferred material is the mixed-phase material microcrystalline silicon oxide ($\mu\text{c-SiO}_x\text{:H}$), but also ZnO:Al is researched [43, 45, 46]. As high efficiency c-Si solar cells approach the thermodynamical limits, c-Si based multi-junction concepts have lately attracted attention [61–63] to further increase the efficiency. A detailed study on the optical requirements of an adequate top cell on a c-Si bottom cell has been conducted by [62] and perovskite has been discussed as possible top cell delivering high current [63]. Additional to the improvement of current and power matching of the sub cells, IRs have the potential to increase the V_{oc} and η of high-efficiency multi-junction solar cells by decreasing the escape cone of the sub cells and minimize radiative recombination losses [144].

4.3. Experimental Methods

For the investigation of light management in tandem solar cells, in this work state-of-the-art thin-film silicon tandem solar cells were used. This Section introduces the materials and production processes of thin-film silicon tandem solar cells and briefly presents the measurements which were used for the characterization of materials and devices.

4.3.1. Solar Cell Fabrication

Deposition of Transparent Contact Layers

The front contact in thin-film silicon solar cells is provided by a transparent conductive oxide (TCO). TCOs are highly doped semi-conductors which are transparent within the visible range and provide sufficient conductivity to act as front electrodes. Typical TCO materials are tin doped indium oxide (ITO), aluminum or boron-doped zinc oxide (ZnO:Al/B), as well as, fluorine-doped tin dioxide (SnO₂:F). The TCO films are deposited by chemical deposition processes under low or atmospheric pressure (LPCVD/APCVD), or physical deposition by sputtering, e.g. from a Rotatable Dual Magnetron (RDM) deposition system [21, 145] onto a glass substrate. The APCVD SnO₂:F substrates in this work were provided from the Asahi Glass Company (AGC) (type VU), LPCVD ZnO:B substrates come from EPFL-IMT [146, 147] and sputtered ZnO:Al are produced at IEK-5 in Jülich basing on [21, 148]. While APCVD/LPCVD substrates exhibit a deposition-inherent surface texture (presented in Fig. 4.17(b) and (c) for APCVD SnO₂:F and LPCVD ZnO:VB, respectively), sputtering on ZnO:Al results in flat surfaces with surface roughness of $\sigma_{\text{RMS}} < 10 \text{ nm}$. Transparency, conductivity and surface morphology of the ZnO:Al layers depends on the various deposition parameters including temperature, pressure, deposition power, oxygen flow and doping of the ZnO:Al₂O₃ target. An additional etching step in diluted hydrochloric acid (HCl) results in the crater-like texture which is presented in Fig. 4.17(a). Deposition parameters, as well as etching is subject of a variety of studies [21, 145, 149, 150]. The empirically optimized ZnO:Al layers which were used in this work were produced at substrate temperatures of 300°C with a doping level of 0.5 wt%. The etching takes place in 0.5% diluted HCl solution for 30 – 40s.

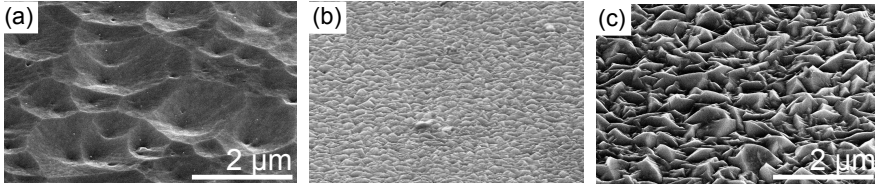


Figure 4.17.: Scanning electron microscopy (SEM) pictures of textured transparent conductive oxides sputter-etched ZnO:Al (a), APCVD SnO₂:F (b) and LPCVD ZnO:B (c).

Deposition of Thin-Film Silicon Layers

The doped and intrinsic layers of the a-Si:H top cell, the $\mu\text{c-Si:H}$ bottom cell, as well as the $\mu\text{c-SiO}_x\text{:H}$ IR layers were deposited in a plasma enhanced chemical vapor deposition (PECVD) system on the TCO front electrode using the standard processes which were discussed in various institute publications [49, 151].

Amorphous silicon (a-Si) is a disordered, amorphous semiconductor based on silicon atoms. Its atoms do not show a long-range order, but the local order leads to the formation of bands of the electron energy levels. Because of the disorder of silicon atoms, dangling bonds exist which create defect states within the band gap. These dangling bonds are saturated by hydrogen atoms which are added to the deposition process resulting in hydrogenated amorphous silicon (a-Si:H). Results of the disordered crystallographic structure are localized tail states. As the mobility of charge carriers is low in these tail states, the band gap of a-Si:H is defined by the mobility resulting in $E_{\text{gap}} = 1.7 - 1.9 \text{ eV}$. Due to its disorder a-Si:H acts as quasi-direct semiconductor with a high absorption coefficient compared to indirect semiconductors. The applied a-Si:H films in this thesis are deposit from the gas phase using the gases silane (SiH_4) and hydrogen in a PECVD process. For more detailed information on material properties and the process of deposition, the reader is directed to [152].

Hydrogenated microcrystalline silicon ($\mu\text{c-Si:H}$) is a two-phase material consisting of silicon crystallites in a matrix of a-Si:H. The a-Si:H matrix provides an excellent passivation of the crystalline silicon which grows in grains showing a higher material quality. $\mu\text{c-Si:H}$ is an indirect semiconductor, its optical properties are similar to c-Si showing a band gap of 1.1 eV (Fig. 4.11). $\mu\text{c-Si:H}$ is produced by PECVD using particular deposition parameters. Best quality $\mu\text{c-Si:H}$ material

has been shown to grow with a crystalline volume fraction depending on the deposition system around 50%. By varying the relevant parameters pressure, gas flow, high frequency power, substrate temperature and plasma excitation frequency the material quality and its optical and electrical properties have been adjusted and optimized [153, 154].

Hydrogenated microcrystalline silicon oxide ($\mu\text{c-SiO}_x\text{:H}$) is a mixed-phase material which is deposited by adding carbon dioxide (CO_2) to the deposition chamber during deposition of p or n -doped $\mu\text{c-SiO}_x\text{:H}$. The resulting material consists of vertical silicon crystallites (p - or n -doped) in a matrix of amorphous silicon and silicon dioxide (SiO_2) [47, 48]. The volume fraction of the low refractive index material SiO_2 determines the refractive index of the whole material while the 'filament'-like silicon crystallites provide the vertical conductivity of the layer [155]. Figure 4.18 shows the influence of the silicon filaments on the optical properties of the $\mu\text{c-SiO}_x\text{:H}$ layer.

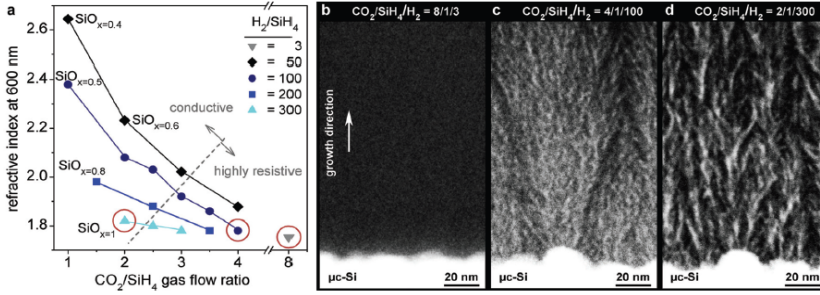


Figure 4.18.: Dependence of the refractive index n on the CO_2/SiH_4 gas flow ratio. The dashed line illustrates the conductivity limit of 10^{-5}Scm^{-1} . (b)-(d) Cross-sections of EFTEM images (white = Si, black = $\text{SiO}_{\gamma-2}$) of the three marked SiO_x films marked in (a). The Figure is taken from [155].

The dependence of the refractive index n on the gas flow ratios (H_2/SiH_4 , as well as CO_2/SiH_4) is shown in Fig. 4.18(a). Two interdependent trends are visible. (i) Increasing the CO_2 -flow decreases the refractive index n of the material. (ii) An increase of H_2/SiH_4 flow ratio effectively leads to a decrease of n . A dashed line depicts the conductivity limit of 10^{-5}Scm^{-1} which has to be fulfilled to be sufficiently conductive to serve as IR in tandem solar cells [48]. Energy filtered transmission electron microscopy (EFTEM) picture in Fig. 4.18(b-d) show silicon

filaments (white) within an amorphous SiO_2 matrix (black) for the three different $\mu\text{c-SiO}_x\text{:H}$ materials from (a) with the same refractive index in different deposition conditions. With increasing H_2 and CO_2 -flow, more filaments are formed resulting in an increased vertical conductivity of the layer. The variation of gas flows enables a variation of the refractive index of the material while keeping the material sufficiently conductive. Detailed information on the optical and electric properties of n -type $\mu\text{c-SiO}_x\text{:H}$ films which have been used within this work is given in [49].

4.3.2. Device Characterization

Current Density - Voltage Characteristic

The current density - voltage (JV) characteristic of a solar cell (Fig. 4.16(b)) is measured in a sun simulator. JV -curves of solar cells in this work are measured in a class I sun simulator using a light pulse of a halogen and Xenon-lamp. Combining both light sources results in an incident spectrum is close to the AM1.5G spectrum (Fig. 4.10) simulating the sun in our geographical region. The solar cell temperature is kept constant at 25° . Inhomogeneities of the illumination are limited to less than 2%

Differential Spectral Response

The differential spectral response (DSR) was measured using a grating monochromator setup ($FWHM$ of the monochromatic light: $\sigma_\lambda = 10\text{ nm}$) measuring in the wavelength range between 300 nm and 1100 nm with a step width of $\Delta\lambda = 10\text{ nm}$. For the measurement of tandem solar cells, an additional bias light with an edge filter of 690 nm and 430 nm was used to flood the sub cell which is not measured. A simultaneous measurement of the spectral response of a calibrated c-Si reference cell, is used to normalize the measurement and obtain the external quantum efficiency EQE of the solar cell. A detailed description of the setup and its modes is found in [156].

Reflection-/ Transmission Measurements

The reflectance R and transmittance T of single layers and solar cells within this work were measured by a two-beam Perkin Elmer UV/Vis spectrophotometer LAMBDA950 which is capable to measure in the wavelength range $175\text{ nm} <$

$\lambda < 3300$ nm. A light beam runs through a monochromator and is separated in a probe and a reference beam. The sample is illuminated by a monochromatic light beam from the superstrate side. An additional reference measurement ensure a normalization of the measurement. As detectors, a photomultiplier ($\lambda < 860$ nm) and a NIR-diode ($\lambda < 860$ nm) are used. By applying an integrating sphere coated by highly reflective white paint also diffusely transmitted or reflected light can be detected. The absorptance of the sample is determined as $A = 1 - R - T$. For a detailed discussion of the setup, the reader is directed to [157].

Photothermal Deflection Spectroscopy

To determine the absorption coefficient close to the band gap of a semiconductor, photothermal deflection spectroscopy (PDS) is used [158, 159]. The investigated sample is positioned in a fluid with a high specific heat and heat conductivity. Tetrachlormethan (CCl_4) is used as it additionally exhibits a temperature-dependent refractive index. The sample is illuminated by a monochromatic light source with variable wavelength. The light is absorbed in the sample. The subsequent non-radiative recombination of charge carriers produces heat which is transferred to the fluid and results in a change of the refractive index. A laser beam which is aligned parallel to the sample surface is refracted by the difference of refractive index in the fluid in adjacency of the sample surface. The deflection of the laser beam is related to the absorptance A in the sample. Inserting the thickness t and refractive index n of the sample, the absorption coefficient α can be determined according to [159].

Optical Data

The complex refractive index $\tilde{n} = n + i\kappa$ of the involved materials in the investigated thin-film silicon solar cells is determined by a combination of ellipsometry, RT-measurements and photothermal deflection spectroscopy. Single layers were deposited on glass and reflectance and transmittance was measured. If the layer thickness of single layers on glass is known, reflectance R and transmittance T can be fitted by a combination of Drude-model, Tauc-Lorentz model and KKR (Kramers Kronig relation) model in the optical spectroscopy software SCOUT [66, 160]. For a determination of the absorption coefficient α below the band gap, where absorptance of the layer is $< 1\%$, PDS of the same layers is additionally applied and κ

by RT-fit is and κ below the band gap is taken from the PDS measurements [66]. The optical data applied in this work are presented in the appendix A.

Atomic Force Microscopy

For the imaging of nano-textured surfaces, atomic force microscopy (AFM) is used. The AFM used for this work is a NANOSTation 300 (SIS GmbH). A silicon tip with a curvature radius of approximately 10 nm and an opening angle of approximately 30° attached on a resonantly oscillating cantilever is positioned in vicinity of the surface. Attractive Van-der-Waals forces between tip and surface result in a change of the resonance frequency of the cantilever. By detecting the change of amplitude of a laser beam which is deflected at the cantilever, the distance between tip and surface can be determined. The distance between tip and surface can be kept constant with a feedback loop and a piezoelectric height control. Scanning the surface with a constant tip-surface distance allows to map the surface and obtain a 3D surface topography with 10 nm resolution. or a detailed discussion of the setup, the reader is directed to [157].

Computational Modeling of External Quantum Efficiency

To model the external quantum efficiency EQE of randomly textured thin-film silicon solar cells, Maxwell's equations have been solved rigorously [56,88–92]. Rigorous optical simulations of the tandem cells were done using the optical material parametrization presented in Cha. A and thickness while just the textures at the different interfaces were implemented. AFM measurements of the TCO topography, after a-Si:H deposition and after $\mu\text{c-Si:H}$ deposition were taken and used as topography for the interfaces in the simulation. The stationary electric and magnetic fields are calculated by the FDTD algorithm (Section 4.1.4). The electric energy density ϵE^2 for a tandem cell at $\lambda = 650$ nm and 900 nm is shown in Fig. 4.19(a) and (b), respectively. As FDTD solver, the MIT tool Meep [100] is used in a modified C++ implementation [103]. Simulations of small periodic systems are performed on a local workstation (4 cores) while large-scale simulations of randomly textured solar cells of up to 10^{12} cells are performed on up to 32 nodes using the JUROPA-cluster [161]. Using Eq. 4.23, the absorptance per mesh cell is calculated. Following the assumption that each absorbed photon generates one charge carrier pair which are entirely collected, the external quantum efficiency

EQE of the layer is calculated as the sum over the absorption in all mesh cells within the concerning layer. Reflectance R and transmission T were calculated as a ratio of reflected/ transmitted Poynting vector in a plane perpendicular to the incident wave propagation direction and free space reference simulations. The absorptance in the different media is calculated from the electric fields by Poynting's theorem (Eq. 4.23). The measured (full line) and simulated *EQE* (dashed line) of the top cell (black) and bottom cell (red), as well as absorptance $A = 1 - R$ (blue) for a tandem solar cell on sputter-etched ZnO:Al texture are shown in Fig. 4.19(c). It is visible that the measured *EQE* can be reasonably reproduced using FDTD simulations. To model the *EQE* of tandem solar cells on randomly textured thin-film silicon solar cells, a domain size of $3.5 \mu\text{m} \times 3.5 \mu\text{m}$ is chosen in order to ensure a sufficient representation of spatial frequencies even of large scale feature surfaces [162, 163].

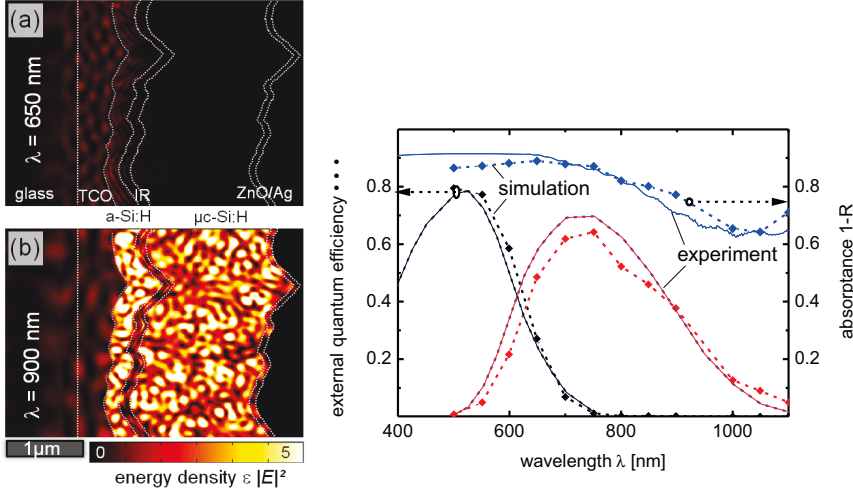


Figure 4.19.: *Simulated electric energy density for a randomly textured tandem solar cells at $\lambda = 650 \text{ nm}$ (a) and $\lambda = 900 \text{ nm}$. (c) Measured (full line) and simulated *EQE* (dashed line) of the top cell (black) and bottom cell (red), as well as absorptance $A = 1 - R$ (blue) for a tandem solar cell on sputter-etched ZnO:Al texture.*

5. Intermediate Reflectors in Tandem Solar Cells - Identification of Loss Mechanisms

To increase the efficiency of series-connected multi-junction solar cells, intermediate reflectors play an important role. However, the integration of IRs is linked to optical losses in the solar cell. Localizing the optical losses is an important step for the optimization of multi-junction solar cell devices. In this chapter, different loss mechanisms are analyzed and quantified to identify possible improvements.

5.1. Motivation

Figure 5.1(a) displays a schematic drawing of such an IR embedded in an exemplary layer stack of a thin-film silicon tandem solar cell. Commonly, thin layers (30 - 150 nm) of transparent and conductive materials with a refractive index n lower than the n of a-Si:H are used as IR. The preferred materials are ZnO:Al and the mixed-phase material microcrystalline silicon oxide ($\mu\text{c-SiO}_x\text{:H}$). In Fig. 5.1(b), the external quantum efficiency (EQE) for two tandem solar cells deposited in one run without (full line) and with IR (dashed line) is shown. The top cell EQE_{top} is shown in orange, bottom cell EQE_{bot} is shown in brown and total $EQE_{\text{sum}} = EQE_{\text{top}} + EQE_{\text{bot}}$ is shown in blue. The solar cells were prepared on sputter-etched ZnO:Al. By introducing the state-of-the-art 70 nm n-type $\mu\text{c-SiO}_x\text{:H}$ layer with a refractive index of $n = 2.6$ at $\lambda = 600\text{ nm}$ between top and bottom cell, a portion of the incident light is reflected back into the top cell increasing EQE_{top} for $500\text{ nm} < \lambda < 800\text{ nm}$ in accordance with [43, 59, 164]. However, this increase is accompanied by a decrease of the bottom cell EQE_{bot} in

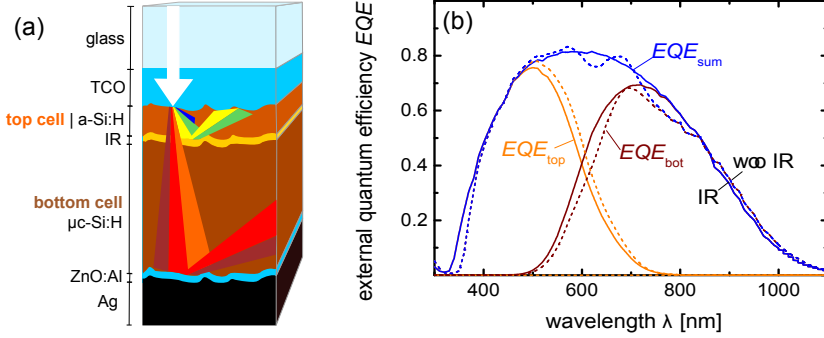


Figure 5.1.: (a) Schematic sketch of a tandem solar cell. (b) The external quantum efficiency (EQE) of a tandem thin-film silicon solar cell without (full line) and with intermediate reflector (dashed line). Orange and brown lines show the EQE of the top cell and bottom cell, respectively. The sum of top and bottom cell EQE_{sum} is shown in blue.

a wide spectral range ($600 \text{ nm} < \lambda < 1000 \text{ nm}$), finally reducing the sum EQE_{sum} (blue line) [45, 165] [48].

5.2. Parasitic Losses in Tandem Solar Cells

As Fig. 5.1(b) shows, EQE_{sum} is reduced by the integration of an IR. This can be basically caused by three different mechanisms:

- Parasitic absorbance in the IR
- Parasitic absorbance in ZnO:Al front contact and doped silicon layers
- Parasitic cell reflectance due to IR/ out-coupling to ambient

To determine the dominating loss mechanism, we make use of an annealing treatment of the ZnO:Al film to decrease the absorption coefficient α . $\alpha(\lambda)$ is determined by PDS measurements (Section 4.3.2). Using Lambert Beer's law (Eq. 4.19), the absorbance for a single light path in a flat thin film with thickness t is determined as $A = 1 - e^{-\alpha t}$, where t is the thickness of the material.

Figure 5.2 shows the absorbance in a $t = 400 \text{ nm}$ thick ZnO:Al layer before (black line) and after annealing treatment (red line). As the band gap of ZnO:Al

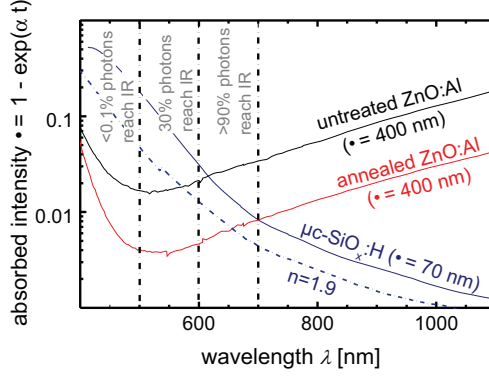


Figure 5.2.: Absorptance A of a 400 nm thick ZnO:Al film on glass untreated (black line) and annealed (red line), as well as the absorptance of a 70 nm thick $\mu\text{c-SiO}_x\text{:H}$ IR with a refractive index $n = 2.6$ (blue full line) and $n_{\text{IR}} = 1.8$ (dash-dotted line).

is $E_{\text{gap}} = 3.4 \text{ eV}$, light in the UV range $\lambda < 365 \text{ nm}$ is absorbed in the ZnO:Al front contact while above 500 nm, absorption is caused by free carrier absorption. By annealing of ZnO:Al, carrier concentration is reduced and, as a consequence, free carrier absorption reduced [?, 166]. More detailed information on the treatment is found in [167]. The absorptance is shifted to lower values by approximately one order of magnitude. Thus, the annealing treatment decreases the absorptance in the whole spectral range reducing it to less than $A < 1.3\%$. The blue lines in Fig. 5.2 indicate the absorptance A of a 70 nm thick $\mu\text{c-SiO}_x\text{:H}$ IR with a refractive index $n_{\text{IR}} = 2.6$ (full blue line) and $n_{\text{IR}} = 1.8$ (dash-dotted line). Dashed-dotted vertical lines mark the percentage of light which is not absorbed in a flat 330 nm thick a-Si:H film and reaches the IR.

5.3. Annealing Experiment

Tandem solar cells on magnetron-sputtered ZnO:Al etched 40 s in a 0.5 % HCl diluted solution were deposited with $t_{\text{a-Si:H}} = 300 \text{ nm}$ and $t_{\mu\text{c-Si:H}} = 1.9 \mu\text{m}$ thick absorber layers. Untreated and annealed ZnO:Al was used as substrates in the same deposition run. In a further run, a 70 nm $\mu\text{c-SiO}_x\text{:H}$ n-layer was deposited as an IR between top and bottom cell (comparable to [49]) while remaining layer thicknesses are kept constant. The comparison between annealed and untreated

ZnO:Al enables to determine the amount of light which is absorbed in the ZnO:Al front contact due to the IR. The EQE of the sub cells is measured by a spectral response measurement setup under bias illumination and is presented in Fig. 5.3. The EQE of the solar cells on annealed ZnO:Al is shown in red and on the untreated ZnO:Al in black. Full lines show the EQE without and the dashed lines with $\mu\text{c-SiO}_x\text{:H}$ IR.

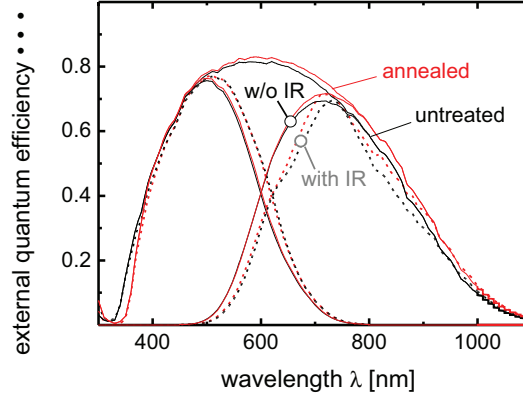


Figure 5.3.: External quantum efficiency EQE of tandem solar cells deposited in the same deposition run on annealed ZnO:Al substrate (red lines) and untreated substrate (black lines) with (dashed lines) and without intermediate reflector (full lines).

EQE_{top} below $\lambda = 400\text{ nm}$ is decreased by the annealing treatment due to Burnstein-Moss-shift reported in [168]. For $\lambda > 600\text{ nm}$, the annealing treatment causes an increase of EQE of approximately $\Delta EQE = 0.05$ which is attributed to the decreased absorption in the front ZnO:Al. By incorporating an IR, in both cases EQE_{top} is increased and EQE_{bot} is decreased. Especially, it is observed that EQE_{bot} is decreased for $\lambda > 700\text{ nm}$. Furthermore, solar cell reflectance R is measured in a PerkinElmer spectrophotometer with integrating sphere. The cell reflectance is presented in Fig. 5.4. The reflectance curves for tandem cells on annealed ZnO:Al substrate are depicted as red lines and untreated substrate as black lines for the tandem cells with (dashed lines) and without IR (full lines). Reflectance is constant for $\lambda < 550\text{ nm}$. In case of the solar cell with IR, local cell reflectance maxima at $\lambda = 580\text{ nm}$, 680 nm and 850 nm are found, whereas for $\lambda = 610\text{ nm}$, 720 nm and $900\text{ nm} < \lambda < 1100\text{ nm}$, the reflectance with IR is lower

than without. This interference effect is caused by light which is reflected at the IR and is not trapped and absorbed in the top cell. This light is coupled out of the solar cell stack. The reflectance of tandem cells on annealed and untreated ZnO:Al is similar for $\lambda < 900$ nm. For $\lambda > 900$ nm, the reflectance of the tandem cell on annealed ZnO:Al is higher and reaches up to $\Delta R = 0.1$ at $\lambda = 1000$ nm. In this regime, absorptance by free carriers in the untreated ZnO:Al front contact is high as seen from Fig. 5.2. Consequently, parasitic absorption in the ZnO:Al is decreased by annealing and the light is reflected back out of the cell. In the case with IR, the reflectance in this regime is reduced due to a minimum of the interference. This effect is the same with and without annealing treatment. The IR does not or just slightly increase the parasitic absorptance in the front ZnO:Al.

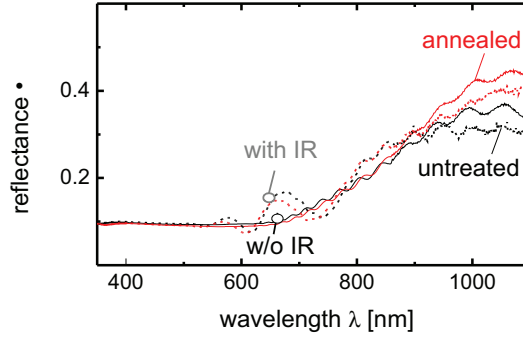


Figure 5.4.: Reflectance R of tandem solar cells deposited in the same deposition run on annealed ZnO:Al substrate (red lines) and untreated substrate (black lines) with (dashed lines) and without intermediate reflector (full lines).

As a measure which amount of light is absorbed apart from the intrinsic absorber layers, the parasitic absorptance A_p is calculated as $A_p = 1 - R - EQE_{\text{sum}}$. A_p is plotted against the wavelength in Fig. 5.5. A_p is generally decreased by the annealing treatment for $\lambda > 600$ nm. The increase in EQE due to annealing from Fig. 5.3 is thus directly related to the decrease of the parasitic absorptance. The parasitic absorptance in the tandem cell with IR is slightly larger for $\lambda > 600$ nm. The difference is more pronounced in case of the annealed front contact which could be due to parasitic absorptance within the $\mu\text{c-SiO}_x\text{:H}$ IR.

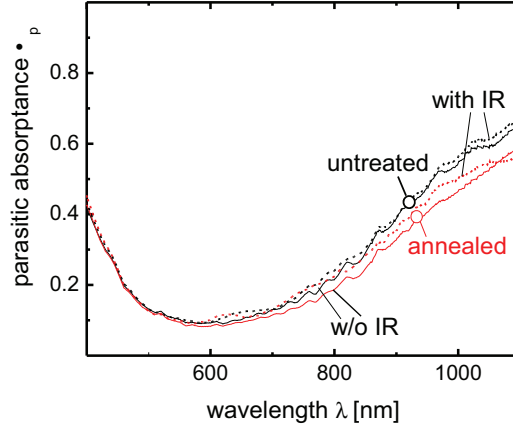


Figure 5.5.: Parasitic absorbance $A_p = 1 - R - EQE$ of tandem solar cells on annealed (red lines) and untreated (black lines) ZnO:Al without (full line) and with intermediate reflector (dashed line).

It was determined that the intermediate reflector increases top cell quantum efficiency and cell reflectance. The parasitic absorbance in the solar cell is decreased by annealing and slightly increased by inserting the intermediate reflector. Experimental data do not show in which layers the parasitic absorption takes place.

5.4. Rigorous Optical Simulation

To get an insight where the parasitic absorption is localized, rigorous optical simulations of a tandem solar cell on untreated ZnO:Al with and without 70 nm $\mu\text{-SiO}_x\text{:H}$ IR ($n = 2.6$) were performed.

In Fig. 5.6(a), the parasitic absorbance extracted from simulation A_p in ZnO:Al (black line) and $\mu\text{-SiO}_x\text{:H}$ IR (red line) for the case without (full line) and with IR (dashed line) are shown. $A_{p,\text{ZnO}}$ is minimal at $\lambda < 550$ nm ($A_{p,\text{ZnO}} < 5\%$). For longer wavelengths, free carrier absorption increases and makes out 23% at $\lambda = 1100$ nm, $A_{p,\text{ZnO}}$ is nearly identical in the tandem solar cell with and without IR, but for $800 \text{ nm} < \lambda < 900 \text{ nm}$, an increase of $A_{p,\text{ZnO}}$ is observed. Here, the

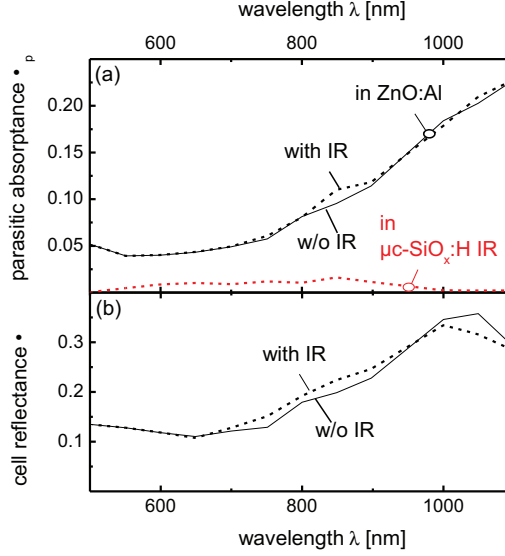


Figure 5.6.: Parasitic absorbance (A_p) in ZnO:Al (black) and $\mu\text{c-SiO}_x\text{:H}$ on untreated ZnO:Al without (full line) and with two different $\mu\text{c-SiO}_x\text{:H}$ IRs extracted from simulation. As IR 70 nm thick $\mu\text{c-SiO}_x\text{:H}$ with a refractive index $n = 2.6$ (dashed line) is used. (b) Cell reflectance R of the tandem solar cell without (full line) and with high- n IR (dashed line) and low- n IR (dotted line).

reflectance of the IR is still high, the a-Si:H top cell does not absorb and the absorbance in the 400 nm thick ZnO:Al film is already 7% according to Fig. 5.2. The parasitic absorbance in the $\mu\text{c-SiO}_x\text{:H}$ IR is depicted as red dashed line. It amounts around 1% in the range of $500\text{ nm} < \lambda < 900\text{ nm}$ with a maximum of $A_{p,\text{IR}} = 1.6\%$ at $\lambda = 850\text{ nm}$. It has, therefore, a larger contribution on J_{sc} than the additional $\Delta A_{p,\text{ZnO}}$ due to the IR which just contributes for $800\text{ nm} < \lambda < 900\text{ nm}$. **The additional parasitic absorbance of the tandem solar cell due to the IR is dominated by the absorbance in the IR.** The increase $A_{p,\text{ZnO}}$ indicates, however, that the reflection at the IR plays a major role concerning the losses of the system. Therefore, the total cell reflectance is investigated. Figure 5.6(b) shows the reflectance of the tandem solar cell without (full line) and with the IR (70 nm, $n = 2.6$, dashed line). Reflectance increases for longer wavelengths

as a smaller portion of light can be absorbed in the solar cell when the absorption length of $\mu\text{c-Si:H}$ is long. By the introduction of an IR, the reflectance R is increased in the range $700\text{ nm} < \lambda < 950\text{ nm}$. The IR reflects light back into the a-Si:H top cell where it is hardly absorbed in that spectral range, but reflected out of the solar cell. Back-reflected light passes through the ZnO:Al front contact and is also parasitically absorbed in the ZnO:Al for $800\text{ nm} < \lambda < 900\text{ nm}$ as the difference between full and dashed line in Fig. 5.6(a) shows. For $\lambda > 1000\text{ nm}$, R is smaller with IR. As EQE_{bot} for $\lambda > 1000\text{ nm}$ is additionally increased up to 10% by implementing an IR, the top cell with IR seems to provide a better light incoupling into the bottom cell. To compare the contributions of the various parasitic losses quantitatively, the absorptance A was integrated and weighted by the AM1.5 spectrum resulting in a top cell short-circuit current density gain $\Delta J_{\text{sc,top}}$ and the short-circuit current density losses $\Delta J_{\text{sc,x}}$ in the various layers and by reflection (with $x = \text{ZnO:Al, IR, R}$). The results are presented in Tab. 5.1. $\Delta J_{\text{sc,top}} = 0.46$ is small for the tandem solar cell with the high- n IR. Here, the losses of $\Delta J_{\text{sc,sum}} = -0.55 \frac{\text{mA}}{\text{cm}^2}$ are dominantly due to parasitic absorptance in the IR and parasitic reflectance out of the tandem solar cell in the maximum of EQE_{bot} , while parasitic absorption in the ZnO:Al front contact plays a minor role. The maximum of parasitic reflectance is in a range $\lambda < 900\text{ nm}$, where the ZnO:Al front contact is highly transparent.

5.4.1. Influence of Refractive Index

To evaluate the influence of the refractive index of the IR, a $\mu\text{c-SiO}_x\text{:H}$ IR with $n = 1.8$ is simulated within the same tandem cell configuration. The IR thickness is optimized to the decreased n resulting in $t_{\text{IR}} = 40\text{ nm}$. The higher refractive index contrast between a-Si:H and IR results in higher reflectance of the IR. Furthermore, low- n $\mu\text{c-SiO}_x\text{:H}$ material is characterized by a lower absorptance as shown in Fig. 5.2. As a result, the decrease in n reduces the parasitic absorption in the IR and increases the IR reflectance and, thus, the top cell gain. The path prolongation of light in the a-Si:H top cell due to the IR can be calculated as $EQE\text{-ratio} = \frac{EQE_{\text{top,IR}}}{EQE_{\text{top,w/o}}}$ and is presented in Fig. 5.7(a) for high- n IR (black, dashed) and low- n IR (gray, dash-dotted). As a larger portion of light travels through the ZnO:Al front contact several times, the parasitic absorptance in the front ZnO:Al layer is increased for the lower n_{IR} . The reflectance of the tandem solar cells R with

Table 5.1.: *Parasitic losses in the tandem solar cell: Top cell short-circuit current density gain $\Delta J_{sc,top}$, total tandem cell short-circuit current density losses $\Delta J_{sc,sum}$, parasitic short-circuit current density losses in ZnO:Al $\Delta J_{sc,ZnO}$, parasitic short-circuit current density losses in IR $\Delta J_{sc,IR}$, parasitic short-circuit current density losses by reflection $\Delta J_{sc,R}$ with a $\mu c\text{-SiO}_x\text{-H}$ IR with refractive index $n_{IR} = 2.6$ and $n_{IR} = 1.8$.*

n_{IR}	t_{IR}	$\Delta J_{sc,top}$	$\Delta J_{sc,sum}$	$\Delta J_{sc,ZnO}$	$\Delta J_{sc,IR}$	$\Delta J_{sc,R}$	$\Delta J_{sc,R,<1000\text{ nm}}$
$[-]$	nm	$\frac{mA}{cm^2}$	$\frac{mA}{cm^2}$	$\frac{mA}{cm^2}$	$\frac{mA}{cm^2}$	$\frac{mA}{cm^2}$	$\frac{mA}{cm^2}$
2.6	70	0.46	-0.55	-0.07	-0.28	-0.10	-0.26
1.8	40	1.36	-0.58	-0.17	-0.10	-0.34	-0.49

both discussed IRs are shown in Fig. 5.7(b). Arrows indicate that the decrease of n_{IR} and absorption coefficient α increase the cell reflectance for $\lambda < 1000\text{ nm}$ and decrease it for $\lambda > 1000\text{ nm}$.

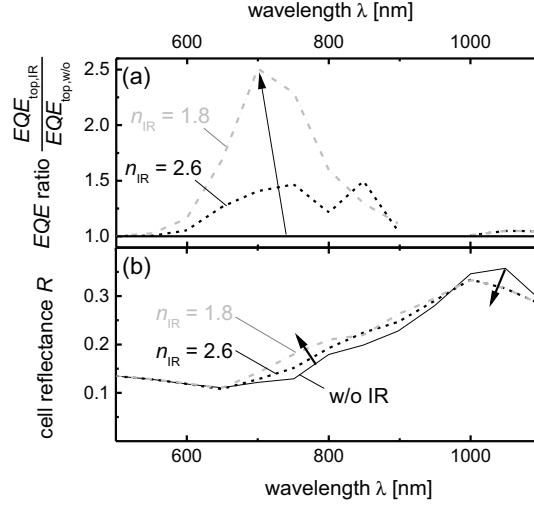


Figure 5.7.: (a) EQE ratio $\frac{EQE_{top,IR}}{EQE_{top,w/o}}$ for high- n IR (black, dashed) and low- n IR (gray, dash-dotted). (b) Cell reflectance R of the tandem solar cell without (full line) and with high- n IR (dashed line) and low- n IR (dotted line).

Table reftab:anneal sums up the gains and losses which are induced by the IR. The parasitic absorptance A_p are spectrally integrated using Eq. 4.48 resulting in parasitic short-circuit density losses $\Delta J_{sc,x}$. An increase of $\Delta J_{sc,top} = 1.36 \frac{mA}{cm^2}$

is observed. Minimizing the losses in the IR, the main loss mechanism is cell reflectance in this case ($\Delta J_{\text{sc,R}} = -0.34 \frac{\text{mA}}{\text{cm}^2}$). If the reflectance decrease for $\lambda > 1000 \text{ nm}$ is not considered, $\Delta J_{\text{sc,R}, < 1000 \text{ nm}}$ is even $-0.49 \frac{\text{mA}}{\text{cm}^2}$. The reflection loss $\Delta J_{\text{sc,R}, < 1000 \text{ nm}}$ is doubled in comparison to the high- n IR and so is the parasitic absorptance in the ZnO:Al due to the IR. If absorptance in the IR is minimized due to low absorption coefficients α of the material, parasitic reflectance is the dominating loss mechanism.

In this chapter, the optical loss mechanisms in tandem thin-film silicon solar cells with intermediate reflector (IR) were systematically investigated. Annealing the front ZnO:Al and, thus, decreasing its absorptance has been used as a tool to experimentally show, that for IRs with high refractive indices, additional parasitic absorptance due to the IR A_p in the ZnO:Al is low. It was determined that the main part of additional parasitic absorption happens in the $\mu\text{c-SiO}_x\text{:H}$ IR. Additionally, parasitic reflection plays an important role in the part of the spectrum of low absorption in the a-Si:H top cell. By rigorous optical simulations, the IR thickness and refractive index was changed without varying the other solar cell parameters. For IRs with a low refractive index, a high IR reflectance is reached, but reflection above $\lambda = 700 \text{ nm}$ is just slightly absorbed in the top cell, but reflected out of the solar cell resulting in parasitic reflection losses or parasitic absorption in the ZnO:Al front contact.

6. Spectrally Selective Intermediate Reflectors

The previous chapter identified the main loss mechanisms for tandem solar cells with intermediate reflector. Reflection losses out of the solar cell account for a large part of these losses. In this chapter, the spectral dependence of the effect of the IR is studied and a multilayer filter from thin-film materials is proposed and designed as IR in thin-film silicon tandem solar cells. The advanced IR is finally successfully integrated into flat and textured solar cells. The chapter concludes with a comparison to literature and a discussion about the potential of further optimization. The results were published in [169].

6.1. Design Criteria

The integration of IRs is linked to reflection losses in the solar cell as demonstrated in Chapter 5. Localizing the optical losses is an important step for the optimization of multijunction solar cell devices. In Fig. 6.1, the EQE of a tandem solar cell without (full line) and with IR (dashed line) is shown. Black lines indicate the EQE of the sub cells; EQE_{sum} is shown as blue line. Three spectral ranges are indicated by I-III. In the range $\lambda < 520$ nm, photons are entirely absorbed in the top cell and do not reach the IR. In range II between $520 \text{ nm} < \lambda < 680$ nm, an increasing amount of photons reaches the back side of the top cell and, consequently, the IR. A part of the light is reflected back depending on the reflectance of the IR. Thus, the light path within the top cell resulting in an increase of EQE_{top} .

In range III ($\lambda > 680$ nm), the absorptance of the a-Si:H top cell is low. Therefore, a path enhancement just slightly increases EQE_{top} . In this range, the $\mu\text{-Si:H}$

bottom cell is highly absorptive so that a decrease of transmission into the bottom cell directly decreases EQE_{bot} as Fig. 6.1 illustrates.

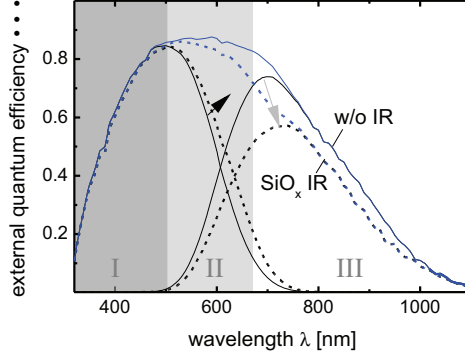


Figure 6.1.: The external quantum efficiency (EQE) of a tandem thin-film silicon solar cell without (full line) and with $\mu\text{c-SiO}_x\text{:H}$ intermediate reflector (dashed line). Black lines show the EQE of the sub cells; EQE_{sum} is shown as blue line.

Further, the dependence of the refractive index on the reflectance in range II and III is investigated. Therefore, solar cells were prepared on APCVD $\text{SnO}_2\text{:F}$ substrate with i-layer thicknesses of $t_{\text{a-Si i}} = 300 \text{ nm}$ and $t_{\mu\text{c-Si:H i}} = 2 \mu\text{m}$. The $\mu\text{c-SiO}_x\text{:H}$ IR has a thickness of 70 nm and the refractive index of the IR was varied between $1.9 < n_{\text{IR}} > 3$. The transfer matrix method was used (Section 4.1.4) to simulate the reflectance of a single $\mu\text{c-SiO}_x\text{:H}$ layer between non-absorbing a-Si:H half spaces. The measured cell reflectance R_c of thin-film silicon solar cells with $\mu\text{c-SiO}_x\text{:H}$ IRs of different refractive indices $n = 1.9$ (red), $n = 2.5$ (green) and $n = 3.0$ (blue) is shown in Fig. 6.2 as full lines. Dashed lines in Fig. 6.2 show the simulated reflectance of flat IR configurations with the same refractive indices (same color code) into a non-absorbing a-Si:H half space as a function of the wavelength.

The single layer IR reflects a portion of the light in the required wavelength range depending on the refractive index contrast. Still, reflectance at longer wavelengths (region III) is approx. 0.1 in the range $680 \text{ nm} < \lambda < 1100 \text{ nm}$ in case of the $\mu\text{c-SiO}_x\text{:H}$ IR with $n = 1.9$ and show low spectral selectivity. As the absorption length of a-Si:H is long in region III, reflectance of the IR in this spectral range does not lead to a significant absorption enhancement in the top cell. Furthermore, the back

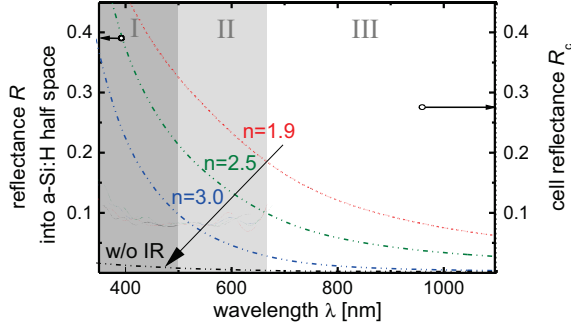


Figure 6.2.: Left axis shows the reflectance R of a $t = 70$ nm thick $\mu\text{-SiO}_x\text{:H}$ intermediate reflector of refractive index $n = 1.9$ (red), $n = 2.5$ (green) and $n = 3.0$ (blue) into a non-absorbing a-Si:H half space. The right axis shows the measured cell reflectance R of tandem solar cells with $\mu\text{-SiO}_x\text{:H}$ IR with $n = 1.9$ (red), $n = 2.5$ (green) and $n = 3.0$ (blue).

reflected light does not couple into the bottom cell and cannot be absorbed and contribute to charge carrier generation. The increase of IR reflectance in range II is linked to parasitic losses in range III which result in a parasitic cell reflectance.

The effect of the IR on charge carrier generation in a tandem solar cell with IR was discussed. Two important criteria for an effective IR are formulated: In the spectral range II, reflection into the top cell shall be maximized while in range III ($\lambda > 680$ nm), transmission into the bottom cell as to be maximized.

6.2. Design of Multilayer Filters

It can be concluded that the ideal IR should exhibit a reflectance of $R = 1$ in range II, while $R = 0$ in range III. This reflectance target function is depicted in Fig. 6.3.

A Bragg reflector or 1D photonic crystal [74] provides spectral selectivity by reflecting back just in a certain wavelength range related to its photonic band gap. The photonic band structure of a $N = 100$ layer thick Bragg stack is shown in Fig. 6.4. A band gap between $f = 0.32$ and 0.39 is visible from the diagram at the

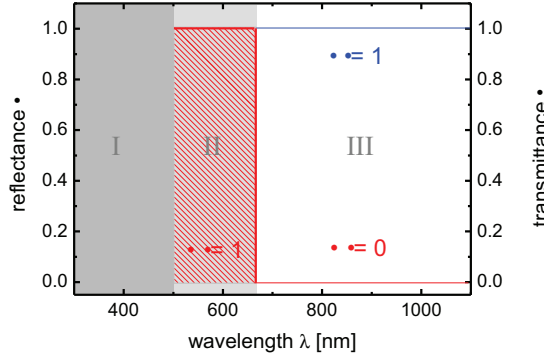


Figure 6.3.: Reflectance R and transmittance T of an ideal filter as intermediate reflector in a tandem solar cell.

X symmetry point.

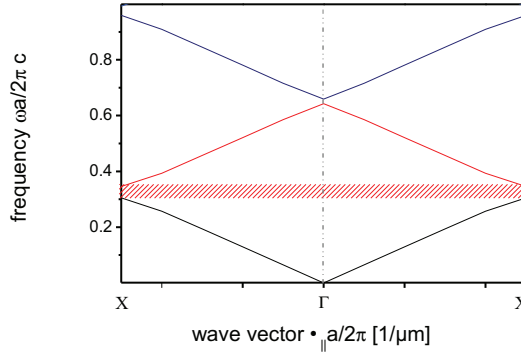


Figure 6.4.: Photonic band structure in the optical dispersion $\omega(k)$ for a 1D photonic crystal (PhC) or Bragg stack.

Within the photonic band gap, no photonic states are allowed resulting in a high reflectance band. The reflectance of a Bragg filter of $N = 100$ layers of the refractive indices $n = 2.0$ and 3.0 with thicknesses subsequently stacked is shown as gray line in Fig. 6.5. The width of the reflection band is determined by the optical contrast of the stacked materials while the layer thicknesses are linked to

the spectral position of the reflectance peak maximum λ_0 according to

$$t = \frac{\lambda_0}{4n_{\text{IR}}} . \quad (6.1)$$

The layer thickness were adjusted to fit the reflectance band into range II where a maximum of reflectance shall be facilitated. A reflectance of almost $R = 1.0$ is achieved within this range. However, the boundaries are defects of the photonic crystal causing reflectance side lobes. This leads to a reflectance of 20 – 60% in range III. As the transmittance into the bottom cell in range II has to be maximized, these side-lobes are parasitic. Side lobes can be totally discriminated by adding further refractive index materials to the filter providing a sinusoidal n -profile. This concept is called Rugate filter and discussed extensively in [170,171]. An additional low refractive index layer with the thickness $t_{\text{IR}} = \frac{\lambda_0}{8n}$ before and behind the filter effectively suppresses side lobes below the photonic band gap [74]. The reflectance of such stack is illustrated as blue line in Fig. 6.5 for thin-film materials with wavelength-independent refractive indices $n_{\text{IR}} = 2.0$ and 3.0 .

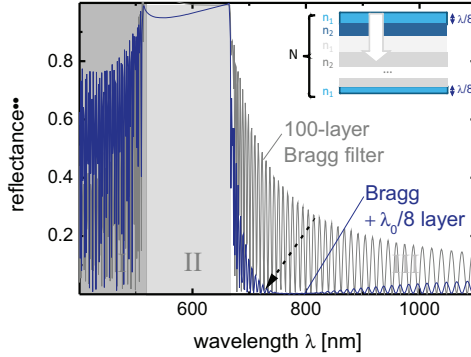


Figure 6.5.: Reflectance R into an $a\text{-Si:H}$ half space for a Bragg filter of 100 layers of the refractive indices $n = 2.0$ and 3.0 with thicknesses $t = \frac{\lambda_0}{4n}$ subsequently stacked (gray line). The introduction of a further low refractive-index $\frac{\lambda_0}{8n}$ -layer results in the reflectance curve indicated in blue.

The spectral filter reflectance is shown in Fig. 6.6 for the incidence angles $\theta = 0^\circ$ (black), 10° (dark blue), 20° (blue) and 30° (light blue). A shift of the reflectance maximum and the reflectance edge to shorter wavelengths is observed by an increase of the angle of incidence. This shift is just slight for 10° , but amounts

$\Delta\lambda = 90 \text{ nm}$ for $\theta = 20^\circ$. For 30° , the reflectance behavior changes significantly as the critical angle of total internal reflection is reached. For $\theta > \theta_{\text{TIR}}$, the IR reflectance is not spectrally selective.

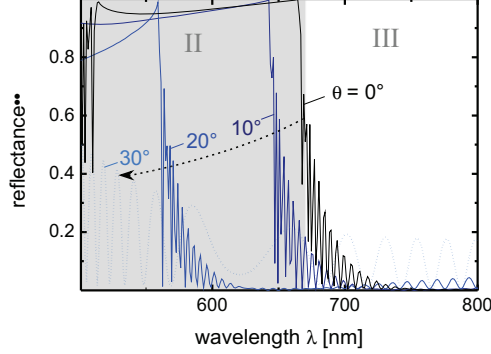


Figure 6.6.: Reflectance R into an $a\text{-Si:H}$ half space for a Bragg filter of 100 layers of the refractive indices $n = 2.0$ and 3.0 with thicknesses $t_{\text{IR}} = \frac{\lambda_0}{4n}$ subsequently stacked for normal incidence (black line) and for incidence angles of 10° (dark blue), 20° (blue) and 30° (light blue).

In a next step, the ideal IR materials were substituted by realistic optical data of ZnO:Al and a high silicon phase $\mu\text{c-SiO}_x\text{:H}$. The used optical data are shown in Appendix A. To integrate multilayer filters into tandem solar cells, besides its reflectance, the following requirements have to be met:

- To maximize transmittance into the bottom cell, a high transparency for photon energies below the photonic band gap and low parasitic absorptance of the IR need to be achieved.
- The IR has to work as a tunnel recombination junction between pin- top and bottom cell. Therefore, the filter has to be conductive. In case of $\mu\text{c-SiO}_x\text{:H}$ IRs, a critical conductivity of $\sigma = 10^{-5} \text{ S/cm}^2$ has been determined to be necessary in order to facilitate a sufficient charge carrier transport [49].

In a series-connected silicon thin-film tandem solar cell, a filter consisting of 100 layers would have a thickness of $t_{\text{IR}} \gg 1 \mu\text{m}$ and would not achieve the presented

criteria. It is a relevant option, however, in a four-terminal multi-junction device where optical and electrical properties are decoupled and transparent, non-conducting materials like TiO_2 or highly transparent polymers can be used [74]. Another concept uses 1D photonic crystals made from ITO/ SiO_2 nanoparticle stacks [172, 173] as intermediate reflectors. As these devices require additional production steps and are not compatible with state-of-the-art large-area thin-film silicon production processes, they will not be further investigated within this work. In contrast, I study how a reduction of layer numbers influences the reflection behavior of the filter. The reflectance into the a-Si:H half space is shown in Fig. 6.7 for $N = 100$ (IR_{100} , black), $N = 10$ (IR_{10} , cyan), $N = 3$ (IR_3 , red) and $N = 1$ (blue) layers. Due to absorption in the IR layers and a varying refractive index, the peak and absorption edge wavelength is shifted to shorter wavelength. A reduction of IR layers has two major effects: The reflectance maximum is decreased and the reflectance edge is smeared out. The $N = 10$ -layer filter, achieves still 95% at its maximum, but the edge is not abrupt anymore. For a reduced number of layers, the effect of the boundaries of the filter becomes dominant. As a result, Eq. 6.1 is not anymore a feasible criterion to determine optimal thicknesses of the IR layers. This is why an in-house developed genetic algorithm [86, 87] is used to optimize the layer thicknesses of the IR. $N_{\text{pop}} = 21$ populations and a mutation rate $n_{\text{mut}} = 0.3$ with a selection fraction of $f = 0.5$ are chosen. $i = 40$ iterations are run to achieve sufficient convergence of the algorithm. As target function, a maximum reflectance in range II of $R_{\text{II}} = 1$ is defined, while the transmittance in range III ($680 \text{ nm} < \lambda < 1100 \text{ nm}$) shall be maximized ($T_{\text{III}} = 1$) as shown in Fig 6.3. For $N = 3$ layers, optimal layer thicknesses are $t_{\text{ZnO:Al},1} = 62 \text{ nm}$, $t_{\text{SiO}_x} = 38 \text{ nm}$ and $t_{\text{ZnO:Al},2} = 52 \text{ nm}$. The reflectance of the optimized $N = 3$ layer stack is shown as red line in in Fig. 6.7. As the red curve shows, with just $N = 3$ layers a spectrally selective filter can be achieved. A maximum reflectance of 0.8 can be achieved with this filter, while the reflectance in range III is $< 10\%$. As a comparison, the reflectance of a $N = 1$ layer ZnO:Al IR with $t_{\text{IR}} = 114 \text{ nm}$ is presented in blue. Reflectance is rather constant independent of the wavelength, resulting in a high reflectance in range III where reflectance should be minimized due to the design criteria from Section 6.1. The filter with $N = 3$ layers (IR_3) has a total thickness of $t_{\text{IR}} = 152 \text{ nm}$ and consists to a large extend of conductive ZnO:Al. This is why, it is considered to be a feasible implementation of an IR in series-connected thin-film silicon solar cells. Its spectrally selective reflectance

is highly favorable compared to 1-layer intermediate reflectors. The IR_3 matches the formulated design criteria and can be integrated in standard thin-film silicon tandem cell process workflow without additional expensive production steps.

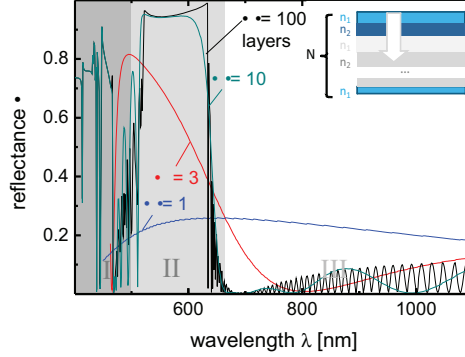


Figure 6.7.: Reflectance R into an $a\text{-Si:H}$ half space for an increasing number of $\mu\text{c-SiO}_x\text{:H}$ and ZnO:Al layers. The reflectance of a single layer of 114 nm ZnO:Al ($n = 2$) into an $a\text{-Si:H}$ half space is shown in blue. Additionally, the reflectance of alternating stacks of $N = 100$ (IR_{100}) (black), $N = 10$ (IR_{10} , cyan) and $N = 3$ (IR_3 , red) is presented.

The feasibility of Bragg filters/ 1D photonic crystals for use as IR was investigated. A 3-layer IR (IR_3) from available thin-film materials ZnO:Al and $\mu\text{c-SiO}_x\text{:H}$ is conductive, has low parasitic absorptance and provides spectrally selective reflectance while ensuring high transmittance in spectral range III and can be easily integrated in thin-film silicon solar cell tandem production.

6.3. Experimental Realization

The designed IR_3 is produced by depositing subsequently ZnO:Al by sputtering and $\mu\text{c-SiO}_x\text{:H}$ layers by PECVD on an $t = 50$ nm $a\text{-Si:H}$ layer on glass. The glass/ $a\text{-Si:H}$ stack was characterized before by RT -measurements. After deposition of the layers, reflectance and transmittance at the same position was measured with a spectrophotometer with integrating sphere. The results were fitted with the

TMM algorithm integrated in the commercially available software SCOUT using the optical nk -data of all involved materials to obtain the real thicknesses of the individual layers. To compare the experimental filter to our TMM calculations, the glass and air half space are substituted by a-Si:H and, respectively, $\mu\text{c-Si:H}$ half spaces. Layer thicknesses of the experimentally realized filter (dotted black line) vary by less than $\Delta t = 3$ nm from the targeted thicknesses resulting in a good accordance between the reflectances of the real layer stack (dotted black line) and the optimized stack (red line) as shown in Fig. 6.8.

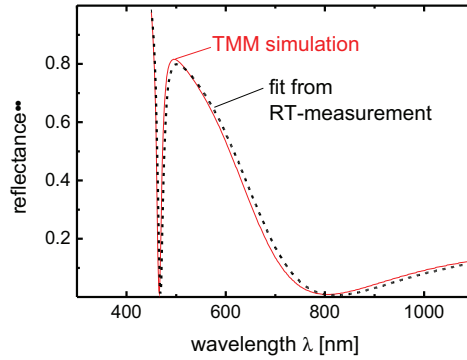


Figure 6.8.: Reflectance R into an a-Si:H half space for the calculated $N = 3$ layer intermediate reflector (IR_3).

6.3.1. Integration into flat solar cells

Subsequent to the conceptual design of the IR, the following section shows the implementation of the IR_3 into state-of-the-art tandem thin-film silicon solar cells.

Tandem solar cells are deposited on a flat ZnO:Al substrate with an a-Si:H i-layer thickness of $t_{\text{a-Si:H i}} = 330$ nm and a $\mu\text{c-Si:H i}$ layer thickness of $t_{\mu\text{c-Si:H i}} = 3.2$ μm . Figure 6.9(a) shows the EQE and absorptance $A = 1 - R$ of a tandem solar cell without IR (black) and with IR_3 (red). As an effect of the IR on the top cell EQE_{top} , a maximum at $\lambda = 620$ nm is found. Here, the absorptance of the solar cell is increased to more than 90%, so nearly the whole portion of back-reflected

light is absorbed. With increasing wavelength, less of the back-reflected photons can be absorbed in the top cell and, thus, escape out of the solar cell. This is resembled in the absorptance minimum (reflectance maximum) at $\lambda = 700$ nm and, consequently, as a dip in EQE_{bot} . Figure 6.9(b) shows the EQE -ratio in the top cell $\frac{EQE_{\text{top,IR}}}{EQE_{\text{top,w/o}}}$. This quantity is related to a path prolongation within the top cell. A local maximum at $\lambda = 620$ nm is found in $EQE_{\text{top,IR}}$ with IR. A decreased EQE_{bot} and absorptance for $\lambda > 800$ nm in comparison to the solar cell without IR is found, which is probably due to the substrate-dependent growth of $\mu\text{c-Si:H}$ i-layer. The substrate dependency is visible in the thickness of the i-layer grown on the IR_3 that is reduced by 105 nm and the Raman crystallinity I_c at a wavelength of $\lambda = 532$ nm that is reduced to 47% in comparison to the reference tandem cell without IR ($I_c = 56\%$).

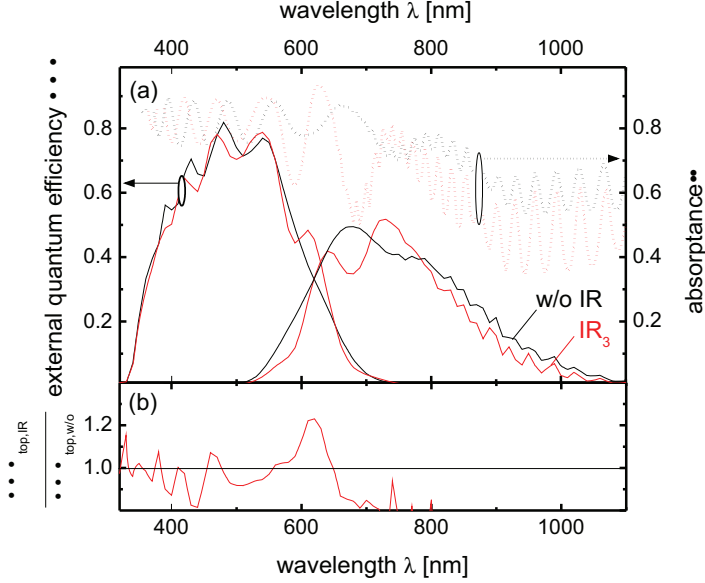


Figure 6.9.: (a) Measured external quantum efficiency EQE and absorptance $A = 1 - R$ of a flat tandem solar cell without (black) and with our IR_3 (red line). (b) The EQE_{top} -ratio $\frac{EQE_{\text{top,IR}}}{EQE_{\text{top,w/o}}}$ in the flat case.

6.4. Influence of the Roughness on Multilayer Intermediate Reflector

As the physical thicknesses of a-Si:H top cell, as well of the $\mu\text{c-Si:H}$ bottom cell are limited due to physical constraints, increasing the optical path within the layers by scattering and diffraction are increasingly important. Light trapping is achieved by rough substrates scattering light into a broad distribution of angles.

In order to integrate the IR_3 into state-of-the-art tandem solar cells, it has to be considered that interfaces are textured in order to provide light scattering and, thus, trap the light. Therefore, rigorous optical simulations of the textured layer stack are performed. The cross-section of the electric field intensity of the tandem solar cell with IR_3 on flat (dashed line, (a)) and APCVD-type $\text{SnO}_2\text{:F}$ substrate (full line, (b)) is presented in Fig. 6.10. Figure 6.10(c) shows the reflectance (red, left axis) of the IR_3 on flat (dashed line) and APCVD-type $\text{SnO}_2\text{:F}$ substrate (full line) into a non-absorbing a-Si:H half space over the wavelength. The reflectance of the rough IR shows the same edge as in the flat case but reflectance is generally reduced by 30% as the symmetry of the filter is disturbed by the roughness [54,174]. A significant portion of the light up to 50 % is still reflected for the target spectral range, while above $\lambda = 700 \text{ nm}$, less than 5% are reflected back. It can be concluded that the designed IR_3 works as a spectrally selective filter despite its random texture due to the roughness of the front contact. The transmittance T of the layer stack glass/ ZnO:Al /a-Si:H / IR_3 into a non-absorbing $\mu\text{c-Si:H}$ half space is shown as blue lines in Fig. 6.10 (blue, right axis) in the flat (dashed line) and rough case (full line). The transmittance edge is shifted to longer wavelengths by introducing the roughness. This is because reflection at the IR induces scattering into large angles resulting in light trapping in the top cell. The interplay of IR reflectance and light trapping in the top cell is highly relevant and will be studied in the following Chapter (Chapter 7). The transmittance T through a layer stack with IR_3 to T with 114 nm-thick ZnO:Al IR (cyan line) and shown in Fig. 6.11. The transmittance with the real layer thicknesses of the top cell and into the $\mu\text{c-Si:H}$ bottom cell in range III is obtained by rigorous optical simulations is significantly increased by the IR_3 as a consequence of spectral selectivity.

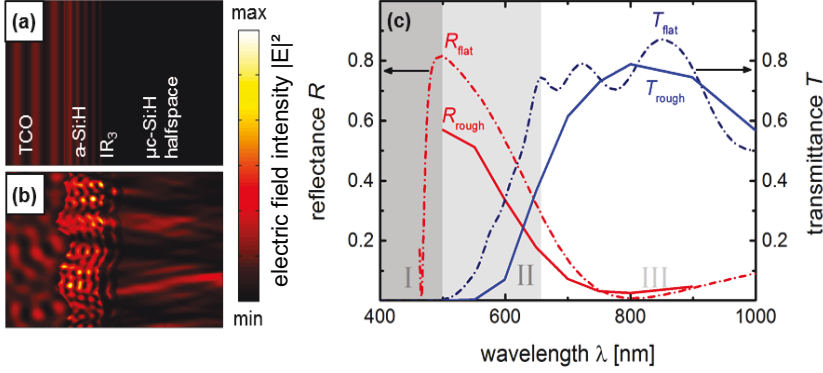


Figure 6.10.: Cross-section of the electric field density in a thin-film solar cell stack with $\mu\text{c-Si:H}$ half space on flat (a) and textured substrate (b). (c) The reflectance R into an a-Si:H half space (red) and the transmittance T (blue) with 3-layer intermediate reflector (IR₃) are shown for the flat (dashed line) and rough case (full line).

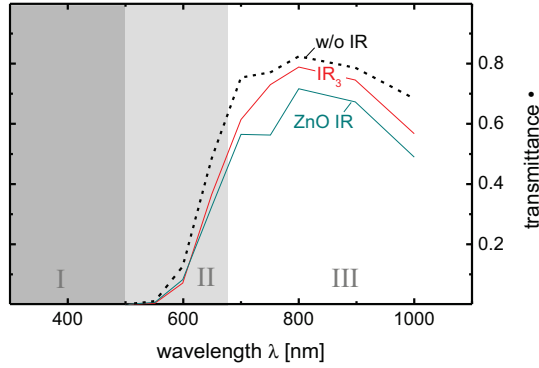


Figure 6.11.: Transmittance T into the non-absorbing $\mu\text{c-Si:H}$ half space is shown for the 3-layer intermediate reflector IR₃ and ZnO:Al IR simulated by rigorous optical simulations.

6.5. Fabrication of Thin-Film Silicon Prototype on Textured Substrates

The IR₃ is then integrated into a state-of-the-art tandem solar cell on APCVD SnO₂:F substrate. The photovoltaic parameters of the tandem solar cells with the

various studied IRs are shown in Table 6.1. Figure 6.12(a) shows the EQE and absorptance $A = 1 - R$ of the solar cell with different IR designs. Without IR (black line), a clear mismatch between top and bottom cell short-circuit current density J_{sc} is seen. Integrating a single layer IR leads to an increase of EQE_{top} for $500 \text{ nm} < \lambda < 750 \text{ nm}$. The amount of increase depends on the refractive index and thickness of the IR. The ZnO:Al IR (cyan line) reflects a large portion of light which yields a reflectance of around 20% (Fig. 6.7). The absence of this large fraction of the incoming light leads to significant losses in the bottom cell. In the case of the $\mu\text{c-SiO}_x\text{:H}$ IR (blue line), bottom cell losses are lower. Yet, the boosting effect on top cell EQE_{top} is low as well. The red line illustrates the EQE and absorptance of the tandem solar cell with IR_3 . For $500 \text{ nm} < \lambda < 600 \text{ nm}$, the EQE_{top} exceeds the one of the tandem solar cell with 114 nm-thick ZnO:Al IR. With increasing wavelength, less photons are absorbed in the top cell resulting in an absorptance dip at around $\lambda = 610 \text{ nm}$.

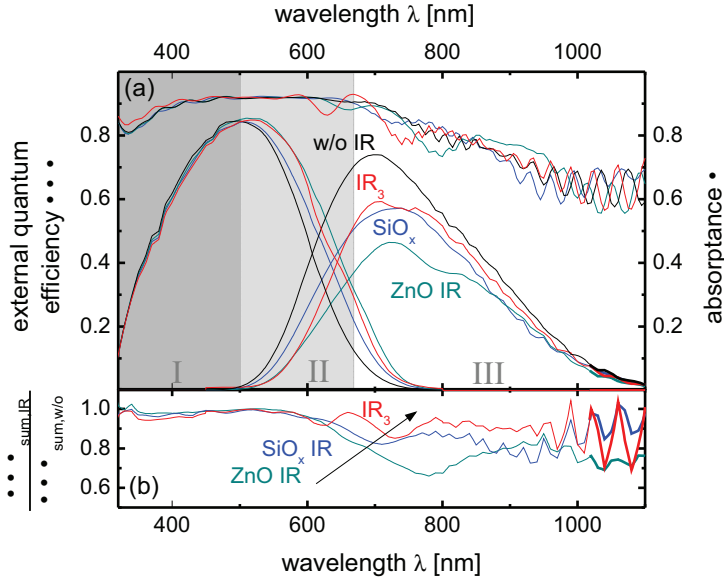


Figure 6.12.: (a) EQE and absorptance $A = 1 - R$ for the various IR designs in a textured tandem solar cell on APCVD $\text{SnO}_2\text{:F}$ substrate. (b) shows the EQE -ratio $\frac{EQE_{sum,IR}}{EQE_{sum,w/o}}$ for the textured tandem solar cells.

Table 6.1.: Photovoltaic parameters short-circuit current density J_{sc} of the sub cells and sum, open-circuit voltage V_{oc} , fill factor FF , as well as conversion efficiency η of the solar cells with the studied IR designs measured in a sun simulator at AM1.5 spectrum. Thicknesses of the intrinsic layers were $t_{a-Si:H} = 330$ nm and $t_{\mu c-Si:H} = 3.2$ μ m.

IR type	$J_{sc,top}$	$J_{sc,bot}$	$J_{sc,sum}$	$J_{sc,meas}$	V_{oc}	FF	η
-	[mA/cm ²]	[mA/cm ²]	[mA/cm ²]	[mA/cm ²]	[mV]	[%]	[%]
w/o IR	11.5	14.2	25.7	11.7	1.323	75.1	11.7
$\mu c-SiO_x:H$ IR	12.0	11.1	23.1	11.0	1.344	71.6	10.8
ZnO:Al IR	13.2	9.4	22.6	9.0	1.352	74.3	9.6
IR ₃	12.7	11.1	23.8	10.7	1.334	73.8	10.7

The decreasing reflectance of the IR is nicely seen here as the top cell EQE_{top} remains below the ZnO:Al IR. EQE_{bot} of the tandem solar cell with IR₃ is higher than the EQE_{bot} of the tandem solar cell with $\mu c-SiO_x:H$ IR for $\lambda > 620$ nm. Comparing this to the reflectance of the textured IR into an a-Si:H half space from Fig. 6.10, this can be attributed to the spectrally selective reflectance of our designed multilayer IR. A meaningful quantity to demonstrate the spectral selectivity is the ratio $\frac{EQE_{sum,IR}}{EQE_{sum,w/o}}$ which is shown in Fig. 6.12(b). An EQE -ratio maximum at $\lambda = 680$ nm is caused by the spectrally selective reflectance of the IR₃. The minimum at about $\lambda = 720$ nm is due to a non-perfect spectral selectivity and could be enlarged by a steeper reflectance edge. The EQE_{sum} -ratio of the IR₃ is below a ratio of one but superior to the other IR designs in range II and III. As can be seen in Table 6.1, all IRs turn the top limitation ($J_{sc,top} < J_{sc,bot}$) of the cell without IR into a bottom limitation. For the IR₃, the short-circuit current density of the top cell $J_{sc,top}$ is increased by 1.2 mA/cm² compared to the configuration without IR and by 0.7 mA/cm² compared to the standard $\mu c-SiO_x:H$ IR. It can be seen, that the presented solar cells are not current matched. A thinner top-cell or an improved light trapping at the back side would be options to improve the matching. Differences of V_{oc} are small and probably due to the variation of crystallinity of the absorber material. The fill factor FF is within the measurement uncertainty not significantly influenced by the incorporation of the IRs.

6.6. Additional Improvements

6.6.1. Variation of the Materials

For the experimental study, the materials ZnO:Al and $\mu\text{c-SiO}_x\text{:H}$ were used due to their availability and low absorption losses. However, a variety of other conducting materials are feasible as well. Achieving a high refractive index contrast with low parasitic absorptance is the main criterion for material choice. In the rigorous simulation, the ZnO:Al layers were substituted with an oxygen-phase rich $\mu\text{c-SiO}_x\text{:H}$ with a refractive index $n = 1.78$ at $\lambda = 650$ nm (Appendix A).

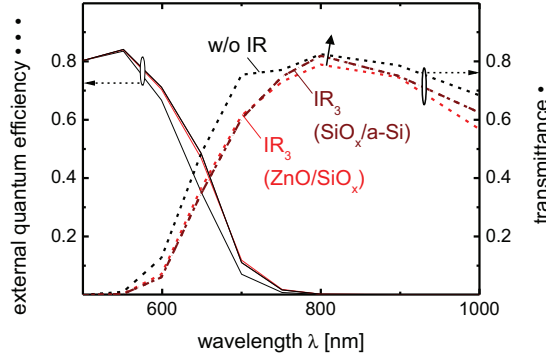


Figure 6.13.: External quantum efficiency EQE_{top} (full lines) and transmittance into the bottom cell T (dashed lines) of a tandem cell without IR (black line), with 3-layer ZnO:Al/ $\mu\text{c-SiO}_x\text{:H}$ /ZnO:Al IR_3 (red) and $\mu\text{c-SiO}_x\text{:H}$ / a-Si:H/ $\mu\text{c-SiO}_x\text{:H}$ IR_3 (brown).

The high- n $\mu\text{c-SiO}_x\text{:H}$ was exchanged by an a-Si:H layer providing a high refractive index ($n = 4.1$ at $\lambda = 650$ nm) and low absorption losses within a thin layer [175]. Layer thicknesses were again optimized for maximum reflectance in range II and maximum transmittance in range III by a genetic algorithm. Optimal layer thicknesses are $t_{\text{SiO}_x,1} = 70$ nm, $t_{\text{a-Si:H}} = 22$ nm and $t_{\text{SiO}_x,2} = 64$ nm. The EQE_{top} (full lines) and transmittance into the $\mu\text{c-Si:H}$ bottom cell (dashed line) are shown in Fig. 6.13 without IR (black) and with IR_3 produced from ZnO:Al/ $\mu\text{c-SiO}_x\text{:H}$ /ZnO:Al IR_3 ($IR_{3,\text{ZnO}}$, red line) and $\mu\text{c-SiO}_x\text{:H}$ / a-Si:H/ $\mu\text{c-SiO}_x\text{:H}$ IR_3 IR_{3,SiO_x} , (brown). EQE_{top} was simulated using rigorous optical simulations. For

Table 6.2.: Enhancement of short-circuit current density of the sub cells $\Delta J_{sc,top}$ and $\Delta J_{sc,bot}$ by varying the layers of the multilayer intermediate reflector.

IR type	$\Delta J_{sc,top}$	$\Delta J_{sc,bot}$
-	[mA/cm ²]	[mA/cm ²]
IR _{3,ZnO}	0.71	-1.53
IR _{3,SiOx}	0.72	-1.41
IR _{5,SiOx}	1.21	-2.27
IR _{10,SiOx}	1.19	-2.87

EQE_{bot} , an upper estimation was done using the Tiedje limit (Eq. 4.46). The short-circuit current density J_{sc} without and with IR₃ was determined using Eq. 4.48. A slight top cell enhancement $\Delta J_{sc,top} = 0.01$ mA/cm² is achieved while improving the transmittance into the bottom cell resulting in $\Delta J_{sc,bot} = 0.12$ mA/cm². The enhancement of short-circuit current density of the sub cells $\Delta J_{sc,top}$ and $\Delta J_{sc,bot}$ is shown in Tab. 6.2.

6.6.2. Influence of the Quantity of Layers

As discussed in Section 6.2, the reflectance of the IR in range II is increased and decreased in range III by augmenting of the layer quantity. Rigorous optical simulations of solar cells on rough APCVD SnO₂:F substrate were performed applying multilayer IRs with 5 and 10 layers (IR₅, IR₁₀). The IR₅ was optimized using the same target function in the genetic algorithm described above (Section 6.2). Layer thicknesses of the IR₁₀ are the same as in Section 6.2. The reflectance of such textured IR into a non-absorbing a-Si:H half space in range II is increased by about 20% while transmittance in range III is slightly increased (not shown here) in accordance to the untextured case (Fig. 6.7). The EQE_{top} (full lines) and transmittance into the bottom cell T (dashed lines) of a tandem cell without IR (black line), with 3-layer IR (IR_{3,SiOx}, red), 5-layer IR (IR_{5,SiOx}, purple) and 10-layer IR (IR_{10,SiOx}, orange) are shown in Fig. 6.14. In the range $600\text{ nm} < \lambda < 680\text{ nm}$, EQE_{top} is further increased by increasing the number of layers from three to five or ten. On the other hand, transmittance into the bottom cell in range III is decreased by increasing the quantity of IR layers as the reflectance of the multilayer stack with a larger number of layers is stronger affected by roughness (not shown here). To achieve a sufficiently high bottom cell short-circuit current density

$J_{sc,bot}$, bottom cell layer thicknesses can be increased or bottom cell light trapping may be increased on the cost of deposition time and device quality. An increase of $J_{sc,top}$ of $\Delta J_{sc,top} = 1.21 \text{ mA/cm}^2$ is accompanied by a potential $J_{sc,bot}$ -loss of $\Delta J_{sc,bot} = 2.27 \text{ mA/cm}^2$ in case of the IR₅.

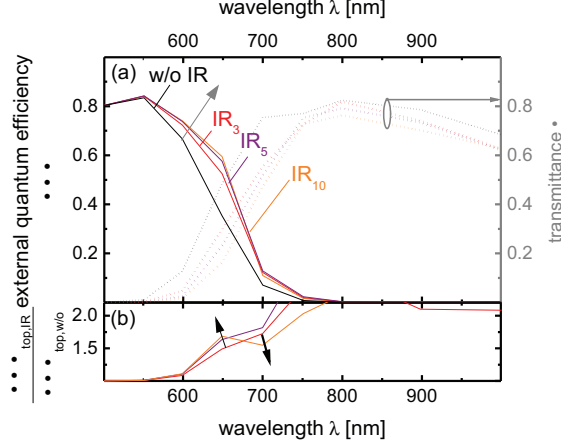


Figure 6.14.: External quantum efficiency EQE_{top} (full lines) and transmittance into the bottom cell T (dashed lines) of a tandem cell without IR (black line), with 3-layer IR (red), 5-layer IR (purple) and 10-layer IR (orange).

6.7. Comparison to Other Spectrally Selective Intermediate Reflectors

6.7.1. 3D Photonic Crystal IR

A prominent example of spectrally selective intermediate reflectors are 3D photonic crystal intermediate reflectors (3DPCIR). There are a variety of possible geometries of 3D photonic crystals including Yablonovite, stacks of 2D photonic crystals, vertical rods of low refractive index medium and inverse opal structures [50]. Inverted opals are feasible as they can be produced by self-organization of nano spheres [78]. To solar cells, they can be beneficial as diffracting back reflectors ?? or intermediate reflectors. They were investigated as IR by simulations in [51, 52, 58, 97] and

already successfully incorporated in thin-film silicon tandem solar cells [53,176]. A schematic sketch (a), as well as a scanning electron microscopy (SEM) image (b) of a FIB-cut thin-film silicon tandem solar cell on APCVD $\text{SnO}_2\text{:F}$ substrate with 3DPCIR taken from [176] are shown in Fig. 6.15. An enhancement of $J_{\text{sc,top}}$ by 24.5 % has been achieved in [53]. The optimized 3DPCIR from [177, 178] with 3 layers of air spheres with a diameter of 150 nm in a ZnO:Al matrix was implemented into our rigorous optical simulation on APCVD $\text{SnO}_2\text{:F}$ substrate. EQE_{top} (full lines), as well as transmittance into the bottom cell (dashed lines) are shown in Fig. 6.16. A clear increase of EQE_{top} is found causing an increase of top cell short-circuit current density by $\Delta J_{\text{sc,top}} = 2.2 \text{ mA/cm}^2$.

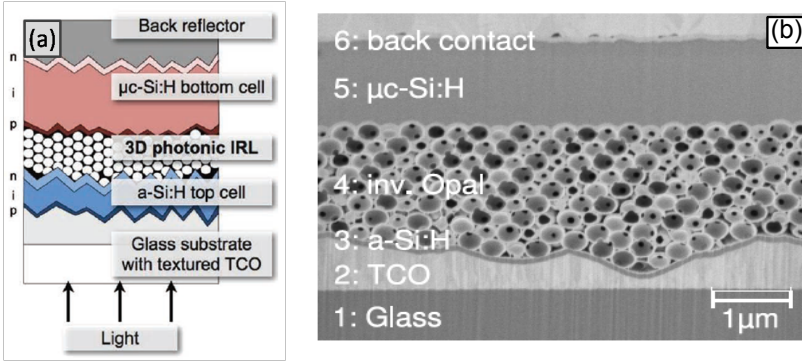


Figure 6.15.: (a) Schematic sketch of a thin-film silicon tandem solar cell with 3D photonic crystal intermediate reflector (3DPCIR). (b) Scanning electron microscopy image of a FIB-cut thin-film silicon tandem solar cell on APCVD $\text{SnO}_2\text{:F}$ substrate with 3DPCIR. Graphs are taken from [176].

However, the transmittance in range III is significantly reduced and does not exceed 58%. As the photonic band structure of the inverse opal structure in Fig. 4.3(b) shows, a variety of flat photonic band which exhibit a low phase velocity are found for the opaline IR. These are additional band gaps and highly diffractive states within the photonic crystal. Light is either reflected or guided within the crystal resulting in a decrease of the transmittance through the photonic crystal in range III. While in the case of multilayer IRs, additional $\lambda_0/8$ layers at the boundary provided a discrimination of low energy side bands, this is, in principle, also achievable for 2D or 3D photonic crystals by an anti-reflection structure of the same dimensionality as presented in [179]. For a 2D photonic crystal of aluminum

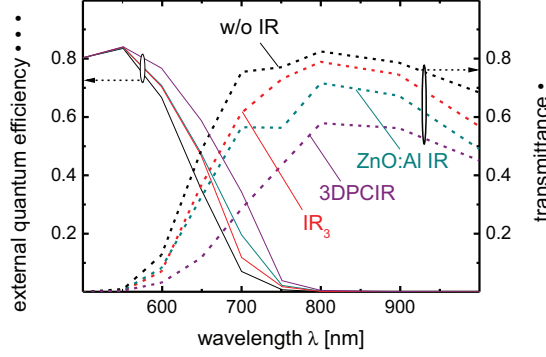


Figure 6.16.: External quantum efficiency EQE_{top} (full lines) and transmittance into the bottom cell T (dashed lines) of a tandem cell without IR (black line), with ZnO:Al IR (cyan), IR_3 (red) and 3D photonic crystal IR according to [178] (purple).

rods, an additional array of square rods in homogeneous medium with different radii and rod distances could be optimized to achieve nearly 100 % transmittance apart from the required photonic band gap. A 1D anti-reflection layer, as the optimized ZnO:Al anti-reflection layer designed in [97], is not sufficient to maximize transmittance in range III. In order to produce 3DPCIR which are feasible for any kind of spectral splitting application in PV, developing an anti-reflection structure with smaller sphere radius and distance is necessary. This structure cannot be produced by simple self-organization like the opal structure.

6.7.2. Plasmonic IR

While dielectric 2D photonic crystals do not exhibit fitting properties as spectrally selective filter in tandem solar cells, 2D plasmonic crystals of metallic nano discs in a dielectric medium reveal promising reflection properties. A concept to facilitate high reflectance in range II combined with a high transmittance in range III is the resonant stop band of a 2D array of Ag nanodiscs in a low refractive index medium caused by coupling of light to local plasmon-polaritons. This plasmonic IR concept was presented and optimized in [180]. With a disc diameter of 57 nm and a period of 101.3 nm, a reflectance in range II of $> 80\%$ can be reached while transmittance for $\lambda > 700$ nm is $> 80\%$. A $J_{sc,top}$ -gain of 14% has been simulated

for a tandem solar cell on flat ZnO:Al substrate [180]. Figure 6.17(a) shows a sketch of the geometry with Ag discs embedded in a ZnO matrix between top and bottom cell. In (b), the absorptance in the top cell (full line) and bottom cell (dashed line) are presented without IR (black), with a ZnO:Al IR (gray) and a plasmonic IR from Ag discs. As reflectance of the plasmonic IR is much higher than the dielectric layer, more light is reflected back into the top cell resulting in an increase of Fabry-Perot resonance peaks at $\lambda = 560$ nm and 630 nm. The IR reflects nearly the entire amount of light for $\lambda < 690$ nm. For $\lambda > 690$ nm, transmittance into the bottom cell and, thus, absorptance in the bottom cell is highly increased up to the level of the system without IR.

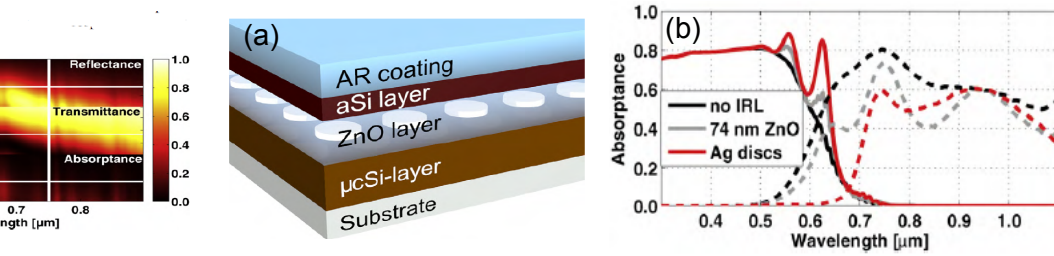


Figure 6.17.: (a) Sketch of a tandem solar cell incorporating plasmonic IR. The illustration is taken from [180]. (b) Absorptance in the top cell (full lines) and in the bottom cell (dashed line) without IR (black), with a ZnO:Al IR (gray) and a plasmonic IR from Ag discs (red).

The high spectral selectivity of plasmonic IRs within a low thickness of <100 nm and low parasitic absorptance are an outstanding combination. Especially the transmittance into the bottom cell is highly increased in comparison to 3DPCIR (Section 6.7.1). However, the fabrication of a periodic arrangement of metallic nano particles of these dimensions is non-trivial, but has been shown already in [181–184]. The available fabrication methods are just possible on flat surfaces. These surfaces do not induce scattering. Thus, no light trapping in the top cell can be achieved and the path length enhancement within the top cell is restricted to a maximum of 2. However, top cell light trapping is crucial in the range of high absorption length of a-Si:H. As the reflectance of the plasmonic IR is omnidirectional, it is, in principle compatible with scattering front textures [178]. In a current cooperation project with the Institute of Physics at the FSU Jena, metallic

nanodiscs are implemented as IR into tandem solar cells. Due to a variety of challenges during the production of nanodiscs, results are not yet available. After experimental demonstration of the concept on a flat substrate, further studies on the application of front scattering and diffraction structures are necessary, as the concept can just be a successful contribution when it is coupled to a light trapping scheme.

6.7.3. Discussion

In the previous sections, a variety of spectrally selective IR concepts have been presented. Both, 3DPCIR and plasmonic IR, convince by their omni-directional photonic band gap and high reflectance in range II. Both concepts are, however, embedded into a low index medium ZnO:Al. For light of longer wavelength than the photonic band gap of resonance band $\lambda > \lambda_{\text{res}}$, the side lobes are produced and reduce the transmittance. The bottom short-circuit current lost by this highly exceeds the possible top cell gain. This is why, these concepts without use of sophisticated anti-reflection structures are not feasible for tandem solar cells. The plasmonic IR can be experimentally just processed on flat substrates with the state-of-the-art fabrication methods. To improve state-of-the-art tandem solar cells, it is, however, necessary to increase the *EQE* in the broad spectral range II which is just possible if the path length enhancement exceeds a factor of 2. In comparison to the technological extensive structures incorporating complex and expensive production steps, a simple straight-forward approach was developed in this chapter which combines the high reflectance of the photonic band gap with state-of-the-art thin-film silicon solar cell fabrication methods. The multilayer IR IR₃ can be combined with APCVD SnO₂:F substrates and provides a high top cell absorption enhancement in range II while minimizing reflection losses in range III. Its ability to significantly boost the top cell current while being highly transmissive in the long-wavelength range makes it attractive for industrial thin-film silicon tandem solar cells. Further optimization steps by substituting the materials and increasing number of layers have been performed and show a further but slight increase of the top cell *EQE*. However, the top cell absorption enhancement of the multilayer IRs is lower than for 3D or plasmonic structures. A general investigation about light trapping in the top cell and its interplay with the surface texture and reflectance are important to evaluate the potential of different IR types.

6.8. Summary

In this section, the spectrally selective behavior of various intermediate reflectors was investigated. Single layer intermediate reflectors usually show a non-sufficient spectral selectivity resulting in the reflection losses determined in Chapter 5. A multilayer intermediate reflector composed of ZnO:Al and $\mu\text{c-SiO}_x\text{:H}$ was designed and experimentally integrated into tandem thin-film silicon solar cells. We have studied the impact of spectral selectivity of various single layer and multilayer intermediate reflectors on the performance of state-of-the-art thin-film silicon tandem solar cells. It was shown by simulations, as well as prototype solar cells that single layer IRs lead to an increased reflection for longer wavelengths while multilayer intermediate reflectors provide a more spectrally selective reflectance minimizing reflection losses. Integrating a multilayer intermediate reflector leads to an increase of top and bottom cell short-circuit current density compared to state-of-the-art single-layer IRs. It is observed that to reach current matching with a limited top cell thickness, a certain light trapping in the a-Si:H top cell has to be ensured which should be studied in the following chapter.

7. Investigation of Light Trapping by Coupling into Guided Modes in the a-Si:H Top Cell

This chapter focuses on the effect of the intermediate reflector on the absorption in the top cell. The reflectance of the intermediate reflector leads to a back-reflection of light into the top cell. As light is transmitted and reflected into larger angles, light trapping in the film is induced. Light is coupled to waveguide modes in the a-Si:H film. The short-circuit current gain in the top cell significantly depends on the light trapping for $\lambda > 550$ nm. In this chapter, the coupling of incident light into waveguide modes is studied for a periodic grating inducing diffraction into discrete angles. Various intermediate reflectors are studied. The theory is extended to a-Si:H top cells on randomly textured surfaces. The studies of these chapter were published in [116] and [?].

7.1. Waveguide Modes in Thin-Films on 2D Grating Structures

In periodically textured thin-films, light trapping is usually achieved by exciting waveguide modes in the film. The waveguide mode coupling is an interplay between diffraction at the front and back grating. In this Section, the influence of a back and intermediate reflectors on the coupling into guided modes is investigated.

Transmission and reflection gratings are powerful tools to facilitate light trapping

in thin films like a-Si:H or $\mu\text{c-Si:H}$ [16, 18, 33, 88]. In thin films, light trapping is usually facilitated by coupling the incident light into leaky waveguide modes of the film [18, 55]. The theoretical description of the limits of light trapping by waveguide modes was presented in Section 4.2.4. However, common literature is restricted to waveguide modes in single junction solar cells which are followed by a metallic mirror usually made of Ag. This section extends the study of guided modes to a-Si:H top cells with a back mirror of non-perfect reflectance, namely an intermediate reflector.

7.1.1. Evaluation of different grating geometries

To determine a feasible grating texture, scalar scattering theory (Section 4.1.4) is applied to the topography of a variety of grating structures in a $\mu\text{c-Si:H}$ single junction solar cell as a simplified system. The quantity light trapping efficiency LTE is defined by the integrated light intensity above the critical angle of total internal reflection at front and rear side in [115, 116]:

$$LTE(\lambda) = \frac{1}{2} \int_{\theta_{TIR}}^{2\pi} AID_{T, Si} + \frac{1}{2} \int_{\theta_{TIR}}^{2\pi} AID_{R, Si} \quad (7.1)$$

Computation of the LTE allows for optimization of grating shape, height h and period p without computationally extensive rigorous simulations. For a variety of grating geometries (Fig. 7.1), LTE is calculated for a broad range of grating heights h and periods p . The resulting maximal values of current density in the light trapping range ($600 \text{ nm} < \lambda < 900 \text{ nm}$) $J_{sc,600-900}$ is shown in the table in Fig. 7.1.

A triangular grating as shown in the right in Fig. 7.1 is found to deliver the highest LTE . Such surface textures can be manufactured for example by selective etching of c-Si [185]. The LTE was compared to rigorous optical simulations of a $\mu\text{c-Si:H}$ single junction solar cell stack and could, thus, be correlated to a short-circuit current density J_{sc} . Scalar scattering theory enables extensive parameter sweeps like in Fig. 7.2(b) where the short-circuit current density between 600 and 900 nm $J_{sc,600-900}$ is shown depending on p and h . Texture heights below $h < 100 \text{ nm}$ and grating constants $p < 200 \text{ nm}$ are unfavorable as just low diffraction efficiencies and a slight absorption enhancement to the flat case is obtained. Most favorable, from the optical point of view, are $h > 200 \text{ nm}$ with $p > 300 \text{ nm}$ enabling high diffraction efficiencies into large angles. Figure 7.2(c) shows $J_{sc,600-900}$ along

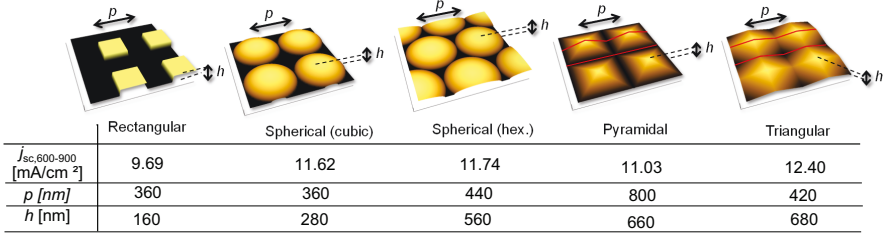


Figure 7.1.: Studied grating geometries. The upper part shows the basic surface geometries: cube grating, cubic half-sphere grating, hexagonal half-sphere grating, pyramidal grating and triangular grating. Calculated $J_{sc,600-900}$ and their geometrical parameters (grating period p , grating height h) are shown below.

the dashed line in (b) calculated by scalar scattering theory (red line) and simulated rigorously by FDTD (black square and line). The short-circuit current densities $J_{sc,600-900}$ for a flat and randomly textured reference cell are depicted as dashed lines. A strong increase in short-circuit current density J_{sc} is found for $300 \text{ nm} < p < 400 \text{ nm}$. For larger periods, J_{sc} increases up to 10 mA/cm^2 in comparison to 5.6 mA/cm^2 (flat front) and 7.6 mA/cm^2 (randomly textured surface). Optimized grating sizes are comparable to the parameters of 1D grating structures optimized in literature [186].

7.1.2. Variation of the back/ intermediate reflector

In the following, a triangular grating structure with $p = 400 \text{ nm}$ and $h = 200 \text{ nm}$ is used which exhibits a high *LTE* and is comparable to texture heights and correlation lengths of typical randomly textured surfaces. The *EQE* of the 330 nm thick a-Si:H solar cell on this triangular grating structure is shown in Fig. 7.3(a). The black line resembles the case of an a-Si:H layer which is followed by a $\mu\text{-Si:H}$ half space. The a-Si:H layer represents the top cell of a tandem solar cell. The purple line indicates the system where the a-Si:H layer is followed by a back reflector of 80 nm ZnO:Al and Ag representing an a-Si:H single junction solar cell. The Ag layer is idealized as a perfectly electric conductor (PEC) for the purpose of convergence of the simulation. The EQE_{top} of the same solar cell stack geometry including a 114 nm thick ZnO:Al IR is depicted as cyan line. The presence of the back reflector leads to a strong increase of *EQE* in the wavelength range between $600 \text{ nm} < \lambda < 800 \text{ nm}$. In particular, resonances at certain wavelengths

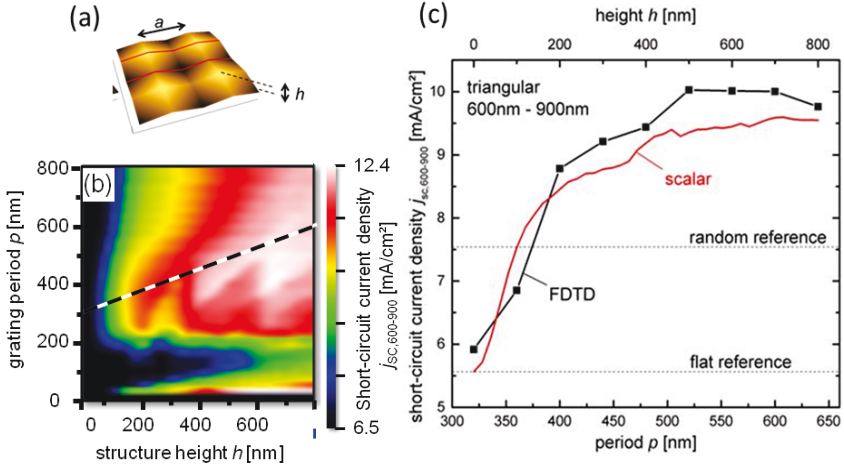


Figure 7.2.: (a) Schematic sketch of the triangular grating with a period p and a height h . (b) Contour plot of short-circuit current density J_{sc} depending on period p and height h . (c) J_{sc} depending on period p along the line in (b) determined by scalar scattering theory (red line) and simulated by rigorous optical simulation (black line).

($\lambda = 700 \text{ nm}$, 730 nm , 770 nm) are visible. These resonances are associated to waveguide modes in the a-Si:H film. They can be allocated to certain grating vectors induced by diffraction at the grating [16]. Waveguide modes of a given stack be visualized by calculating the Eigenmodes for a certain solar cell stack as shown in [18]. In the case of the tandem solar cell with ZnO:Al IR, excitations at the same wavelengths are found. It is evident that the maximum results from a strong periodic light localization pattern within the a-Si:H film. It can be associated to a guided mode, while in case of the minimum of the EQE , the light localization within the film is less pronounced.

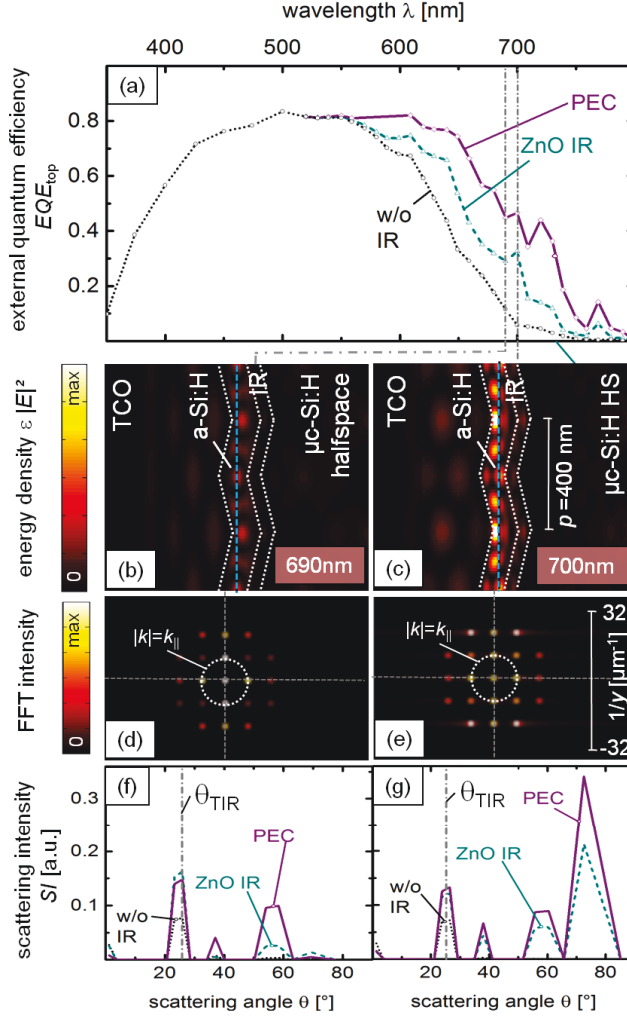


Figure 7.3.: (a) External quantum efficiency of the top cell EQE_{top} on the triangular grating structure for a tandem cell without IR (black, dotted), with a highly reflective ZnO:Al IR (cyan, dashed) and a metal back reflector (purple, full). The electromagnetic energy density at $\lambda = 690$ nm and $\lambda = 700$ nm are shown in (b) and (c), respectively (Min/Max of the color scale are identical). The Fast Fourier Transform (FFT) of the complex electric field electric field for 690 nm (d) and 700 nm (e). The angular scattering intensity distribution for the different reflector types in the blue dashed plane within the a-Si:H film is shown in (f) and (g) at $\lambda = 690$ nm and $\lambda = 700$ nm, respectively.

To have a detailed look at these resonances, a cross-section of the electromagnetic energy density at $\lambda = 690$ nm and $\lambda = 700$ nm is shown in Fig. 7.3(b) and (c), respectively. A periodic intensity pattern within the a-Si:H film indicates the presence of guided modes in the film. The energy density in this pattern is significantly higher for the local maximum of EQE_{top} at $\lambda = 700$ nm than at $\lambda = 690$ nm. A plane perpendicular to the incident wave is extracted out of the computed complex electric fields in the a-Si:H layer at the position of the dashed blue lines in (b) and (c). A fast Fourier transform (FFT) of the electric fields is performed and results in the FFT intensity patterns shown in Fig. 7.3(d,e) for $\lambda = 690$ nm and 700 nm, respectively. The dashed white circle indicates the limit where $|k| > k_{\parallel}$. In the following, the FFT intensity is integrated along the circle. The intensity per wave vector component parallel to the interface k_{\parallel} can be transformed into an angular scattering intensity by Eq. 4.39. The scattering intensity SI of the grating is depicted as gray line for $\lambda = 690$ nm (f) and $\lambda = 700$ nm (g). Light impinging on the grating is diffracted into the $\mu\text{c-Si:H}$ halfspace in these particular angles. However, the coupling efficiency into guided modes is determined by the thin-film stack geometry taking into account refractive index, layer thickness and texture. The intensity for the system without IR, with ZnO:Al IR and PEC are again indicated by black, cyan and purple lines, respectively. The critical angle of total internal reflection θ_{TIR} for the a-Si:H/ ZnO:Al interface is indicated by the dash-dotted line. Without IR, a low scattering intensity is observed. Preferably, light is diffracted into the first diffraction order. Incorporating the back reflector strongly increases scattering into higher diffraction orders and thus, coupling into leaky waveguide modes. The ZnO:Al IR has a similar effect. The same waveguide modes are excited, although intensity is significantly lower due to a lower reflectivity of the IR. At $\lambda = 690$ nm, most of the intensity is found in modes associated to an angle below θ_{TIR} . These modes can couple out of the film leading to a lower energy density in the film (Fig. 7.3(b)), as well as a local minimum in the EQE_{top} in Fig. 7.3(a). In case of $\lambda = 700$ nm (Fig. 7.3(e)), a large amount of the light is diffracted into angles above the critical angle θ_{TIR} and coupled into guided modes. The EQE_{top} is clearly enhanced and a higher light intensity is found in the a-Si:H film. The intensity at the certain parallel wave vector component or angle is directly related to the absorption in the a-Si:H film at this particular wavelength. As real and imaginary part of the electric field are taken into account, the result is independent of the plane position within the a-Si:H film.

7.2. Waveguide Modes in Randomly Textured a-Si:H Films

In case of periodic gratings, light trapping can be attributed to the excitation of certain discrete waveguide modes by a combination of diffraction at the grating and reflection. In contrast, randomly textured surfaces, as commonly used in thin-film silicon tandem solar cells, scatter light into a broad distribution of angles. In this Section, the wave guide excitation theory is extended to randomly textured films. The integrated scattering intensity (ISI) is introduced as a quantity of light trapping and correlated to the external quantum efficiency of tandem solar cells.

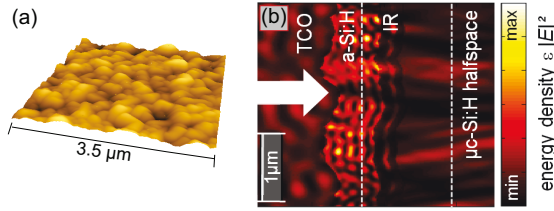


Figure 7.4.: (a) Surface topography of randomly textured as-grown APCVD $\text{SnO}_2\text{:F}$ substrate. (b) Cross-section of the energy density of a simulated tandem solar cell on APCVD $\text{SnO}_2\text{:F}$ substrate. Dashed white lines mark the planes which will be evaluated in the following.

The impact of different IRs on the EQE is investigated experimentally by deposition of a-Si:H/ $\mu\text{c-Si:H}$ tandem solar cells on APCVD $\text{SnO}_2\text{:F}$ front TCO layers. Therefore, the tandem solar cells produced in Chapter 6 are chosen ($t_{\text{top}} = 330 \text{ nm}$ and $t_{\text{bot}} = 3.2 \mu\text{m}$). Thicknesses of the IRs are analogous to Chapter 6: $t_{\text{IR}} = 40 \text{ nm}$ in case of the $\mu\text{c-SiO}_x\text{:H}$ IR, $t_{\text{IR}} = 115 \text{ nm}$ for the ZnO:Al and the IR_3 which has been designed in Chapter 6.2. Additionally, an a-Si:H single-junction solar cell with the same a-Si:H thickness and a highly reflective ZnO:Al/Ag back reflector [187] was deposited. The surface topography of a randomly textured as-grown APCVD $\text{SnO}_2\text{:F}$ substrate is shown in Fig. 7.4(a). Figure 7.4(b) shows the cross-section of the energy density within the simulated solar cell on APCVD $\text{SnO}_2\text{:F}$ substrate extracted from rigorous optical simulations. EQE_{top} and EQE_{bot} were measured individually by applying bias light in a spectral response setup. The results are shown in Fig. 7.5.

As expected, the lowest EQE_{top} is found for the reference tandem cell without IR. By introducing different IRs, the top cell response is significantly improved for $500 \text{ nm} < \lambda < 800 \text{ nm}$. The IR consisting of ZnO:Al provides the highest charge carrier generation in the top cell ($13.3 \frac{\text{mA}}{\text{cm}^2}$) followed by the IR₃ ($12.7 \frac{\text{mA}}{\text{cm}^2}$). The highest charge carrier generation in the bottom cell ($14.2 \frac{\text{mA}}{\text{cm}^2}$) is found for the tandem cell without IR. The tandem cell with IR₃ provides the highest charge carrier generation in the bottom cell for the samples with intermediate reflector ($11.0 \frac{\text{mA}}{\text{cm}^2}$). Additionally, in a further run, an a-Si:H single junction solar cell was deposited using the same parameters. The EQE of this device is depicted as purple line in Fig. 7.5. As here no $\mu\text{c-Si:H}$ bottom solar cell is present, a much larger amount of photons between $600 \text{ nm} < \lambda < 800 \text{ nm}$ is absorbed in the a-Si:H cell resulting in a highly increased short-circuit current density of $14.5 \frac{\text{mA}}{\text{cm}^2}$.

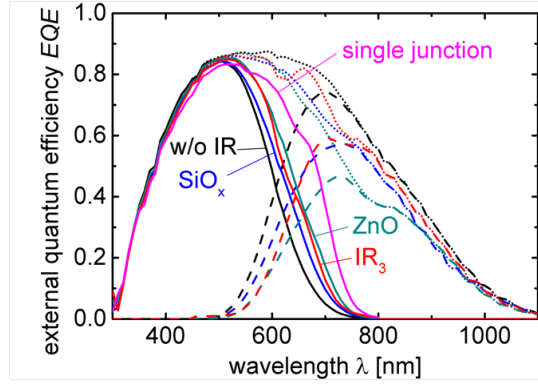


Figure 7.5.: Measured external quantum efficiency (EQE) of the top and bottom cells of tandem solar cells with different intermediate reflectors. The reference tandem cell without IR is plotted in black, the results for hydrogenated $\mu\text{c-SiO}_x\text{:H}$ and ZnO:Al single layers are shown in blue and cyan, respectively. The EQE of the tandem cell with IR₃ is shown in red and a single junction a-Si:H cell in purple.

By applying FFT analysis on the 2D simulation output plane inside the top cell and after the IR in the $\mu\text{c-Si:H}$ half space, the SI in the top and bottom cell is extracted. The results are shown in Fig. 7.6 for the different tandem cells. The SI in the top cell is presented in Fig. 7.6(a) for the wavelength $\lambda = 650 \text{ nm}$. The light scattering distribution in the bottom cell for the same wavelength is shown in Fig. 7.6(b). The tandem cell without IR provides only low intensities in angles $\theta > \theta_{\text{TIR}}$ (θ_{TIR} at the a-Si:H/ ZnO:Al interface, depicted as vertical lines

in Fig. 7.6). The solar cell without IR shows the highest SI into large angles in the μc -Si:H half space (b). The light with $\theta > \theta_{TIR}$ is not kept in the top cell and transmitted into the bottom cell.

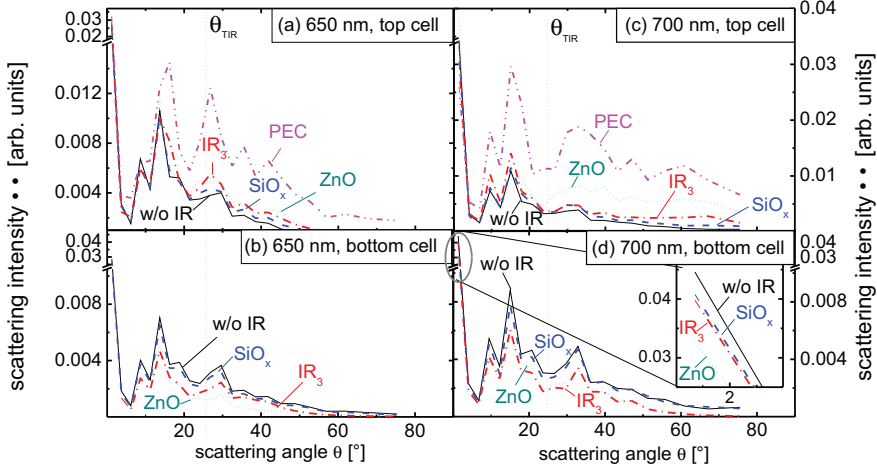


Figure 7.6.: (a) Light scattering distribution SI in the top cell of thin-film silicon tandem solar cells with different intermediate reflectors at a wavelength of $\lambda = 650$ nm. The system without intermediate reflector is shown as black full line, the μc -SiO_x:H IR system by a dashed blue line, IR₃ by a dash-dotted red line, ZnO:Al as a dotted cyan line. The PEC back reflector is indicated by the dash-dot-dot purple line. In (b) the SI in the μc -Si:H half space at $\lambda = 650$ nm is shown. The vertical lines depict the critical wave vector for total internal reflection θ_{TIR} at the a -Si:H/ ZnO:Al interface. (c) SI in the top cell of thin-film silicon tandem solar cells with different intermediate reflectors at a wavelength of $\lambda = 700$ nm. (d) SI in the μc -Si:H half space at $\lambda = 700$ nm. The vertical line depicts the critical angle for total internal reflection θ_{TIR} at the a -Si:H/ ZnO:Al interface.

It is found that for the tandem cells with IR, the light intensities for large wave vectors/ angles increases in the top cell, whereas it decreases in the bottom cell. In particular, this demonstrates the efficient light coupling to leaky waveguide modes by the interplay of the front interface and the IR. The same evaluation is made for other wavelengths, e.g. $\lambda = 700$ nm and shown in Fig. 7.6(c),(d). The solar cell without IR is shown as black full line, the μc -SiO_x:H IR system by a dashed blue line, IR₃ by a dash-dotted red line, ZnO:Al IR as a dotted

cyan line. For comparison, results of an a-Si:H single junction solar cell with a ZnO:Al/Ag back reflector are shown in Fig. 7.6(a) and (c) as purple dash-dotted lines. ZnO:Al IR and IR₃ perform equally at $\lambda = 650$ nm in terms of coupling into guided modes (Fig. 7.6(a), (b)), as well in EQE . For $\lambda = 700$ nm, a different trend is found. Here, the ZnO:Al IR couples much more light into guided modes than the IR₃ resulting in a higher EQE_{top} and lower total light intensity in the bottom cell (Fig. 7.6(d)) which is strongest pronounced for the specular light ($\theta = 0^\circ$). This can be attributed to the spectrally selective reflectance of the IR₃ which was designed to highly transmit above $\lambda = 680$ nm (Chapter 6). The increase of coupling into the waveguide modes in the top cell by the IR₃ and ZnO:Al IR is linked to a decrease of SI in the bottom cell (inlet in Fig. 7.6(d)). This is in accordance to the measured EQE_{bot} which is decreased by the IR reflectivity and light trapping in the top cell. Coupling into waveguide modes seems to be detrimental for transmission into the bottom cell which will be subject of the following chapter.

To demonstrate the importance of the efficient coupling to leaky waveguide modes for the performance of the solar cell, the EQE_{top} is plotted against the integrated scattering intensity (ISI) which quantifies the overall amount of light intensity beyond the critical angle for total internal reflection. The results are shown for a wavelength of $\lambda = 650$ nm in Fig. 7.7(a) and for $\lambda = 700$ nm in Fig. 7.7(b). Results for the corresponding a-Si:H single junction are shown in purple. The strong correlation between the EQE_{top} and the integrated scattering intensity demonstrates that light scattering into angles beyond the critical angle is beneficial for the a-Si:H top cell. Furthermore, the introduction of an IR significantly improves coupling to leaky waveguide modes by increasing the IR reflectivity.

7.3. Local Effects of Surface Features in a-Si:H Films

Apart from integrated quantities like the external quantum efficiency, rigorous optical simulations give access to local properties. FFT analysis enables to 'locate' trapped light and correlate it to certain surface features of the randomly textured TCO surface [188].

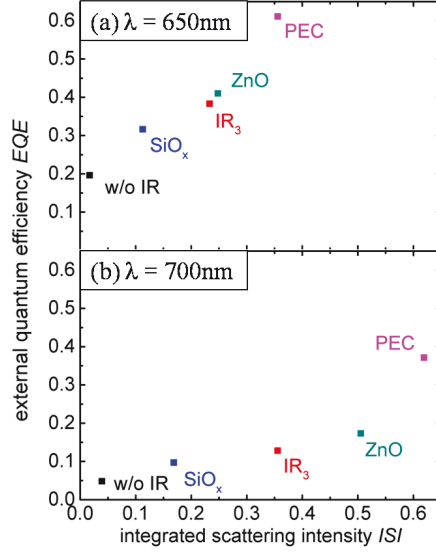


Figure 7.7.: Measured external quantum efficiency in the top cell EQE_{top} as a function of the integrated scattering intensity ISI for the different tandem solar cell configurations at a wavelength $\lambda = 650 \text{ nm}$ (a) and $\lambda = 700 \text{ nm}$ (b).

The correlation between the integrated scattering intensity of a small representative area with the macroscopic EQE shows that $3.5 \times 3.5 \mu\text{m}^2$ show already a satisfying statistics of surface features. However, our analysis provides the opportunity to evaluate scattering locally and attribute certain coupling behavior to certain features. In a previous study, we demonstrated that applying near-field scanning optical microscopy is able to spatially resolve light localizations in the solar cell and correlate it to the surface topography [188]. To gain similar evaluation from the simulated data, the complex electric field plane is Fourier-transformed and high-pass filtered, thus that just the part above the θ_{TIR} of the a-Si:H/ ZnO:Al is back-transformed. The high-pass filtered electric field intensity at $\lambda = 700 \text{ nm}$ is shown in Fig. 7.8(b). For identification of the surface features, furthermore, the surface topography is shown in Fig. 7.8(a). Characteristic features are observed. In Fig. 7.8(c) and (d), the topography is super-imposed with the high-pass filtered electric field intensity images for $\lambda = 650 \text{ nm}$ (c) and $\lambda = 700 \text{ nm}$ (d). Red color implies a horizontal wave vector component corresponding to a large scattering

angle. Above rather flat areas of the surface texture, a little amount of light in the light-trapping regime is found. Exemplary areas are indicated by black circles. The surface roughness is too low to scatter light into large angles, thus the largest portion of light is just transmitted specularly. In contrast, areas with a combination of high pyramidal features which are characterized by steep surface angles provide an efficient in-coupling into large angles. Two exemplary areas are marked by blue circles in Fig. 7.8 (c) and (d). For both studied wavelengths, the trapped light is localized at the flanks of the pyramidal surface features. Comparing the local trapped intensities at $\lambda = 650$ nm (c) and $\lambda = 700$ nm (d), there are little differences in details, although all general local trends are maintained.

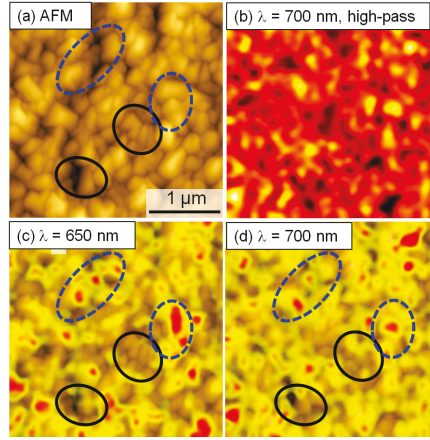


Figure 7.8.: Surface topographies of an AFM measured APCVD $\text{SnO}_2:\text{F}$ surface (a) is shown. (b) shows the electric field intensity after application of a high-pass filter (just above critical angle) for $\lambda = 700$ nm. In (c) and (d) these electric field distributions are superimposed to the topography for $\lambda = 650$ nm and 700 nm, respectively.

Top cell absorption enhancement in tandem solar cells is facilitated by coupling incident light into leaky waveguide modes of the a-Si:H film by diffraction/scattering at a back or intermediate reflector. It is shown that a waveguide description can be extended from single junction solar cells with a back mirror to top cells with an IR of variable reflectance. This description is further extended to films on randomly textured surfaces where the discrete waveguide modes are substituted

by a broad distribution of 'smeared out' waveguide modes. The integrated intensity above the critical angle of total internal reflection θ_{TIR} is found as quantity describing light trapping and was correlated to the external quantum efficiency of the solar cell. The analysis further reveals, that these waveguide modes remain in the top cell and do not propagate into the bottom cell leading to a decreased bottom cell external quantum efficiency.

8. Interplay of Intermediate Reflector and Surface Texture

In Chapter 5, parasitic reflectance has been identified as the main loss mechanism for tandem cells with intermediate reflectors. To overcome this, a spectrally selective IR has been designed as a multilayer stack and was successfully integrated into a solar cell on commercial APCVD $\text{SnO}_2\text{:F}$ substrate (Chapter 6). The influence of leaky waveguide modes on light trapping in the a-Si:H top cell has been studied in detail for different IR materials (Chapter 7). Light trapping can be achieved either by as-grown random textures, or gratings and photonic crystals. In this chapter, the influence of different surface textures on the behavior of the IR is studied. Remarkable differences in the reflection mechanism at the IR are identified and investigated by experimental and simulation studies revealing the dependence on the relevant optical parameters. Finally, a design strategy for IRs on given substrate is formulated.

8.1. Multilayer IR on Various Substrates

In the last chapter, rigorous simulations were used to study the process of light trapping in a thin a-Si:H top cell with different IRs in detail. This was just done for one particular substrate morphology (APCVD $\text{SnO}_2\text{:F}$). In a further step, the before discussed layer stack of a glass half space followed by a textured ZnO:Al front contact, an a-Si:H top cell, IR and non-absorbing $\mu\text{c-Si:H}$ half space was simulated using the surface texture of front side and after a-Si:H deposition measured by AFM. The used front contact topographies are shown in Fig. 8.1 for the case of APCVD $\text{SnO}_2\text{:F}$ (a) and LPCVD ZnO:B (b). The top cell quantum efficiency EQE_{top} (full lines), as well as the transmittance T into the bottom cell (dashed lines) are demonstrated in Fig. 8.1 for the APCVD $\text{SnO}_2\text{:F}$ texture (c) and LPCVD

ZnO:B texture (c

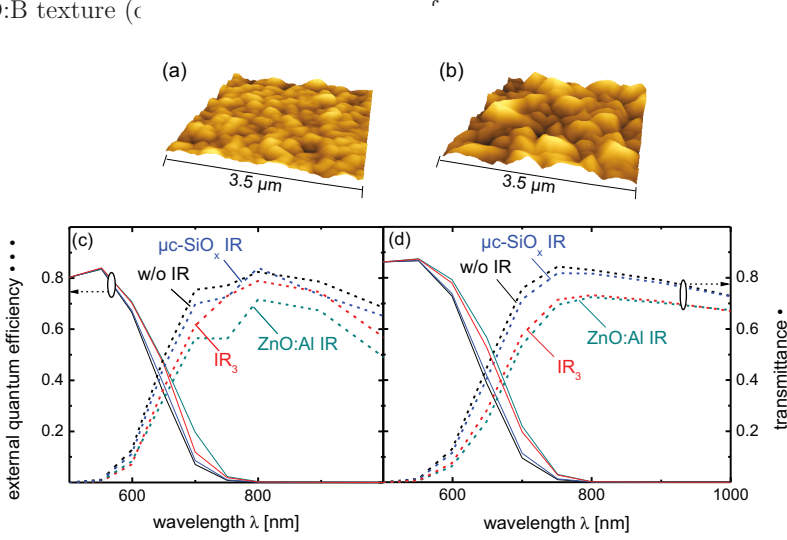


Figure 8.1.: (a) and (b) show the topography of SnO₂:F and ZnO:B. The top cell external quantum efficiency EQE_{top} and transmittance into the bottom cell T is shown for SnO₂:F (c) and ZnO:B (d) without IR (black), with $\mu c\text{-SiO}_x\text{:H}$ IR (blue), with ZnO:Al IR (cyan) and IR₃ (red).

In black, the EQE_{top} (full line) and transmittance T (dashed) for the solar cell stack without IR is shown. Furthermore, EQE and T for a 38 nm thin $\mu c\text{-SiO}_x\text{:H}$ IR (blue), 114 nm ZnO:Al IR (cyan), as well as the IR₃ (red) are depicted. On both substrates, EQE_{top} is increased by applying an IR. The comparison between (c) and (d) shows further, that the increase of EQE_{top} on LPCVD ZnO:B texture is higher than on the APCVD SnO₂:F texture. EQE_{top} and T of the system with IR₃ and ZnO:Al IR show nearly the same behavior for the tandem cell on LPCVD ZnO:B texture; the EQE is slightly lower for IR₃ and the transmission accordingly slightly higher. The spectrally selective behavior which was observed for the IR₃ on APCVD SnO₂:F substrate in Chapter 6 and in Fig. 8.1 is not observed on LPCVD ZnO:B substrate. The transmittance for solar cells deposited on SnO₂:F substrate in Fig. 8.1(c) shows interference effects with transmittance minima ($\lambda = 770$ nm) and maxima ($\lambda = 810$ nm). These interference effects are not visible in case of LPCVD ZnO:B in Fig. 8.1(d). A more detailed analysis of the deviant behavior of IRs on different substrates and the interplay of texture and IR is necessary.

In this chapter, the influence of the relevant texture and IR parameters on light propagation and absorption in the tandem solar cell will be studied in detail.

8.2. Substrate Variation

In this study, the effectiveness of the IR on a variety of substrates is investigated by a combination of measurements and rigorous optical simulations. The study bases on the experimental work of C. Zhang. This chapter focuses on the conducted simulations. For further details on the experiment and further discussions, I refer to our publication [189].

To understand the nature of the reflection losses and the different behavior on different substrates, tandem solar cells were deposited on eight different substrates covering a broad distribution of feature sizes and heights. As important parameters for the description of a texture, the auto correlation length (ACL) describing the lateral feature sizes, as well as the RMS roughness (σ_{RMS}) have been proposed by other groups [45, 59, 165, 190]. ACL and RMS were determined from AFM measurements by a statistical surface evaluation at all studied substrates.

8.2.1. From Experiment to Simulation

On the shown substrates, tandem solar cells with i-layer thicknesses of 300 nm (top cell) and 1500 nm (bottom cell) without and with a 70 nm thick $\mu\text{-SiO}_x\text{:H}$ IR were deposited. The refractive index of the IR was $n = 2.7$ at $\lambda = 600\text{ nm}$. The measured EQE_{top} and EQE_{bot} for the tandem solar cells on APCVD $\text{SnO}_2\text{:F}$ (red lines) and ZnO:B substrates (cyan lines) are depicted in Fig. 8.2(a) without (dotted line) and with IR (full lines). For both textures, $\Delta J_{\text{sc,top}}$ is increased by roughly 1 mA/cm^2 . But EQE_{bot} losses due to cell reflection lead to a decrease of sum of short-circuit current density of $\Delta J_{\text{sc,sum}} = 2\text{ mA/cm}^2$ in case of APCVD $\text{SnO}_2\text{:F}$ while losses add up to -0.4 mA/cm^2 for LPCVD ZnO:B .

The experimental comparison suffers from various points. The compared TCO substrates in this study are produced on different glass materials and exhibit different thicknesses, transparency and band gap. Furthermore, solar cells with and without IR were deposited in different deposition runs resulting in variations of layer thicknesses and material quality. Rigorous optical simulations enable to sim-

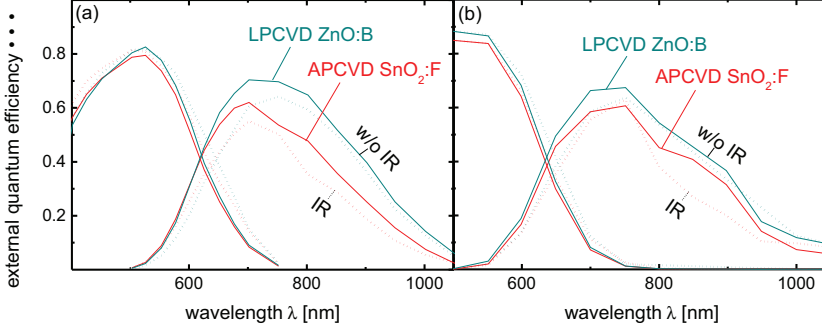


Figure 8.2.: Measured (a) and simulated (b) external quantum efficiency EQE of tandem solar cells on APCVD $\text{SnO}_2\text{:F}$ (red) and LPCVD ZnO:B (cyan) substrate without (full) and with IR (dotted line).

ulate the EQE of tandem solar cells with the identical material data (n , κ , layer thicknesses) basing on the measured AFM topographies. Thus, it is possible to compare the EQE without (full line) and with IR (dotted line) for APCVD and LPCVD ZnO:B texture in Fig. 8.2(b). Note that the wavelength-axis starts at 500 nm. The EQE of tandem cells on LPCVD ZnO:B is higher than on APCVD $\text{SnO}_2\text{:F}$ texture throughout the whole spectral range. The LPCVD ZnO:B texture provides a better light incoupling and enables that more light reaches the absorber and is available for absorption in the solar cell. This can be seen in the short wavelength range where the maximum at $\lambda = 500$ nm is significantly smaller for the APCVD $\text{SnO}_2\text{:F}$ texture. Additionally, a large difference is found for the EQE in the bottom cell for $\lambda > 700$ nm. Here, the EQE_{bot} for the tandem cell without IR is lower due to a less scattering into large angles and, thus, worse light trapping. The IR induces losses in the bottom cell around $\lambda = 900$ nm on APCVD $\text{SnO}_2\text{:F}$ texture. Thereby, EQE_{bot} is decreased in that region. In case of LPCVD ZnO:B texture, this dip is not present. Here, EQE_{bot} for $\lambda > 900$ nm and EQE_{sum} is not decreased by the integration of the IR. The loss is attributed to reflection losses by parasitic reflection at the IR following the arguments of Chapter 5. To ensure that the reflection loss is induced by the IR and no effect of the reflection at the back reflector, further simulations of the tandem cell on APCVD $\text{SnO}_2\text{:F}$ texture were performed substituting the bottom cell and back reflector by a non-absorbing

$\mu\text{c-Si:H}$ half space. The EQE of the sub cell, as well as, the transmittance T into the $\mu\text{c-Si:H}$ half space are presented in Fig. 8.3(a). Black and red lines show the EQE_{top} and EQE_{bot} , respectively, of the tandem solar cell without (full line) and with IR (dashed line). A decrease of EQE_{bot} between $\lambda = 800$ nm and 1000 nm is observed for the tandem solar cell with IR. The transmittance into a non-absorbing $\mu\text{c-Si:H}$ half space T is shown in brown. Interference minima and maxima can be identified in the presence of an IR. At $\lambda = 900$ nm, the minimum of transmittance is found. The position of the minimum correlates to the position of the loss in EQE_{bot} . It is concluded that the loss is due to reflection at the IR and does not even reach the bottom cell. Figure 8.3(b) shows the transmittance T into $\mu\text{c-Si:H}$ (brown) and, additionally, the reflectance R back into the glass in blue lines without (full line) and with IR (dashed). Light of these wavelengths is reflected by the IR and not absorbed in the top cell as its photon energy E_{phot} is below the band gap of a-Si:H and, thus, coupled out of the cell to the continuum. It is furthermore noticed, that, for $\lambda > 1000$ nm, T is increased by the IR in comparison to without due to interference. This results in an increase of EQE_{bot} with IR in this range which has in the past been attributed to an increased light trapping in the bottom cell by the IR [191].

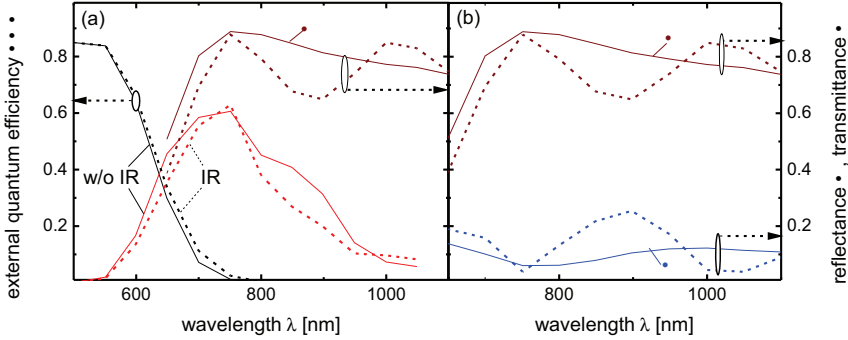


Figure 8.3.: (a) EQE for top and bottom solar cell on APCVD $\text{SnO}_2\text{:F}$ substrate. In brown the transmittance T into a $\mu\text{c-Si:H}$ half space is shown. (b) shows the transmittance T into a $\mu\text{c-Si:H}$ half space in brown and the reflectance R in blue without (full line) and with IR (dashed line).

These high reflection losses are not found for the EQE of tandem cells on

LPCVD ZnO:B texture, as seen in Fig. 8.2(a),(b). For $\lambda > 800$ nm, the EQE_{bot} is not decreased by parasitic reflection.

8.2.2. Variation of Surface Parameters

The question arises which surface parameters influence the top cell EQE -gain and the reflection losses by intermediate reflectors. Kirner et al [59] stated that the effectiveness of the intermediate reflector depends mainly on the auto-correlation length ACL . Following up that study, the APCVD $\text{SnO}_2\text{:F}$ texture is artificially modified to identify the relevant surface parameters.

The measured surface height topography of APCVD $\text{SnO}_2\text{:F}$ was artificially modified. A schematic sketch of the applied stretching is shown in Fig. 8.4(a). Three different modifications have been done:

- Increase of auto correlation length ACL from $ACL = 200$ nm to 320 nm which corresponds to the ACL of LPCVD ZnO:B. This case is referred to as xy -stretched and indicated in blue.
- Increase of ACL from 200 nm to 320 nm and RMS roughness from 60 nm to 95 nm corresponding to the ACL and σ_{RMS} of LPCVD ZnO:B. This case is referred to as xyz -stretched and indicated in red.
- Increase of surface height (minimum-maximum difference) to the height of LPCVD ZnO:B. This case will be called z -stretched and is shown in orange.

A representative $4.3 \times 4.3 \mu\text{m}^2$ cut-out of the modified surface textures is used as input topography for FDTD simulations. A simple growth model for isotropic a-Si:H growth on the textured TCO topography from [192–194] is applied on the texture to obtain the texture after a-Si:H top cell deposition. Layer thicknesses and optical data are kept identical. The simulated EQE_{top} and EQE_{bot} of the solar cells without IR are shown in Fig. 8.5 for the different texture modifications following the introduced color code. In the case of xyz -stretching, the surface angles are maintained and EQE_{top} is maintained. The xy -stretching leads to a decrease of EQE_{top} , in particular for $\lambda < 620$ nm. This is due to less effective light incoupling into the solar cell as the surface feature do not behave as an effective medium anymore. By increasing the surface height an improvement of

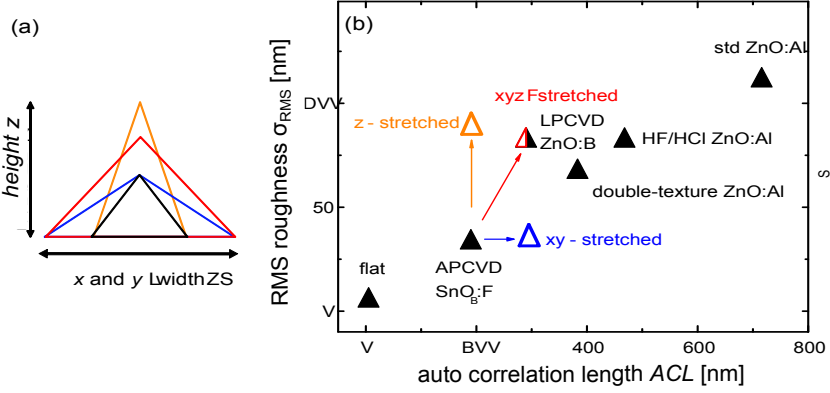


Figure 8.4.: (a) Schematic sketch of the applied surface modifications. The APCVD $\text{SnO}_2:\text{F}$ texture is stretched laterally (xy) and vertically (z) and as a mixture of both in order to reproduce the statistic surface parameters of LPCVD $\text{ZnO}:\text{B}$ substrate (xyz). (b) Topography parameters of different surface textures presenting the three surface modification steps as red, blue and orange triangles.

light incoupling is found. Thus, for the z -stretching, EQE_{top} at $\lambda = 500 \text{ nm}$ is increased to 88% and is similar to the EQE_{top} of the LPCVD $\text{ZnO}:\text{B}$ texture. Similar trends can be observed for the bottom cell: In case of z -stretching, the maximum of EQE_{bot} at $\lambda = 750 \text{ nm}$ could be significantly increased by improved light incoupling. The xy -stretching (blue line) results in a decrease of EQE_{bot} for $\lambda > 750 \text{ nm}$ as the smaller surface angles lead to worse back surface scattering and, thus, to a reduction of bottom cell light trapping [113]. For xyz -stretching, EQE_{bot} is just slightly increased in comparison to the original APCVD $\text{SnO}_2:\text{F}$ texture. The z -stretched surface provides larger surface angles resulting in (i) a better incoupling of light into the bottom cell and (ii) larger scattering angles and, as a consequence, an increased light trapping.

The same solar cell geometries are simulated with a 70 nm thick $\mu\text{-SiO}_x:\text{H}$ IR between top and bottom cell. The simulated $EQEs$ of the tandem cells on the modified substrates are shown in Fig. 8.6(a). The EQE_{top} is increased for z -stretching in comparison to the original APCVD $\text{SnO}_2:\text{F}$ texture. The increase of top cell EQE_{top} is due to the better light incoupling into the solar cell. However, the high EQE -enhancement of the tandem cells on LPCVD $\text{ZnO}:\text{B}$ texture is not reached, as the ACL is too low in order to scatter the light in sufficiently large

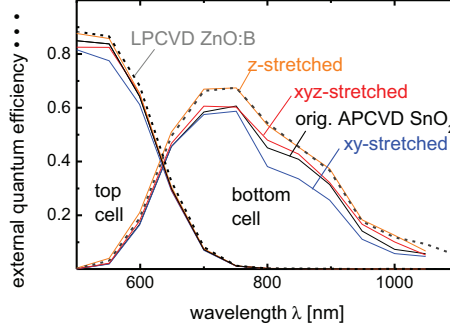


Figure 8.5.: External quantum efficiency EQE of the tandem solar cells without IR on modified substrates. The EQE of the solar cell on APCVD SnO_2 texture is shown as full black line. The dashed black line indicates the EQE on LPCVD ZnO:B texture.

angles and trap it in guided modes. As without IR, the EQE_{top} of the solar cell on xyz -stretched texture, which has the same surface angles as the APCVD $\text{SnO}_2\text{:F}$ texture, except a slight reduction in the maximum at $\lambda = 500$ nm. EQE_{top} of the tandem cell on the xy -stretched substrate is lower along the whole range and is just slightly enhanced by presence of the IR. The surfaces angles α do not induce significant scattering to couple light into guided modes by the IR in accordance to the theory in Chapter 7. The bottom cell losses at $\lambda = 900$ nm which have been attributed to reflection at the IR are found for the xy -stretching (blue line) and the xyz -stretching (red line) as well. Due to worse light trapping, the xy -stretched texture exhibits a lower EQE_{bot} than the APCVD $\text{SnO}_2\text{:F}$ reference. Although ACL is increased, the lower surface angles lead to a decrease of bottom cell EQE . EQE_{top} of the xyz -texture are increased to an extend which exceeds the increase due to better light trapping in Fig. 8.5. Thus, the parasitic reflection losses could be decreased by this surface modification. Finally, the solar cell with z -stretched texture behaves like LPCVD ZnO:B showing nearly no reduction of EQE_{sum} by integration of an IR. This can be seen as well in the solar cell reflectance presented in Fig. 8.6(b). In this case, the z -stretched and LPCVD ZnO:B texture show the lowest cell reflection without interference maxima and minima. The reflectance maximum at $\lambda = 900$ nm which is clearly visible for the APCVD $\text{SnO}_2\text{:F}$ texture, is changed by the various surface modifications. A xy -stretching increases the

reflectance for long wavelengths as the light path is not prolonged by scattering. The reflectance of the tandem solar cell on *xyz*-stretched texture is decreased for $\lambda > 800$ nm. The surface angles α and the surface angle distribution (*SAD*) of a texture do not only determine the quality of light trapping but, additionally, how well light is coupled into the bottom cell instead of being reflected.

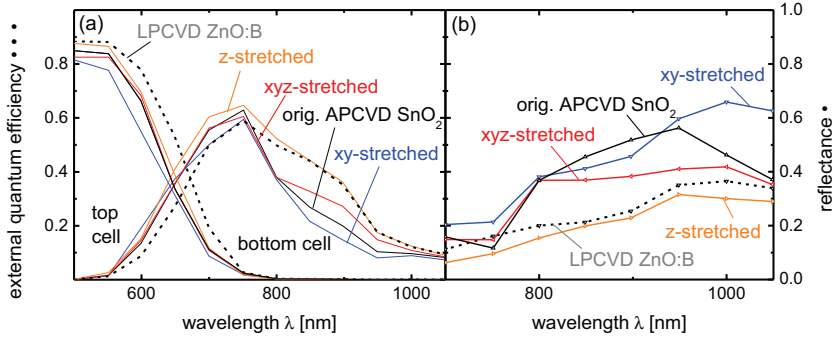


Figure 8.6.: External quantum efficiency *EQE* of the tandem solar cells with IR on modified substrates (*xy*-stretching = blue full line, *xyz*-stretching = red, *z*-stretching = orange). The *EQE* of the solar cell on APCVD SnO₂:F texture is shown as full black line. The dashed black line indicates the *EQE* on LPCVD ZnO:B texture. (b) Reflectance of the solar cells on modified substrates.

8.2.3. Conclusion

Four basic conclusions can be drawn from this study.

- Light incoupling is augmented by an increase of surface texture height (if lateral sizes are not equally increased),
- Coherent reflectance in the long wavelength range below the band gap of the a-Si:H top cell is decreased by increasing the texture height.
- To excite guided modes in the top cell, the *ACL* has to be sufficiently large enabling scattering into large angles.

- *ACL* and *RMS* both determines IR effectiveness. Indications are given that the surface angle α is the crucial parameter uniting *ACL* and *RMS*.

The increase of light incoupling is explained well by effective medium theory whereas the influence on reflectance remains unclear. It can be concluded that the angle with which the light impinges the IR is crucial. The increase of surface angles in this study has an impact on two important quantities namely the angular intensity distribution into a silicon half space in transmission $AID_{T, Si}$ and the surface angle distribution *SAD* of the top cell/ IR interface.

8.3. Angular Reflection Modes

Basing on the result of the previous section, the impact of the angle of incidence on the intermediate reflector is analyzed. The basic reflection mechanisms are identified and the role of the critical angle of total internal reflection is discussed.

Figure 8.7(a) shows the $AID_{T, Si}$ at $\lambda = 650$ nm of APCVD $SnO_2:F$, sputter-etched $ZnO:Al$ and LPCVD $ZnO:B$ texture calculated by the phase model (Chapter 4.1.4). The APCVD $SnO_2:F$ texture has a strong specular peak with roughly 40% of the light transmitted without being scattered. It is seen that an increase of surface height leads to a decrease of the specular peak and an increase of scattering into large angles. In particular, scattering beyond the critical angle of total internal reflection θ_{TIR} (dashed line) of the $a-Si:H/TCO$ interface is of particular interest. Light with an internal angle $\theta > \theta_{TIR}$ will be totally internally reflected and, thereby, trapped within the $a-Si:H$ film. Light can be, furthermore diffracted/scattered at the IR. The distribution of surface facets of the IR is given by the surface angle distribution SAD after $a-Si:H$ deposition is shown in Fig. 8.7(b). All IR textures show a broad distribution of surface angles. While in case of APCVD $SnO_2:F$ the largest part of SAD is found below the critical angle ($\theta < \theta_{TIR}$), the maximum, as well as the mean angle of the SAD are increased by raising the surface texture height like in case of LPCVD $ZnO:B$.

8.3.1. Reflection of Thin Layers

The previous Section revealed that the incident angle of the light onto the intermediate reflector plays a decisive role on the reflectance and scattering behavior of the IR. The evaluation of the angular behavior of a thin film shall be investigated in the following. As a simple model system, a flat thin-film layer with the refractive index of $n_{IR} = 2$ similar to that of $ZnO:Al$ or $\mu c-SiO_x:H$ is sandwiched between two non absorbing high-refractive index half spaces ($n_{HI} = 4$). As all interfaces are flat, a simple transfer matrix model (TMM) (Chapter 4.1.4) is used. Changing the IR film thickness at the same wavelength ($\lambda = 650$ nm) enables to investigate the coherent effects within the layer stack without changing the geometry, angles and relative lateral sizes [56]. The thickness of the IR is varied between $t = 0$ nm and 400 nm and the reflectance into the high refractive index half space is evaluated

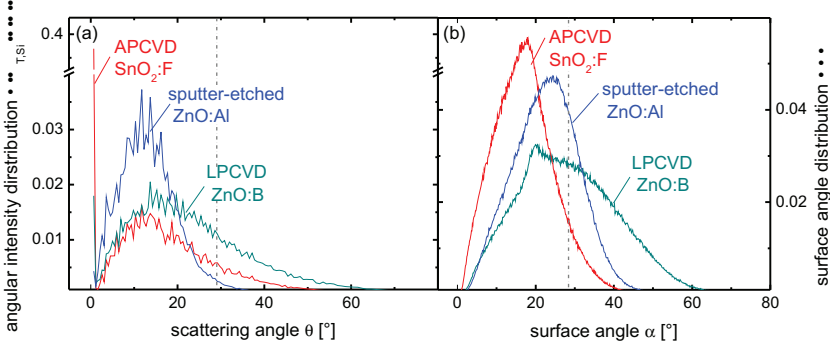


Figure 8.7.: (a) Calculated angular intensity distribution in transmission into a silicon half space $AID_{T,Si}$ for the investigated surface textures APCVD $SnO_2:F$ (red), sputter-etched $ZnO:Al$ (blue) and LPCVD $ZnO:B$ (cyan) at $\lambda = 650$ nm. The critical angle of total internal reflection θ_{TIR} is marked as dashed line. (b) Surface angle distribution SAD after top cell deposition of the investigated surface textures $SnO_2:F$ (red), $ZnO:Al$ (blue) and $ZnO:B$ (cyan).

from the reflection coefficients. The reflectance in dependence of t at $\lambda = 650$ nm is shown in Fig. 8.8(a). A sinusoidal curve progression is observed. The maximum (i) is found at $t_{IR} = 81$ nm corresponding to the condition:

$$t = \frac{\lambda}{4 \cdot n_{IR}}. \quad (8.1)$$

Figure 8.8(b) shows, that if one quarter of the wavelength in the IR medium fits to the IR thickness, constructive interference of the reflected wave with the incoming wave results in a Fabry-Pérot mode within the absorber medium resulting in a maximum of reflected field intensity. In the case of $t = \frac{\lambda}{2n}$, IR in Fig. 8.8(c) (case ii), the wave reaches the back interface of the IR at the turning point of the electric field. The resulting destructive interference leads to a decrease of reflected electric field intensity.

An increase of the angle of incidence of the electromagnetic wave results in a decrease of the perpendicular component of the wave vector k_\perp . For the interference condition like the quarter-wave rule shown in Eq. 8.1, just k_\perp is responsible. According to:

$$t = \frac{\pi}{2k_\perp} \stackrel{\theta=0}{=} \frac{\lambda}{4n_{IR}}, \quad (8.2)$$

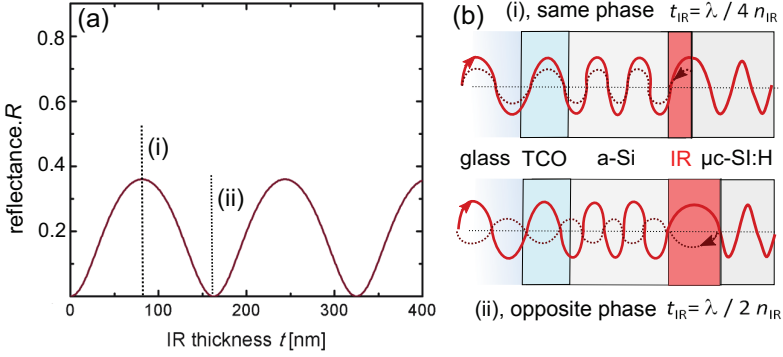


Figure 8.8.: Reflectance R of an intermediate reflector layer of refractive index $n_{\text{IR}} = 2$ between two non-absorbing silicon half spaces of refractive index of $n = 4$ at $\lambda = 650$ nm for varied layer thickness. (b) Schematic sketches illustrate the cases of maximum (i) and minimum reflectance (ii), respectively, in terms of simple wave optics.

the maximum of reflectance is shifted to larger IR thicknesses for longer wavelengths. Figure 8.9 shows the reflectance at $\lambda = 650$ nm for various angle of incidences $\theta = 0^\circ$ (black line), 10° (gray, dashed), 20° (gray, dotted), 25° (gray, dash-dotted) and 30° (red, full line). Up to an angle of $\theta = 25^\circ$, the maximum is shifted to larger IR thicknesses while the value of the reflectance R at the maximum is maintained. For $\theta = 25^\circ$, the maximum is found at a thickness of $t_{\text{IR}} = 220$ nm. The red line indicates the reflectance for an angle of incidence of $\theta = 30^\circ$ which is larger than θ_{TIR} for the given refractive indices (Eq. 4.24).

A distinct reflectance behavior is found in this case. The oscillation of the reflectance is replaced by a monotonic increase. Light with an internal angle $\theta > \theta_{\text{TIR}}$ is entirely reflected at the first interface. Due to the continuity of the electric fields at the interface, the parallel component of the electric field E_{\parallel} extends into the low index film. The concerning wave in the low-index medium is called evanescent wave and its electric field E_{evan} is described by Eq. 4.24. In case of an infinite thickness of the low index film, the evanescent field intensity decays to zero and all the light is totally internally reflected resulting in $R = 1$. In the case of $t < \lambda$, E_{evan} has not yet decayed to 0. If the following medium is a high index medium n_3 , k_{\parallel} may decrease to $k_{\parallel} < k$. As a consequence, the wave is able to propagate in medium n_3 . This results in an increase of T and an decrease

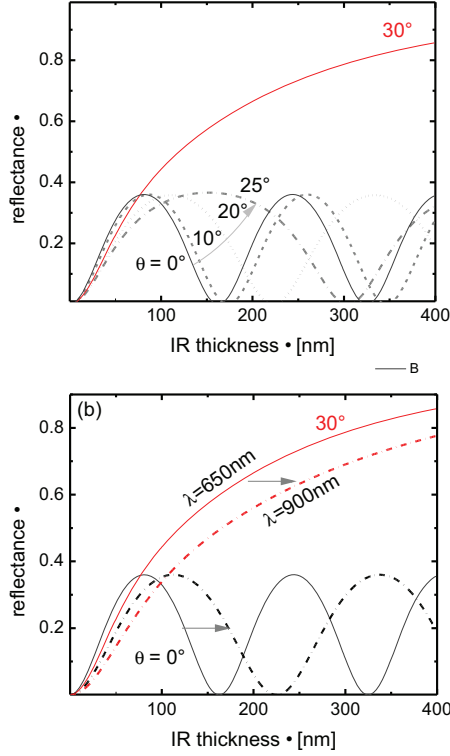


Figure 8.9.: (a) Reflectance of an IR between two a-Si:H and μ c-Si:H half spaces depending on the thickness of the IR layer at $\lambda = 650$ nm for angle of incidences of $\theta = 0^\circ$ (gray, full line), 10° (black, dashed), 20° (gray, dotted), 25° (gray, dash-dotted) and 30° (red, full). (b) reflectance at the low-refractive index medium for an incident angle of 0° (black) and 30° (red) at a wavelength of $\lambda = 650$ nm (full lines) and 900 nm (dash-dotted lines).

of R . This effect is called frustrated or attenuated total internal reflection (ATR) and is analogous to the quantum mechanical tunnel effect. Photons incident at an angle $\theta > \theta_{\text{TIR}}$ are able to tunnel through the barrier of finite thickness. This effect is also described as **evanescent-wave coupling** or **photon tunneling** as the two high index media are coupled by an evanescent wave (Section 4.1.3). The thickness of the barrier determines how much E_{evan} has decayed until the second interface. Figure 8.9(b) shows the reflectance R depending on t for $\lambda = 650$ nm

(full line) and $\lambda = 900 \text{ nm}$ (dash-dotted line) for an $\theta = 0^\circ$ (black) and 30° (red) in comparison. If the wavelength of the incident light is increased according to Eq. 8.1, the reflectance maximum is shifted to larger thicknesses.

8.3.2. Summary

In this section, two different modes of reflection at the IR have been identified:

- Fabry-Pérot thin-film resonance following Eq. 8.1 (**reflection mode A**).
- Attenuated total internal reflection at the top cell/IR interface (**reflection mode B**).

These modes exhibit their particular reflectance behavior. Which behavior occurs to the light depends on whether the angle of incidence is below or above the critical angle θ_{TIR} .

8.4. Theory applied to Randomly Textured Tandem Solar Cells

The IR effectiveness for the APCVD $\text{SnO}_2\text{:F}$ and LPCVD ZnO:B textures has been shown to behave significantly different and surface and scattering angles have been identified to play the decisive role. In this section, the effect of the IR on tandem solar cells on APCVD $\text{SnO}_2\text{:F}$ and LPCVD ZnO:B textures is investigated by rigorous optical simulations and is attributed to the reflection modes which were introduced in the last section.

8.4.1. Spatial Dependence

In the following, tandem solar cells on these particular substrates are investigated by FDTD simulations to identify the dominating effects. $t_{\text{IR}} = 300 \text{ nm}$ is chosen as the reflectance between reflection mode (A) and (B) differs significantly for this thickness. As a reference system, a tandem solar cell on a flat substrate is

simulated. The 500 nm thick front ZnO:Al film is followed by a 330 nm thick a-Si:H top cell and a 300 nm-thick ZnO:Al IR. A cross section of the electric field intensity $|E_{z,\text{total}}|^2$ at $\lambda = 650\text{ nm}$ within the tandem solar cell is presented in Fig. 8.10(a). Fabry-Perot resonances are found in each layer. Period and intensity are determined by the refractive index of the concerning medium. In Fig. 8.10(b), the electric field intensity is plotted against the distance d from the a-Si:H/IR interface. An oscillating sinusoidal curve progression is found with a period of $p = \frac{\lambda}{2 \cdot n_{\text{IR}}}$. The wave is propagating within the IR and a large part is reflected back at the IR/ $\mu\text{c-Si:H}$ interface. Thus, a Fabry-Pérot mode is excited within the low-refractive index IR. As a part of light is transmitted through the IR and is not involved in the interference, the intensity curve described by $\sin^2(kd)$ with an offset $|E_{z,\text{total}}|^2 = 0.12$.

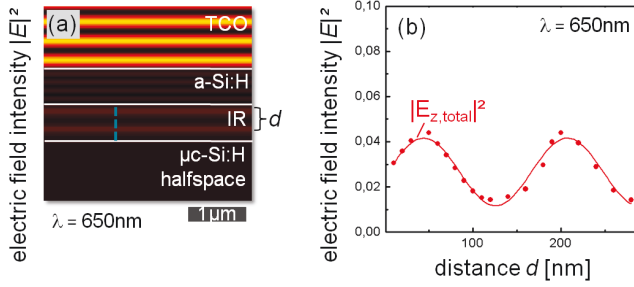


Figure 8.10.: (a) Electric field intensity of a tandem solar cell stack with a 300 nm thick ZnO:Al intermediate reflector for a flat substrate. (b) Electric field intensity within the ZnO:Al IR at $\lambda = 650\text{ nm}$.

The same evaluation is performed for a tandem solar cell on APCVD $\text{SnO}_2\text{:F}$ texture. The cross section of the electric field intensity $|E_{z,\text{total}}|^2$ at $\lambda = 650\text{ nm}$ in Fig. 8.11(a) shows lines of higher and lower intensity parallel to the surface indicating that an oscillation of $|E_{z,\text{total}}|^2$ similar to the flat solar cell is found. This electric field intensity is superimposed with a lateral interference pattern due to the texture. In the following, the average electric field intensity $|E_{z,\text{total}}|^2$ for planes parallel to the a-Si:H/IR interface is extracted. An exemplary plane is shown as white dashed line in Fig. 8.11(a). In Fig. 8.11(b), $|E_{z,\text{total}}|^2$ is plotted against the distance d from the interface. For $d < 220\text{ nm}$, an oscillation with the same period as in the flat case in Fig. 8.10 is found. In this case, the offset is $|E_0|^2 = 0.27$, as more light is coupled into the bottom cell. For $d > 220\text{ nm}$,

$|E_{z,\text{total}}|^2$ rapidly decreases which might be an effect of increasing incoherence of the light at these thicknesses. A similar curve progression is found at a wavelength of $\lambda = 900$ nm (Fig. 8.11(c)). The oscillation period is increased due to the longer wavelength. A Fourier analysis enables the extraction of the evanescent part of the light ($k_{\parallel} > |k|$) in this particular IR plane as described in Chapter 4.1.5. The intensity of the evanescent part of the electric field $|E_{z,\text{evan}}|^2$ is found to be negligible in case of $\lambda = 650$ nm (b) and $\lambda = 900$ nm (c).

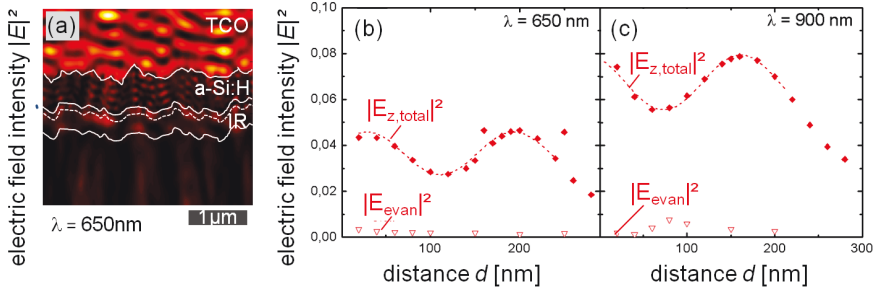


Figure 8.11.: (a) Electric field intensity of a tandem solar cell stack with a 300 nm thick ZnO:Al intermediate reflector for APCVD SnO_2 :F texture. (b) Entire (full) and evanescent (dashed) electric field intensity within the ZnO:Al IR in a plane parallel to the top cell/IR interface at $\lambda = 650$ nm and (c) at $\lambda = 900$ nm.

The same evaluation is done for a tandem solar cell on LPCVD ZnO:B substrate. Figure 8.12(a) shows a cross section of the simulated solar cell stack. As all involved interfaces are much rougher and the texture height surmounts the a-Si:H film thickness, also the local electric field intensity changes. More field localizations than in the case of APCVD SnO_2 :F are found instead of Fabry-Perot like resonances. The total electric field intensity $|E_{z,\text{total}}|^2$ is evaluated in the plane parallel to the interface and plotted against the distance from the a-Si:H/IR interface for $\lambda = 650$ nm (Fig. 8.12(b)) and $\lambda = 900$ nm (Fig. 8.12(c)).

The curve progression differs significantly from the cases before. It is found that the total electric field intensity $|E_{z,\text{total}}|^2$ decreases with increasing distance from the interface. The extraction of the evanescent part results in a decrease of $|E_{\text{evan}}|^2$ which is described by an exponential decay (dashed line). In order to highlight and investigate the exponential decay in more detail, $|E_{z,\text{total}}|^2$ is plotted on a logarithmic scale in Fig. 8.12 for $\lambda = 650$ nm (d) and $\lambda = 900$ nm (e). The exponential decay of $|E_{\text{evan}}|^2$ can be fitted with a linear function on the logarithmic

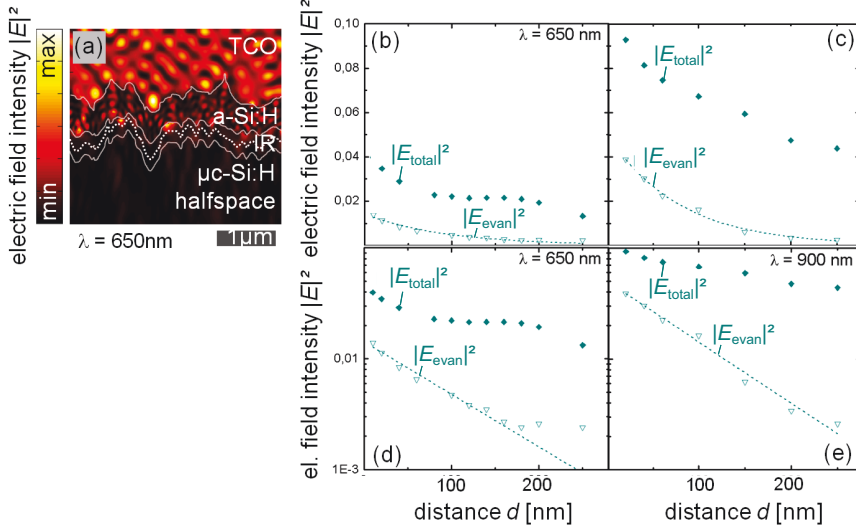


Figure 8.12.: (a) Electric field intensity $|E|^2$ of a tandem solar cell stack with a 300 nm thick ZnO:Al intermediate reflector. (b) Entire $|E_{\text{total}}|^2$ (full) and evanescent $|E_{\text{evan}}|^2$ (dashed) electric field intensity within the ZnO:Al IR in a plane parallel to the top cell/ IR interface for LPCVD ZnO:B texture at $\lambda = 650$ nm (b) and $\lambda = 900$ nm (c). Entire (full) and evanescent (dashed) electric field intensity on a logarithmic scale (\log_{10}) within the ZnO:Al IR in a plane parallel to the top cell/ IR interface for LPCVD ZnO:B texture at $\lambda = 650$ nm (d) and at $\lambda = 900$ nm (e).

scale resulting in the evanescent decay parameters $\gamma(\lambda = 650 \text{ nm}) = 0.0109$ and $\gamma(\lambda = 900 \text{ nm}) = 0.0032$. For $d > 200$ nm, the slope is reduced in the case of $\lambda = 650$ nm. This may be result of incoherent effects that dominate for thicker IRs. Within the first $d = 60$ nm, the decay of $|E_{z,\text{total}}|^2$ is determined by the decay of the evanescent field. Thus, a large portion of the light in the IR is present as evanescent light. The slope of $|E_{z,\text{total}}|^2$ decreases for $d > 70$ nm but stays monotonically decreasing without oscillating behavior. Solving Eq. 4.27 to θ_1 results in:

$$\theta(\gamma) = \arcsin \left(\left(\frac{n_2}{n_1} \right)^2 \cdot \left(\left(\frac{\gamma}{k_2} \right)^2 + 1 \right) \right) \quad (8.3)$$

Equation 8.3 can be used to plot the internal angle θ versus the evanescent decay constant γ in Fig. 8.13 for $\lambda = 650$ nm (black line), $\lambda = 700$ nm (red line)

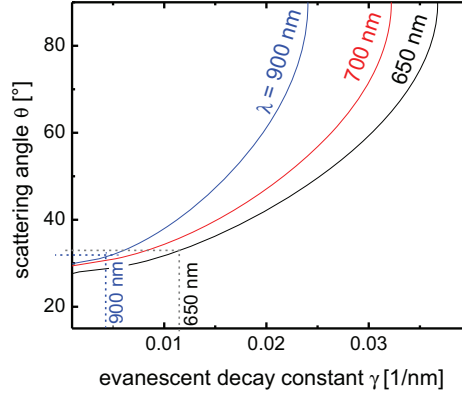


Figure 8.13.: Incident angle θ on the intermediate reflector as a function of the evanescent decay constant γ for $\lambda = 650$ nm (black line), $\lambda = 700$ nm (red line) and $\lambda = 900$ nm (blue line). The decay constants in the IR on LPCVD ZnO:B substrate extracted from Fig. 8.12(b) are marked by dotted lines.

and $\lambda = 900$ nm (blue line). The internal angle is defined as the incident angle of light onto the a-Si:H/IR interface. γ is larger for shorter wavelengths. It follows that the electric field decays faster for shorter wavelengths. The decay constants calculated by the linear logarithmic fit from Fig. 8.12(b) are marked by dotted lines in Fig. 8.13. They can be attributed to an angle which is the average value of the effective angular distribution approaching the IR. This angle is found to be $\theta(650 \text{ nm}) = 34^\circ$ and $\theta(900 \text{ nm}) = 32^\circ$.

The near-field analysis shows that the dominant mechanism of reflection at the IR on LPCVD substrate is frustrated total internal reflection. The finite thickness of the IR leads to an evanescent-wave coupling between top and bottom cell. As the decay constant of the evanescent wave is wavelength-dependent, the IR exhibits a certain spectral selectivity. This effect will be investigated in more detail in the following Sections.

8.4.2. Intermediate Reflector Thickness Dependence

To identify the dominating reflection mode according to Fig. 8.9, FDTD simulations of the tandem solar cell stacks on APCVD $\text{SnO}_2\text{:F}$, sputter-etched ZnO:Al and LPCVD ZnO:B substrate were performed for $\lambda = 650\text{ nm}$ and t is varied. A similar study has been performed for sputter-etched ZnO:Al by Rockstuhl et al. and Kirner et al. [59, 89]. In Fig. 8.14, the IR thickness variation between 0 nm and 300 nm is shown. The EQE_{top} of a solar cell on APCVD SnO_2 is shown as red line and symbols, sputter-etched ZnO:Al in blue lines and symbols and LPCVD ZnO:B as cyan lines and symbols. The EQE_{top} of all investigated tandem solar cells increases with increasing thickness up to $t_{\text{IR}} = 60\text{ nm}$. In the case of APCVD $\text{SnO}_2\text{:F}$, the slope of the curve decreases and a local EQE_{top} maximum is reached at $t_{\text{IR}} = 90\text{ nm}$. For increasing t , the EQE_{top} decreases and follows an oscillation with the next local maximum at $t = 240\text{ nm}$. In case of sputter-etched ZnO:Al (blue), the same trend is found. Reflectance minima and maxima are slightly shifted to larger thicknesses t and the minimum nearly reaches the value without IR. In comparison, the EQE_{top} of the solar cell on LPCVD ZnO:B substrate increases monotonically with decreasing slope and asymptotically reaches a value of $EQE_{\text{top}} = 0.6$ for $t = 300\text{ nm}$.

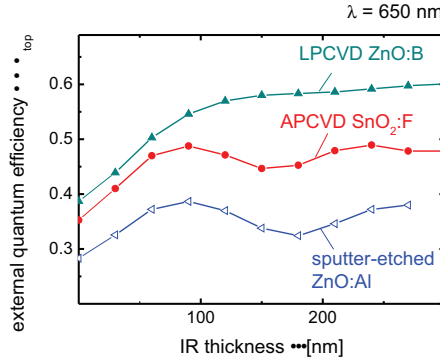


Figure 8.14.: Calculated external quantum efficiency of the top cell EQE_{top} of a solar cell on sputter-etched ZnO:Al (blue triangles), APCVD SnO_2 (red circles) and LPCVD ZnO:B (cyan triangles) substrate for varying IR thickness at $\lambda = 650\text{ nm}$.

To evaluate the thickness dependence of IR behavior below the band gap of the a-Si:H top cell, the transmittance T into the bottom cell for APCVD $\text{SnO}_2\text{:F}$

(red) and LPCVD ZnO:B substrate (cyan) is shown in Fig. 8.15 for $\lambda = 650$ nm (a) and $\lambda = 800$ nm (b). In (a), T is inverse to the EQE_{top} from Fig. 8.14. At the maximum of EQE_{top} , a minimum of transmittance is found and vice versa. For photon energies $E_{ph} > E_{gap,aSi}$, EQE_{top} is negligible. Transmittance oscillations depending on the IR thickness are well pronounced in case of APCVD SnO₂:F. The transmittance into the bottom cell on LPCVD substrate decreases from $T = 0.86$ without IR to $T = 0.71$ at $t_{IR} = 300$ nm. At the same time, cell reflectance R is increased (dotted cyan line). This is because γ of the evanescent field is larger for longer wavelengths as shown in Fig. 8.13. The maximum of R for the top cell on APCVD SnO₂:F is found at $t_{IR} = 100$ nm resulting in a minimum of T . Thus, T of top cells on APCVD SnO₂:F is lower than in case of LPCVD ZnO:B for all $0 \text{ nm} < t_{IR} < 180 \text{ nm}$ while parasitic reflectance out of the solar cell is higher in this range.

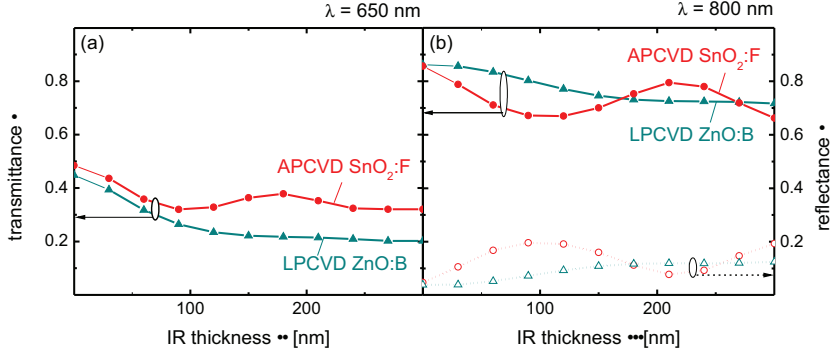


Figure 8.15.: Simulated transmittance into the bottom cell T of a solar cell on APCVD SnO₂:F (red) and LPCVD ZnO:B (cyan) substrate in dependence of the IR thickness t at $\lambda = 650$ nm (a) and $\lambda = 800$ nm (b). In (b), the reflectance R of the solar cell stack is shown as dotted line.

As stated before, the main origin of light engaging onto the IR with a certain angle are scattering at the front surface into a broad distribution (Fig. 8.7(a)) and at the texture of the a-Si:H/IR interface (Fig. 8.7(b)). The reflectance R of the IR layer into a non-absorbing a-Si:H half space is calculated by TMM (Section 4.1.4) for each angle from $\theta = 0^\circ$ to 90° in steps of 1° . $R(t)$ for the particular angle of incidences are summed up and weighted by the $AID_{T,Si}$ from Fig. 8.7(a) for the following substrates: flat (black), APCVD SnO₂:F (red line), sputter-etched

ZnO:Al (blue line) and LPCVD ZnO:B (cyan line). As a result, an effective reflectance R for the front texture is determined and shown in Fig. 8.16(a). In Fig. 8.16(a), R is shown for the flat (black), APCVD SnO₂:F (red), sputter-etched ZnO:Al (blue) and LPCVD ZnO:B substrate (cyan). Dash-dotted vertical lines indicate the first interference maximum.

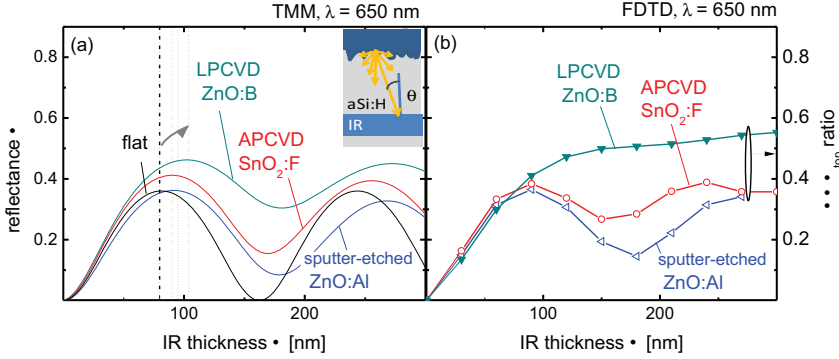


Figure 8.16.: (a) Reflectance R of a flat ZnO:Al IR calculated by transfer matrix method using just front scattering at the front texture (see small inset sketch) of the flat (black), APCVD SnO₂:F (red), sputter-etched ZnO:Al (blue) and LPCVD ZnO:B substrate (cyan). Dash-dotted vertical lines indicate the first interference maximum. (b) EQE_{top} -ratio $\frac{EQE_{\text{top,IR}}}{EQE_{\text{top,w/o}}}$ of the same textures simulated by rigorous optical simulations (FDTD).

In this approach, the IR is flat and the AID is illuminating onto the IR layer from an infinite half-space. Figure 8.16(b) shows the EQE_{top} -ratio $\frac{EQE_{\text{top,IR}}}{EQE_{\text{top,w/o}}}$ of the same textures simulated by rigorous optical simulations (FDTD). The EQE_{top} -ratio $\frac{EQE_{\text{top,IR}}}{EQE_{\text{top,w/o}}}$ sputter-etched ZnO:Al is excellently reproduced and accordance is quite well for APCVD SnO₂:F (Fig. 8.16(b)). The maximal EQE_{top} is found at $t_{\text{IR}} = 90$ nm with an IR reflectance $R = 0.4$ (Fig. 8.16) translating into an EQE_{top} increase from $EQE_{\text{w/oIR}} = 0.35$ to $EQE_{t=90\text{nm}} = 0.49$. For higher t_{IR} , the EQE_{top} -gain is slightly higher than the R . The curve progression and the position of the maxima reproduce the trends which have been shown experimentally and by simulations by [56, 59]:

- The maximum of the oscillation is shifted to higher IR thicknesses turning from a flat IR ($t_{\text{max}} = 80$ nm) to APCVD SnO₂:F (red) ($t_{\text{max}} = 90$ nm),

sputter-etched ZnO:Al (blue) ($t_{\max} = 90 \text{ nm}$) and LPCVD ZnO:B (cyan) ($t_{\max} = 110 \text{ nm}$).

- The reflectance of the IR LPCVD ZnO:B is higher resulting in a higher EQE -gain.

Furthermore, these points can be added:

- In case of sputter-etched ZnO:Al, light reflected at the IR is not trapped but leaves the top cell after one path.
- The monotonic increase of the EQE_{top} of the tandem cell on LPCVD ZnO:B substrate is not reproduced by the coherent TMM model.

For APCVD SnO₂ and sputter-etched ZnO:Al, the simple model of a flat IR already provides a satisfying approximation. In this case the IR acts as a flat layer which is illuminated by the angular distribution of light induced by the scattering at the front texture. For LPCVD ZnO:B, the amount of angles of incidence above θ_{TIR} is higher than the percentage of these angles in the AID scattered at the front side. This is not surprising as the surface of the IR exhibits a large portion of angles above θ_{TIR} (Fig. 8.7).

As a next step, the dependence of the reflectance of a textured IR on the IR thickness t shall be analyzed. Therefore, a ZnO:Al layer with LPCVD ZnO:B texture with thickness t is placed between two non-absorbing a-Si:H and $\mu\text{-Si:H}$ half spaces and R is evaluated depending on t . R of the textured IR (triangles) is compared to that of the system basing just on scattering (full line) in Fig. 8.17.

The reflectance R increases similarly for both cases until $t = 60 \text{ nm}$. In contrast to the oscillating t -dependent reflectance of the scattering case, R of the textured IR increases monotonously to $R = 0.63$ for $t = 300 \text{ nm}$. The monotonic, saturating increase of the reflectance leads to an increase of EQE_{top} consistent with Fig. 8.14. In case of the large facet angles of substrates like LPCVD ZnO:B, the influence of the IR facet angles seem to be the dominating factor.

It has been shown that the dominating reflection mode at the IR are Fabry-Pérot reflection in the case of APCVD SnO₂:F and sputter-etched ZnO:Al and total internal reflection in case of LPCVD ZnO:B. By a decoupling of the different scattering mechanisms it was shown that a combination of the AID at the front

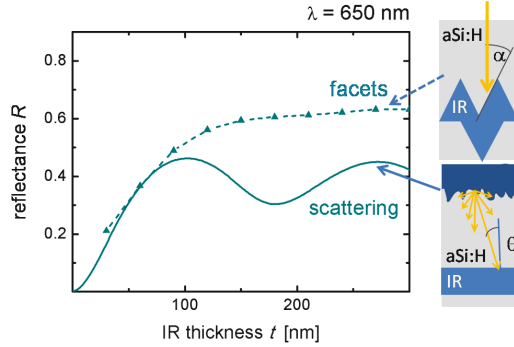


Figure 8.17.: Calculated reflectance R of a ZnO:Al IR using just front scattering of the ZnO:B substrate (full line) and simulated reflectance of the IR on a topography after a-Si:H growth (triangles) for $\lambda = 650 \text{ nm}$.

texture and the distribution of surface angles are necessary to describe the impact of the IR on the gain of EQE_{top} and transmittance into the bottom cell. The Fabry-Pérot reflection mode can be described by a simple coherent 1D wave-optical model with angle that is determined by scattering at the TCO/a-Si:H texture. This simplification is not possible in the ATR reflection mode (B). The IR reflectance behavior in this case is suggested to be much more depending on the IR facets. A more detailed analysis of the interplay of front texture and IR in this reflection mode is necessary.

8.5. Theory applied to Tandem Solar Cells on Periodic Grating Textures

Evanescent wave coupling between top and bottom cell has been identified as the dominant reflection mechanism in LPCVD ZnO:B tandem cells. The interplay of front texture and IR, as well as the optical properties of the intermediate reflector (IR) need to be further investigated. In the following, a simplified system will be used to elaborate a general theory of the working principle of IRs on texture.

As front texture, the triangular grating which was already introduced in Chapter 7.1 will be used (schmatic sketch in Fig. 8.18(a)). It exhibits (i) a particular diffraction pattern into discrete angles at the front side and (ii) at the facets of the IR. This section unites a series of studies which address certain aspects of the interplay of diffraction and reflection in top cells. The variations of the distinct studies are illustrated in Fig. 8.18(b-e).

In Section 8.5.1, spectral and angular properties of the reflectance and diffraction of an isolated IR will be studied. Thereafter, textured interfaces and IRs are regarded in a tandem cell configuration with $\mu\text{c-Si:H}$ bottom cell and the dependence of top cell absorptance and transmittance into the bottom cell on the relevant parameters are investigated systematically:

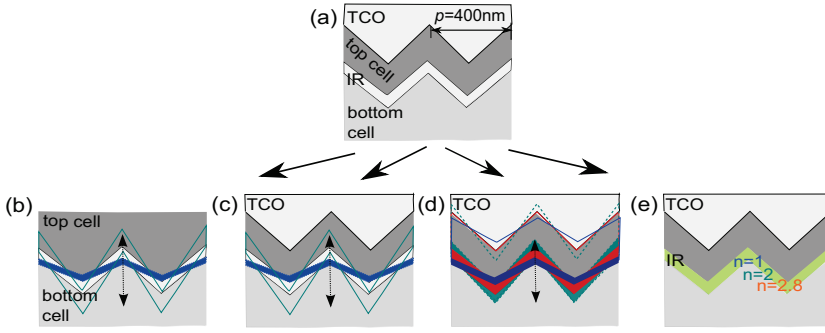


Figure 8.18.: (a) Sketch of the triangular grating studied in these Sections. In the following Sections, different aspects of the interplay will be studied. (b) Dependence of IR thickness and height of the isolated IR between a-S:H/ $\mu\text{c-Si:H}$ half spaces. (c) Variation of IR facet angles/ height in the tandem cell with fixed front grating geometry. (d) Variation of front surface height/ angles at constant top cell layer thickness. (e) Variation of the refractive index of the IR n_{IR} for fixed tandem cell geometry.

Section 8.5.2 focusses on the interplay of a fixed front grating with a variation of IR geometry (IR grating period p_{IR} , IR facet angles α_{IR}) (Fig. 8.18(b)).

In Section 8.5.3, the a-Si:H layer is kept conformal and the influence on the grating height h and IR thickness T_{IR} is studied (Fig. 8.18(c)).

The role of leaky waveguide modes on absorptance and parasitic reflectance in the a-Si:H top cell regarded as planar waveguide is studied in Section 8.5.4 (Fig. 8.18(d)).

The influence on the refractive index of the IR n_{IR} is determined in Section 8.5.5 (Fig. 8.18(e)).

Finally, Section 8.5.6 summarizes the dependencies of the tandem cell performance on these parameters and introduces a Figure of Merit which characterizes the spectral selective reflectance and diffraction. This allows for an optimization of tandem cell currents basing on angular distributions.

A triangular grating with a period of $p = 400 \text{ nm}$ which was already introduced in Chapter 7.1 is used in the following simulation series: Texture heights $h = 100 \text{ nm}$ (indicated in blue), $h = 200 \text{ nm}$ (red) and $h = 300 \text{ nm}$ (cyan) are chosen to cover a variety of surface angles.

8.5.1. Influence of the Grating Height on IR Reflectance

In the following, a periodically textured IR between two silicon half spaces is investigated concerning the dependence of IR thickness and height of the geometry and modifications is shown in Fig. 8.19. The reflectance of angle ZnO:Al IR layer with this periodic texture between two silicon half spaces is plotted in Fig. 8.20 as a function of the IR thickness for $\lambda = 700 \text{ nm}$ (a) and 900 nm (b). A flat thin-film IR is indicated as system with texture height $h = 0 \text{ nm}$.

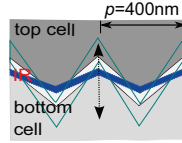


Figure 8.19.: (Sketch of the triangular grating studied in this Section. Dependence of IR thickness and height of the isolated IR between $a\text{-Si:H}/\mu\text{c-Si:H}$ half spaces.

For the case $h = 0 \text{ nm}$, the reflectance R shows the thickness-dependent oscillation which was discussed before in Fig. 8.8. In contrast, the reflectance of the grating with $h = 300 \text{ nm}$ increases monotonically to $R = 0.7$. This behavior can be associated to ATR. The surface angles resulting from the grating period and height are $\alpha_{h100} = 19.3^\circ$, $\alpha_{h200} = 35^\circ$ and $\alpha_{h300} = 46^\circ$. For $h = 100 \text{ nm}$ and 200 nm , the maximum of reflectance is shifted to larger thicknesses at $\lambda = 700 \text{ nm}$ indicating a larger angle of incidence. It can be concluded that the incident light sees an effective distribution of surface facets. For $\lambda = 900 \text{ nm}$ (Fig. 8.20(b)),

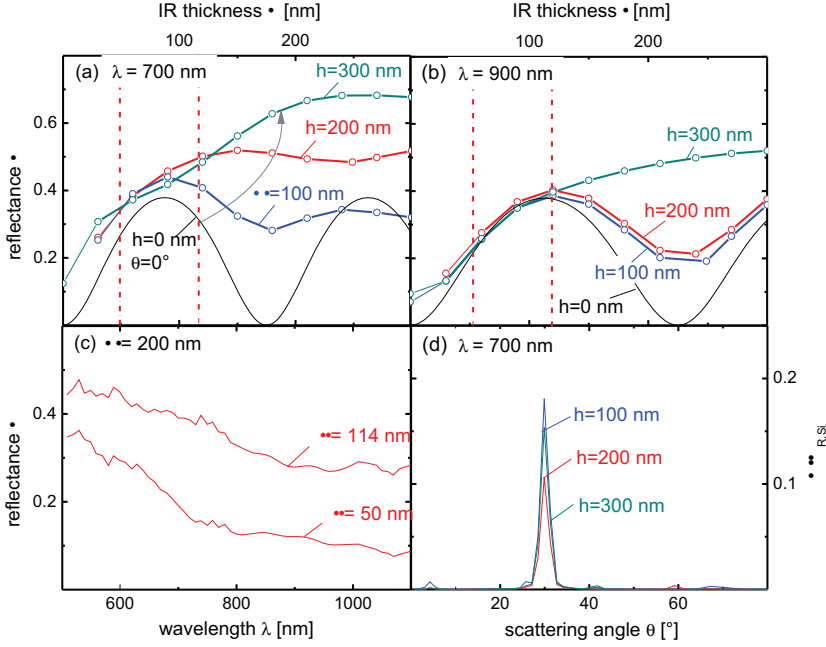


Figure 8.20.: Thickness-dependent reflectance R for normal incidence of a ZnO:Al IR with the triangular texture and texture heights of $h = 0$ nm (black), $h = 100$ nm (blue), $h = 200$ nm (red), $h = 300$ nm (cyan) at $\lambda = 700$ nm (a) and $\lambda = 900$ nm (b). The black dashed line indicates the reflectance of a flat IR under an angle of incidence of $\theta = 27^\circ$. (c) Wavelength-dependent reflectance R for normal incidence of a ZnO:Al IR with the triangular texture and texture heights of $h = 200$ nm for an IR thickness of $t = 50$ nm and $t = 114$ nm. (d) Angular intensity distribution in reflection $AID_{R,Si}$ into a non-absorbing a-Si:H half space for the above described grating heights.

the maximum of reflectance is shifted to larger thicknesses. Further, the oscillating behavior is much stronger for $h = 100$ nm and $h = 200$ nm. As the texture height is significantly smaller than the wavelength, the diffraction efficiency and, consequently, the percentage of light with large k_{\parallel} -components is decreased. The spectral dependence of the reflectance of an IR with $t = 50$ nm and 114 nm is shown in Fig. 8.20(c) for a triangular grating with $h = 200$ nm. A general reduction of IR reflectance for longer wavelengths is observed and can be explained by

the increase of the evanescent decay constant γ (see Fig. 8.13). Figure 8.20(d) shows the angular intensity distribution in reflection $AID_{R, Si}$ into a non-absorbing a-Si:H half space for the above described $h = 100$ nm (blue line), 200 nm (red line) and 300 nm (cyan line) for a 220 nm-thick IR at $\lambda = 700$ nm. The dominant amount of light is found at a scattering angle of 28° related to the first diffraction order. Despite the different surface angles related to different surface heights, light is diffracted into this particular angle which is determined by the grating period.

Regarding the IR as an isolated device between two silicon half spaces reveals that the IR reflectance depends significantly on the IR texture. The surface angle is a crucial parameter as it determines with which angle light faces the low refractive index layer. While low angle surfaces lead to a more coherent interference behavior in the IR, for larger angles, attenuated total internal reflection and, as a consequence, photon tunneling are the dominant effects. As the texture dimensions are in sub-wavelength range the periodically textured IR acts as reflection grating. Ray tracing is not feasible in this case and rigorous optical simulations of the coupled layer stack are necessary to understand the interaction of different mechanisms.

8.5.2. Influence of the IR Texture and Geometry on Absorption

As the intermediate reflector is integrated in a solar cell stack, an interplay between the scattering at the front interface and the reflectance at the IR is found. In this study, the impact of the geometry of the IR (period, height) on the interplay between front texture and investigated exemplary on a periodic triangular grating. Therefore, the front texture is kept constant while the IR textures are permuted

To study the interplay of the front texture and IR texture a $h = 200$ nm, $p =$

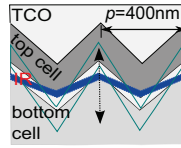


Figure 8.21.: Sketch of the triangular grating studied in this Section. IR facet angles/ height are varied in the tandem cell with fixed front grating geometry.

400 nm front grating is chosen (in accordance with Chapter 7) and implemented into a tandem cell stack (glass/TCO/a-Si:H/IR/ μ c-Si:H half space). Figure 8.21 illustrates the studied geometry. The front texture is kept constant, while four different IR geometries are regarded. In all cases, an average a-Si:H absorber thickness of $t_{\text{a-Si:H}} = 330$ nm and a 114 nm-thick ZnO:Al IR layer are defined. The simulated electric field intensity within these stacks are shown in Fig. 8.22(a-d). In Fig. 8.22(a), the electric field intensity $|E_{z,\text{total}}|^2$ with flat IR (orange) is presented, in (b) the a-Si:H growth is conformal (cyan line) and the IR exhibits the same grating texture as the front texture. The IR in (c) exhibits an increased texture height at the IR ($h = 300$ nm) resulting in larger angles (purple line). In (d), a conformal a-Si:H growth is combined with a different IR back interface (red line). This device is a diffractive intermediate reflector (DIR) in accordance with [57]. It combines the strong coupling into waveguide modes in the top cell in case of the conformal IR with an improved light trapping in the bottom cell due to a larger period of $p = 1200$ nm which is more suitable for light trapping in the bottom cell. A plane extracted from the electric field distribution within the a-Si:H film is used to perform a FFT analogously to Chapter 7. The scattering intensity SI determined by FFT is shown in Fig. 8.22(e) for the above presented structures (a-

d). While the *SI* in case of the flat IR is dominated by lower scattering angles, like the first diffraction order at 23° , for the configuration with conformal IR, higher diffraction orders are found which contribute to trap light within the a-Si:H layer. In particular, a large portion of light is coupled into waveguide modes which are found at a scattering angle of $\theta = 72^\circ$. Large angle IR (purple) and DIR (red) exhibit a large portion of light in larger angles but less than the conformal IR which is in resonance.

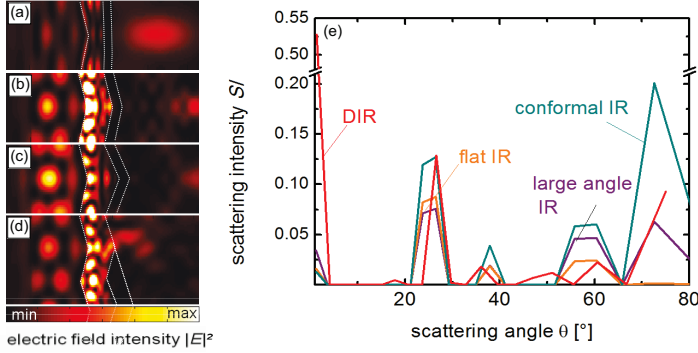


Figure 8.22.: *Electric field intensity $|E_{z,\text{total}}|^2$ at $\lambda = 700$ nm for flat IR $t = 114$ nm (a), conformal IR (b), an IR with large-angle IR facets (c) and a diffractive IR with a larger IR back texture (d). (e) Scattering Intensity *SI* into the diffraction angles θ at $\lambda = 700$ nm for flat IR (orange line), a conformal IR (cyan line), an IR with large-angle IR facets (purple line) and a diffractive IR with a larger IR back texture (red line).*

The interplay between front and back texture of the a-Si:H film is investigated by determining the angular scattering distribution into a non-absorbing a-Si:H half space of a triangular grating with $p = 400$ nm and $h = 200$ nm for transmission (front grating, blue) and reflection (back grating, black dotted) at $\lambda = 700$ nm by scalar scattering theory (Section 4.1.4). The resulting angular intensity distribution $AID_{\text{Si,T/R}}$ is shown in Fig. 8.23. The incident light is diffracted at the TCO/a-Si:H interface into discrete diffraction angles. Diffraction angles are determined by the grating period:

$$\theta_n = \arcsin \left(\frac{\sqrt{l^2 + m^2} \cdot \lambda}{n \cdot p} \right) \quad (8.4)$$

where m, l are the 2D diffraction orders. In Fig. 8.23(a), these diffraction modes

are indicated by gray lines and assigned as $(l, m) = (0, 0), (1, 0), (1, 1), (2, 1)$. Transmission and reflection grating diffract into the same diffraction orders, but while diffraction efficiencies into low diffraction orders ($(l, m) = (0, 0), (1, 0)$) prevail in case of the transmission grating. For the reflection grating, light is predominantly diffracted into large angles. The scattering intensity SI in the a-Si:H top cell on the conformal $h = 200$ nm substrate (cyan line from Fig. 8.22(e)) is shown in Fig. 8.23(b). Scattering angles within the layer correspond to the diffraction angles of the grating. The SI is found to be a superposition of the diffraction at the front and the rear side of the a-Si:H film. Within the film, just a really low specular component is found. The specularly transmitted light at the front grating (zeroth diffraction order) is redistributed to larger diffraction angles by scattering at the back grating. Comparing the conformal triangular grating to the flat IR from Fig. 8.22(e) (orange line), it is observed that the SI of the solar cell with flat IR does not exhibit the higher diffraction orders which are induced by the reflection grating as just one k_{\parallel} -transfer takes place. The surface texture at the IR acts as reflection grating and transfers of Δk_{\parallel} to the wave in order to access waveguide modes. Thus, the coupling efficiency into waveguide modes of the a-Si:H film is increased by the reflection grating.

To study the impact of the IR texture on the absorption in the top cell, the EQE_{top} of a solar cell on $h = 200$ nm and $p = 400$ nm front texture is simulated by FDTD and shown in Fig. 8.24. The front ZnO:Al/a-Si:H interface is textured with the triangular grating of $h = 200$ nm, while the a-Si:H/ IR interface is chosen conformal (cyan line), flat (orange line), large angle IR ($h = 300$ nm, purple line) and the diffracting IR (red line). EQE_{top} of the conformal IR has already been discussed in Chapter 7.1. For this IR, a waveguide mode is excited within the a-Si:H film at $\lambda = 700$ nm.

In case of the flat IR (orange line) the resonance frequency of the waveguide mode is shifted because the geometry of the a-Si:H film is changed. The EQE_{top} with flat IR is higher than without IR (black line), but does not exceed EQE_{top} in case of the conformal IR. This is surprising as the light reflected at the flat IR will interact with the front interface again, which acts as a reflection grating in that case. Increasing the IR grating height to $h = 300$ nm (purple line) shifts the waveguide mode frequencies and, furthermore, increases the generated photo current $J_{\text{sc, top}}$. The gain in short-circuit current density of the top cell $\Delta J_{\text{sc, top}}$ is shown in the table next to Fig. 8.24. The top cell short-circuit current density

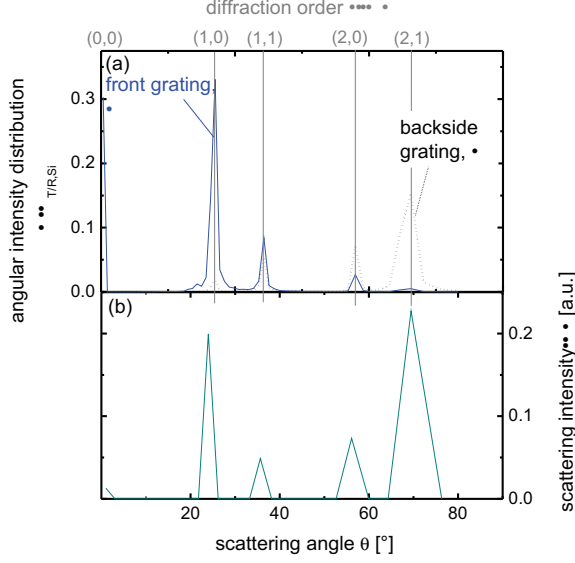


Figure 8.23.: (a) Angular intensity distribution AID_{Si} at $\lambda = 700$ nm into a non-absorbing $a\text{-Si:H}$ half space of a triangular grating with $p = 400$ nm and $h = 200$ nm for transmission (front grating, blue) and reflection (back grating, black dotted). (b) Scattering intensity SI within the $a\text{-Si:H}$ film in a tandem cell with $t = 114$ nm thick IR at $\lambda = 700$ nm.

is increased by the conformal IR in comparison to flat IR. An increase of back side grating height results in a further increase of the top cell short-circuit current density ($\Delta J_{sc,top} = 1.43$). In case of the DIR (red line), waveguide modes are not well pronounced. The absorption enhancement of the DIR does, however, strongly depend on the thickness of low index layer between the facets. As studied by Obermeyer et al. in [191], bottom cell absorption is enhanced by the back side grating of the IR while the reflectance of light into the top cell is increased by increasing the IR thickness.

The diffraction grating defines the discrete angles in which the light is distributed. By increasing the IR facet angles, a redistribution to higher diffraction orders is provided. The scattering intensity in the layer is a superposition of the

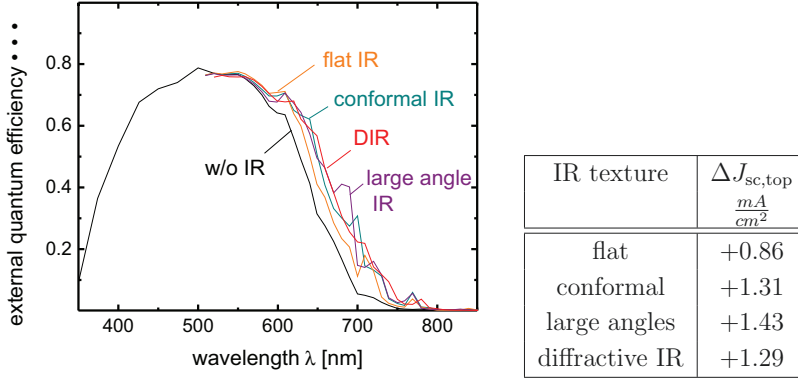


Figure 8.24.: External quantum efficiency EQE_{top} of the tandem solar cell on triangular grating with height $h = 200$ nm without IR (black), with a flat IR interface (orange), a conformal a-Si:H solar cell (cyan), an IR with an increased texture height of $h = 300$ nm resulting in larger surface angles α at the top cell/ IR interface and a diffractive IR with a larger period behind the IR.

different diffraction processes at the front texture and at the IR. The absorption enhancement in the top cell is enhanced by a textured IR.

8.5.3. Influence of the Grating Height on Absorption

It has been shown, that the texture plays a role both at the front side, as well as at the IR. In Fig. 8.20, the dependence of the reflectance of the IR on the grating height has been presented. In the previous section, various IR textures were implemented in tandem solar cells with triangular front grating. By the change of back grating height, a redistribution of light to lower and higher diffraction orders is provided. The influence of the IR absorption in the a-Si:H top cell for different front texture heights is subject of this study.

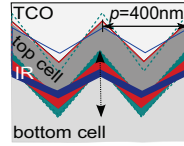


Figure 8.25.: Sketch of the triangular grating studied in this Section. In the following Sections, different aspects of the interplay will be studied. Front surface height/ angles are varied at constant top cell layer thickness.

The simulation setup for this study is illustrated in Fig. 8.25. Front surface height h and angles are varied at constant top cell layer thickness. The top cell is kept conformal for this series. The dependence of EQE_{top} on the IR thickness t in the tandem cell is studied in Fig. 8.26. Here, the top cell EQE -ratio $= \frac{EQE_{\text{top,IR}}}{EQE_{\text{top,w/o}}}$ is shown for $h = 100$ nm (blue), $h = 200$ nm (red), $h = 300$ nm (cyan) at the wavelength of a local maximum corresponding to $\lambda = 680$ nm ($h = 100$ nm), $\lambda = 700$ nm ($h = 200$ nm) and $\lambda = 670$ nm ($h = 300$ nm). For comparison, the reflectance of the textured IRs into a non-absorbing silicon half space was shown in Fig. 8.20.

The EQE_{top} of the solar cell on a grating texture with $h = 100$ nm follows the progression of the IR reflectance. The position of the reflectance maximum ($t = 90$ nm) and minimum ($t = 160$ nm) is the same as R of the IR between silicon half spaces (Fig. 8.20). The thickness dependence of the EQE_{top} -gain of this grating is similar to APCVD SnO_2 :F. The grating height $h = 100$ nm leads to a high specular transmission. The facet angle of 19° is close to the maximum

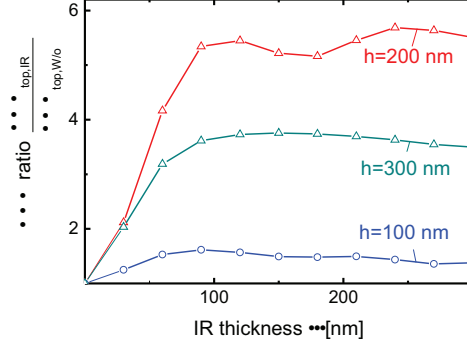


Figure 8.26.: Thickness-dependent top cell EQE -ratio $= \frac{EQE_{top,IR}}{EQE_{top,w/o}}$ for the tandem solar cells on different texture heights $h = 100$ nm (blue), $h = 200$ nm (red), $h = 300$ nm (cyan) at neighboring resonance to $\lambda = 700$ nm.

of the surface angle distribution SAD of APCVD $SnO_2:F$ (Fig. 8.7(b)). For a grating height of $h = 200$ nm, a much larger gain (EQE -ratio = 5.4) with a similar behavior as $h = 200$ nm is found. In the case of the $h = 300$ nm grating, the saturation starts much earlier as well at $t = 100$ nm and slightly decreases for $t > 180$ nm. It is concluded that the reflectance of the IR alone is not a good measure, the whole optical system including top cell and TCO has to be studied as soon as the specular transmission is not the dominating contribution.

The incident light is diffracted at the TCO/a-Si:H interface into discrete diffraction angles. Figure 8.27 shows the scattering intensity SI of the triangular grating for $h = 100$ nm (blue), $h = 200$ nm (red) and $h = 300$ nm (cyan) at $\lambda = 650$ nm. The diffraction orders are indicated by gray lines and assigned as $(l, m) = (0, 0), (1, 0), (1, 1), (2, 1)$. For the studied 2D grating, diffraction angles of $\theta_{(1,0)} = 24.0^\circ$, $\theta_{(1,1)} = 36^\circ$, $\theta_{(2,0)} = 54.3^\circ$ and $\theta_{(2,1)} = 74^\circ$ are obtained by Eq. 8.4 for $\lambda = 700$ nm. The scattering intensity SI corresponding to the diffraction orders within the a-Si:H film is determined by FFT of the complex electric fields by the Ansatz described in Chapter 7.1. By varying the IR thickness t_{IR} , it is possible to assign the contribution of the different diffraction modes to the absorption in the a-Si:H film. In Fig. 8.28, this is shown exemplary for $h = 100$ nm (a-b) at the maximum $\lambda_{h100} = 680$ nm and for $h = 200$ nm at $\lambda_{h200} = 700$ nm (c-d). In (a) and (c), the influence of IR thickness on EQE_{top} is shown for $h = 100$ nm and $h = 200$ nm,

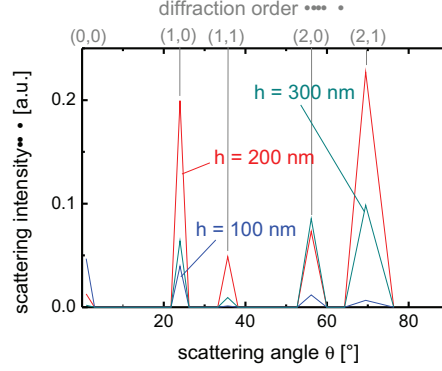


Figure 8.27.: Scattering intensity SI in the a -Si:H film over scattering angle θ for the different texture heights $h = 100$ nm (blue), $h = 200$ nm (red), $h = 300$ nm (cyan) at $\lambda = 650$ nm. The diffraction orders m are indicated by gray vertical lines.

respectively, like already shown in Fig. 8.26. In (b) and (d), SI within the a -Si:H film into the above assigned diffraction orders $(l, m) = (0, 0), (1, 0), (1, 1), (2, 1)$ for the variation of the IR thickness t is shown. For $h = 100$ nm, the zeroth and first diffraction order are strongly pronounced while higher orders show $SI < 0.01$. An oscillation of SI is observed which is most pronounced for the zeroth diffraction order (oscillation period of 150 nm) and first diffraction order (oscillation period of 200 nm). The sum of all SI is shown as black dotted line (Σ_1) in (b). It is dominated by the effect of the zeroth and first diffraction order and exhibits a maximum at $t = 150$ nm which is in contradiction to the progress of EQE_{top} . EQE_{top} is increased by rising IR thickness up to a maximum of absorption enhancement at $t = 90$ nm as seen in (a). According to Chapter 7.2, the EQE -enhancement by an IR is related to the integrated scattering intensity ISI above the critical angle of total internal reflection θ_{TIR} . The sum of all SI above θ_{TIR} is shown as blue dotted line in (b) ($\Sigma_2 = ISI$). Here, an excellent agreement to the EQE_{top} is found.

In case of the triangular front grating with $h = 200$ nm (Chapter. 7, without IR, the zeroth $((0,0)$, black line) and first diffraction order $((1,0)$, grey line) dominates. By introducing the IR, the interface acts as a reflection grating and contributions with larger parallel wave vector component $((l, m) = (0, 0), (1, 0), (1, 1), (2, 1))$ are increased. The thickness dependence of the first diffraction order is maintained

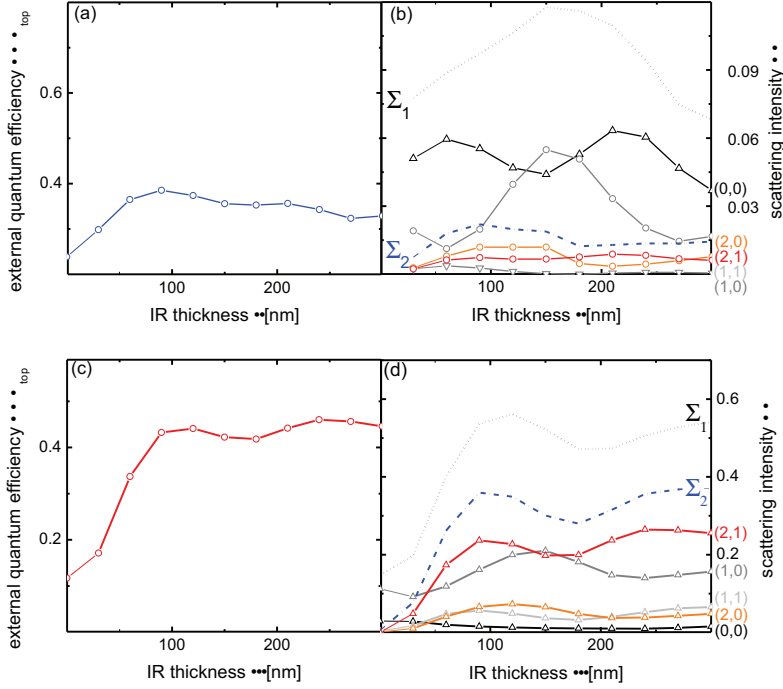


Figure 8.28.: (a) EQE_{top} of a tandem solar cell on triangular front texture with a height $h = 100$ nm depending on the thickness t of a ZnO:Al IR. (b) IR thickness depended scattering intensity SI into the certain diffraction orders indicated in Fig. 8.27 within the a-Si:H top cell absorber at a wavelength of $\lambda = 680$ nm. The sum of all SI is shown as black dotted line (Σ_1), while the blue dash-dotted line indicates the sum of all SI above θ_{TIR} ($\Sigma_2 = ISI$). (c) and (d) show the corresponding results for $h = 200$ nm.

showing a minimum at $t = 30$ nm and a pronounced maximum at 150 nm. For IR thicknesses $t > 45$ nm, the diffraction order (2,1) at $\theta = 73^\circ$ which has been attributed to the waveguide mode (Chapter 7) provides the dominant contribution. The sum of intensity in angles $\theta > \theta_{TIR}$ (Σ_2) is depicted as blue dash-dotted line and correlates well with the increase and oscillation of the EQE_{top} with increasing thickness. In the range of weak absorptance in the a-Si:H top cell, EQE_{top} -enhancement is determined by the contribution of large $k_{||}$ -components resulting in $\theta > \theta_{TIR}$. For larger grating heights, even more light is redirected to large

parallel wave vector components and results in a stronger contribution of higher diffraction orders.

The previous results indicate that for the evaluation of IR effectiveness, the reflectance of the IR alone is not a sufficient indicator. The induced light path prolongation in the top cell absorber by coupling light into waveguide modes by reflection at the IR has to be taken into account. As a quantity incorporating the top cell absorption enhancement and IR reflectance, I introduce the IR induced waveguide coupling parameter WCP_{IR} . It is the ratio of absorption enhancement in the top cell $\frac{EQE_{\text{IR}}}{EQE_{\text{w/o}}}$ by the IR and the reflectance of the isolated IR into a non-absorbing a-Si:H half space (like shown in Fig. 8.20). The WCP_{IR} indicates how effectively the reflected light at the IR is coupled into waveguide modes in the a-Si:H film. In Fig. 8.29, the WCP_{IR} for an IR thickness of $t = 50$ nm (a) and 114 nm (b) are shown for the triangular texture and texture heights of $h = 100$ nm (blue line), $h = 200$ nm (red line), $h = 300$ nm (cyan line).

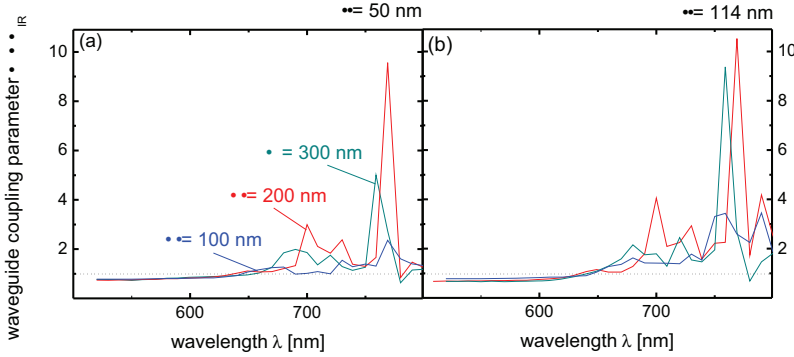


Figure 8.29.: Wavelength-dependent EQE_{top} -gain per reflectance R (waveguide coupling parameter WCP_{IR}) for normal incidence of a ZnO:Al IR with the triangular texture and $h = 100$ nm (blue), $h = 200$ nm (red), $h = 300$ nm (cyan) for an IR thickness of $t = 50$ nm (a) and $t = 114$ nm (b).

The WCP_{IR} for $h = 100$ nm is predominantly around 1 but does not exceed a value of 2. As just a small parallel wave vector is transferred by the grating, the predominant part of the light does not exhibit a sufficient k_{\parallel} -component to be trapped in the a-Si:H film. This light is coupled out to the ambient resulting in an increased reflectance at the front of the solar cell. The reflectance of the solar cell is shown in Fig. 8.30 for an IR thickness of $t = 50$ nm (a) and $t = 114$ nm (b).

Depending on the wavelength, between 8% and 31% ($t = 50$ nm) and 46% ($t = 114$ nm) are reflected back. Reflectance for $\lambda < 640$ nm is caused by insufficient light incoupling into the solar cell, while reflectance for $\lambda > 640$ nm is due to insufficient light trapping in the top cell resulting in an incomplete absorption of the light spectrum dedicated to the top cell.

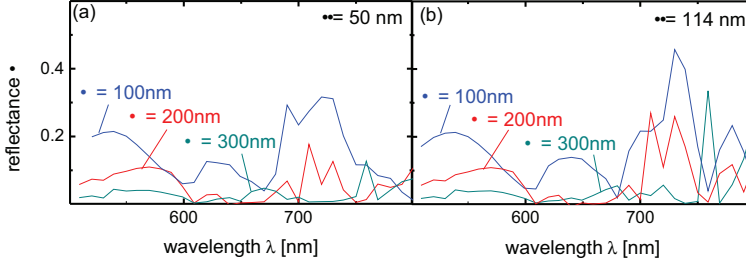


Figure 8.30.: Wavelength-dependent cell reflectance R for normal incidence of a ZnO:Al IR with the triangular texture and texture heights of $h = 100$ nm (blue), $h = 200$ nm (red), $h = 300$ nm (cyan) for an IR thickness of $t = 50$ nm (a) and $t = 114$ nm (b).

The increase of surface texture height has two effects: (i) Light incoupling is significantly increased with an increase of h . Just 3% of reflectance remains for $h = 300$ nm. (ii) The top cell light trapping is improved by a transfer of large k_{\parallel} -components by the grating. The coupling of incident light into waveguide modes is significantly increased. A WCP_{IR} of up to 10 in case of the 114 nm thick IR is reached (Fig. 8.29(b)) resulting in an increased light path in the a-Si:H absorber. For $h = 200$ nm and 300 nm, the WCP_{IR} is predominantly ≈ 2 , showing certain resonances with higher WCP_{IR} . These resonances of WCP_{IR} in Fig. 8.30 are obtained for wavelengths $\lambda > 750$ nm where absorptance of the a-Si:H absorber is weak. These waveguide modes increase the light path, but do not contribute to absorption in the top cell. This demands for a detailed study dedicated to the gains and losses of waveguide modes in tandem cell.

The absorption enhancement in the a-Si:H top cell with IR depends significantly on the grating height. Here, the top cell has to be considered as a nano-optical device. The coupling efficiency into certain waveguide modes of the top cell is defined by the diffraction efficiency of the front grating, the backside grating (at

the IR) and the a-Si:H film thickness. As total internal reflection is the driving effect for light trapping, the critical angle of total internal reflection defines which diffraction orders are efficiently trapped and contribute to absorption enhancement. It is revealed that a transfer of high k_{\parallel} -components is important to secure complete absorption of the top cell spectrum. **An effective IR has to reflect effectively its aiming spectral range, but, additionally, has to cause effective light trapping in the top cell in this range.**

8.5.4. Role of Leaky Waveguide Modes in a-Si:H Top Cell

In the previous section, the coupling into leaky waveguide modes has been identified as the mechanism induced by the intermediate reflector. Gains and losses of the coupling into leaky waveguide modes are studied in the following. In particular, it shall be investigated how a trade-off between high top cell enhancement and low reflection losses can be designed.

In the following, tandem cells on triangular grating with $h = 300$ nm and $p = 400$ nm are investigated as they show large contributions of waveguide modes and scattering into large angles. The top cell absorption enhancement $A_e = \frac{EQE_{\text{top,IR}}}{EQE_{\text{top,w/o}}}$ for the tandem cell of $h = 300$ nm triangular grating is presented in Fig. 8.31(a). The transmittance into the $\mu\text{c-Si:H}$ bottom cell for the same configuration is shown in Fig. 8.31(b). As IR, ZnO:Al of three different thicknesses is applied. The $t = 114$ nm has been discussed in Chapter 7.1 and is printed as cyan line. The EQE -ratio for an IR thickness of $t = 50$ nm is included as blue line, while the orange line is for the case of an infinitely thick IR. According to Fig. 8.31(a), the IR with $t = 50$ nm results in a strong absorption enhancement at $\lambda = 760$ nm while, simultaneously, just slightly decreased transmittance into the $\mu\text{c-Si:H}$ at $\lambda = 850$ nm. In the regime of long absorption length of a-Si:H ($\lambda > 700$ nm), the EQE -ratio exceeds values above 10. Resonances are found here. These resonances are due to coupling of the incident light into waveguide modes in the a-Si:H film [16, 18]. In the range of weak absorption, these waveguide modes are just slightly attenuated leading to such absorption enhancements. In this regime, the a-Si:H top cell can be interpreted as a waveguide [55, 195] which is resonant

to certain wavelengths. Increasing the IR thickness t , results in an increase of absorption enhancement according to Fig. 8.26. A strong absorption enhancement in the top cell in (a) is associated to a minimum of transmittance. In particular, the pronounced waveguide modes at $\lambda_m = 820$ nm, 860 nm, 980 nm and 1070 nm result in minima of transmittance. In case of an infinitely thick ZnO:Al IR, no photon tunneling occurs, so light with $\theta > \theta_{\text{TIR}}$ is totally internally reflected at the a-Si:H/ IR interface. Consequently, transmittance is close to 0 at these wavelength as most part of the light in the a-Si:H film exhibits a parallel wave vector component above θ_{TIR} . By decreasing the ZnO:Al layer thickness to $t = 114$ nm and 50 nm, the absorption enhancement in the particular waveguide modes is decreased, and transmittance into the $\mu\text{c-Si:H}$ bottom cell is increased. In this case, transmission is realized by the above describe photon tunneling process resulting in an exponential dependence from the IR thickness.

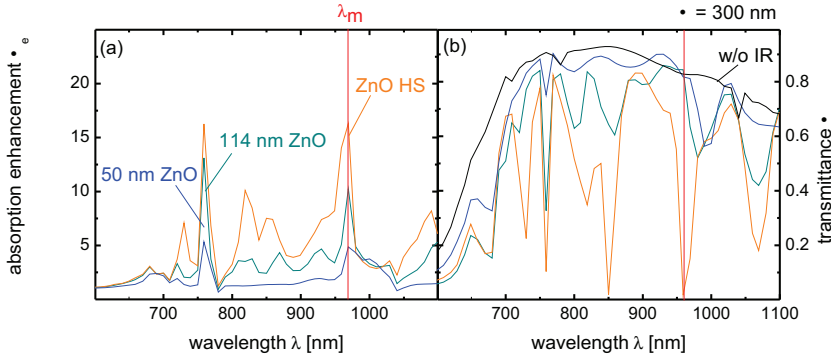


Figure 8.31.: (a) Top cell absorption enhancement $A = \frac{EQE_{\text{top,IR}}}{EQE_{\text{top,w/o}}}$ in a-Si:H top cell with $t = 50$ nm (blue), $t = 114$ nm (cyan) thick ZnO:Al IR and an infinite ZnO:Al half space (orange) for a grating height of $h = 300$ nm. (b) Transmittance into the $\mu\text{c-Si:H}$ bottom cell without IR (black), with $t = 50$ nm (blue) and $t = 114$ nm (cyan) thick ZnO:Al IR, as well as, into an infinite ZnO:Al half space (orange).

One resonant mode at $\lambda = 980$ nm is indicated as λ_m by the red line in Fig. 8.31(a) and is exemplarily investigated in detail in the following. The electric field distribution of the a-Si:H top cell with 114-nm-thick ZnO:Al IR for the wavelength $\lambda_m = 980$ nm and at an adjacent wavelength with weak absorption enhancement ($\lambda = 960$ nm) is taken and evaluated by FFT. The concerning scattering intensity in the a-Si:H layer SI is plotted in Fig. 8.32. It is observed that in the resonance

of the waveguide mode, contributions into the second diffraction order ($\theta = 68^\circ$) increase significantly in accordance to Section 7.1.

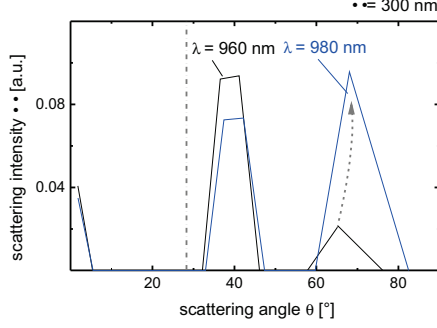


Figure 8.32.: Scattering intensity SI into the diffraction angles θ for the periodic triangular surface texture of $h = 300$ nm and a ZnO:Al half space for $\lambda = 960$ nm (black line) and 980 nm (blue).

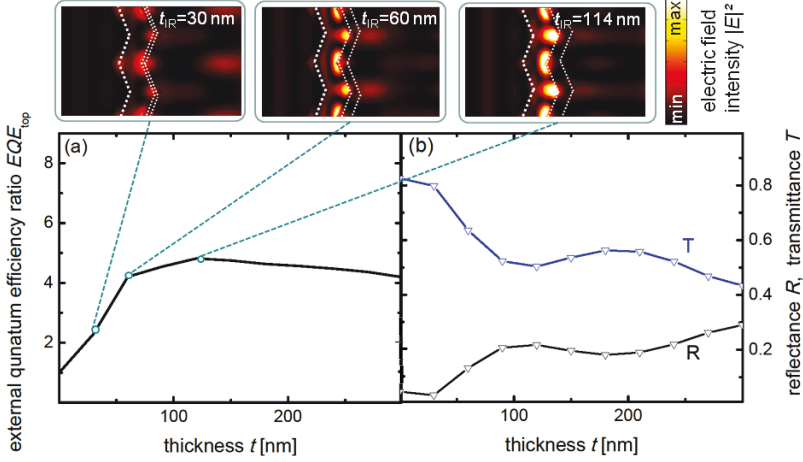


Figure 8.33.: (a) External quantum efficiency EQE_{top} for $\lambda = 980$ nm for increasing IR thickness of a tandem cell on $h = 300$ nm triangular grating. (b) Reflectance (R , black line) and transmittance (T , blue line) of the tandem cell system from (a) at $\lambda = 980$ nm. Inlets above the graph show cross sections of the rigorous optical simulations for IR thicknesses of $t_{IR} = 30$ nm, 60 nm and 114 nm.

As the waveguide modes are excited by the front and back grating, the wave vector transfer from the grating can also lead to an outcoupling or leaking of the waveguide. In Fig. 8.33(a), the absorption enhancement in the top cell for $\lambda = 980$ nm is shown for increased IR thickness t . The absorption enhancement increases monotonically induced by the increase in IR reflectance shown in Fig. 8.20(b). The insets in Fig. 8.33 show cross sections of the simulated electric field intensity for IR thicknesses of $t_{\text{IR}} = 30$ nm, 60 nm and 114 nm. With increase of the IR layer thickness, the top cell acts as cavity and leads to the excitation of a waveguide mode in the top cell. The reflectance R (black line) into glass half space and transmittance T (blue line) into the $\mu\text{-Si:H}$ bottom cell are shown in Fig. 8.33(b). Reflectance shows the same increase with increasing IR thickness. The transmittance which is around 90% without IR decreases dramatically with the IR thickness up to 48 % at $t = 100$ nm, reaches a local maximum at $t = 180$ nm and slowly decreases for larger thicknesses. The curve progression indicates a superposition of the reflection modes of Fabry-Perot reflectance (A) and total internal reflection (B) from Section 8.3. Increasing the IR thickness, results in a discrimination of photon tunneling. Evanescent wave-coupling to the $\mu\text{-Si:H}$ bottom cell is reduced and for $t > 110$ nm, leaking out into the ambient is the more probable loss channel. A schematic illustration of the waveguide mode in the top cell and the involved processes is presented in Fig. 8.34. Incident light (white arrow) is diffracted by the TCO front grating (1) and coupled to the waveguide mode (2) if the wave vector transfer k_{\parallel} meets the condition of the waveguide mode (Eq. 4.28). The waveguide mode is illustrated as red curve indicating maxima and minima. A further wave vector transfer can couple out the wave to the ambient (red arrow to the left) (4) where it is measured as reflected light. Depending on the thickness of the IR, the waveguide mode may leak into the IR, where it decays exponentially. For a thick IR, top and bottom cell are de-coupled and no photon tunneling happens. If the IR thickness is $t \ll \lambda$, the evanescent wave has not yet decayed to 0 and light tunnels through the IR (3).

To achieve a spectrally selective IR as a selective tunneling barrier according to Chapter 6, a high reflectance in range II ($500 \text{ nm} < \lambda < \lambda_c$) and a low reflectance in range III ($\lambda_c < \lambda < 1100 \text{ nm}$) is desirable. To quantify the spectral selectivity, the reflectance in wavelength range II and III is calculated and integrated in dependence of IR thickness t and angle of incidence θ . λ_c is the critical wavelength of the gain function for spectral selectivity (Section 6.1). The resulting quantity

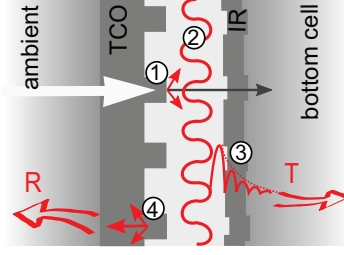


Figure 8.34.: Schematic sketch of the loss mechanisms from a waveguide mode. Light is diffracted at the front grating (1) and coupled to the leaky waveguide mode (2). By interaction with the grating, light can be diffracted out of the cell to the ambient (4, reflectance R) or tunnel through the IR into the bottom cell (3, transmittance T).

spectral reflectance parameter

$$SRP(t_{\text{IR}}, \theta) = \frac{1}{\Delta\lambda} \int_{500 \text{ nm}}^{\lambda_c} R(\lambda, t_{\text{IR}}, \theta) d\lambda \cdot \frac{1}{\Delta\lambda} \int_{\lambda_c}^{1100 \text{ nm}} (1 - R(\lambda, t_{\text{IR}}, \theta)) d\lambda \quad (8.5)$$

is a measure of the spectral reflectance of the IR. λ_c depends on the used materials and thicknesses and is chosen to be $\lambda_c = 670 \text{ nm}$ in accordance to Section 6.1. The SRP for a single layer with a refractive index $n_{\text{IR}} = 2$ is plotted over IR thickness t and angle of incidence θ in Fig. 8.35. The two reflection modes can be clearly identified. Below the critical angle of total internal reflection θ_{TIR} (mode (A)), an oscillating behavior of the spectral selectivity is found. It is found for the IR thickness of the second maximum of the Fabry Perot resonance. In accordance with Fig. 8.9, the second maximum of reflectance at $\lambda = 650 \text{ nm}$ coincides with the reflectance minimum at $\lambda = 900 \text{ nm}$. This results in a maximum of the reflectance ratio $R_{\text{II}}/R_{\text{III}}$ at $t = 220 \text{ nm}$ for normal incidence. The maximum is shifted to larger thicknesses by increasing the angle of incidence in accordance with Fig. 8.9. In case of reflectance mode (B), a clear trend can be formulated: **Best spectral selectivity is found for thin IRs which provide a trade-off between sufficient top cell light trapping and low parasitic reflectance below the top cell band gap energy.** The parasitic reflectance in the spectral range III rises by an increase of IR layer thickness or angle of incidence. Large k_{\parallel} -components, like in case of waveguide modes in the top cell, results in reflection losses.

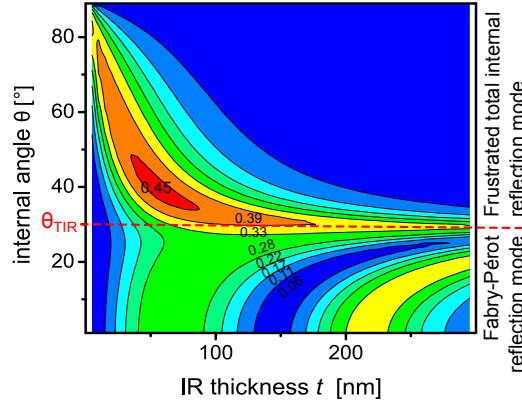


Figure 8.35.: Spectral reflectance parameter SRP in dependence of the angle of incidence θ and IR thickness t . The red line indicates the critical angle of total internal reflection θ_{TIR} .

Regarding the top cell in a tandem solar cell as a nano-optical device, the excitation of waveguide modes play a decisive role in generating light trapping in the top cell. However, this section reveals that these leaky waveguide modes below the band gap of the top cell absorber result in reflection losses. Light coupled to waveguide modes of the top cell is preferably coupled to the ambience. The IR thickness has to be carefully chosen in order to permit photon tunneling into the bottom cell. Tuning the IR thickness to the diffraction orders facilitates a good spectral selectivity as a trade-off between good top cell light trapping and low reflection losses.

8.5.5. Influence of the Refractive Index of the IR on Absorption Enhancement

The absorption enhancement in the top cell of thin-film tandem solar cells with IR strongly depends on the refractive index of the IR. Chapter 5 showed that a lower refractive index of the IR results in higher reflection and, thus, a higher gain of top cell short-circuit current density. In this section, the influence of the refractive index of the IR on

8. Interplay of Intermediate Reflector and Surface Texture

the previously described theory is studied.

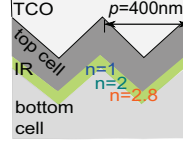


Figure 8.36.: Sketch of the triangular grating studied in this Section. The refractive index of the IR n_{IR} is varied for fixed tandem cell geometry.

Taking the triangular front grating with $p = 400$ nm, $h = 200$ nm and a flat IR, the scattering intensity SI within the a-Si:H top cell is simulated for a flat a-Si:H/air (blue line) and a-Si:H/ZnO:Al interface (cyan line) at $\lambda = 700$ nm. A scheme of the geometry is shown as inset in Fig. 8.37(b). The air and ZnO:Al is implemented as half space in this simulation. The scattering intensity SI within the a-Si:H top cell is shown in Fig. 8.37(a). Vertical dotted lines indicate the angle of total internal reflection θ_{TIR} for the a-Si:H/air (blue) and a-Si:H/ZnO:Al (cyan) interface. The highest intensity is found in the first diffraction order associated to an angle of 24° independent of the refractive index of the half space. The intensity is decreased by increasing the refractive index. This happens due to (i) a decrease of the reflectance of the IR and (ii) an increase of θ_{TIR} allowing more light to couple out of the a-Si:H film.

Figure 8.37(b) shows the electric field intensity $|E_{z,total}|^2$ behind the a-Si:H layer depending on the distance d from the interface at $\lambda = 700$ nm. $|E_{z,total}|^2$ decays exponentially with the distance. $|E_{z,total}|^2$ of the a-Si:H/ air configuration is indicated as blue line and the a-Si:H / ZnO:Al interface as cyan line. Two important conclusions can be drawn: (i) $|E_{z,total}|^2$ at the interface is much higher for the air medium ($|E_{z,total}|^2(0) = 0.23$) than in ZnO:Al ($|E_{z,total}|^2(0) = 0.13$). (ii) The decay asymptotically approaches a value $|E_{z,total}|^2(\infty)$. The decay in case of the a-Si:H / air interface is steeper and decays to $|E_{z,total}|^2(\infty) = 0.03$ while in the ZnO:Al half space, $|E_{z,total}|^2(\infty) = 0.11$. The electric field intensity at the interface splits up into two different parts:

- $|E_{prop}|^2 = |E_{z,total}|^2(\infty)$ is the propagating part of the light with $k_{||} < |k|$ in the a-Si:H film in Fig. 8.37(a).

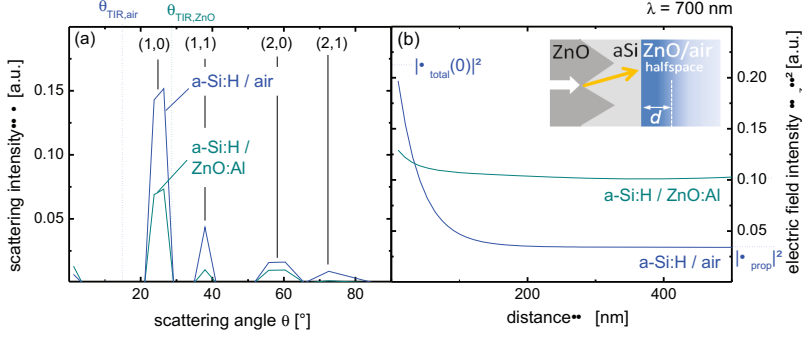


Figure 8.37.: (a) Scattering intensity SI within the $a\text{-Si:H}$ top cell layer for a $h = 200$ nm triangular diffraction grating and a flat $a\text{-Si:H} / \text{air}$ (blue) and $a\text{-Si:H} / \text{ZnO:Al}$ interface (cyan) at $\lambda = 700$ nm. (b) Decay of the electric field intensity $|E_{z,\text{total}}|^2$ at $\lambda = 700$ nm behind a flat $a\text{-Si:H} / \text{air}$ (blue) and $a\text{-Si:H} / \text{ZnO:Al}$ interface (cyan) in distance d from interface. The lines show exponential fits.

- $|E_{\text{evan}}|^2 = |E_{z,\text{total}}(0) - E_{\text{prop}}|^2$ is the evanescent part of the light in the $a\text{-Si:H}$ film with $k_{\parallel} > |k|$.

A reduction of the refractive index of the IR results in a decrease of θ_{TIR} to $\theta_{\text{TIR,air}} = 14^\circ$. In this case, the first diffraction order (1,0) ($\theta_1 = 24^\circ$) is above θ_{TIR} and, thus, totally internally reflected at the interface. In case of the $a\text{-Si:H} / \text{air}$ interface, E_{prop}^2 is low ($E_{\text{prop}} = 0.03$) and represents the intensity which is found in the (0,0) diffraction order within the $a\text{-Si:H}$ film. In case of the $a\text{-Si:H} / \text{ZnO:Al}$ interface, the (1,0) diffraction order is $\theta < \theta_{\text{TIR,ZnO}}$ and, thus, propagates into the ZnO:Al half space.

To investigate the behavior within a tandem solar cell, the ZnO:Al half space is replaced by a ZnO:Al IR with thickness t and a bottom cell half space is added. Figure 8.38(a) shows the external quantum efficiency EQE_{top} at $\lambda = 700$ nm of a top cell for varied IR thickness t , while the transmittance into the $\mu\text{-Si:H}$ bottom cell is shown in (b). EQE and transmittance T for the ZnO:Al IR are printed in cyan, while the curves for the air IR are shown in blue. In comparison to Fig. 8.37, the IR in this case is not flat, but conformal to the front texture. For a sufficiently thick IR ($t = 300$ nm), the transmittance T into the bottom cell corresponds to the transmittance into the $\text{ZnO:Al} / \text{air}$ half space discussed in Fig. 8.37(b). Due to the additional large-angle facets of the IR, the percentage of light which is totally internally reflected is increased like discussed in Section 8.5.2.

The transmittance T is reduced to 0 in case of the air IR for $t > 200$ nm. The EQE -curve does not show interference effects but a monotonic increase up to $t = 150$ nm before a slight decrease is present. In case of the ZnO:Al IR, the EQE increases less and a weakly pronounced oscillation with the maximum at $t = 110$ nm is found (corresponding to Fig. 8.28(c)). Oscillation minima and maxima are also found in the transmission curve in Fig. 8.38(a), but just slightly pronounced. The transmittance of $T(\infty) = 0.32$ for $t > 250$ nm corresponds to the propagating part of the electric field intensity $|E_{\text{prop}}|^2$. In contrast to the air IR, the first diffraction order is not totally internally reflected and is not directly trapped in the a-Si:H film, but propagates into the IR.

Analogous to Fig. 8.28, the IR thickness dependency of the intensities in the distinct diffraction orders $(l, m) = (0, 0), (1, 0), (1, 1), (2, 1)$ in the a-Si:H film are shown for an air IR ($n = 1.0$) in Fig. 8.39(a). Here, the EQE_{top} at $\lambda = 700$ nm of a tandem solar cell on triangular front texture with $h = 200$ nm is plotted against the thickness t of an air IR (blue symbols). In (b) the scattering intensity SI into certain diffraction orders within the a-Si:H film at a wavelength of $\lambda = 700$ nm is shown.

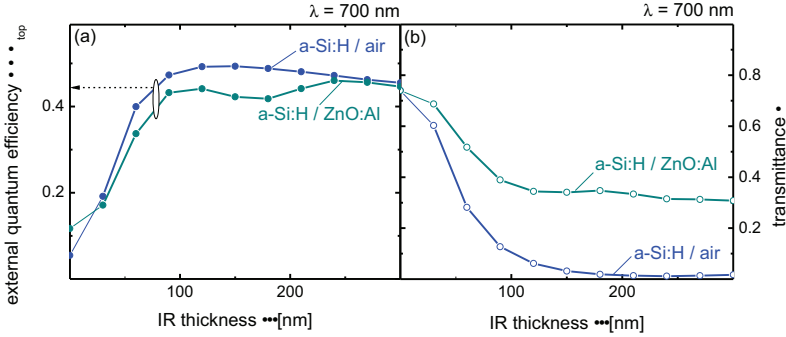


Figure 8.38.: (a) EQE_{top} at $\lambda = 700$ nm of a tandem solar cell on triangular front texture with a height $h = 200$ nm depending on the thickness t for an air IR (blue symbols) and a ZnO:Al IR (cyan symbols), respectively. (b) Transmittance T at $\lambda = 700$ nm into the $\mu\text{c-Si:H}$ bottom cell for a tandem cell with air IR (blue symbols) and ZnO:Al IR (cyan symbols).

The scattering intensity SI in Fig. 8.39(b) is similar to that of the ZnO:Al IR (Fig. 8.28) for thin IRs. But while the intensity in the first diffraction order

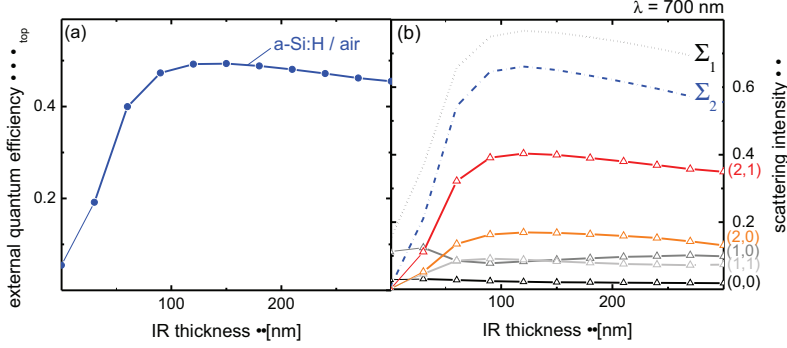


Figure 8.39.: (a) EQE_{top} at $\lambda = 700$ nm of a tandem solar cell on triangular front texture with a height $h = 200$ nm dependent on the thickness t of an air IR. (b) IR thickness dependent scattering intensity SI into the certain diffraction orders indicated in Fig. 8.27 within the a-Si:H top cell absorber at a wavelength of $\lambda = 700$ nm. The sum of all SI Σ_1 is shown as black dotted line. The sum of all SI with $\theta > \theta_{TIR}$ Σ_2 is shown as black dash-dotted line.

increases in the case of the ZnO:Al IR in Fig. 8.28, it decreases for the air IR with increasing thickness. This light is redistributed to higher diffraction orders in the waveguide. As a result, the intensities of the diffraction orders (1,1) and (2,1) increase. The sum of all diffraction orders Σ_1 is shown as black dotted line while the blue dash-dotted line shows the sum Σ_2 of all diffraction angles with $\theta > \theta_{IR}$. In agreement with Chapter 7.1, the amount of light within the a-Si:H film which exhibits angles above θ_{TIR} , contributes to top cell enhancement and, thus, to an increase of EQE_{top} . The thickness-dependent behavior of Σ_1 is, however, similar as the specular light (0,0) just leads to a thickness-invariant offset. The EQE_{top} and transmittance T of a tandem cell stack with μc -Si:H half space and varied IR refractive index from $n_{IR} = 1.0$ to 2.7 are shown in Fig. 8.40(a) and (b), respectively for an IR thickness of $t = 50$ nm ($n_{IR} = 1$ (blue), 1.8 (light gray), 2.0 (cyan) and 2.7 (gray)). For decreasing n , the EQE enhancement in the top cell is increased, in particular at the top cell waveguide resonance wavelengths (e.g. $\lambda = 700$ nm). On the other hand, at these particular wavelengths, the transmittance is decreased by reduction of n_{IR} as more light is already trapped in the top cell.

The short-circuit current density J_{sc} is calculated from the EQE using Eq. 4.48 and the increase of short-circuit current density by the IR ΔJ_{sc} is calculated. An upper limit approximation of EQE_{bot} is done using the Tiedje limit (Eq. 4.46).

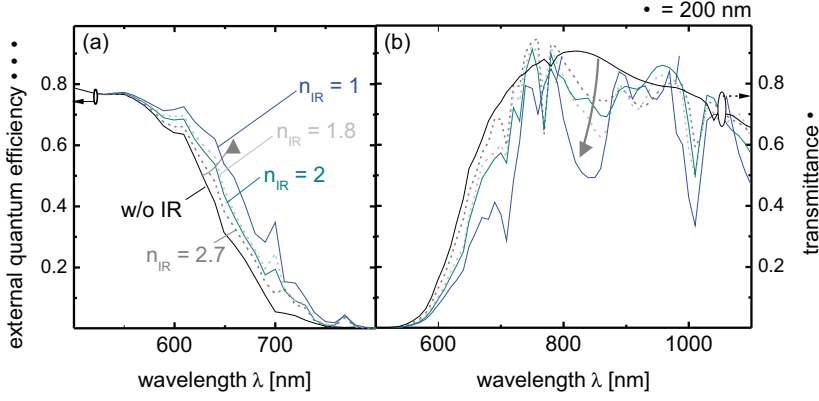


Figure 8.40.: (a) EQE_{top} over the wavelength λ of a tandem solar cell on triangular front texture with a period $p = 400$ nm, height $h = 200$ nm and $t_{IR} = 50$ nm depending on the refractive index of the IR ($n_{IR} = 1$ (blue), 1.8 (light gray), 2.0 (cyan) and 2.7 (gray)). The transmittance into the bottom cell T for the same configuration .

For comparison $J_{sc,top}$ and $J_{sc,bot}$ considering a Lambertian distribution of angles in the top cell is calculated. Figure 8.41 shows the top cell gain $\Delta J_{sc,top}$ (a) and total cell J_{sc} -loss $\Delta J_{sc,sum}$ (b). Red dots show the results from rigorous simulations, the Lambertian curve is shown in cyan. A linear increase of top cell J_{sc} -gain by decreasing the refractive index is identified for this particular grating. For the total cell loss, a similar correlation is found allocating higher $J_{sc,sum}$ -losses to lower n .

It can be concluded that a careful choice of the IR material depending on the diffraction orders or $k_{||}$ components, makes it possible to shift the critical angle of total internal reflection and, thus, the fraction of light in reflection mode (A) and (B).

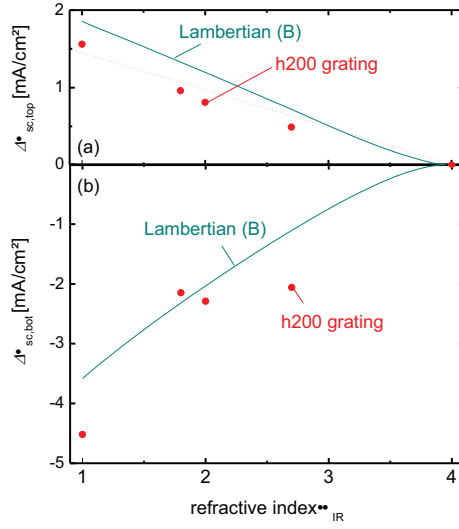


Figure 8.41.: (a) Top cell short-circuit current density gain $\Delta J_{sc,top}$ by different refractive indices of the intermediate reflectors n_{IR} on triangular grating with $h = 200$ nm (red triangles) with $t_{IR} = 50$ nm and considering a Lambertian angular distribution (cyan line). (b) Total tandem solar cell short-circuit current density loss $\Delta J_{sc,sum}$ for $h = 200$ nm grating and a Lambertian angular distribution (cyan line).

8.5.6. Figure of Merit for Spectral Selectivity

In the previous sections, the influence of IR layer thickness, refractive index and texture have been discussed. The issue of optimizing the spectral selectivity of the IR has already been raised in the last section. A quantity containing all this information seems necessary to evaluate evanescent coupling IRs.

In the previous sections, the periodic triangular grating has been used to identify the influence of IR texture height, waveguide geometry, front texture height, IR thickness and refractive index on the optics of tandem solar cells with intermediate reflectors. By changing the height of the grating with a constant grating period, the diffraction efficiency and coupling into certain waveguide modes of the a-Si:H film could be tuned. The reflection behavior of the IR basically breaks down on how much diffraction goes beyond the critical angle of total internal reflection θ_{TIR} . In case of a grating height $h = 100$ nm where most light is found in angles $\theta < \theta_{\text{TIR}}$, light propagates into the IR and reflectance is caused by interference (Fabry-Perot reflection mode (A)). As a consequence, the back-reflection into the top cell depends on the IR/bottom cell interface. If the IR is replaced by a ZnO:Al half space, reflection into the top cell should be low (just remaining Fresnell reflection at the interface). The $h = 300$ nm grating works in reflection mode B (TIR) as diffraction efficiencies into large diffraction orders are high and a large amount of light is coupled into waveguide modes. The thickness of the IR determines in reflection mode B how much light is able to tunnel into the bottom cell. A ZnO:Al half space behind the a-Si:H film results in the suppression of photon tunneling and, finally, a total back reflection and a maximum of light absorption in the top cell.

Equation 4.48 is used to calculate J_{sc} from EQE_{top} for the triangular grating with $p = 400$ nm and $h = 100$ nm, $h = 200$ nm and $h = 300$ nm. Figure 8.42(a) shows the top cell short-circuit current density gain $\Delta J_{\text{sc,top}}$ on a triangular grating texture of $h = 100$ nm (blue triangles), $h = 200$ nm (red triangles) and $h = 300$ nm (cyan diamonds). A $t = 50$ nm air- and ZnO:Al IR, as well as, a 114 nm-thick ZnO:Al IR, the ZnO:Al half space, as well as a perfectly electric conductor are shown. Dotted and dash-dotted lines are guides to the eye. Furthermore, the Tiedje law (Eq. 4.46) is used to determine the EQE_{bot} of a $t = 2$ μm bottom

cell from transmittance and the short circuit current density J_{sc} is calculated by Eq. 4.48. The bottom cell loss is calculated as $\Delta J_{sc} = J_{sc,w/o\ IR} - J_{sc,IR}$ and presented in (b). (c) shows $\Delta J_{sc,sum}$ summing up losses and gains in the sub cells.

Tandem solar cells on each substrate behave differently depending on the grating height h . $\Delta J_{sc,top}$ increases with increasing IR thickness up to roughly $t = 100$ nm which is in accordance to the observations in Section 8.5.3. As in Section 8.5.3, the maximal top cell gain is increased by larger grating height. Bottom cell losses are in accordance to this. As a results, the sum of sub cell currents is independent of the grating height and directly depending on the thickness of the IR. If the IR is substituted by an infinite ZnO:Al half space (HS, fourth column), the discussion above is consolidated and the different reflection modes can be distinguished. In case of the tandem cell on $h = 300$ nm (reflection mode (B)), $J_{sc,top}$ rises asymptotically with t and reaches its maximum in case of the ZnO:Al half space. In contrary, $\Delta J_{sc,top}$ for the grating with $h = 100$ nm (reflection mode (A)) reaches its maximum for $t = 114$ nm and is minimal in case of the ZnO:Al half space (nearly reaches 0). The back reflection which is released by the IR thickness-dependence of the interference of the incoming and reflected wave is not found in this case as no back interface is present. The bottom cell loss shown in Fig. 8.42(b) for the ZnO HS is calculated in the same way as before by Eq. 4.46 from the transmittance. In this case, the transmittance into the ZnO:Al half space is used to quantify and compare losses. As IR thickness is larger than the wavelength, this incoherent reflectance is a valuable approximation. The gains and losses for tandem cells on $h = 200$ nm are between $h = 100$ nm and $h = 300$ nm indicating that light is partly specularly transmitted (reflection mode (A)), while another part is totally internally reflected (reflection mode (B)). Overall, losses predominate the gain as **every back reflection is associated with a reflection loss** either by incomplete light trapping in reflection mode (A) or parasitic light trapping in reflection mode (B).

As EQE_{top} and EQE_{bot} both shall be maximized, as a figure of merit FOM , the ratio $-\frac{\Delta J_{sc,top}}{\Delta J_{sc,sum}}$ is proposed in Fig. 8.43. The FOM is 0 in case of no IR absorption enhancement is present and increases for an increased absorption enhancement. The top cell gain is weighted by the loss of $J_{sc,sum}$ in order to ensure minimal parasitic losses. For a thick IR like $t = 114$ nm and the half space, top cell gains are strongly overcompensated by the losses which are mainly due to reflection. A thin ZnO:Al IR with $t = 50$ nm in combination with a large-angle substrate

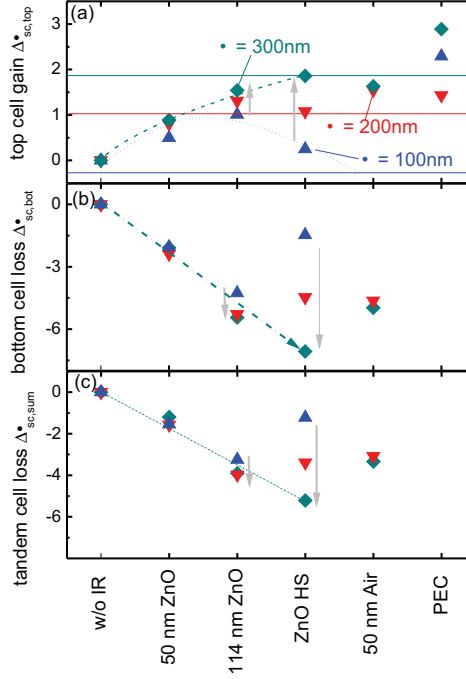


Figure 8.42.: (a) Top cell short-circuit current density gain $\Delta J_{sc,top}$ by different intermediate reflectors on triangular grating with grating period of 400 nm and grating heights $h = 100$ nm (blue triangles), 200 nm (red triangles) and 300 nm (cyan diamonds). (b) Bottom cell short-circuit current density loss $\Delta J_{sc,bot}$ for the same structures. (c) Total tandem solar cell short-circuit current density loss $\Delta J_{sc,sum}$ for the discussed structures.

reaches a maximal FOM of 0.74. This is in agreement to literature from EPFL where the higher reflection losses by thicker IRs have also been reported by various groups [43, 45, 59].

To ensure that this thickness of $t = 50$ nm fits the figure of merit criterion indeed the best, further simulations with the tandem solar cell on triangular grating with $h = 300$ nm were performed applying various IR thicknesses. The resulting $FOM = -\frac{\Delta J_{sc,top}}{\Delta J_{sc,sum}}$ is presented in Fig. 8.44. The FOM increases with the IR thickness t up to 50 nm and then rapidly drops due to an increase of losses in $J_{sc,sum}$. This shows that an IR thickness of $t = 50$ nm ($n_{IR} = 2$), in reflection mode

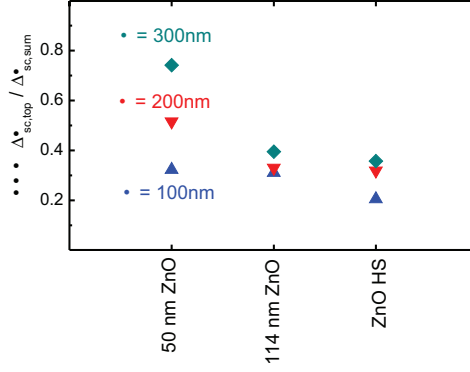


Figure 8.43.: Figure of merit $FOM = -\frac{\Delta j_{sc,top}}{\Delta j_{sc,sum}}$ for various IRs and a triangular grating texture with period $p = 400$ nm and height $h = 100$ nm (blue), $h = 200$ nm (red) and $h = 300$ nm (cyan).

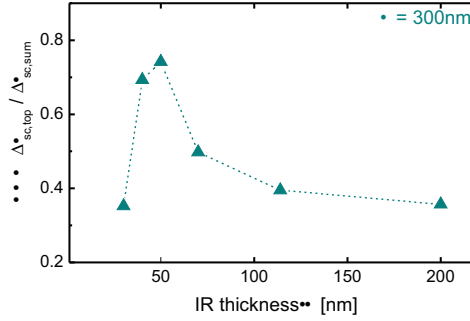


Figure 8.44.: Figure of merit $FOM = -\frac{\Delta j_{sc,top}}{\Delta j_{sc,sum}}$ depending on IR thickness t and a triangular grating with period $p = 400$ nm and height $h = 300$ nm (cyan).

(B) of total internal reflection, results in the best trade-off between back reflection and, thus, coupling into leaky waveguide modes in the top cell and transmission into the bottom cell. It is noticed, however, that in case of the absence of an IR, FOM will be 0 which would indicate a loss-less transfer of current from bottom to the top cell. A loss of potential bottom cell current due to a transmittance $T < 1$ into the bottom cell is inherent if total internal reflection is present (reflection mode (B)). On the other hand, tandem cells with low front scattering for which Fabry-Perot reflection is the dominating process (triangular grating $h = 100$ nm, APCVD

SnO₂:F, sputter-etched ZnO:Al), suffer from incomplete light trapping in the top cell and do not reach high top cell short-circuit current densities. As a quantity for light trapping, the integrated scattering intensity ISI has been introduced before. For the triangular grating, Fig. 8.28 showed the correlation between Σ_2 and the EQE_{top} -enhancement. It was further revealed that the portion of light with $k_{\parallel} > |k|$ are not transmitted into the bottom cell. For photon energies below the band gap of a-Si:H, this is however, not desirable. The criterion of the target function of spectral selectivity which has been demanded in Fig. 6.3 has to be extended by the parameter of the ISI . Figure 8.45 shows the target function for the optimization of spectral selectivity for IRs in tandem solar cells. Up to a target wavelength λ_c which is 670 nm in this case, reflectance R and integrated scattering intensity ISI have to be maximized, while a minimal R and ISI shall be reached for $\lambda > 670$ nm.

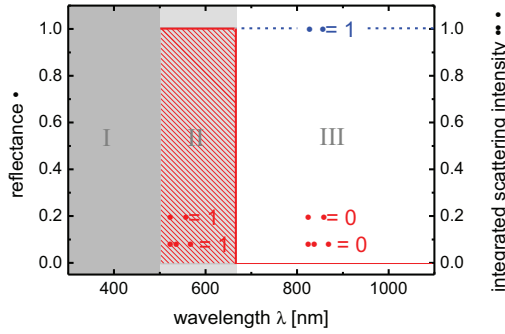


Figure 8.45.: Wavelength dependent target function for IR reflectance R and integrated scattering intensity in the top cell ISI .

This is in accordance to Lal et al. [62] where the maximum efficiency of tandem solar cells on base of a c-Si bottom cell has been calculated depending on the reflectance R of the IR and the light trapping cut-off frequency L_c of the top cell. It reveals that high scattering angles at the front side above the cut-off wavelength λ_c will be trapped in the top cell instead of being transmitted to the bottom cell. As top cell in such multi-junction devices, high current densities are favorable to gain current matching. Perovskite top cells are recently put into attention [?, 62, 63].

Examining the scattering intensity SI within the top cell is presented as a

powerful tool to determine the optimal refractive index and thickness of the IR. Figure 8.46 shows the scattering intensity in the a-Si:H top cell SI depending on the photon energy E_{ph} and the transverse wave vector $k_{||}$ in the a-Si:H top cell. SI is calculated from the electric fields in the simulated a-Si:H layer in analogy to Chapter 7. The intensity maxima are found at the $k_{||}$ value corresponding to the diffraction orders of the grating. The diagonal lines indicate the light escape cones assuming different IR materials with a refractive index of $n = 1$ (green), 1.8 (yellow), 2.0 (red) and 2.7 (blue). The white horizontal line is the cut-off energy E_c : For higher energies (shorter wavelengths) light trapping is beneficial and leads to a top cell gain, whereas for $E < E_c$, a good top cell light trapping results in losses for the bottom cell. The representation of the distribution of $k_{||}$ can be used to choose the optimum refractive index of an IR defining the escape cone and θ_{TIR} , respectively.

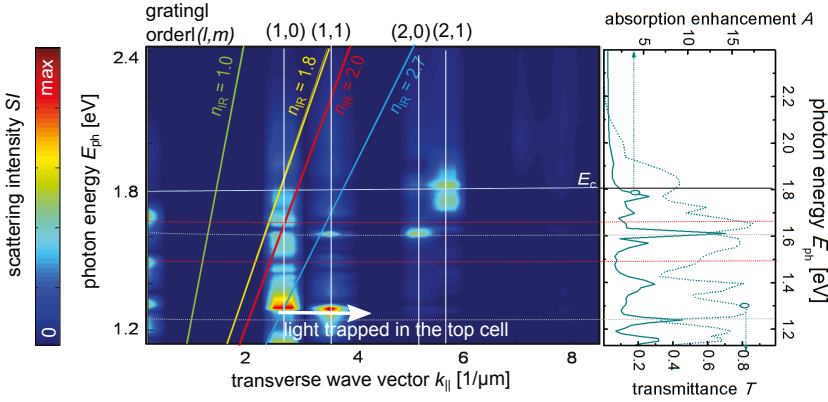


Figure 8.46.: Scattering intensity within the a-Si:H top cell on $h = 300$ nm triangular grating structure depending on the photon energy E_{phot} and the transverse wave vector $k_{||}$. The colored lines indicate the dispersion relation of the Si/ IR interface for certain IR materials of a refractive index of $n = 1$ (green), 1.8 (yellow), 2.0 (red) and 2.7 (blue). The cut-off energy E_c indicates the limiting energy for which light trapping in the top cell (range I + II) is relevant and when this light trapping should be minimal for maximized transmittance (range III).

This section reveals that no gain in the top cell can be generated without losses for the total tandem cell short-circuit current density $J_{\text{sc,sum}}$. These happen either due to incomplete light absorption of back reflected light in the top cell (small feature height, $h = 100$ nm) or a mitigation of transmission into the bottom cell by coupling into leaky waveguide modes in the top cell below the band gap of the top cell absorber (large feature height, large surface angles, heights). To find the best compromise in case of current-matching, the IR refractive index and thickness has to be carefully optimized to a given substrate morphology. The introduced Figure of Merit $\frac{\Delta J_{\text{sc,top}}}{\Delta J_{\text{sc,sum}}}(t)$ exhibits a maximum for an IR thickness of $t = 50$ nm in case of the $h = 300$ nm grating.

8.6. From Periodic to Random Textures

The examination of well-defined periodic structures enabled a detailed analysis of the dependency of the intermediate reflector effectiveness for particular substrates. Coming back to the starting point of this chapter, observed findings shall now be applied to randomly textured substrates, i.e. LPCVD ZnO:B.

For the investigated periodic gratings, leaky waveguide modes induce absorption enhancement and prevent transmission into the bottom cell as shown and discussed in Fig. 8.31(Section 8.5.4). For randomly textured surfaces like LPCVD ZnO:B reflectance and transmittance spectra are continuous and no particular resonances are found (Fig. 8.1). Figure 8.47 shows the cell reflectance R (a) and transmittance T into the bottom cell (b) of tandem cells on a triangular grating with $p = 400$ nm and $h = 300$ nm (cyan circles, dotted line). Additionally, reflectance and transmittance of the tandem cell on LPCVD ZnO:B texture are plotted as full cyan lines in (a) and (b). Reflectance and transmittance curve of LPCVD ZnO:B traverses through the turning points of the curves for periodic textures. The randomly textured surface combines a broad distribution of different periods and heights of pyramids. Well-pronounced waveguide modes with high cavity modes are broadened by a continuum of states as already reported in Chapter 7. The scattering intensity within the a-Si:H layer SI is shown in Fig. 8.48 for a-Si:H

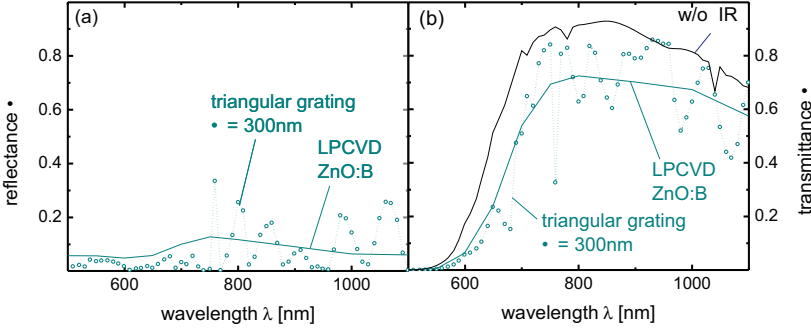


Figure 8.47.: (a) Reflectance R of the tandem solar cell on triangular grating with period $p = 400$ nm and height $h = 300$ nm (cyan triangles + dotted line), as well as on LPCVD ZnO:B texture (full cyan line). (b) Transmittance into $\mu\text{c-Si:H}$ bottom cell with $t = 114$ nm ZnO:Al IR on LPCVD ZnO:B (full cyan line) and grating (dotted cyan line).

top cells on on triangular grating with period $p = 400$ nm and heights $h = 100$ nm (blue dotted line) and $h = 300$ nm (cyan dotted) at $\lambda = 650$ nm. Furthermore, the SI is evaluated in a top cell on LPCVD ZnO:B texture (full cyan line). As the surface roughness of the texture is larger than the layer thickness $t_{\text{a-Si:H}}$, the complex electric fields in a 'plane' conformal to the a-Si:H/ IR interface are extracted and corrected by the phase collected by the surface topography (analogous to Section 4.1.4). Discrete grating orders of different pyramid sizes are broadened and peaks smear out into a continuous distribution. It is observed, that especially the large-angle components in the diffraction order (2,1) which have been attributed to the contribution of waveguide mode resonances (Chapter 7, Section 8.5.4) is suppressed in case of tandem solar cells on randomly textured surface.

In the following, the tandem solar cells on LPCVD substrate are simulated with different IR thicknesses. Figure 8.49 shows a comparison of the EQE_{top} (full lines) and transmittance T (dotted lines) of the tandem cells on ZnO:B texture without IR (black), with $t_{\text{IR}} = 50$ nm (blue) and $t_{\text{IR}} = 114$ nm (cyan). The 50 nm-thick ZnO:Al IR boosts the top cell EQE and induces just slight losses to transmittance into the bottom cell above $\lambda = 800$ nm due to its spectrally selective behavior. Increasing the IR thickness increases EQE_{top} and transmittance into the bottom cell. In accordance to Section 8.5.4, a larger IR thickness results in a decreased

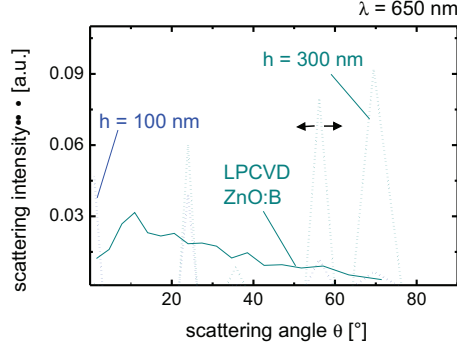


Figure 8.48.: Scattering intensity SI in the $a\text{-Si:H}$ film over scattering angle θ for top cell on LPCVD ZnO:B (cyan line) and on triangular grating of with period $p = 400$ nm and heights $h = 100$ nm (blue dotted line) and $h = 300$ nm (cyan dotted) at $\lambda = 650$ nm.

spectral reflectance parameter SRP .

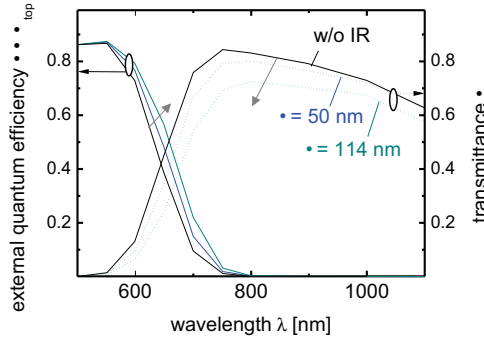


Figure 8.49.: External quantum efficiency EQE_{top} (full lines) and transmittance T into the $\mu\text{-Si:H}$ bottom cell (dotted lines) of the tandem solar cell on LPCVD ZnO:B front texture without IR (black), with a 50 nm (blue) and 114 nm IR (cyan). The dashed lines indicate the transmittance of the periodic system on $h = 300$ nm triangular grating.

Randomly textured surfaces lead to a broadening of leaky waveguide resonances which is similar to a smoothing of the EQE curves. However, it was seen that

it is crucial to regard the top cell as a nano-optical system which does not follow geometrical behavior of light propagation. In particular, waveguide modes in the top cell play a decisive role, both for top cell gain and bottom cell loss. They prevent that a highly reflective IR leads to a top cell with high optical confinement resulting in high transmission losses. For LPCVD ZnO:B, IR thicknesses of $t = 50$ nm provide a suitable compromise between top cell gain and bottom cell losses.

8.7. Summary and Discussion

In this chapter, a comprehensive model of the working principle of the interplay of texture and IR has been developed and applied to solar cells on periodic and randomly textured surfaces. The physical mechanisms of intermediate reflectors in tandem solar cells with nano-optical textures have been determined. A detailed behavior of nano-textured IRs, two different reflection modes have to be considered. Depending on the surface angles and angular distribution of light within the layer, reflection can take place either by (A) a Fabry-Perot-like constructive interference within the IR or (B) by total internal reflection at the a-Si:H/ IR interface. An analysis of the top cell as a leaky waveguide revealed that best top cell currents can be obtained if the grating/ front texture couples incident light effectively into leaky waveguide modes within the a-Si:H film. The a-Si:H film acts as a cavity, but further interaction with the front side grating can lead to an out-coupling of the light to the ambient. This happens particularly below the band gap of a-Si:H where the waveguide mode is not absorbed and results in a reduction of transmittance into the bottom cell. To increase the efficiency of tandem solar cells, light transmittance into the spectral range ($\lambda > \lambda_c$) has to be maximized. If the IR is sufficiently thin, top and bottom cell are evanescently coupled allowing for tunneling of photons from the a-Si:H waveguide into the bottom cell. As the evanescent decay constant is wavelength-dependent, high transmittance for long wavelengths can be achieved. For grating with high coupling efficiencies into large angles, an optimum IR thickness can be obtained by a trade-off between top cell enhancement and transmittance into the bottom cell. The waveguide model is valid for periodic gratings where discrete waveguide modes are excited. It has been extended to randomly textured surfaces where thin waveguide mode resonances are smeared out to a broad distribution of states in the a-Si:H film. The model was

compared to experimental data and rigorous optical simulations for the commonly used textures APCVD $\text{SnO}_2\text{:F}$, sputter-etched ZnO:Al and LPCVD ZnO:B , as well as to a periodic triangular grating texture. Surfaces with rather small surface angles α like APCVD $\text{SnO}_2\text{:F}$, sputter-etched ZnO:Al and gratings with low surface angles exhibit small k_{\parallel} -components resulting in the reflection mode (A). Tandem cells on this textures have been extensively studied by [44, 59] for APCVD $\text{SnO}_2\text{:F}$ and [49, 56, 59, 143, 196, 197] for sputter-etched ZnO:Al . The presented model is able to reproduce and explain the behavior of the IR in these studies and, furthermore, unifies it with large angle substrates like LPCVD ZnO:B [43, 45, 47, 165] or periodic structures [57, 198]. It is compatible with other comparative studies in [59, 199] and concepts like e.g. asymmetric or diffractive IRs [57, 200]. It is revealed that losses due to parasitic reflection are inevitable if the ideal reflectance and light trapping of the filter target function in Fig. 8.45 is not reached. These losses are, in particular, of interest for future high efficiency multi-junction concepts like tandems on base of crystalline silicon where a maximal transmittance into the bottom cell has to be secured. Spectrally selective intermediate reflectors, like developed in Chapter 6, provide a high transmittance, do, however, not work for large angle substrates inducing a strong front-side scattering [201] which results in total internal reflection (reflection mode (B)). To reduce transmission losses for these substrates, spectrally selective light trapping in the a-Si:H top cell is desirable. The investigated randomly textured surfaces, as well as periodic gratings exhibit high diffraction and coupling efficiencies to higher diffraction orders (than the zeroth) and, as a consequence, trap a large amount of light in the a-Si:H top cell above the angle of total internal reflection over a broad spectrum. Future works should identify structures with large scattering/diffraction efficiencies below a certain critical wavelength (λ_c) and weak scattering above. The combination of different textures at the front side and the IR like proposed by [57, 200] and discussed in Section 8.5.2, enables an independent optimization of light in-coupling at the front and diffraction into large angles at the IR or back side of the solar cell. In this case, the spatial differences in the IR thickness breaks down the clear definition of the reflection modes, as there is neither Fabry-Perot reflection (A), nor a constant photon tunneling.

8.7.1. Design Workflow For IR Optimization for Multijunction Solar Cells

Basing on the results of this Chapter, an optimized workflow for the design of IRs in tandem solar cells would be as follows:

- 1.) Simulate multi-junction on given substrate with unoptimized IR
- 2.) Extract scattering intensity SI within the layer as shown in Chapter 7
- 3.) Determine which reflection mode applies: Fabry-Perot reflection mode (A) or TIR reflection mode (B)
- 4.) Choose method to improve IR
in case of reflection mode (A): spectrally selective multilayer IR or in case of reflection mode (B): follow the following points:
- 5.) Choose critical angle of total internal reflection θ_{TIR} on basis of the SI according to the Section 8.5.5.
- 6.) Adjust the IR thickness to trade-off between top cell enhancement and reflection losses by maximizing the spectral reflectance parameter SRP Fig. 8.35

9. Summary and Outlook

Within this work, light management in silicon-based multi-junction solar cells by intermediate reflectors (IR) was studied. IRs get essential for light management, as soon as, the thickness of absorber layers in multi-junction devices is physically limited. In this case, IRs can be introduced to match the currents and power of the sub cells in series-connected multijunction solar cells. As each element added to a working device increases its complexity, the understanding and decrease of loss mechanisms is crucial to obtain an improvement of the device.

This work focusses on the analysis of the optics in multijunction solar cells. Thin-film silicon tandem solar cells made of hydrogenated amorphous and microcrystalline silicon (also called 'micromorph') were chosen as model system, as they are a well established, industrially up-scalable technology and exhibit the important characteristics of other multijunction cell material systems: Thin-film layers, nano-structured surfaces, as well as, physical limitations of thicknesses and a broad utilization of the solar spectrum. The combination of thin-film layer stack and nano-structured surfaces demands for a treatment of the solar cell as a nano-optical device. Motivated by the results of experimental studies, tandem solar cells are modeled by thin-film optics and rigorous optical simulations. An agreement between simulation to experimental results allows for an investigation and optimization of these devices.

First, the optical losses induced by intermediate reflectors in tandem solar cells were studied. Therefore, tandem solar cells without and with micro-crystalline silicon oxide intermediate reflectors were fabricated on different aluminum-doped zinc oxide front contacts which had partially been treated to decrease absorption within the zinc oxide. Increased cell reflectance and parasitic absorption due to the IR were observed. The comparison to tandem solar cells on non-treated front contacts showed that in spite of the increased reflectance, parasitic absorption in the front contacts due to the IR is negligible. The results are supported by optical simulations of tandem solar cells with intermediate reflector which, additionally,

allowed to quantify parasitic losses. Furthermore, it was shown that the decrease of the refractive index of the silicon oxide intermediate reflector results in a decrease of parasitic absorption and an increase of total tandem cell current if layer thicknesses are adapted. In this case, parasitic reflection of light by the IR out of the solar cell is determined to be the dominating optical loss mechanism.

Second, the reflection losses were assigned to the low spectral selectivity of reflection of single layer IRs. Basing on this, a 1D photonic crystal produced of conductive and low absorptive thin-film materials which are available in-situ in thin-film silicon solar cell production is designed for a flat layer stack. The influence of surface texture on the effectiveness of the multilayer IR is studied and it is shown that the IR functionality remains for a textured solar cell. A multilayer IR consisting of aluminum-doped zinc oxide (ZnO:Al) and microcrystalline silicon oxide($\mu\text{c-SiO}_x\text{:H}$) layers was successfully integrated into a nano-textured thin-film silicon solar cell and decreases the bottom cell losses in comparison to other IRs while still increasing the top cell current density by $\Delta J_{\text{sc,top}} = 1.2 \text{ mA/cm}^2$. A further optimization of material choice and layer quantity shows that top cell enhancement and spectral selectivity can be slightly increases by increasing the number of layers and increasing refractive index contrast.

Third, the light trapping in the top cell was investigated in detail. Therefore, a new method to extract the angular distribution of light within a thin amorphous silicon film from rigorous optical simulations was developed and applied to a-Si:H cells on both, periodic gratings and randomly textured front structures. For photonic structures, absorption in the silicon film is assigned to the coupling of incident light to leaky waveguide modes by the grating. It is shown that in case of silicon films on randomly textured surfaces, these waveguide modes are present, as well, but they are broadened due to the superposition of a variety of distinct periods and heights. As a quantity for light trapping in thin films, the integrated scattering intensity ISI could be established which describes the coupling to waveguide modes and correlates well to the absorption enhancement in a-Si:H film with different reflectors.

Fourth, absorption and transmission enhancements are investigated on a variety of periodic and randomly textured substrates. In a broad experimental and simulation study, tandem solar cells on various substrates have been deposited and reproduced by rigorous optical simulations. An artificial modification of the substrate texture, revealed the front texture scattering distribution and the surface

angles at the IR to be the decisive surface parameters to determine the effectiveness of the IR. A dependence of the functionality of the IR on the angular intensity distribution in the top cell is observed. In particular, two different reflection modes of the IR are observed: In reflection mode (A) below the critical angle of total internal reflection, light propagates into the IR and the reflectance depends on interference of the incident light and light reflected at the back IR interface. The effectiveness of the IR on surface textures comprising low surface angles and low parallel wave vector transfer as APCVD $\text{SnO}_2\text{:F}$ or sputter-etched ZnO:Al textures can be well reproduced by a thin-film model applying the angular scattering distribution at the front side. If the critical angle is surpassed, light is totally internally reflected and tunnels through the IR as an evanescent wave. This reflection mode (B) results in large absorption enhancements for thick intermediate layers but is always connected to reflection losses. A spectral reflectance parameter *SRP* was introduced. It was used as a tool to analyze the influence of IR refractive index and thickness on the absorption enhancement and bottom cell transmission losses. The theory is successfully applied to understand the interplay of front side texture and IR reflectance on the relevant randomly textured surfaces. The study of the IR effectiveness on photonic structures emphasized the importance to examine the waveguide modes, which do not just increase top cell enhancement, but further induce parasitic reflection losses in the NIR range which are disadvantageous to the current of further bottom cells. The analysis gives a hint that these losses can be decreased by broadening the resonances as it is the case in randomly textured solar cells. Simulations on tandem solar cells on LPCVD ZnO:B reproduce the results of previous experimental studies.

The model allows for the optimization of the IR on a given surface topography. In **future work**, this model should be used for a variety of multijunction concepts:

- Tandem solar cells on nano-imprinted periodic substrates.
- Thin-film Silicon-based quadrupole junction solar cells regarded as a disordered 1D photonic crystal.
- Crystalline Silicon based tandem solar cells with organic/perovskite top cells.

Until now, optical simulations are still de-coupled from electrical simulation part. Computationally extensive rigorous optical simulations are necessary to determine

the effectiveness of the IR. The implementation of scattering intensities and angular dependent reflection into optoelectronic device simulator (ASA) is one next step to be done.

The influence of disorder on waveguide modes in the top cell has been partially addressed in this work. The Fourier-based method for guided modes in the a-Si:H film is a powerful tool to investigate the influence of partially disordered systems and photonic quasi-crystals on the absorption in a-Si:H and in thin semiconducting films. Thus, a goal is to determine a trade off between periodicity and disorder for light management in multijunction solar cells.

Patterning the IR with a different texture has been shown to de-couple top and bottom cell light trapping while the remaining IR thickness accounts for the reflectance/ transmittance of the IR. Using nanoimprint lithography [202], the IR could be textured differently according to [57]. Especially, the usage of blazed gratings like proposed in [17] in combination with IRs is of large interest to facilitate a directionally selective light trapping and an improved guidance of light in the bottom cell.

A. Appendix

A.1. Optical Data

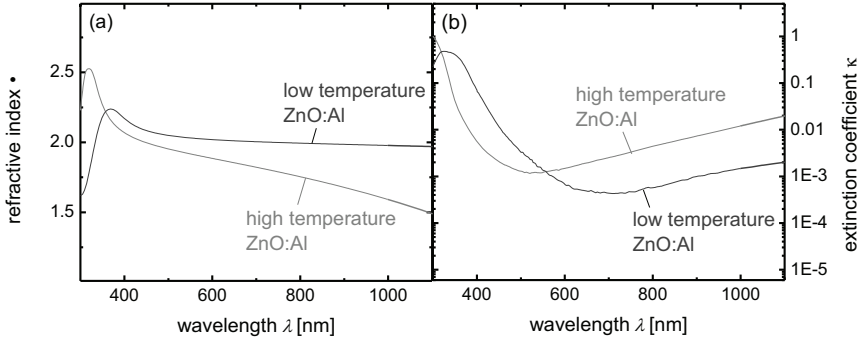


Figure A.1.: (a) Refractive index n of the ZnO:Al layers used for optical simulation within this work. Dark grey lines indicate the low temperature ZnO:Al, the highly conductive high temperature ZnO:Al is shown in light grey. (b) Extinction coefficient κ of the ZnO:Al layers used for optical simulation within this work.

A.2. FDTD simulations

The absorption cross section of a dielectric particle ($r = 100$ nm (red) and 200 nm (black)) of ZnO:Al was calculated using FDTD in the described resolution (symbols) and compared to analytically calculated absorption cross section using the freeware software 'MiePlot' [205] which implements Mie theory described in [206].

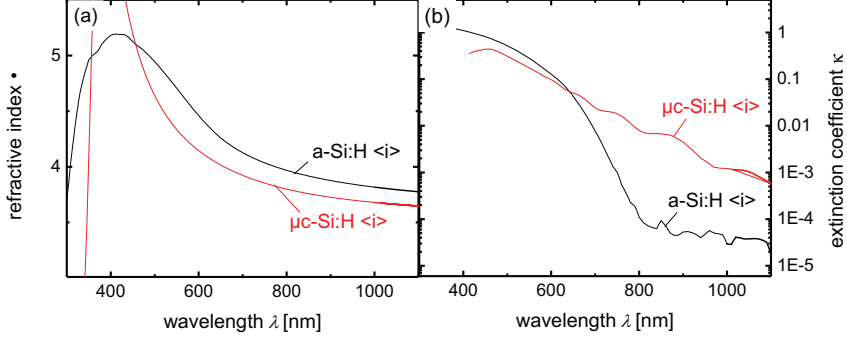


Figure A.2.: (a) Refractive index n of the intrinsic $a\text{-Si:H}$ (black) and $\mu c\text{-Si:H}$ (red) layers used for optical simulation within this work. (b) Extinction coefficient κ of the intrinsic $a\text{-Si:H}$, $\mu c\text{-Si:H}$ layers used for optical simulation within this work.

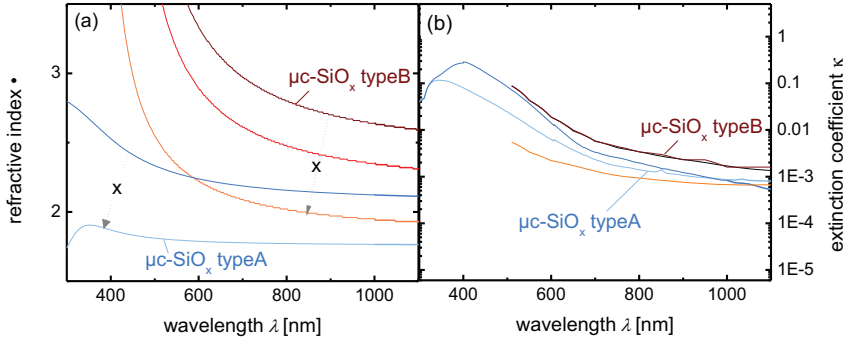


Figure A.3.: (a) Refractive index n of the different $\mu c\text{-SiO}_x\text{:H}$ layers used for optical simulation within this work. $\mu c\text{-SiO}_x\text{:H}$ is deposited in two different PECVD reactors (type A: 6-chamber system [49, 203, 204]; type B: large area system [189]). (b) Extinction coefficient κ of the $\mu c\text{-SiO}_x\text{:H}$ layers used for optical simulation within this work.

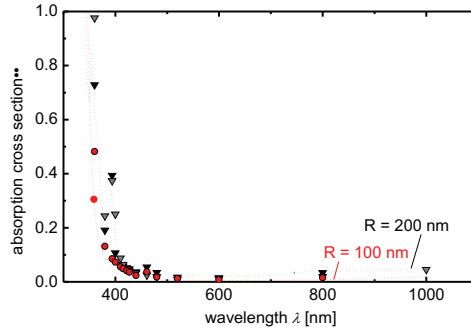


Figure A.4.: Absorption cross section Q of a ZnO:Al nanosphere with radius $r = 100$ nm (red) and 200 nm (black) determined from FDTD simulation (symbols) and from analytical Mie theory calculations [205, 206].

Bibliography

- [1] M. Z. Jacobson and M. A. Delucchi, *Providing all global energy with wind, water, and solar power, Part I: Technologies, energy resources, quantities and areas of infrastructure, and materials*, Energy Policy **39** (2011), 1154–1169.
- [2] R. Margolis, *SunShot Vision Study*, Tech. Report February, U.S. Department of Energy, 2012.
- [3] D. M. Chapin, C. S. Fuller, and G. L. Pearson, *A New Silicon p-n-junction Photocell for Converting Solar Radiation to electric Power*, Journal of Applied Physics **25** (1954).
- [4] M. A. Green, *Silicon Solar Cells*, Center for Photovoltaic Devices and Systems, Sydney, 1995.
- [5] Pvchange.org, *PVXChange*, <http://www.pvxchange.com>, 2014.
- [6] EPIA, *Global Market Outlook for Photovoltaics 2014-2018*, Tech. report, 2014.
- [7] B. für Energie und Wirtschaft, *Die Energie der Zukunft*, Tech. report, 2014.
- [8] Z. BW, *Press Releas 12/2014*, Tech. report, 2014.
- [9] Panasonic, *Press Release HIT Record Cell*, Tech. report, 2014.
- [10] W. Shockley and H. J. Queisser, *Detailed Balance Limit of Efficiency of p-n Junction Solar Cells*, Journal of Applied Physics **32** (1961), 510.
- [11] R. Brendel and H. Queisser, *On the thickness dependence of open circuit voltages of pn junction solar cells*, Solar energy materials and solar cells **29** (1993), 397–401.

- [12] U. Rau, U. W. Paetzold, and T. Kirchartz, *Thermodynamics of light management in photovoltaic devices*, Physical Review B **90** (2014), 035211.
- [13] H. Stiebig, N. Senoussaoui, C. Zahren, C. Haase, and J. Müller, *Silicon thin-film solar cells with rectangular-shaped grating couplers*, Progress in Photovoltaics: Research and Applications **14** (2006), 13–24.
- [14] K. R. Catchpole and M. A. Green, *A conceptual model of light coupling by pillar diffraction gratings*, Journal of Applied Physics **101** (2007), 063105.
- [15] M. Kroll, S. Fahr, C. Helgert, C. Rockstuhl, F. Lederer, and T. Pertsch, *Employing dielectric diffractive structures in solar cells - a numerical study*, Physica Status Solidi (a) **205** (2008), 2777–2795.
- [16] V. Ferry, M. Verschuuren, and H. Li, *Light trapping in ultrathin plasmonic solar cells*, Optics express **18** (2010), 237–245.
- [17] J. Gjessing, A. S. Sudbbo, and E. S. Marstein, *Comparison of periodic light-trapping structures in thin crystalline silicon solar cells*, Journal of Applied Physics **110** (2011), 033104.
- [18] U. W. Paetzold, E. Moulin, D. Michaelis, W. Böttler, C. Wächter, V. Hagemann, M. Meier, R. Carius, and U. Rau, *Plasmonic reflection grating back contacts for microcrystalline silicon solar cells*, Applied Physics Letters **99** (2011), 181105.
- [19] K. R. Catchpole, S. Mookapati, F. Beck, E.-C. Wang, A. McKinley, A. Basch, and J. Lee, *Plasmonics and nanophotonics for photovoltaics*, MRS Bulletin **36** (2011), 461–467.
- [20] H. Sai, K. Saito, and M. Kondo, *Investigation of Textured Back Reflectors With Periodic Honeycomb Patterns in Thin-Film Silicon Solar Cells for Improved Photovoltaic Performance*, IEEE Journal of Photovoltaics **3** (2013), 5–10.
- [21] M. Berginski, J. Hüpkens, M. Schulte, G. Schöpe, H. Stiebig, B. Rech, and M. Wuttig, *The effect of front ZnO:Al surface texture and optical transparency on efficient light trapping in silicon thin-film solar cells*, Journal of Applied Physics **101** (2007), 074903.

- [22] H. Sai, H. Jia, and M. Kondo, *Impact of front and rear texture of thin-film microcrystalline silicon solar cells on their light trapping properties*, Journal of Applied Physics **108** (2010), 044505.
- [23] S. Faỹ, J. Steinhäuser, S. Nicolay, and C. Ballif, *Polycrystalline ZnO: B grown by LPCVD as TCO for thin film silicon solar cells*, Thin Solid Films **518** (2010), 2961–2966.
- [24] O. E. Daif, E. Drouard, and G. Gomard, *Absorbing one-dimensional planar photonic crystal for amorphous silicon solar cell*, Optics express **18** (2010), 2092–2095.
- [25] G. Gomard, E. Drouard, X. Letartre, X. Meng, A. Kaminski, A. Fave, M. Lemiti, E. Garcia-Caurel, and C. Seassal, *Two-dimensional photonic crystal for absorption enhancement in hydrogenated amorphous silicon thin film solar cells*, Journal of Applied Physics **108** (2010), 123102.
- [26] X. Meng, G. Gomard, O. El Daif, E. Drouard, R. Orobtcouk, A. Kaminski, A. Fave, M. Lemiti, A. Abramov, P. Roca i Cabarrocas, and C. Seassal, *Absorbing photonic crystals for silicon thin-film solar cells: Design, fabrication and experimental investigation*, Solar Energy Materials and Solar Cells **95** (2011), S32–S38.
- [27] V. Depauw, X. Meng, O. El Daif, G. Gomard, L. Lalouat, E. Drouard, C. Trompoukis, A. Fave, C. Seassal, and I. Gordon, *Micrometer-Thin Crystalline-Silicon Solar Cells Integrating Numerically Optimized 2-D Photonic Crystals*, IEEE Journal of Photovoltaics **4** (2014), 215–223.
- [28] C. Becker, D. Lockau, T. Sontheimer, P. Schubert-Bischoff, E. Rudigier-Voigt, M. Bockmeyer, F. Schmidt, and B. Rech, *Large-area 2D periodic crystalline silicon nanodome arrays on nanoimprinted glass exhibiting photonic band structure effects.*, Nanotechnology **23** (2012), 135302.
- [29] J. Mutitu, S. Shi, C. Chen, and T. Creazzo, *Thin film solar cell design based on photonic crystal and diffractive grating structures*, Optics Express **16** (2008), 15238–15248.

- [30] P. Kowalczewski, M. Liscidini, and L. C. Andreani, *Engineering Gaussian disorder at rough interfaces for light trapping in thin-film solar cells.*, Optics letters **37** (2012), 4868–70.
- [31] A. Oskooi, P. A. Favuzzi, Y. Tanaka, H. Shigeta, Y. Kawakami, and S. Noda, *Partially disordered photonic-crystal thin films for enhanced and robust photovoltaics*, Applied Physics Letters **100** (2012), 181110.
- [32] C. Battaglia, C. Hsu, and K. Söderström, *Light trapping in solar cells: can periodic beat random?*, ACS Nano (2012), 2790–2797.
- [33] U. W. Paetzold, M. Smeets, M. Meier, K. Bittkau, T. Merdzhanova, V. Smirnov, D. Michaelis, C. Waechter, R. Carius, and U. Rau, *Disorder improves nanophotonic light trapping in thin-film solar cells*, Applied Physics Letters **104** (2014), 131102.
- [34] F. Pratesi, M. Burrelli, and F. Riboli, *Disordered photonic structures for light harvesting in solar cells*, Optics express **21** (2013), 460–468.
- [35] M. A. Green, *Third Generation Photovoltaics*, Springer, Berlin, 2003.
- [36] a. D. Vos, *Detailed balance limit of the efficiency of tandem solar cells*, Journal of Physics D: Applied Physics **13** (1980), 839–846.
- [37] A. Marti and G. Araújo, *Limiting efficiencies for photovoltaic energy conversion in multigap systems*, Solar Energy Materials and Solar Cells **43** (1996), 203–222.
- [38] M. Peters, J. C. Goldschmidt, P. Löper, B. Groß, J. Üpping, F. Dimroth, R. B. Wehrspohn, and B. Bläsi, *Spectrally-Selective Photonic Structures for PV Applications*, Energies **3** (2010), 171–193.
- [39] F. Dimroth, *World Record Solar Cell with 44.7 %Efficiency*, Tech. Report 22, 2013.
- [40] F. Dimroth, M. Grave, and P. Beutel, *Wafer bonded four-junction GaInP/GaAs//GaInAsP/GaInAs concentrator solar cells with 44.7 %efficiency*, Progress in Photovoltaics: Research and Applications **22** (2014), 277–282.

-
- [41] A. V. Shah, M. Van, J. Meier, F. Meillaud, J. Guillet, D. Fischer, C. Droz, X. Niquille, and S. Fa, *Basic efficiency limits, recent experimental results and novel light-trapping schemes in a-Si: H, μ c-Si: H and micromorph tandem solar cells*, Journal of Non-Crystalline (2004), 639–645.
- [42] D. L. Staebler and C. R. Wronski, *Reversible conductivity changes in discharge-produced amorphous Si*, Applied Physics Letters **31** (1977), 292.
- [43] N. P. Vaucher and J. Nagel, *Light management in tandem cells by an intermediate reflector layer*, Proceedings 2nd World Conference on Photovoltaic Energy Conversion (1998).
- [44] K. Yamamoto and A. Nakajima, *Novel hybrid thin film silicon solar cell and module*, Proceedings of 3rd PVWC (2003), 2789–2792.
- [45] D. Domine, J. Bailat, J. Steinhauser, A. Shah, and C. Ballif, *Micromorph Solar Cell Optimization using a ZnO Layer as Intermediate Reflector*, IEEE 4th World Conference on Photovoltaic Energy Conference, Ieee, 2006, pp. 1465–1468.
- [46] G. Bugnon, T. Söderström, S. Nicolay, L. Ding, M. Despeisse, A. Hedler, J. Eberhardt, C. Wachtendorf, and C. Ballif, *LPCVD ZnO-based intermediate reflector for micromorph tandem solar cells*, Solar Energy Materials and Solar Cells **95** (2011), 2161–2166.
- [47] P. Buehlmann, J. Bailat, D. Domine, A. Billet, F. Meillaud, A. Feltrin, and C. Ballif, *In situ silicon oxide based intermediate reflector for thin-film silicon micromorph solar cells*, Applied Physics Letters **91** (2007), 143505.
- [48] T. Grundler, A. Lambertz, and F. Finger, *N-type hydrogenated amorphous silicon oxide containing a microcrystalline silicon phase as an intermediate reflector in silicon thin film solar cells*, Physica Status Solidi (C) **1088** (2010), NA–NA.
- [49] A. Lambertz, V. Smirnov, T. Merdzhanova, K. Ding, S. Haas, G. Jost, R. Schropp, F. Finger, and U. Rau, *Microcrystalline silicon “oxygen alloys for application in silicon solar cells and modules*, Solar Energy Materials and Solar Cells **119** (2013), 134–143.

- [50] J. Joannopoulos, S. Johnson, J. Winn, and R. Meade, *Photonic crystals: molding the flow of light*, 2011.
- [51] A. Bielowny, P. T. Miclea, R. B. Wehrspohn, A. v. Rhein, C. Rockstuhl, M. Lisca, F. L. Lederer, L. B., R. Zentel, and R. Carius, *Diffraction and energy selective photonic crystals for thin-film tandem solar cells*, Solar Energy Materials & Solar Cells (2007).
- [52] P. O'Brien, A. Chutinan, and K. Leong, *Photonic crystal intermediate reflectors for micromorph solar cells: a comparative study*, Optics express **18** (2010), 1393–1399.
- [53] J. Üpping, A. Bielowny, R. B. Wehrspohn, T. Beckers, R. Carius, U. Rau, S. Fahr, C. Rockstuhl, F. Lederer, M. Kroll, T. Pertsch, L. Steidl, and R. Zentel, *Three-dimensional photonic crystal intermediate reflectors for enhanced light-trapping in tandem solar cells.*, Advanced Materials **23** (2011), 3896–900.
- [54] S. Fahr, C. Rockstuhl, and F. Lederer, *The interplay of intermediate reflectors and randomly textured surfaces in tandem solar cells*, Applied Physics Letters **97** (2010), 173510.
- [55] Z. Yu, A. Raman, and S. Fan, *Fundamental limit of nanophotonic light trapping in solar cells.*, Proceedings of the National Academy of Sciences of the United States of America **107** (2010), 17491–6.
- [56] C. Rockstuhl, F. Lederer, K. Bittkau, T. Beckers, and R. Carius, *The impact of intermediate reflectors on light absorption in tandem solar cells with randomly textured surfaces*, Applied Physics Letters **94** (2009), 211101.
- [57] P. Obermeyer, C. Haase, and H. Stiebig, *Advanced light trapping management by diffractive interlayer for thin-film silicon solar cells*, Applied Physics Letters **92** (2008), 181102.
- [58] A. Bielowny, J. Üpping, and R. Wehrspohn, *Spectral properties of intermediate reflectors in micromorph tandem cells*, Solar Energy Materials and Solar Cells **93** (2009), 1909–1912.

- [59] S. Kirner, M. Hammerschmidt, and C. Schwanke, *Implications of TCO Topography on Intermediate Reflector Design for a-Si/ μ c-Si Tandem Solar Cells - Experiments and Rigorous Optical Simulations*, IEEE Journal of Photovoltaics **4** (2014), 10–15.
- [60] M. Boccard, M. Despeisse, and J. Escarre, *High-Stable-Efficiency Tandem Thin-Film Silicon Solar Cell With Low-Refractive-Index Silicon-Oxide Interlayer*, IEEE Journal of Photovoltaics **4** (2014), 1368–1373.
- [61] M. A. Green, *Silicon wafer-based tandem cells: the ultimate solution*, Proceedings of SPIE (2013).
- [62] N. N. Lal, T. P. White, and K. R. Catchpole, *Optics and Light Trapping for Tandem Solar Cells on Silicon*, IEEE Journal of Photovoltaics (2014), 1–7.
- [63] B. W. Schneider, N. N. Lal, S. Baker-Finch, and T. P. White, *Pyramidal surface textures for light trapping and antireflection in perovskite-on-silicon tandem solar cells*, Optics Express **22** (2014), A1422.
- [64] J. Maxwell, *A Dynamical Theory of the Electromagnetic Field.*, Proceedings of the Royal Society of Science (1864).
- [65] J. D. Jackson, *Classical Electrodynamics Third Edition*, de Gruyter, Berlin, 2006.
- [66] M. Ermes, *Study of optical properties of individual layers and layer stacks as used in silicon based thin-film solar cells*, Ph.D. thesis, RWTH Aachen, 2010.
- [67] R. Brendel, *Thin-film silicon solar cells*, Wiley-VCH Verlag, 2003.
- [68] A. Beer, *Bestimmung der Absorption des rothen Lichts in farbigen Flüssigkeiten” (Determination of the absorption of red light in colored liquids)*, Annalen der Physik und Chemie **86** (1852), 78–88.
- [69] L. Novotny, *Light confinement in scanning near-field optical microscopy*, Ultramicroscopy **61** (1995), 1–9.
- [70] S. Ramo, J. R. Whinnery, and T. Van Duzer, *Fields and Waves in Communication Electronics*, Wiley, 1994.

- [71] F.-J. Haug, K. Söderström, A. Naqavi, and C. Ballif, *Resonances and absorption enhancement in thin film silicon solar cells with periodic interface texture*, Journal of Applied Physics **109** (2011), 084516.
- [72] C. Huygens, *Traite de la Lumière*, 1690.
- [73] L. Rayleigh, *On the remarkable phenomenon of crystalline reflexion described by Prof. Stokes*, The London, Edinburgh and Dublin Philosophical Magazine **26** (1888), 256–265.
- [74] H. Macleod, *Thin-film Optical Filters*, taylor ed., Francis, 2001.
- [75] E. Yablonovitch, *Inhibited spontaneous emission in solid-state physics and electronics*, Physical review letters **58** (1987), 2059–2062.
- [76] S. John, *Strong localization of photons in certain disordered dielectric superlattices*, Physical review letters **58** (1987).
- [77] T. Krauss, *Two-dimensional photonic-bandgap structures operating at near-infrared wavelength*, Nature (1996).
- [78] Y. Vlasov, X. Bo, J. Sturm, and D. Norris, *On-chip natural assembly of silicon photonic bandgap crystals*, Nature **414** (2001), 289–293.
- [79] E. Yablonovitch and T. Gmitter, *Photonic band structure: The face-centered-cubic case*, Physical Review Letters **63** (1989), 1950–1953.
- [80] S. Johnson and J. Joannopoulos, *Block-iterative frequency-domain methods for Maxwell’s equations in a planewave basis*, Optics Express **8** (2001), 363–376.
- [81] K. Tajima and J. Zhou, *Ultralow loss and long length photonic crystal fiber*, Journal of Lightwave Technology **22** (2004), 7–10.
- [82] P. Russell, *Photonic crystal fibers*, Science **299** (2003), 358–62.
- [83] P. Bermel, C. Luo, and L. Zeng, *Improving thin-film crystalline silicon solar cell efficiencies with photonic crystals*, Optics express **1113** (2007), 1104–1113.

- [84] P. Bienstman and R. Baets, *Optical modelling of photonic crystals and VC-SELs using eigenmode expansion and perfectly matched layers*, Optical and Quantum Electronics (2001), 327–341.
- [85] S. Byrnes, *Fresnel equation solver for multi- layer thin films*, 2011, pp. 1–15.
- [86] R. Haupt and S. Haupt, *Practical Genetic Algorithms*, 2004.
- [87] S. Krumscheid, *Optimizing the interconnection geometry of thin-film solar modules using the finite element method*, Ph.D. thesis, Aachen University of Applied Science, 2010.
- [88] C. Haase, D. Knipp, and H. Stiebig, *Optics of thin-film silicon solar cells with efficient periodic light trapping textures*, Proceedings of SPIE **6645** (2007), 66450W–66450W–9.
- [89] C. Rockstuhl, S. Fahr, F. Lederer, K. Bittkau, T. Beckers, and R. Carius, *Local versus global absorption in thin-film solar cells with randomly textured surfaces*, Applied Physics Letters **93** (2008), 061105.
- [90] U. Paetzold, *Optical simulations of microcrystalline silicon solar cells applying plasmonic reflection grating back contacts*, Journal of Photonics for Energy **2** (2012), 1–9.
- [91] D. Lockau and L. Zschiedrich, *Rigorous optical simulation of light management in crystalline silicon thin film solar cells with rough interface textures*, Proceedings of SPIE (2011).
- [92] M. Ermes, K. Bittkau, and R. Carius, *Comparison of light scattering in solar cells modeled by rigorous and scalar approach*, Journal of Applied Physics **113** (2013), 073104.
- [93] COMSOL, *COMSOL Wave Optics FEM*, 2014.
- [94] JCMwave, *JCM Suite*, <http://www.jcmwave.com/jcmsuite/jcmsuite-overview>, 2014.
- [95] J. Pomplun and E. al., *Adaptive finite element method for simulation of optical nano structures*, Phys. Status Solidi B (2007), 3419–3434.
- [96] S. Fan, *S4*, <http://web.stanford.edu/group/fan/S4/index.html>, 2014.

- [97] S. Fahr, T. Kirchartz, C. Rockstuhl, and F. Lederer, *Approaching the Lambertian limit in randomly textured thin-film solar cells*, Optics express **19** (2011), 899–907.
- [98] Innovent, *Diffraction model Rigorous Coupled Wave Analysis (RCWA)*, 2014.
- [99] CST, *CST Microwave Studio*, <https://www.cst.com/Products/CSTMWS>, 2014.
- [100] A. F. Oskooi, D. Roundy, M. Ibanescu, P. Bermel, J. Joannopoulos, and S. G. Johnson, *Meep: A flexible free-software package for electromagnetic simulations by the FDTD method*, Computer Physics Communications **181** (2010), 687–702.
- [101] Lumerical, *FDTD Solutions*, <https://www.lumerical.com/tcad-products/fdtd>, 2014.
- [102] Synopsys, *FullWAVE*, <http://optics.synopsys.com/rsoft/rsoft-passive-device-fullwave.html>, 2014.
- [103] M. Ermes, *Optical near-field investigations of photonic structures for application in silicon-based thin-film solar cells*, Ph.D. thesis, 2013.
- [104] A. Taflov, *Computational Electrodynamics: The Finite-Difference Time-Domain Method*, 3 ed., Artech House, 2005.
- [105] Wikispaces, *The Yee-Cell*, 12 2014.
- [106] J. Krc, F. Smole, and M. Topic, *Analysis of light scattering in amorphous Si:H solar cells by a one-dimensional semi-coherent optical model*, Progress in Photovoltaics: Research and Applications **11** (2003), 15–26.
- [107] M. Zeman, R. A. C. M. M. van Swaaij, J. W. Metselaar, and R. E. I. Schropp, *Optical modeling of a-Si:H solar cells with rough interfaces: Effect of back contact and interface roughness*, Journal of Applied Physics **88** (2000), 6436.
- [108] K. Jäger, O. Isabella, L. Zhao, and M. Zeman, *Light scattering properties of surface-textured substrates*, Physica Status Solidi (C) **948** (2010), 945–948.

- [109] J. E. Harvey, *Fourier treatment of near-field scalar diffraction theory*, American Journal of Physics **47** (1979), 974.
- [110] J. Harvey and C. Vernold, *Diffacted radiance: a fundamental quantity in nonparaxial scalar diffraction theory*, Applied Optics **38** (1999), 6469–6481.
- [111] D. Dominé, F.-J. Haug, C. Battaglia, and C. Ballif, *Modeling of light scattering from micro- and nanotextured surfaces*, Journal of Applied Physics **107** (2010), 044504.
- [112] K. Bittkau, M. Schulte, M. Klein, T. Beckers, and R. Carius, *Modeling of light scattering properties from surface profile in thin-film solar cells by Fourier transform techniques*, Thin Solid Films **519** (2011), 6538–6543.
- [113] K. Bittkau, W. Böttler, M. Ermes, V. Smirnov, and F. Finger, *Light scattering at textured back contacts for n-i-p thin-film silicon solar cells*, Journal of Applied Physics **111** (2012), 083101.
- [114] M. Schulte, K. Bittkau, K. Jäger, M. Ermes, M. Zeman, and B. E. Pieters, *Angular resolved scattering by a nano-textured ZnO/silicon interface*, Applied Physics Letters **99** (2011), 111107.
- [115] K. Bittkau, A. Hoffmann, and R. Carius, *Improvement of light trapping in thin-film silicon solar cells by combining periodic and random interfaces 1*, Canadian Journal of Physics **92** (2014), 888–891.
- [116] K. Bittkau and A. Hoffmann, *Optical simulation of photonic random textures for thin-film solar cells*, Proceedings of SPIE (2014).
- [117] K. Bittkau, M. Schulte, T. Beckers, and R. Carius, *Fourier analysis for the study of light scattering properties of randomly textured ZnO films*, Proceedings of SPIE **5** (2010), 77250N–77250N–8.
- [118] A. Einstein, *über einen die Erzeugung und Verwandlung des Lichtes betreffenden heuristischen Gesichtspunkt*, Annalen der Physik (1905).
- [119] C. Gueymard, D. Myers, and K. Emery, *Proposed reference irradiance spectra for solar energy systems testing*, Solar energy **73** (2002), 443–467.

- [120] A. S. for Testing and M. (ASTM), *Standard Tables for References Solar Spectral Irradiance at Air Mass 1.5: Direct Normal and Hemispherical for a 37° Tilted Surface*, (2005).
- [121] P. Siffert and E. Krimmel, *Silicon - Evolution and Future of a Technology*, Springer, 2004.
- [122] J. Zhao, A. Wang, P. Altermatt, and M. A. Green, *Twenty-four percent efficient silicon solar cells with double layer antireflection coatings and reduced resistance loss*, Applied Physics Letters **66** (1995), 3636.
- [123] J. Zhao, A. Wang, M. A. Green, and F. Ferrazza, *19.8 %Efficient 'Honeycomb' Textured Multicrystalline and 24.4 %Monocrystalline Silicon Solar Cells*, Applied Physics Letters **73** (1998), 1991.
- [124] M. Green and M. Keevers, *Optical properties of intrinsic silicon at 300 K*, Prog. in Photov.: Res. and App. (1995), 189—192.
- [125] R. Scheer and H.-W. Schock, *Chalcogenide Photovoltaics Physics, Technologies, and Thin Film Devices*, 2011.
- [126] B. O'Regan and M. Grätzel, *A low-cost, high efficiency solar cell based on dye-sensitized colloidal TiO₂ films*.
- [127] C. J. Brabec, V. Dyakonov, J. Parisi, and N. Serdar Sariciftci, *Organic Photovoltaics: Concepts and Realization*, Wiley-VCH Verlag, 2003.
- [128] M. A. Green, A. Ho-Baillie, and H. J. Snaith, *The emergence of perovskite solar cells*, Nature Photonics **8** (2014), 506–514.
- [129] E. Yablonovitch, *Statistical ray optics*, Journal of the Optical Society of America **72** (1982), 899.
- [130] T. Tiedje, E. Yablonovitch, G. D. Cody, and B. G. Brooks, *Limiting Efficiency of Silicon*, IEEE Transactions on Electron Devices (1984), 711–716.
- [131] H. W. Deckman, *Optically enhanced amorphous silicon solar cells*, Applied Physics Letters **42** (1983), 968.
- [132] V. K. Narasimhan and Y. Cui, *Nanostructures for photon management in solar cells*, Nanophotonics **2** (2013), 1–24.

- [133] J. Eisenlohr, J. Benick, and M. Peters, *Hexagonal sphere gratings for enhanced light trapping in crystalline silicon solar cells*, Optics Express **22** (2014), 1529–1533.
- [134] Z. Yu, A. Raman, and S. Fan, *Fundamental limit of nanophotonic light trapping in solar cells.*, Proceedings of the National Academy of Sciences of the United States of America **107** (2010), 17491–6.
- [135] X. Sheng, L. Z. Broderick, and L. C. Kimerling, *Photonic crystal structures for light trapping in thin-film Si solar cells: Modeling, process and optimizations*, Optics Communications **314** (2014), 41–47.
- [136] R. L. Moon, L. W. James, H. A. Vander Plas, T. O. Yep, G. A. Antypas, and Y. Chai, *Multi Gap Solar Cell Requirements an the Performance of AlGaAs and Si Cells in Concentrated Sunlight*, Conference Record of the IEEE Photovoltaic Specialists Conference (1978), 859–867.
- [137] M. A. Green and A. Ho-Baillie, *Forty three per cent composite split-spectrum concentrator solar cell efficiency*, Progress in Photovoltaics: Research and Applications **18** (2010), 42–47.
- [138] N. Mingirulli, J. Haschke, R. Gogolin, R. Ferré, T. F. Schulze, J. Düsterhöft, N.-P. Harder, L. Korte, R. Brendel, and B. Rech, *Efficient interdigitated back-contacted silicon heterojunction solar cells*, physica status solidi (RRL) - Rapid Research Letters **5** (2011), 159–161.
- [139] A. Mojiri, R. Taylor, E. Thomsen, and G. Rosengarten, *Spectral beam splitting for efficient conversion of solar energy: A review*, Renewable and Sustainable Energy Reviews **28** (2013), 654–663.
- [140] C. Ulbrich, C. Zahren, and A. Gerber, *Matching of Silicon Thin-Film Tandem Solar Cells for Maximum Power Output*, International Journal of Photoenergy **2013** (2013).
- [141] B. Rech, T. Repmann, M. van den Donker, M. Berginski, T. Kilper, J. Hüpkes, S. Calnan, H. Stiebig, and S. Wieder, *Challenges in microcrystalline silicon based solar cell technology*, Thin Solid Films **511-512** (2006), 548–555.

- [142] R. A. Street, J. E. Northrup, and B. S. Krusor, *Radiation induced recombination centers in organic solar cells*, Physical Review B **85** (2012), 205211.
- [143] A. Lambertz, F. Finger, B. Holländer, J. Rath, and R. Schropp, *Boron-doped hydrogenated microcrystalline silicon oxide ($\mu\text{-SiO}_x\text{:H}$) for application in thin-film silicon solar cells*, Journal of Non-Crystalline Solids **358** (2012), 1962–1965.
- [144] V. Ganapati, C. Ho, and E. Yablonovitch, *Intermediate Mirrors to Reach Theoretical Efficiency Limits of Multi-Bandgap Solar Cells*, arXiv preprint arXiv:1406.3126 (2014).
- [145] G. Jost, T. Merdzhanova, T. Zimmermann, and J. Hüpkes, *Process monitoring of texture-etched high-rate ZnO:Al front contacts for silicon thin-film solar cells*, Thin Solid Films **532** (2013), 66–72.
- [146] M. Boccard, T. Soderstrom, P. Cuony, C. Battaglia, S. Hänni, S. Nicolay, L. Ding, M. Benkhaira, G. Bugnon, A. Billet, M. Charrière, F. Meillaud, M. Despeisse, and C. Ballif, *Optimization of ZnO front electrodes for high-efficiency micromorph thin-film Si solar cells*, IEEE Journal of Photovoltaics **2** (2012), 229–235.
- [147] L. Ding, L. Fanni, D. Messerschmidt, S. Zabihzadeh, M. M. Masis, S. Nicolay, and C. Ballif, *Tailoring the surface morphology of zinc oxide films for high-performance micromorph solar cells*, Solar Energy Materials and Solar Cells **128** (2014), 378–385.
- [148] O. Kluth, B. Rech, L. Houben, and S. Wieder, *Texture etched ZnO: Al coated glass substrates for silicon based thin film solar cells*, Thin Solid Films **351** (1999), 247–253.
- [149] J. I. Owen, J. Hüpkes, H. Zhu, E. Bunte, and S. E. Pust, *Novel etch process to tune crater size on magnetron sputtered ZnO:Al*, Physica Status Solidi (a) **208** (2011), 109–113.
- [150] J. I. Owen, *Growth, Etching and Stability of Sputtered ZnO:Al for Thin-Film Silicon Solar Cells*, Ph.D. thesis, RWTH Aachen, 2011.

- [151] O. Vetterl, P. Hapke, O. Kluth, A. Lambertz, S. Wieder, B. Rech, F. Finger, and H. Wagner, *Intrinsic Microcrystalline Silicon for Solar Cells*, Solid State Phenomena **67** (1999), 101–106.
- [152] R. A. Street, *Hydrogenated Amorphous Silicon*, Cambridge University Press, Cambridge, 1991.
- [153] S. Klein, T. Repmann, and T. Brammer, *Microcrystalline silicon films and solar cells deposited by PECVD and HWCVD*, Solar Energy **77** (2004), 893–908.
- [154] M. Houben, L. Luysberg, P. Hapkea, R. Carius, F. Finger, and H. Wagner, *Structural properties of microcrystalline silicon in the transition from highly crystalline to amorphous growth*, Philosophical Magazine A **77** (1998), 1447–1460.
- [155] P. Cuony, D. T. L. Alexander, I. Perez-Wurfl, M. Despeisse, G. Bugnon, M. Boccard, T. Söderström, A. Hessler-Wyser, C. Hébert, and C. Ballif, *Silicon filaments in silicon oxide for next-generation photovoltaics.*, Advanced materials **24** (2012), 1182–6.
- [156] W. Reetz, T. Kirchartz, A. Lambertz, J. Hüpkens, and A. Gerber, *Current-voltage and spectral response based characterization of thin film silicon solar cells – investigation of primary error sources*, Proc. 24th EUPVSEC (2009).
- [157] M. Schulte, *Streuverhalten von texturierten TCO-Substraten in Silizium-Dünnschichtsolarzellen*, Ph.D. thesis, RWTH Aachen, 2009.
- [158] W. Jackson, N. Amer, A. Boccara, and D. Fournier, *Photothermal deflection spectroscopy and detection*, Applied Optics **20** (1981), 1333–1344.
- [159] F. Becker, R. Carius, J.-T. Zettler, J. Klomfass, C. Walker, and H. Wagner, *Photothermal Deflection Spectroscopy on Amorphous Semiconductor Heterojunctions and Determination of the Interface Defect Densities*, Materials Science Forum **173-174** (1995), 177–182.
- [160] W. Theiss, *SCOUT Software Package*.
- [161] J. Jülich Supercomputing Center, *JUROPA / HPC-FF*, 2014.

- [162] D. Lockau and L. Zschiedrich, *Rigorous optical simulation of light management in crystalline silicon thin film solar cells with rough interface textures*, Proceedings of SPIE (2011).
- [163] D. Lockau, *Optical modeling of thin film silicon solar cells with random and periodic light management textures*, Ph.D. thesis, TU Berlin, 2013.
- [164] J. Krc, F. Smole, and M. Topic, *Optical simulation of the role of reflecting interlayers in tandem micromorph silicon solar cells*, Solar Energy Materials and Solar Cells **86** (2005), 537–550.
- [165] D. Dominé, P. Buehlmann, J. Bailat, A. Billet, A. Feltrin, and C. Ballif, *Optical management in high-efficiency thin-film silicon micromorph solar cells with a silicon oxide based intermediate reflector*, physica status solidi (RRL) - Rapid Research Letters **2** (2008), 163–165.
- [166] F. Ruske, M. Roczen, K. Lee, M. Wimmer, S. Gall, J. Hüpkes, D. Hrunski, and B. Rech, *Improved electrical transport in Al-doped zinc oxide by thermal treatment*, Journal of Applied Physics **107** (2010), 013708.
- [167] E. Schumann, *Entwicklung eines Laserprozesses zur gezielten Veränderung elektrooptischer Eigenschaften von Zinkoxid*, Ph.D. thesis, RWTH Aachen, 2012.
- [168] Z.-C. Jin, I. Hamberg, and C. G. Granqvist, *Optical properties of sputter-deposited ZnO:Al thin films*, Journal of Applied Physics **64** (1988), 5117.
- [169] A. Hoffmann, U. W. Paetzold, C. Zhang, T. Merdzhanova, A. Lambertz, C. Ulbrich, K. Bittkau, and U. Rau, *Advancing tandem solar cells by spectrally selective multilayer intermediate reflectors*, Opt. Express **22** (2014), A1270–A1277.
- [170] B. G. Bovard, *Rugate filter theory*, Applied Optics **32** (1993), 5427–5442.
- [171] S. Fahr, C. Ulbrich, T. Kirchartz, and U. Rau, *Rugate filter for light-trapping in solar cells*, Optics Express **16** (2008), 9332–9343.
- [172] P. G. O’Brien, D. P. Puzzo, A. Chutinan, L. D. Bonifacio, G. a. Ozin, and N. P. Kherani, *Selectively transparent and conducting photonic crystals.*, Advanced Materials **22** (2010), 611–6.

- [173] P. G. O'Brien, Y. Yang, A. Chutinan, P. Mahtani, K. Leong, D. P. Puzzo, L. D. Bonifacio, C.-W. Lin, G. A. Ozin, and N. P. Kherani, *Selectively transparent and conducting photonic crystal solar spectrum splitters made of alternating sputtered indium-tin oxide and spin-coated silica nanoparticle layers for enhanced photovoltaics*, Solar Energy Materials and Solar Cells **102** (2012), 173–183.
- [174] C. Rockstuhl and F. Lederer, *The effect of disorder on the local density of states in two-dimensional quasi-periodic photonic crystals*, New Journal of Physics **8** (2006), 206–206.
- [175] P. Chen, G. Hou, Q. Fan, Q. Huang, J. Zhao, J. Zhang, J. Ni, X. Zhang, and Y. Zhao, *An efficient light trapping scheme based on textured conductive photonic crystal back reflector for performance improvement of amorphous silicon solar cells*, Applied Physics Letters **105** (2014), 073506.
- [176] J. Üpping, *3D-photonische Kristalle für photovoltaische Anwendungen*, Ph.D. thesis, Martin-Luther-Universität Halle-Wittenberg, 2011.
- [177] S. Fahr, C. Rockstuhl, and F. Lederer, *Sandwiching intermediate reflectors in tandem solar cells for improved photon management*, Applied Physics Letters **101** (2012), 133904.
- [178] S. Fahr, *Photon-Management in Dünnschicht-Solarzellen Dissertation*, Ph.D. thesis, Friederich-Schiller Universität Jena, 2011.
- [179] T.-T. Kim, S.-G. Lee, M.-W. Kim, H. Y. Park, and J.-E. Kim, *Experimental demonstration of reflection minimization at two-dimensional photonic crystal interfaces via antireflection structures*, Applied Physics Letters **95** (2009), 011119.
- [180] S. Fahr, C. Rockstuhl, and F. Lederer, *Improving the efficiency of thin film tandem solar cells by plasmonic intermediate reflectors*, Photonics and Nanostructures - Fundamentals and Applications **8** (2010), 291–296.
- [181] H. A. Atwater and A. Polman, *Plasmonics for improved photovoltaic devices.*, Nature materials **9** (2010), 205–13.

- [182] F. Kretschmer and M. Fruhnert, *Plasmonic nanoparticle clusters with tunable plasmonic resonances in the visible spectral region*, Journal of Materials Chemistry C (2014), 6415–6422.
- [183] F. Kretschmer, S. Mühlig, S. Hoeppener, A. Winter, M. D. Hager, C. Rockstuhl, T. Pertsch, and U. S. Schubert, *Survey of Plasmonic Nanoparticles: From Synthesis to Application*, Particle & Particle Systems Characterization **31** (2014), 721–744.
- [184] N. P. Hylton, X. F. Li, V. Giannini, K.-H. Lee, N. J. Ekins-Daukes, J. Loo, D. Vercrusse, P. Van Dorpe, H. Sodabanlu, M. Sugiyama, and S. a. Maier, *Loss mitigation in plasmonic solar cells: aluminium nanoparticles for broadband photocurrent enhancements in GaAs photodiodes.*, Scientific reports **3** (2013), 2874.
- [185] G. Li, H. Li, J. Y. L. Ho, M. Wong, and H. S. Kwok, *Nanopyramid structure for ultrathin c-Si tandem solar cells.*, Nano letters **14** (2014), 2563–8.
- [186] A. CìEampa, O. Isabella, R. van Erven, P. Peeters, H. Borg, M. TopicìE, and M. Zeman, *Optimal design of periodic surface texture for thin-film a-Si:H solar cells*, Progress in Photovoltaics: Research and Applications **18** (2010), 160–167.
- [187] E. Moulin, U. W. Paetzold, J. Kirchhoff, A. Bauer, and R. Carius, *Study of detached back reflector designs for thin-film silicon solar cells*, physica status solidi (RRL) - Rapid Research Letters **6** (2012), 65–67.
- [188] K. Bittkau and T. Beckers, *Near-field study of light scattering at rough interfaces of a-Si:H/ μ c-Si:H tandem solar cells*, Physica Status Solidi (a) **207** (2010), 661–666.
- [189] C. Zhang, M. Meier, W. Zhang, K. Bittkau, G. Jost, U. W. Paetzold, M. Ermes, and T. Merdzhanova, *Influence of Interface Textures on Light Management in Thin-Film Silicon Solar Cells With Intermediate Reflector*, IEEE Journal of Photovoltaics (2014), 1–7.
- [190] P. Kowalczewski, M. Liscidini, and L. C. Andreani, *Engineering Gaussian disorder at rough interfaces for light trapping in thin-film solar cells.*, Optics letters **37** (2012), 4868–70.

- [191] P. Obermeyer, *Entwicklung von spektral selektiven Zwischenreflektoren für Dünnschichtsolarzellen*, Ph.D. thesis, RWTH Aachen, 2008.
- [192] V. Jovanov, X. Xu, S. Shrestha, M. Schulte, J. Hüpkens, M. Zeman, and D. Knipp, *Influence of interface morphologies on amorphous silicon thin film solar cells prepared on randomly textured substrates*, Solar Energy Materials and Solar Cells **112** (2013), 182–189.
- [193] V. Jovanov, X. Xu, and S. Shrestha, *Predicting the interface morphologies of silicon films on arbitrary substrates: application in solar cells*, ACS Applied Materials & Interfaces (2013).
- [194] M. Sever, B. Lipovšek, J. Krč, A. Čampa, G. Sánchez Plaza, F.-J. Haug, M. Duchamp, W. Soppe, and M. Topič, *Combined model of non-conformal layer growth for accurate optical simulation of thin-film silicon solar cells*, Solar Energy Materials and Solar Cells **119** (2013), 59–66.
- [195] Z. Yu, A. Raman, and S. Fan, *Fundamental limit of light trapping in grating structures*, Optics express **18** (2010), 366–380.
- [196] S. Kirner, S. Calnan, O. Gabriel, S. Neubert, M. Zelt, B. Stannowski, B. Rech, and R. Schlattmann, *An improved silicon-oxide-based intermediate-reflector for micromorph solar cells*, Physica Status Solidi (C) **9** (2012), 2145–2148.
- [197] J. Ostertag and I. Ramsteiner, *Experimental and simulation study of thin film silicon solar cells with intermediate reflector*, Progress in Photovoltaics: Research and Application (2013).
- [198] G. Li, H. Li, J. Y. L. Ho, M. Wong, and H. S. Kwok, *Nanopyramid structure for ultrathin c-Si tandem solar cells.*, Nano letters **14** (2014), 2563–8.
- [199] A. Čampa, M. Meier, M. Boccard, L. Mercaldo, M. Ghosh, C. Zhang, T. Merdzhanova, J. Krč, F.-J. Haug, and M. Topič, *Micromorph silicon solar cell optical performance: Influence of intermediate reflector and front electrode surface texture*, Solar Energy Materials and Solar Cells **130** (2014), 401–409.

- [200] T. Söderström, F.-J. Haug, X. Niquille, V. Terrazzoni, and C. Ballif, *Asymmetric intermediate reflector for tandem micromorph thin film silicon solar cells*, Applied Physics Letters **94** (2009), 063501.
- [201] C. Rockstuhl, S. Fahr, and K. Bittkau, *Comparison and optimization of randomly textured surfaces in thin-film solar cells*, Optics express **18** (2010), 335–342.
- [202] C. Battaglia, J. Escarré, K. Söderström, L. Erni, L. Ding, G. Bugnon, A. Bilet, M. Boccard, L. Barraud, S. De Wolf, F.-J. Haug, M. Despeisse, and C. Ballif, *Nanoimprint lithography for high-efficiency thin-film silicon solar cells.*, Nano letters **11** (2011), 661–5.
- [203] T. Grundler, *Silicon Oxide as an Intermediate Reflector in Silicon Thin Film Solar Cells*, Ph.D. thesis, RWTH Aachen, 2009.
- [204] A. Lambertz, T. Grundler, and F. Finger, *Hydrogenated amorphous silicon oxide containing a microcrystalline silicon phase and usage as an intermediate reflector in thin-film silicon solar cells*, Journal of Applied Physics **109** (2011), 113109.
- [205] P. Laven, *Mieplot*, <http://philiplaven.com/mieplot.htm>, 2014.
- [206] C. F. Bohren and D. R. Huffman, *Absorption and scattering of light by small particles*, John Wiley, New York, 1983.

B. Publications

B.1. Journal publications related to this work

- **Hoffmann, A.**, Bittkau, K., Zhang, C., Meier, M., Carius, R., Rau, U.
Photon Tunneling in Tandem Solar Cells With Intermediate Reflector, IEEE Journal of Photovoltaics 6 (3), 2532468, pp. 597 - 603 (2016)
- Zhang, C., Meier, M. , **Hoffmann, A.** , Zhang W. , Bittkau, K. , Jost, G. , Paetzold, U.W. , Ermes, M. , Merdzhanova, T.
Influence of interface textures on light management in thin-film silicon solar cells with intermediate reflector, IEEE Journal of Photovoltaics 5 (1), 6960073, pp. 33-39 (2014)
- **Hoffmann, A.**, Bittkau, K., Zhang, C., Merdzhanova, T., Rau, U.
Coupling incident light to guided modes in thin-film tandem solar cells with intermediate reflector, IEEE Journal of Photovoltaics 5 (1), 6936859, pp. 3-8 (2014)
- **Hoffmann, A.** , Paetzold, U.W., Zhang, C., Merdzhanova, T., Lambertz, A., Ulbrich, C., Bittkau, K., Rau, U.
Advancing tandem solar cells by spectrally selective multilayer intermediate reflectors Optics Express 22 (SUPPL. 5), pp. A1270-A1277 (2014)
- Bittkau, K., **Hoffmann, A.**
Optical simulation of photonic random textures for thin-film solar cells, Proceedings of SPIE - The International Society for Optical Engineering 9140, 91400L (2014)
- Bittkau, K., **Hoffmann, A.**, Carius, R.
Improvement of light trapping in thin-film silicon solar cells by combining periodic and random interfaces, Canadian Journal of Physics 92 (7-8), pp. 888-891 (2014)

- **Hoffmann, A.**, Paetzold, U.W., Merdzhanova, T., Lambertz, A., Höhn, O., Ulbrich, C., Bittkau, K., Rau, U.
Spectrally selective intermediate reflectors for tandem thin-film silicon solar cells, Proceedings of SPIE - The International Society for Optical Engineering (2013)

B.2. Further contributions to journal publications

- Moulin, E., Müller, T.C.M., Warzecha, M., **Hoffmann, A.**, Paetzold, U.W., Aeberhard, U.
Highly transparent front electrodes with metal fingers for p-i-n thin-film silicon solar cells, EPJ Photovoltaics 6, 60501 (2015)
- **Hoffmann, A.**, Jost, G., Bittkau, K., Carius, R.
Correlation between surface topography and short-circuit current density for thin-film silicon solar cells, Proceedings of SPIE - The International Society for Optical Engineering 8438, 84381H (2012)
- Höhn, O., Peters, M., Ulbrich, C., **Hoffmann, A.**, Schwarz, U.T., Bläsi, B.
Optimization of angularly selective photonic filters for concentrator photovoltaic, Proceedings of SPIE - The International Society for Optical Engineering 8438, 84380A (2012)

C. Danksagung

Auf unterschiedlichste Weise haben verschiedenste Menschen zum Gelingen dieser Arbeit beigetragen. Ihnen gebührt mein Dank.

- Prof. Uwe Rau für seine Inspiration, hervorragende Ideen und Visionen. Vielen Dank auch für die sehr angenehme Institutsatmosphäre, Ihren Einsatz für gute Doktorandenbetreuung und die Unterstützung von interdisziplinären Zusatzangeboten.
- Dr. Karsten Bittkau für seine gute Betreuung, seine hervorragenden Ideen und sein sehr guter wissenschaftlicher Sachverstand. Seine Tür war immer offen und seine Geduld hat mich selbst in stressigen und verzweifelte Zeiten immer wieder auf den Boden geholt.
- Prof. Ralf B. Wehrspohn für die freundliche Annahme des Zweitprüfers und für die Koordination eines inspirierenden Projektes, gute wissenschaftliche Diskussionen und kritische Fragen.
- Prof. R. Carius für gute wissenschaftliche Diskussionen, das Teilen seinen reichen Erfahrungsschatzes, jede Menge kritischen Fragen und seine Begeisterung für die Nanooptik.
- Dr. Ulrich W. Paetzold für seine Unterstützung, kritische Fragen und für das Teilen seines Wissens zum wissenschaftlichen Schreiben, optischen Simulationen und Prototypen.
- Dr. Carolin Ulbrich für wissenschaftliche und persönliche Beratung und Diskussion und dafür mich einer Menge Leute vorzustellen.
- Dr. Markus Ermes für die Einführung in das High Performance Computing, für technischen Support und die gute Zusammenarbeit im Bereich Supercomputing und optische Simulationen.

- Andrea Mülheims and Petra Lorbach für eine reibunsarme Administration im Institut.
- Dr. Stephan Lehen für unzählige wissenschaftliche Diskussionen, Zusammenarbeit im Labor, seinen unvergleichlichen Humor und Korrekturlesen. Chao Zhang für Diskussionen, Depositionen und eine hervorragende Zusammenarbeit. Nicolas Sommer für unzählige gute Diskussionen, wissenschaftlichen Rat und eine hervorragende Büroatmosphäre im Büro 24. Michael Smeets für spannende Diskussionen, Korrekturlesen und die Zusammenarbeit beim Prototyping. Unserer 'späten' Essensgruppe für die intensiven Diskussionen beim Essen.
- Dr. Andreas Lambertz für sein Wissen über Dünnschichtsilizium, unzählige Diskussionen über Zwischereflektoren und $\mu\text{-SiO}_x\text{:H}$. Dr. Matthias Meier, Michael Ghosh und Dr. Tsevetelina Merzhandonova für fruchtbare Diskussionen zu Tandemsolarzellen.
- Joachim Kirchhof für seine hervorragende Arbeit bei der Deposition von Dünnschichtsolarzellen und das richtige Gespür für das Detail.
- Hilde Siekmann, Ulrike Gerhards, Peter Hennigs, Josef Klomfass, Oliver Thimm, Alain Doumit, Andreas Bauer, Markus Hülsbeck, Wilfried Reetz, Christoph Zahren, Sandra Moll für die technische Unterstützungen, sowie zahlreiche Messungen und Depositionen.
- Dr. Bart E. Pieters und Dr. Urs Aeberhardt für einen Einblick in verschiedenste Typen von Simulationen und ein offenes Ohr für Code Probleme.
- Martin Vieten für die Einführung in genetische Algorithmen und die Bereitstellung seines Codes..
- Jülich Supercomputing Center (JSC) für die Bereitstellung einer sehr guten Supercomputing Infrastruktur und guten Support.
- Ich Projektpartner im InfraVolt Konsortium, vor allem Matthias Zilk, Oliver Höhn, Deepu Kumar, Dr. Alexander Spraffke, Daniela Schneevoigt und Prof. von Plessen für unzählige Diskussionen und eine gute Zusammenarbeit.
- Ich danke der Rurtalbahn Pendelgruppe für eine angenehme 'quality time' selbst bei Bahnverspätungen.

-
- Margreth und Johannes Hoffmann für eine großartige Kindheit und alles was sie für mich getan haben.
 - Nicht zuletzt danke ich all den anderen, mit denen ich in den letzten Jahren zusammenarbeiten durfte für eine sehr angenehme Zeit.

D. Curriculum Vitae

Name: André Hoffmann
Address: Reissstraße 2
50823 Köln
E-Mail: andre.hoffmann@rwth-aachen.de
Date of Birth: 07.05.1985
Place of Birth: Aachen, Germany

Education and Professional Experience

from 2016 Next Level Integration GmbH
2011-2015 PhD candidate at IEK-5 Photovoltaics, Forschungszentrum Jülich
(Jülich, Germany)
2005-2011 Diploma studies Physics RWTH Aachen (Aachen, Germany)
Major subject: Solid State Physics
Diploma Thesis at Forschungszentrum Jülich IEK 5- Photovoltaics
2009 Abroad semester Universidad Santa Maria (Valparaíso, Chile)
2008-2009 Abroad semester Universitat Valencia
2006-2010 Laboratory assistant for measuring instrumentation at OWI Aachen gGmbH
(Aachen, Germany)
1994-2004 Grammar School: Städtisches Gymnasium Eschweiler
(Eschweiler, Germany)

Band / Volume 333

Temperature Dependence of Carbon Kinetic Isotope Effect for The Oxidation Reaction of Ethane by Hydroxyl Radicals Under Atmospherically Relevant Conditions: Experimental and Theoretical Studies

T. Piansawan (2016), 196 pp

ISBN: 978-3-95806-166-8

Band / Volume 334

Konzeption von Membranmodulen zur effizienten Abtrennung von Kohlendioxid aus Gasgemischen

S. Luhr (2016)

ISBN: 978-3-95806-170-5

Band / Volume 335

Einfluss fehlpassungsinduzierter Spannungsfelder auf den Transportprozess bei ionischer Leitung

J. Keppner (2016), viii, 171 pp

ISBN: 978-3-95806-171-2

Band / Volume 336

Production and Characterization of Monodisperse Uranium Particles for Nuclear Safeguards Applications

A. Knott (2016), A-H, 123, xxviii, xiii pp

ISBN: 978-3-95806-172-9

Band / Volume 337

3D hydrological simulation of a forested headwater catchment: Spatio-temporal validation and scale dependent parameterization

Z. Fang (2016), XVII, 119 pp

ISBN: 978-3-95806-174-3

Band / Volume 338

Influence of Thermomechanical Treatment on High Temperature Properties of Laves Phase Strengthened Ferritic Steels

M. Talík (2016), xxiii, 130 pp

ISBN: 978-3-95806-175-0

Band / Volume 339

Groundwater recharge in Slovenia

Results of a bilateral German-Slovenian Research project

Mišo Andjelov, Zlatko Mikulič, Björn Tetzlaff, Jože Uhan & Frank Wendland (2016)

ISBN: 978-3-95806-177-4

Band / Volume 340

**Atomic oxygen derived from SCIAMACHY O(¹S)
and OH airglow measurements in the Mesopause region**

Y. Zhu (2016), 206 pp

ISBN: 978-3-95806-178-1

Band / Volume 341

**Diagnostic Mirror Concept Development for Use
in the Complex Environment of a Fusion Reactor**

A. Krimmer (2016), x, 123 pp

ISBN: 978-3-95806-180-4

Band / Volume 342

**Long-Term Measurements of the Radiation Exposure of the Inhabitants
of Radioactively Contaminated Regions of Belarus –
The Korma Report II (1998 – 2015)**

P. Zoriy, H. Dederichs, J. Pillath, B. Heuel-Fabianek, P. Hill, R. Lennartz
(2016), ca 105 pp

ISBN: 978-3-95806-181-1

Band / Volume 343

**Entwicklung und Charakterisierung von Nickel/Gadolinium-Ceroxid-
basierten Anoden für die metallgestützte Festoxid-Brennstoffzelle**

V. Rojek-Wöckner (2016), XVI, 136 pp

ISBN: 978-3-95806-182-8

Band / Volume 344

**Reaction-diffusion modelling of hydrogen retention
and release mechanisms in beryllium**

M. Wensing (2016), 100 pp

ISBN: 978-3-95806-184-2

Band / Volume 345

**Light Management by Intermediate Reflectors
in Silicon-based Tandem Solar Cells**

A. Hoffmann (2016), 197 pp

ISBN: 978-3-95806-186-6

Weitere **Schriften des Verlags im Forschungszentrum Jülich** unter
<http://www.wzb1.fz-juelich.de/verlagextern1/index.asp>

Energie & Umwelt /
Energy & Environment
Band / Volume 345
ISBN 978-3-95806-186-6

